

Higgs-pair production via gluon fusion at NLO QCD in the Standard Model and Beyond

Thesis presented for the Degree of Doctor of Philosophy

Author:

Jonathan Ronca

Under the supervision of:

Francisco Campanario



VNIVERSITAT DE VALÈNCIA

Programa Oficial de Doctorado en Física

Instituto de Física Corpuscular, Departamento de Física Teórica
Universitat de València - Consejo Superior de Investigaciones Científicas

December 2020

Francisco Campanario Pallás, Investigador Ramón y Cajal del Departamento de Física Teórica de la Universidad de Valencia,

CERTIFICA que la presente memoria “**Higgs-pair production via gluon fusion at NLO QCD in Standard Model and Beyond**” ha sido realizada bajo su dirección, en el Departamento de Física Teórica de la Universidad de Valencia, por D. **Jonathan Ronca**, y constituye su Tesis Doctoral para optar al grado de Doctor por la Universidad de Valencia.

Y para que así conste, en cumplimiento de la legislación vigente, presenta ante la Facultad de Física de la Universidad de Valencia la referida memoria, y firma el presente certificado

en Burjassot, a 16 de Diciembre de 2020

Francisco Campanario Pallás

Abstract

The discovery of a neutral scalar boson compatible with the Standard Model Higgs boson in 2012 has opened the possibility of studying the Higgs potential. The current experimental uncertainties do not preclude this particle from belonging to models beyond the Standard. The study of the Higgs self-interactions is needed to clarify its nature.

The quartic Higgs self-coupling is out of reach from the experimental perspective. However, the future upgrade of the LHC and other colliders will open the possibility of investigating the trilinear Higgs self-coupling. A direct measurement of the trilinear Higgs coupling involves the Higgs-pair production channels. The dominant channel is the QCD induced gluon fusion with top-quark loops. A next-to-leading order calculation is mandatory to accomplish the demanded precision for a comparison with the experimental data.

The Feynman diagrams contributing to the cross section virtual corrections contain four-point two-loop Feynman integrals, which represent the nowadays bottleneck for many higher order corrections. Since an analytical calculation is not a viable strategy yet, a numerical approach is needed. A general numerical framework which includes both Standard Model and Two-Higgs-Doublets model is presented in this thesis. The crucial part of the calculation is the isolation and cancellation of the ultraviolet and infrared divergences coming from the (divergent) Feynman integrals. The ultraviolet divergences will be isolated through the end-point subtraction, the infrared ones by a dedicated subtraction term motivated by the heavy-quark limit calculation. The remaining part of the virtual amplitude can be computed by considering the single-Higgs production amplitude and the Higgs decay into a Z boson and a photon. The real corrections are calculated using public libraries for one-loop integral calculations. The outcome of this study is the differential cross section depending on the Higgs-pair invariant mass and its integral, namely the NLO Higgs-pair production via gluon fusion total cross section.

The top-mass effects at next-to-leading order introduce a significant deviation of the differential cross section from its heavy quark limit of more than 20% in the tail, which increases with the collider energy as well. This deviation at the level of the differential cross section is reflected in a decreasing of the total hadronic cross section by 15%. The uncertainties related with the choice of the top-mass renormalization scale and scheme are proven to be sizable. Such uncertainties are of the same order of the usual strong coupling renormalization and factorization scale ones, bringing a strong impact on the estimation of the theoretical uncertainties.

Contents

Resumen	v
Introduction	xiii
1 Theoretical background	1
1.1 The Standard Model	1
1.1.1 The Higgs mechanism	2
1.2 Two-Higgs-Doublet Model	4
1.3 Higgs boson detection	6
1.4 Higgs boson pair production	7
1.4.1 Measurement	9
1.5 Cross section: an overview on the calculation	10
1.5.1 Divergences and their treatment	11
1.6 Present status	12
1.6.1 Low energy region	12
1.6.2 Threshold region	13
1.6.3 High energy region	13
1.6.4 p_T expansion and full top-mass NLO contribution	13
1.7 Topic of this thesis	14
2 Leading Order Cross Section	17
2.1 Preliminaries: Single-Higgs production with one off-shell gluon	17
2.1.1 Projection onto the tensor basis: form factors	18
2.1.2 Analytic amplitude of $gg^* \rightarrow H$	19
2.2 Leading Order amplitude for $H_1 H_2$ production	20
2.2.1 Triangle contribution	20
2.2.2 Box diagrams	21
2.2.3 Applying the procedure	25
2.2.4 LO amplitude in the Heavy top limit	31
2.3 Projecting onto the Lorentz structure	32
2.4 Leading-Order Cross section	35
3 NLO Cross Section	37
3.1 Virtual contributions	37
3.1.1 One-particle reducible diagrams	38
3.1.2 Two-loop box diagrams	39
3.1.3 Extracting the singularities	42
3.1.4 Infrared divergences	44
3.2 Renormalization	47
3.3 Virtual cross-section	49
3.4 Real corrections	50
3.4.1 Heavy-top limit	51
3.4.2 Full m_t dependence	52

3.5	Real cross section	53
4	Numerical integration	57
4.1	Integrating the Box form factors	57
4.2	Richardson Extrapolation	59
4.2.1	Convergence of the Richardson extrapolation: two examples	61
4.3	Total Cross Section	62
5	Results and Discussion	65
5.1	SM Differential and Total cross section	65
5.1.1	Dependence on the trilinear Higgs coupling	67
5.2	Top-mass uncertainties	70
5.2.1	Preferred scale choice	70
5.2.2	Combining the uncertainties	73
6	Conclusions	75
A	HTL gluon-Higgs effective vertex	77
A.1	ggH_j effective vertex	78
B	General tensors for the $gg \rightarrow H_1H_2$ process	81
C	Phase space integral	85
C.1	$2 \rightarrow 2$ process	85
C.1.1	Kinematics	85
C.1.2	d -dimensional Phase space integrals	86
C.1.3	Differential partonic cross section: setup	89
C.1.4	Polarization sum	89
C.1.5	Differential partonic cross section: Virtual corrections	91
C.2	$2 \rightarrow 3$ process	92
C.2.1	d -dimensional Phase space integrals	93
C.2.2	Differential cross section: real corrections	96
D	Passarino-Veltmann reduction	99
D.1	Reduction to scalar integrals	99
D.1.1	2-point tensor integrals	99
D.2	3-point tensor integrals	101
D.3	Recurrence relations	102
E	Evaluating the basis of one-loop integrals	105
E.1	2-points scalar integrals	105
E.2	3-point scalar integrals	109
E.2.1	Scaleless scalar integrals	110
F	Utilities	115
F.1	Useful kinematical identities	115
F.2	Feynman Parameter Tricks	116
F.2.1	Boundaries	116
F.2.2	Transformations	117
G	Running of α_s in QCD	121
G.1	Gluon propagator	121
G.1.1	Massless flavours	121
G.1.2	Top-mass contribution	122
G.2	Quark Self-energy	124

G.3 Vertices	124
G.4 $\overline{\text{MS}}$ scheme for α_s with $N_f = 5$ massless flavours with the top quark decoupled	126
H Feynman Diagrams for $gg \rightarrow H_1 H_2$	127
H.1 Real corrections	128
H.2 Virtual contributions	130
H.2.1 Vertex contributions	130
H.2.2 Box contributions	131
I Feynman Rules	133
I.1 2HDM scalar propagators and Yukawa couplings	133
I.2 2HDM trilinear Higgs couplings	134
I.3 SM QCD Feynman rules	135
Bibliography	136
Acknowledgements	146

Resumen

La física de las partículas elementales está bien descrita por el Modelo Estándar (SM, por sus siglas en inglés.). La presencia de la interacción electrodébil prohíbe los términos cuadráticos con respecto a los campos, i.e. términos de masa, en el Lagrangiano del SM. La presencia de tales términos de masa requieren de la llamada ruptura espontánea de la simetría, introduciendo un doblete electrodébil con un valor esperado de vacío no nulo. Como recordatorio, la ruptura espontánea de la simetría genera un bosón escalar neutro, el renombrado bosón de Higgs [1–4]. Aunque fue predicho en los años 60 por argumentos teóricos, en el 2012 los experimentos del Large Hadron Collider (LHC), ATLAS y CMS, encontraron una señal perteneciente a la resonancia de una partícula neutra de masa alrededor de 125 GeV [5, 6]; análisis posteriores han confirmado que su espín, propiedades de CP y acoplamiento con las otras partículas son compatibles con el bosón de Higgs del SM [7, 8]. Para asegurar que este bosón neutro escalar es definitivamente la partícula de Higgs del SM, sus auto-acoplamientos deben medirse y compararse con las predicciones fenomenológicas del SM.

Restricciones provenientes de invariancia Lorentz e invariancia gauge, renormalizabilidad y argumentos de unitariedad establecen que el sector escalar de un modelo de teoría cuántica de campos (QFT) debe tener como máximo auto-interacciones de tipo triple y cuádruple en su contenido de partículas escalares. Estos términos constituyen el potencial de Higgs, y su presencia permite la ruptura espontánea de la simetría. Las presentes incertidumbres experimentales son insuficientes para establecer límites estrictos en los auto-acoplamientos del Higgs; la posibilidad de que el bosón detectado pertenezca a un sector escalar extendido de un modelo más general no se puede descartar. Muchos modelos más allá del Modelo Estándar (BSM, por sus siglas en inglés.) predicen sectores escalares más complejos, con muchos bosones de Higgs, y nada evita que la señal del LHC se refiera a la detección de un bosón de Higgs perteneciente a un modelo BSM [9–11]. El acoplamiento cuádruple del Higgs todavía está fuera de alcance a nivel experimental [12–16]; el auto-acoplamiento triple del Higgs será accesible en el futuro próximo, gracias a la actualización de alta luminosidad del LHC y otros futuros colisionadores [17–28]. Una manera de investigar el potencial de Higgs es considerando los observables directos provenientes de canales de producción de pares de bosones de Higgs. Sin embargo, la determinación experimental de tales procesos es complicada, debido a que los canales de producción de pares de Higgs tienen una sección eficaz muy pequeña y un vasto fondo de QCD [23, 28–31]. Este hecho señala la necesidad de predicciones teóricas precisas de la sección eficaz de producción de pares de Higgs, para la cual se requieren términos de orden superior de la expansión en teoría de perturbaciones con respecto al acoplamiento fuerte.

El proceso dominante implicado en la producción de pares de Higgs es la fusión de gluones en QCD [30]. Dado que ningún mecanismo produce una interacción directa gluón-Higgs, la amplitud de Feynman de este proceso ya contiene contribuciones a un lazo (loop en Inglés) en el término de orden cero (Leading Order, LO). Además, tiene una fuerte supresión del espacio fásico y electrodébil en comparación con el canal de producción de un Higgs. Por lo tanto, para cumplir con la precisión teórica exigida, la sección eficaz total para este proceso requiere un cálculo a primer orden en teoría de perturbaciones (Next-to-Leading Order, NLO), por lo que es necesario tener en cuenta diagramas de Feynman de dos loops.

Dentro del SM, las contribuciones con loops del quark cima (top en Inglés) son responsables de más del 99% de la sección eficaz total debido al acoplamiento de Yukawa, que es proporcional a la masa del top. Otros modelos con un sector escalar extendido, como el Two-Higgs-Doublet Model (2HDM), puede tener contribuciones no despreciables del quark belleza (bottom en Inglés), ya que el espacio de parámetros de tales modelos permite un aumento del impacto de los acoplamientos de

Yukawa [10, 23]. Este último escenario será considerado en proyectos futuros.

El cálculo de la sección eficaz total de producción de pares de Higgs vía fusión de gluones más allá del LO es muy desafiante: el cálculo a NLO en el SM implica integrales de Feynman de cuatro-puntos con dos loops, que contribuyen a las correcciones virtuales, e integrales de Feynman de cinco-puntos a un loop, que son la base de las correcciones reales. Además de las invariantes cinemáticas del proceso, dos escalas de masa deben tenerse en cuenta, a saber, la masa del quark top y la masa del bosón de Higgs. Mientras que para las contribuciones de un loop existen técnicas de cálculo consolidadas, con un buen grado de automatización, para los diagramas de Feynman de dos loops, involucradas en este proceso, aún no se ha establecido dicho estándar.

A lo largo de los últimos 25 años, se han realizado grandes esfuerzos para estudiar las correcciones de orden superior a la sección eficaz diferencial de este proceso en regiones cinemáticas específicas [24, 32–46]. Para energías bajas, el límite de top pesado (heavy-top limit, HTL) ofrece una buena aproximación y una importante simplificación de la amplitud en ordenes superiores, ya que cada orden contiene un loop menos. Esta aproximación es conocida hasta tercer orden en teoría de perturbaciones ($N^3\text{LO}$) y proporciona aproximadamente un aumento del 120% de la sección eficaz diferencial a LO. Se han introducido refinamientos masivos hasta el segundo orden en teoría de perturbaciones (Next-to-Next-to Leading Order, NNLO) en las correcciones reales, lo que conduce a la llamada "aproximación de teoría completa" (Full-theory approximation), como términos de orden superior en la expansión de masa del quark top. Los efectos de masa del top tienen un impacto del -20% con respecto al HTL. Otras regiones que han sido investigadas son los umbrales de producción $t\bar{t}$, que contienen la mayor parte de la sección eficaz, y el límite de alta energía, para el cual resultados analíticos recientes han sido producidos. A NLO, todos los análisis coinciden en un efecto de masa del 20% con respecto al HTL.

Una predicción completa de la sección eficaz de producción de pares de Higgs a NLO QCD vía fusión de gluones es necesaria para obtener los efectos debidos a la masa del top que ocurren a primer orden en teoría de perturbaciones. Se ha realizado un primer cálculo [47] aplicando identidades de integración-por-partes [48, 49] a la amplitud, logrando su desarrollo en integrales maestras (master integrals). La integración de las integrales maestras se ha realizado numéricamente, explotando la descomposición sectorial [50] y la deformación de contorno para realizar la integración en la región física. Para aplicar con éxito el método de reducción de la amplitud, las masas del top y del Higgs tenían que ser ajustadas respectivamente a $m_t = 173$ GeV y $m_H = 125$ GeV desde el inicio del cálculo. Este cálculo representa la primera evaluación de la sección eficaz a NLO QCD que incluye todos los efectos de la masa del top.

El objetivo de esta tesis es presentar un cálculo alternativo de la sección eficaz mediante la producción de pares de Higgs vía fusión de gluones a NLO en un marco adecuado tanto para el SM y el 2HDM. En particular, el Capítulo 1 está dedicado a definir el contexto teórico sobre los que se construye esta tesis, presentando los modelos en consideración, los fundamentos de los resultados fenomenológicos con respecto al bosón de Higgs, el marco general utilizado para calcular una sección eficaz que involucra contribuciones de QCD, y su aplicación en el cálculo de la producción de pares de Higgs vía fusión de gluones. Se considerará un estado final con dos bosones de Higgs con diferentes masas. La novedad que introduce la estrategia aquí presentada es el tratamiento de las masas como parámetros libres para la integración numérica. Esta característica permite el estudio de las incertidumbres relacionadas con la elección del esquema de renormalización y escala de la masa del quark top.

Metodología

La teoría de la perturbación en QCD representa el marco ideal para calcular la sección eficaz de la producción de pares de Higgs a través de la fusión de gluones. En esta tesis, consideraremos la producción de dos bosones de Higgs escalares neutros, $pp \rightarrow H_1 H_2$.

La sección eficaz total se puede escribir como una serie perturbativa con respecto a la constante de acoplamiento fuerte, proporcionando la siguiente expresión

$$\sigma(pp \rightarrow gg \rightarrow H_1 H_2) = \sigma_{\text{LO}} + \Delta\sigma_{\text{NLO}} + \cdots + \Delta\sigma_{\text{N}^n\text{LO}} + O(\alpha_s^{n+3}). \quad (1)$$

Los teoremas de factorización de QCD [51] establecen la condición bajo la cual los hadrones de alta energía pueden describirse como estados ligados de sus constituyentes, quark y gluones, que llevan una fracción de su momento total. Por lo tanto, en las colisiones protón-protón, sus constituyentes interactúan. Nos interesa el caso en el que un gluón de momento $p_1 = x_1 P_1$ interactúa con un gluón que transporta momento $p_2 = x_2 P_2$, con P_i los momentos de los protones en colisión. Esto representa una interacción de corta distancia que puede estudiarse de manera perturbativa y es independiente del hadrón externo; interacciones de corta distancia *factorizan* de la de larga distancia que están codificadas en las funciones de distribución de partones (parton distribution functions, PDF) [52]. Estos objetos tienen un carácter no perturbativo y tienen en cuenta la estructura de los hadrones. Las PDF se interpretan como la probabilidad de que un partón dentro de un protón lleve una cierta fracción del impulso total.

Partiendo de la sección eficaz a LO, los teoremas de factorización establecen que

$$\sigma_{\text{LO}} = \int_0^1 dx_1 dx_2 f_g(x_1, \mu_F) f_g(x_2, \mu_F) \hat{\sigma}_{\text{LO}}(g(p_1)g(p_2) \rightarrow H_1 H_2), \quad (2)$$

donde $f_g(x_i, \mu_F)$ son las PDF de los gluones, x_i es la fracción del impulso del protón i , μ_F es la *escala de factorización* y $\hat{\sigma}$ es la sección eficaz partónica; μ_F es mucho mayor que la escala a la que se aplican los teoremas de factorización.

Las PDF se determinan mediante ajustes experimentales de datos obtenidos de procesos de dispersión inelástica profunda. La parte perturbativa es la sección eficaz partónica $\hat{\sigma}$. El enfoque perturbativo de QCD lo relaciona con el cuadrado de la amplitud de dispersión integrada sobre el espacio fásico en un orden fijo:

$$\hat{\sigma}_{\text{LO}}(g(p_1)g(p_2) \rightarrow H_1 H_2) = \int d\text{PS}_2 \overline{|\mathcal{M}_{\text{LO}}|^2}, \quad (3)$$

donde $d\text{PS}_2$ es el elemento de espacio fásico y \mathcal{M}_{LO} es la amplitud de dispersión. La línea por encima de la amplitud al cuadrado representa el promedio de polarización. La amplitud de dispersión, es decir, la suma de los diagramas de Feynman [53], se puede construir a partir del conocimiento del Lagrangiano, que introduce una dependencia de la teoría. Dado que tanto en 2HDM como en SM no hay vértices de interacción entre Higgs y gluones, la amplitud de $gg \rightarrow H_1 H_2$ ya está inducida por loop al LO. La parte dominante de la amplitud debido a las interacciones Yukawa, proporcional a las masas de los quarks, viene dada por el loop de top-quarks. Esto nos lleva a considerar solo los loops de quark top.

Al NLO, se requiere el cálculo de amplitudes de dos loops; además, también deben tenerse en cuenta los diagramas de un loop con un partón radiante en el estado final. Estos últimos pertenecen a tres nuevos canales QCD con diferentes estados iniciales: los estados iniciales quark-antiquark $q\bar{q}$, quark-gluon qg y gluón-gluón gg . La sección eficaz partónica a NLO puede escribirse como

$$\begin{aligned} \Delta\hat{\sigma}_{\text{NLO}} &= \Delta\hat{\sigma}_{\text{virt}} + \Delta\hat{\sigma}_{q\bar{q}} + \Delta\hat{\sigma}_{qg} + \Delta\hat{\sigma}_{gg} \\ \Delta\hat{\sigma}_{\text{virt}} &= \int d\text{PS}_2 \, 2\text{Re} \left[\overline{\mathcal{M}_{\text{LO}}^*} \mathcal{M}_{\text{virt}} \right], \\ \Delta\hat{\sigma}_{ij} &= \int d\text{PS}_3 \, \overline{|\mathcal{M}_{ij}|^2}, \end{aligned} \quad (4)$$

donde $\mathcal{M}_{\text{virt}}$ es la *amplitud virtual* que contiene los diagramas de dos loops, \mathcal{M}_{ij} son las contribuciones del estado inicial ij , llamado *correcciones reales*, y $d\text{PS}_3$ es el elemento de espacio fásico de tres partículas.

Amplitud

La sección eficaz al LO representa el primer paso de este cálculo. Aunque no es el tema principal de esta tesis, es esencial considerar los elementos de la matriz al LO no solo para establecer el marco, sino también porque la contribución de NLO se define como la interferencia entre los factores de forma de un loop y dos loops; además, la amplitud al LO participará en la renormalización de la amplitud al

NLO y en el esquema de sustracción de las divergencias IR. Es un cálculo muy antiguo [54], pero no obstante es instructivo y se presentará extensamente en el Capítulo 2, junto con su HTL.

Las contribuciones de la sección eficaz al NLO son de dos tipos: contribuciones virtuales y reales. La amplitud virtual está formada por diagramas de Feynman de dos loops de tres categorías: diagramas caja, diagramas reducibles de una partícula y diagramas triangulo. Los 47 diagramas de cajas se agrupan en seis topologías: la topología 1 consiste en correcciones de autoenergía de top-quarks a las cajas del LO; las topologías 2 y 3 son las correcciones de vértice a las cajas al LO, que contienen correcciones abelianas y no abelianas; la topología 4 y 5 son respectivamente los diagramas doble caja planos y no planos; la topología 6 contiene los diagramas caja de dos loops con un intercambio de un gluón virtual en el estado inicial, tanto planos como no planos. Los diagramas reducibles de una partícula se pueden construir a partir de la producción de Higgs en QCD via fusión de gluones donde un gluón externo no está en su capa másica (off-shell). La expresión analítica se puede encontrar en el Capítulo 2. Los diagramas triangulo son los que contienen el acoplamiento triple de Higgs: son los diagramas que representan la señal de detección de un estado final de un par de Higgs producido por un decaimiento de un boson de Higgs, mientras que las otras amplitudes virtuales representan un fondo irreducible. Los 24 diagramas triángulo se pueden agrupar de la misma manera que se ha mostrado para los diagramas caja: 6 correcciones de autoenergías del propagador de top-quarks a los diagramas triángulo al LO; 10 correcciones de vértice a los diagramas triángulo al LO, tanto abelianos como no abelianos; 4 diagramas triángulo no planos y 4 contribuciones con un intercambio de un gluón virtual en el estado inicial. Es importante notar que el número de diagramas de triángulos del 2HDM se duplica con respecto al SM, ya que el Higgs off-shell puede ser ligero (H_1) o pesado (H_2).

Las contribuciones reales están formadas por 43 diagramas de un loop donde se emite un partón adicional en el estado final. Hay tres canales que contribuyen a la sección eficaz real: $q\bar{q} \rightarrow H_1 H_2 g$, $qg \rightarrow H_1 H_2 q$ y $gg \rightarrow H_1 H_2 g$. La mayoría de los diagramas de amplitud real se pueden construir a partir de la amplitud al LO donde un gluón externo se considera off-shell. Esta característica es relevante en la integración sobre el espacio fásico, donde el subproceso $2 \rightarrow 2$ se puede integrar por separado de todo el proceso explícitamente. El último canal contiene contribuciones provenientes de diagramas pentágono.

Singularidades

Al NLO, aparecen divergencias ultravioleta (UV) e infrarroja (IR). Se necesita un *esquema de regularización* para aislar las divergencias UV. En este cálculo se utilizará *regularización dimensional* [55–57]. La idea es tratar la amplitud como una función analítica de la dimensión espacio-tiempo $d = 4 - 2\epsilon$:

$$\int_{\mathbb{M}} \frac{d^4 k}{(2\pi)^4} \rightarrow (\mu^2)^{\frac{4-d}{2}} \int_{\mathbb{M}} \frac{d^d k}{(2\pi)^d}, \quad (5)$$

donde μ es la *escala de 't Hooft* y tiene la función de preservar la dimensionalidad de masa de la amplitud. El procedimiento de regularización hace que las divergencias UV e IR sean polos en la expansión analítica ϵ alrededor de $\epsilon = 0$ (es decir, el límite de 4 dimensiones). Al NLO, la estructura analítica manifiesta polos de segundo orden.

El procedimiento de cancelar las divergencias UV se llama *renormalización*. Al interpretar los campos, el acoplamiento y los parámetros del Lagrangiano como cantidades *desnudas*, desarrollan divergencias en órdenes superiores. Para obtener predicciones físicamente significativas, deben expresarse en términos de cantidades físicas (es decir, las *renormalizadas*). Sus términos de orden superior que entran en la expansión perturbativa son los *contra-términos*. La elección de los contra-términos fija el *esquema* y la *escala de renormalización*. La única restricción es que los contra-terminos tienen que cancelar los polos UV provenientes de la amplitud a NLO. El esquema de renormalización influye en la parte finita de la amplitud, lo que introduce una dependencia en el esquema de renormalización orden por orden en la amplitud. Sin embargo, esta dependencia desaparece por completo si se considera toda la serie de perturbaciones. Se pueden encontrar más detalles sobre el esquema de renormalización específico que hemos elegido en el Capítulo 3.

Las divergencias IR se tratan de forma diferente. El teorema de Kinoshita-Lee-Nauenberg (KLN) [58, 59] garantiza la ausencia de divergencias IR para un observable suficientemente inclusivo. La in-

clusividad necesaria para la producción del par de Higgs indica que además de la amplitud virtual, que tiene el mismo estado final, se deben considerar contribuciones adicionales: estas son las correcciones reales. Dado que desarrollan divergencias suaves y colineales, se pueden combinar con la contribución virtual para obtener un observable libre de divergencias IR.

Dado que el cálculo se realizará numéricamente, la cancelación de las divergencias IR es más complicada, ya que se produce entre términos que se integran sobre diferentes estados finales: esto podría introducir grandes inestabilidades numéricas. Hay diferentes formas de superar este problema, representadas por diferentes *técnicas de sustracción* [60–65]. Estas se basan en la introducción de una sección eficaz diferencial auxiliar $d\sigma_A$ con la misma estructura de polos IR del proceso en consideración. Este término se sumará y quitará a nivel de la sección eficaz diferencial de la siguiente manera:

$$\Delta\hat{\sigma}_{\text{NLO}} = \int d\text{PS}_2 \left[\overline{|2\mathcal{M}_{\text{LO}}^* \mathcal{M}_{\text{virt}}|} + \int d\text{PS}_1 d\sigma_A \right] + \int d\text{PS}_3 \left[\overline{|\mathcal{M}_{q\bar{q}}|^2} + \overline{|\mathcal{M}_{gg}^2} + \overline{|\mathcal{M}_{gq}^2} - d\sigma_A \right]. \quad (6)$$

Cada integral separada ahora es finita y la integración numérica será estable. Para este proceso en particular, el término auxiliar se ha construido a partir del conocimiento del comportamiento del HTL del proceso. Se presentarán más detalles en el Capítulo 3.

La última fuente de divergencias proviene de las singularidades colineales del estado inicial, para las cuales el teorema de KLN no es válido, ya que no se suman los estados iniciales. Pueden ser absorbidas por una renormalización de las PDF, lo que significa que el comportamiento de la emisión colineal de un parton por el estado inicial está relacionado con las PDF de parton no perturbativas y se ha eliminado de la dispersión dura.

Aplicando el método

Dado que no existe una estrategia sistemática para los diagramas de dos loops, se presentará un método de cálculo para dicha amplitud. No se utilizará el método de reducción tensorial durante el cálculo. Para cada uno de los 47 diagramas caja pertenecientes a la amplitud virtual se realizará una proyección sobre los factores de forma y se aplicará una parametrización de Feynman basada en la topología, junto con un cambio dedicado de las variables de integración que hace posible la sustracción de los puntos finales (end-point subtractions) de las divergencias UV.

Las divergencias infrarrojas (IR) se restan a nivel integrando explotando la universalidad de la estructura IR en relación con la amplitud LO, y siguiendo el espíritu del método de sustracción de Catani-Seymour [60, 61]. Las posibles inestabilidades numéricas debidas a la presencia del umbral de producción $t\bar{t}$ se evitan dando a la masa del top quark una pequeña parte imaginaria.

La suma de los contra-términos de renormalización a la amplitud virtual produce cantidades libres de divergencias UV. El esquema $\overline{\text{MS}}$ con cinco sabores activos y el quark top en su capa másica desacoplado del running se utilizará para renormalizar el acoplamiento fuerte. Finalmente, después de la renormalización UV y la end-point subtraction de las divergencias IR, los factores de forma de los diagramas caja estarán listos para integrarse sobre los parámetros de Feynman y el espacio fásico de dos partículas. El procedimiento de renormalización y la introducción de correcciones reales aseguran la ausencia de divergencias UV y IR de la sección eficaz diferencial y total. Los diagramas reducibles de una única partícula (one-particle-reducible diagrams) se obtendrán combinando dos decaimientos del Higgs en amplitudes a LO de gluones on- y off-shell, empleadas como vértices efectivos. Por último, las contribuciones de los triángulos a NLO se construirán a partir de los factores de forma de producción de un único bosón de Higgs.

Las correcciones reales se obtendrán mediante algoritmos estándar, involucrando la descomposición tensorial de la amplitud real en la base tensorial de Passarino-Veltman, y tomando su promedio cuadrático analítico. Cada paso analítico se implementa en un código de MATHEMATICA que proporciona la amplitud al cuadrado para cada canal de correcciones reales. A las divergencias IR se le restará el mismo término utilizado para restar las singularidades IR de las contribuciones virtuales. La integración sobre el espacio fásico de tres partículas proporcionará la sección eficaz diferencial de las correcciones reales.

Integración numérica

La configuración numérica involucra el algoritmo VEGAS para la integración de Monte Carlo [66], implementado en un código FORTRAN construido con un enfoque de múltiples semillas: reduce drásticamente el error de integración a través de la *importancia de muestreo*, optimizando el muestreo en la región de integración que más aporta a la integral. Inestabilidades numéricas surgen para energías que se encuentran por encima de los umbrales virtuales, que pueden ser los umbrales de producción de $t\bar{t}$ o gg . Además, se aplicará integración por partes para disminuir la importancia de los denominadores, con el fin de mejorar la estabilidad numérica de la integración.

La parte imaginaria ϵ_t introducida en la masa del top-quark como $m_t^2 \rightarrow m_t^2(1 - i\epsilon_t)$ juega el papel de una anchura de desintegración finita del top-quark. De acuerdo con la literatura, consideramos el quark top en la aproximación de una anchura de desintegración estrecha, lo que nos induce a tomar el límite $\epsilon_t \rightarrow 0$. Dado que usamos un enfoque numérico, el "límite" no es una opción viable; además, la integración numérica para $\epsilon_t < 10^{-2}$ se vuelve muy inestable.

Se necesitará un método para restaurar el límite de anchura de desintegración estrecha del top-quark ($\epsilon_t \rightarrow 0$). Este se ha extraído de la combinación de evaluaciones lineales de la sección eficaz diferencial para diferentes valores del regulador ϵ_t , lo que constituye el núcleo del método de extrapolación de Richardson, cuyo error de extrapolación es inversamente proporcional al número de nodos, es decir, diferentes valores de la (pequeña) amplitud ϵ_t . El resultado de este marco numérico es la sección eficaz diferencial de producción de un par de Higgs en el límite de anchura de desintegración estrecha del top-quark. La integral de la sección eficaz se encontrará utilizando el método de Romberg, que combina la regla trapezoidal y la extrapolación de Richardson para disminuir las incertidumbres numéricas.

Resultados y Perspectivas

Los resultados de este procedimiento aplicado a la producción de pares de Higgs a NLO en el SM vía fusión de gluones [67–69] se discutirá en detalle en esta tesis, presentando las distribuciones de la sección eficaz diferencial y total para diferentes energías de centro de masa. Se demostrará que los efectos debidos a considerar una masa del quark top finitos en la sección eficaz total a NLO son del orden del 15% sobre el cálculo a NLO HTL. Se pueden ver efectos más notables a nivel de la distribución diferencial, donde la masa del top finita introduce una desviación en su cola hasta del 40%. Los resultados para los valores centrales en diferentes energías del centro de masas están en completo acuerdo con la literatura, así como la reducción de las escalas de renormalización y factorización. La sección eficaz total en función del acoplamiento triple del bosón de Higgs muestra una desviación significativa del HTL debido a efectos de masa del top, lo que lleva a un cambio notable de su mínimo.

El marco construido para este cálculo permite la elección de diferentes esquemas y escalas de renormalización de la masa del top, adecuados para la primera estimación de las incertidumbres que introducen. Se mostrará cómo la masa del top en el esquema de renormalización $\overline{\text{MS}}$ a diferentes escalas resalta la importancia de estas incertidumbres: ascienden al -15% a nivel de sección eficaz total y al -35% a nivel de sección eficaz diferencial. El comportamiento de la sección eficaz diferencial a diferentes escalas de renormalización mostrará que una escala de renormalización dinámica es la elección más natural para grandes masas invariantes de pares de Higgs. La cuasi-independencia de las incertidumbres relativas de la masa del top del esquema de renormalización y de factorización conduce a una suma lineal de las incertidumbres, ya que se definirán como la envoltura de las múltiples elecciones. Se discutirán la combinación de las incertidumbres debido a la masa del top a NLO y las incertidumbres de renormalización y factorización a NNLO, y con un argumento de factorización de la sección eficaz se demostrará que el tratamiento más conservador de las incertidumbres es su suma lineal.

Los detalles de los resultados presentados en esta sección se discutirán ampliamente en el Capítulo 5, con especial atención a las incertidumbres de la masa del top, su impacto en la sección eficaz diferencial a NLO y la sección eficaz integrada y cómo combinarlas junto a las predicciones más modernas. El marco descrito en esta tesis ya se ha aplicado con éxito al 2HDM; algunos resultados con respecto a la producción de pares de Higgs escalares neutros se muestran en el Capítulo 4. Como se mencionará

en el Capítulo 6, otras aplicaciones futuras implican estados finales que contienen pseudo-escalares. Además, la dependencia del ángulo β de los acoplamientos de Yukawa en el 2HDM puede conducir a contribuciones no despreciables de los loops del quark bottom, para los cuales tratamientos adicionales sobre los factores de forma se necesitan para aumentar la estabilidad numérica, como expandir la amplitud en términos de la masa del quark bottom y el método de integración por partes.

Introduction

The physics of the elementary particles is well described by the Standard Model (SM). The presence of the electroweak interaction prohibits quadratic terms with respect to the fields, i.e. mass terms, into the SM Lagrangian. Introducing such mass terms requires the so-called spontaneous symmetry breaking, which can be induced by a scalar field with non-vanishing vacuum expectation value. As a reminder, the spontaneous symmetry breaking generates a neutral scalar boson, the Higgs boson [1–4]. Although it has been predicted in the '60s by theoretical arguments, in 2012 the LHC experiments ATLAS and CMS found a signal belonging to the resonance of a neutral particle of mass around 125 GeV [5, 6]; further analyses have confirmed that its spin, CP properties and coupling with the other particles are compatible with a SM Higgs boson [7, 8]. In order to definitely attest that this scalar neutral boson is the SM Higgs particle, its self-couplings have to be measured and compared with the phenomenological predictions of the SM.

Constraints coming from the Lorentz and gauge invariance, UV completeness and unitarity arguments set the scalar sector of a QFT model to have at most trilinear and quartic self-interactions with its scalar particle content. These terms constitute the Higgs potential, and their presence allows the spontaneous symmetry breaking. The present experimental uncertainties are insufficient to set strong bounds on the Higgs self-couplings; the possibility of the detected boson to belong to an extended scalar sector of a more general model rather than the SM can not be discarded. Many Beyond the Standard Models (BSM) predict more complex scalar sectors with many Higgs bosons, and nothing prevents the eventuality that the LHC signal was referred to the detection of one particular Higgs boson of a BSM [9–11]. The quartic Higgs coupling is still out of reach at experimental level [12–16]; the trilinear Higgs self-coupling will be accessible in the next future, thanks to the high luminosity upgrade of the LHC or other future colliders [17–28]. An investigation of the Higgs potential can be done by considering direct observables coming from the Higgs-pair production channels. However, the experimental determination of such processes is nonetheless complicated, because of the very small cross section related with the Higgs-pair production channels and its vast QCD background [23, 28–31]. This fact enlightens the importance of a precise theoretical prediction of the cross section of the Higgs-pair production, for which higher order terms of the perturbative expansion with respect to the strong coupling are demanded.

The dominant process involving a Higgs-pair production is the QCD induced gluon fusion [30]. Since no mechanism produces a direct gluon-Higgs interaction, the Feynman amplitude of this process already contains one-loop contributions at its leading order (LO). In addition, it has a strong electroweak and phase space suppression in comparison with the single-Higgs production channel. Therefore, to fulfill the demanded theoretical precision, the total cross section for this process requires a next-to-leading order (NLO) calculation, for which two-loop Feynman graphs have to be taken into account.

Within the SM, the top-quark loops are responsible for more than 99% of the total cross section caused by the presence of the Yukawa couplings, which is proportional to the top mass. Other models with an extended scalar sector, like the Two-Higgs-Doublets Model (2HDM), might have non-negligible contributions from the bottom quark, since the parameter space of such models permits enhancements of the their Yukawa couplings [10, 23]. This latter case will be considered in future projects.

The calculation of the Higgs-pair production via gluon fusion total cross section beyond the LO is very challenging: at NLO in the SM it involves four-point two-loop Feynman integrals, entering the virtual corrections, and five-point one-loop Feynman integrals, which are the building blocks of

the real corrections. Besides the kinematic invariants of the process, two masses have to be taken into account, namely the top-quark and the Higgs boson mass. While for the one-loop contributions, there are well-grounded calculation techniques with a good degree of automation, for the two-loop Feynman diagrams involved in this process such standard has not been established yet.

Along the past 25 years, great efforts have been made to study the higher order corrections to the differential cross section of this process in specific kinematic regions [24, 32–46]. For low energies, the heavy top limit offers a very good approximation and an important simplification of the higher order amplitudes, since they will carry one less loop to each order. This approximation is known up to the third perturbative order (N³LO) and provides a rough 120% increasing of the LO differential cross section. Mass refinements have been introduced up to the second perturbative order (NNLO) on the real corrections, leading to the so-called full-theory approximation, as higher order terms into the top-quark mass expansion. The top-mass effects have an impact of the -20% with respect to the sole heavy top limit. Other regions that have been investigated are the $t\bar{t}$ -production thresholds, that contains the bulk of the total cross section, and the high-energy limit, for which recently analytical results have been produced. At NLO, all the analysis agree on a 20% mass effect with respect to the heavy top limit.

A complete NLO QCD Higgs-pair production via gluon fusion cross section is needed to obtain the exact top-mass effects occurring at the first perturbative order. A first calculation [47] has been carried out by applying integration-by-parts identities [48, 49] of the amplitude, achieving its master integral decomposition. The integration of the master integrals has been done numerically, exploiting the sector decomposition [50] and the contour deformation to perform the integration in the physical region. In order to successfully apply the amplitude reduction method, the top and Higgs masses had to be set respectively to $m_t = 173$ GeV and $m_H = 125$ GeV from the beginning of the calculation. This calculation represents the first NLO cross section with full top-mass dependence.

The aim of this thesis is to present an alternative calculation of the NLO Higgs-pair production via gluon fusion in a framework suitable for both the SM and the 2HDM. A final state with two Higgs bosons with different masses will be considered. The novelty introduced by the strategy here presented is the treatment of the masses as free parameters for the numerical integration. This feature allows the study of the uncertainties related to the choice of the renormalization scheme and scale of the top-quark mass. The procedure can be summarized as follows: every diagram will firstly be projected into its form factors; on each integral contained in them, the Feynman parametrization will be applied together with a dedicated change of the integration variables that makes the end-point subtraction of the ultraviolet (UV) divergences possible; the infrared (IR) divergences are subtracted at integrand level exploiting the universality of the IR structure in the ratio to the LO amplitude, in the spirit of the Catani-Seymour subtraction method [60, 61]; the numerical instabilities due to the $t\bar{t}$ -production threshold are avoided by giving to the top quark a small width; the finite part of the form factors treated in this way can be safely integrated over the Feynman parameters and the phase space. The renormalization procedure and the introduction of the real corrections ensure the UV finiteness and the IR safety of the differential and total cross section. A method to restore the narrow width of the top quark is needed. The Richardson extrapolation method offers a way to combine results for different top-quark widths to extract the narrow width "limit". The outcome of this framework is the Higgs-pair production differential cross section. The integrated cross section will be found by using the Romberg's method, which combines the trapezoidal rule and the Richardson extrapolation in order to decrease its numerical uncertainties method.

Results for this procedure applied to the NLO SM Higgs-pair production via gluon-fusion [67–69] will be discussed in detail in this thesis, presenting the differential cross section distributions and the total cross section for different center-of-mass energies. There will be shown how the uncertainties related to the renormalization and factorization scales together with the top-mass renormalization scheme and scale uncertainties have a huge impact, leading to sizable relative errors. At last, it will be discussed how a dynamical top-mass renormalization scale choice is needed to control the top-mass effects at high energies. The possibility of choosing variable top-quark masses is nowadays possible only with the method described in this thesis, and it will be discussed in details.

This thesis is structured as follows: Chapter 1 is devoted to define the theoretical background on

which this work is built, presenting the models under consideration, the basics of the phenomenological results regarding the Higgs boson, the general framework used for calculating a cross section involving QCD contributions, and the state-of-the-art of the Higgs-pair production via gluon fusion; Chapter 2 and 3 will describe in detail the LO and NLO cross section calculation respectively in the common framework suitable both for SM and 2HDM, with particular focus on the isolation of the UV and IR divergences from the virtual correction, the renormalization of the UV divergences and the dedicated subtraction terms for the IR divergences, and the calculation of the real contributions; Chapter 4 shows the numerical setup employed to obtain the differential cross section distribution and the total cross section, presenting the Monte Carlo integration algorithm to evaluate numerically the form factors, the Richardson extrapolation method to extract the narrow width limit of the top-quark mass and the integration of the differential distribution through the trapezoidal method combined with the Richardson extrapolation; Chapter 5 will present the discussion of the results obtained by applying the procedure shown in the previous Chapters, with particular focus on the top-mass uncertainties, their impact on the NLO differential and integrated cross section and how to combine them together with the state-of-the-art predictions; at last, Chapter 6 will recap all the core arguments discussed in this thesis, present the conclusions and an outlook on the future perspective of this project.

Chapter 1

Theoretical background

1.1 The Standard Model

The Standard Model (SM) represents the most successful model describing the particle interactions. It has been built and tested along 60 years of data from collider experiments embedded into a quantum field theory framework. The discovery of a scalar particle compatible with a Higgs boson [1–6] represent the most recent success of the SM. It further provides a solid theoretical framework for a plethora of phenomenological outcomes comparable with the experiment.

Theoretically speaking, it is a quantum field theory described by the Lorentz invariant Lagrangian \mathcal{L}_{SM} symmetric with respect to the gauge group $SU(3)_C \otimes SU(2)_L \otimes U(1)_Y$. The $SU(3)_C$ Lie group is the representation of the strong interactions [70–77] between quarks mediated by the gluons; the associated charge is called *color charge*. The $SU(2)_L \otimes U(1)_Y$ product represents the electroweak interaction (EW) between leptons [78–80]; its associated conserved quantities are the weak isospin I and the hypercharge Y . As will be described later on, the spontaneous symmetry breaking $SU(2)_L \otimes U(1)_Y \rightarrow U(1)_{\text{EM}}$ will lead to the conservation of the *electric charge* $Q = I_3 + Y$, known as Gell-Mann-Nishijima formula [81, 82].

The Lagrangian \mathcal{L}_{SM} can be written as

$$\mathcal{L}_{\text{SM}} = \mathcal{L}_{\text{G}} + \mathcal{L}_{\text{f}}, \quad (1.1)$$

where

$$\begin{aligned} \mathcal{L}_{\text{G}} &= -\frac{1}{4} \sum_b^{\{C,L,Y\}} \text{Tr} [F_b^{\mu\nu} F_{b,\mu\nu}], & \mathcal{L}_{\text{f}} &= \sum_q i\bar{\psi}_q \not{D}\psi_q + \sum_l i\bar{\psi}_l \not{D}\psi_l, \\ [D_\mu, D_\nu] &= -i \sum_b^{\{C,L,Y\}} g_b T_b^a F_b^{a,\mu\nu}, & D_\mu &= \partial_\mu - i \sum_b^{\{C,L,Y\}} g_b T_b^a A_{b,\mu}^a, \\ \psi_q &= \begin{Bmatrix} u & c & t \\ d & s & b \end{Bmatrix}, & \psi_l &= \begin{Bmatrix} \nu_e & \nu_\mu & \nu_\tau \\ e & \mu & \tau \end{Bmatrix}. \end{aligned} \quad (1.2)$$

The index b runs over the gauge group, a is the index of the adjoint representation, $A_{b,\mu}^a$ are the fields that represent the boson which mediate the b interactions and g_b are the coupling constants. For each generator of the gauge group, a boson field has to be added.

The adjoint representation of the SM gauge group is characterized by

$$\begin{aligned} T_C^a &= \frac{\lambda^a}{2}, & [T_C^a, T_C^b] &= if^{abc} T_C^c, & a &= \{1, \dots, 8\}, & A_C^{a,\mu} &= G^{a,\mu} \\ T_L^i &= \frac{\sigma^i}{2}, & [T_L^i, T_L^j] &= i\frac{\epsilon^{ijk}}{2} \sigma^k, & a &= \{1, 2, 3\}, & A_L^{i,\mu} &= W^{i,\mu} \\ T_Y &= \mathbf{1}Y, & A_Y^\mu &= B^\mu \end{aligned} \quad (1.3)$$

where σ^i are the Pauli matrices and λ^a are the Gell-Mann matrices. There are 8 *gluons* $G^{a,\mu}$, and 4 electroweak bosons $W^{i,\mu}$ and B^μ .

Quarks	Leptons
$Q_L = \begin{pmatrix} u_L \\ d_L \end{pmatrix}, \begin{pmatrix} c_L \\ s_L \end{pmatrix}, \begin{pmatrix} t_L \\ b_L \end{pmatrix} \in \mathbf{3} \otimes \mathbf{2} \otimes \frac{1}{6}$	$L_L = \begin{pmatrix} \nu_{e,L} \\ e_L \end{pmatrix}, \begin{pmatrix} \nu_{\mu,L} \\ \mu_L \end{pmatrix}, \begin{pmatrix} \nu_{\tau,L} \\ \tau_L \end{pmatrix} \in \mathbf{1} \otimes \mathbf{2} \otimes -\frac{1}{2}$
$u_R, c_R, t_R \in \mathbf{3} \otimes \mathbf{1} \otimes \frac{2}{3}$	$e_R, \nu_R, \tau_R \in \mathbf{1} \otimes \mathbf{1} \otimes -1$
$d_R, s_R, b_R \in \mathbf{3} \otimes \mathbf{1} \otimes -\frac{1}{3}$	

Table 1.1: Matter content of the SM with the relative representation in the SM gauge group. The right-handed neutrinos are singlets w.r.t. the gauge transformation, hence they are not included within the Standard Model. Each weak isospin doublet has quantum isospin numbers $I = \frac{1}{2}$ and $I_3 = \pm \frac{1}{2}$.

The matter content is encoded into the spinors ψ_p ($p = q, l$). Each spinor has two chiral components labeled left-handed and right-handed. Strong interactions are not sensitive to the chiral components, while isospin interactions act only on the left-handed components: fermions are organized in left-handed doublets and right-handed singlets under the EW gauge group. The fermions that form a triplet under $SU(3)_C$ are the *quarks*.

The physical EW bosons are obtained by combining the $W^{i,\mu}$ and B^μ as follows:

$$\begin{pmatrix} A^\mu \\ Z^\mu \end{pmatrix} = \begin{pmatrix} \cos \theta_W & \sin \theta_W \\ -\sin \theta_W & \cos \theta_W \end{pmatrix} \begin{pmatrix} B^\mu \\ W^{3,\mu} \end{pmatrix}, \quad W^{\pm,\mu} = \frac{1}{\sqrt{2}}(W^{1,\mu} \mp iW^{2,\mu}). \quad (1.4)$$

The field A^μ is the *photon* and the *EW boson* Z^μ induces the neutral currents. The EW bosons $W^{\mp,\mu}$ lead to charged currents. The fermions which interact only via EW interaction are the *leptons*. The matter content that goes into the spinors ψ_p are depicted in Table 1.1.

Imposing the invariance under the SM gauge group requires all the fields in \mathcal{L}_{SM} to be massless, since the EW gauge subgroup prohibits mass terms. Experimentally, it is known that the EW bosons have a large mass and, of course, fermions are massive too. Therefore, a mechanism that introduces a mass term into the SM Lagrangian is needed.

1.1.1 The Higgs mechanism

Scalars

$\Phi = \begin{pmatrix} \phi^+ \\ \phi^0 \end{pmatrix} \in \mathbf{1} \otimes \mathbf{2} \otimes \frac{1}{2}, \quad \langle \Phi \rangle = \frac{1}{\sqrt{2}} \begin{pmatrix} 0 \\ v \end{pmatrix}$

Table 1.2: Scalar sector of the SM. This complex doublet has isospin $I = \frac{1}{2}$.

The mass terms allowed in a Lagrangian which satisfy the Lorentz invariance are quadratic in the fields for which the mass is demanded. Unfortunately, the structure of a mass term violates the gauge symmetry. The problem has been solved by the *Higgs mechanism* [1–4], based on the *spontaneous symmetry breaking*.

The potential of a free complex scalar isospin doublet Φ which satisfies the renormalizability and the unitarity is

$$V_\Phi = \mu^2 \Phi^\dagger \Phi + \frac{\lambda}{2} |\Phi^\dagger \Phi|^2, \quad (1.5)$$

where $\mu^2 < 0$ and $\lambda > 0$. The field Φ has a non-vanishing vacuum expectation value (VEV):

$$\langle \Phi \rangle = \frac{1}{\sqrt{2}} \begin{pmatrix} 0 \\ v \end{pmatrix}, \quad v = \sqrt{-\frac{2\mu^2}{\lambda}} \approx 246 \text{ GeV}. \quad (1.6)$$

Notice that only a neutral scalar field can acquire a VEV because of the conservation of the electric charge. This VEV spontaneously breaks the symmetry:

$$SU(2)_L \otimes U(1)_Y \rightarrow U(1)_{\text{EM}}, \quad (1.7)$$

that underlines the fact that electromagnetism is not broken.

Fixing the gauge of the field Φ to be the *unitary gauge*¹:

$$\Phi(x) = \frac{1}{\sqrt{2}} \begin{pmatrix} 0 \\ v + H(x) \end{pmatrix}, \quad (1.8)$$

where $H(x)$ is the *physical Higgs* field. The unitary gauge makes manifest the non-zero expectation value of Φ .

Embedding the Lagrangian \mathcal{L}_Φ into the Standard Model implies the replacement of $\partial^\mu \rightarrow D^\mu$, therefore:

$$\begin{aligned} \mathcal{L}_H &= D^\mu \Phi^\dagger D_\mu \Phi - \mu^2 \Phi^\dagger \Phi - \frac{\lambda}{2} |\Phi^\dagger \Phi|^2, \\ D^\mu \Phi^\dagger D_\mu \Phi &\sim_{\langle \Phi \rangle} \frac{v^2}{8} [g_L^2 (W^{1,\mu} + iW^{2,\mu})(W_\mu^1 - iW_\mu^2) + (g_L W_\mu^3 - g_Y B_\mu)(g_L W^{3,\mu} - g_Y B^\mu)] \\ &= m_W^2 W^{+,\mu} W_\mu^- + m_Z^2 Z^\mu Z_\mu, \end{aligned} \quad (1.9)$$

where $g_L = \sqrt{g_L^2 + g_Y^2} \cos \theta_W$, and

$$m_W = \frac{g_L v}{2}, \quad m_Z = \frac{v}{2} \sqrt{g_L^2 + g_Y^2} = \frac{m_W}{\cos \theta_W}, \quad m_A = 0, \quad m_H = \sqrt{-2\mu^2}. \quad (1.10)$$

The mass terms introduced by adding the scalar field $\Phi(x)$ does not break the EW gauge symmetry: three of the four degrees of freedom of $\Phi(x)$ have been eaten by the weak bosons and thus they acquire mass. Notice that the SM with spontaneous symmetry breaking is still gauge invariant, even though it is not immediately manifest [55, 83].

The interaction of the particles with the ground state of the Higgs makes the particles acquire a mass term. For the fermion, the *Yukawa Lagrangian* offers the simplest way to introduce such mass term:

$$\begin{aligned} -\mathcal{L}_Y &= Y_{ij}^d \bar{Q}_{i,L} \Phi d_{j,R} + Y_{ij}^u \bar{Q}_{i,L} \Phi^c u_{j,R} + Y_{ij}^l \bar{L}_{i,L} \Phi l_{j,R} + h.c. \\ &\quad \Downarrow \\ -\mathcal{L}_Y &\sim_{\langle \Phi \rangle} Y_{ij}^d \frac{v}{\sqrt{2}} \bar{d}_{i,L} d_{j,R} + Y_{ij}^u \frac{v}{\sqrt{2}} \bar{u}_{i,L} u_{j,R} + Y_{ij}^l \frac{v}{\sqrt{2}} \bar{l}_{i,L} l_{j,R} + h.c. \quad , \end{aligned} \quad (1.11)$$

where Φ^c is the charge conjugate of Φ , $Q_{i,L}$ and $L_{i,L}$ are the quark and lepton isospin doublet, the Y_{ij}^k are the *Yukawa couplings* and

$$m_{ij}^k = Y_{ij}^k \frac{v}{\sqrt{2}}, \quad (1.12)$$

are the mass matrices. The diagonalization of these mass matrices induces the CKM matrix, for the quark sector, [84, 85] and the PMNS [86, 87] matrix, for the lepton sector.

The Standard Model Lagrangian² is the sum of the massless $\mathcal{L}_G + \mathcal{L}_f$ and the Higgs and Yukawa Lagrangian

$$\mathcal{L}_{\text{SM}} = \mathcal{L}_G + \mathcal{L}_f + \mathcal{L}_H + \mathcal{L}_Y. \quad (1.13)$$

The Feynman rules that this Lagrangian provides are depicted in Appendix I.

¹It is based on the fact that a complex field $\phi(x)$ can be expressed into polar coordinates, obtaining two real fields $r(x)$ and $\Theta(x)$. A gauge transformation acts like a shift of $\Theta(x) \rightarrow \Theta'(x)$. Therefore, fixing the function $\Theta(x)$ is equivalent to perform a gauge transformation. In general, gauge symmetry ensures that a doublet can be rotated with a $SU(2)$ transformation that sets the first component to 0 and the second to be real.

²The actual SM Lagrangian contains additional terms related to the gauge fixing and the ghost Lagrangian. We did not discuss it in details since it is not the main focus of the discussion.

1.2 Two-Higgs-Doublet Model

The study of the scalar sector of the SM can be made experimentally by measuring the parameter ρ : for a model locally invariant under $SU(2)_L \otimes U(1)_Y$ with n multiplets with weak isospin $I^{(i)}$, hypercharge $Y_{(i)}$ and VEV v_i , the tree-level parameter ρ is

$$\rho = \frac{\sum_i^n [I^{(i)}(I^{(i)} + 1) - Y_{(i)}^2] v_i}{2 \sum_i^n Y_{(i)}^2 v_i}. \quad (1.14)$$

The experimental data [88] shows that ρ is compatible with 1, which is the case of the SM with its single complex doublet. However, this constraint does not exclude other possibilities, i.e. higher multiplets with zero VEVs or higher dimensional representations. The latter cases tend to introduce over-complexities that are not the main focus of this thesis; we will consider the simplest extension of the SM scalar sector that leads the introduction of additional singlets and doublets.

An extended SM scalar sector is motivated by its presence in many other models, like supersymmetry [89] and the Peccei-Quinn model [90, 91], and it might explain the baryon asymmetry [92–94]. Further details can be found in the review of Ref. [10].

Scalars

$\Phi_1 = \begin{pmatrix} \phi_1^+ \\ \phi_1^0 \end{pmatrix} \in \mathbf{1} \otimes \mathbf{2} \otimes \frac{1}{2}, \quad \langle \Phi_1 \rangle = \frac{1}{\sqrt{2}} \begin{pmatrix} 0 \\ v_1 \end{pmatrix}$
$\Phi_2 = \begin{pmatrix} \phi_2^+ \\ \phi_2^0 \end{pmatrix} \in \mathbf{1} \otimes \mathbf{2} \otimes \frac{1}{2}, \quad \langle \Phi_2 \rangle = \frac{1}{\sqrt{2}} \begin{pmatrix} 0 \\ v_2 \end{pmatrix}$

Table 1.3: Scalar sector of the 2HDM. This complex doublet has isospin $I = \frac{1}{2}$.

The model we are going to introduce is the *Two-Higgs-Doublet Model* (2HDM) [95], which consists in the extension of the scalar sector of the SM with one additional scalar doublet with a different non-vanishing VEV. This model respects the experimental constraint $\rho = 1$ and represents one of the most simple UV-complete model with an extended scalar sector.

The most general potential for the scalar content of the 2HDM that respects Lorentz invariance, SM gauge symmetry, unitarity and renormalizability is

$$\begin{aligned} V_{2\text{HDM}} = & \mu_{11}^2 \Phi_1^+ \Phi_1 - \mu_{12}^2 [\Phi_1^+ \Phi_2 + \Phi_2^+ \Phi_1] + \mu_{22}^2 \Phi_2^+ \Phi_2 + \frac{\lambda_1}{2} (\Phi_1^+ \Phi_1)^2 + \frac{\lambda_2}{2} (\Phi_2^+ \Phi_2)^2 + \\ & + \lambda_3 \Phi_1^+ \Phi_1 \Phi_2^+ \Phi_2 + \lambda_4 \Phi_1^+ \Phi_2 \Phi_2^+ \Phi_1 + \frac{\lambda_5}{2} [(\Phi_1^+ \Phi_2)^2 + (\Phi_2^+ \Phi_1)^2]. \end{aligned} \quad (1.15)$$

where the details of the two Higgs doublets are depicted in Table 1.3. Imposing hermiticity and stability of the vacuums state, the following conditions can be imposed [96–99]:

$$\begin{aligned} \lambda_1 > 0, \quad \lambda_2 > 0, \quad \lambda_3 > -\sqrt{\lambda_1 \lambda_2}, \quad \lambda_3 + \lambda_4 - |\lambda_5| > -\sqrt{\lambda_1 \lambda_2} \\ \lambda_1, \lambda_2, \lambda_3 \in \mathbb{R}, \end{aligned} \quad (1.16)$$

and the non-zero VEVs of the scalar doublets

$$\Phi_1 = \frac{1}{\sqrt{2}} \begin{pmatrix} 0 \\ v_1 \end{pmatrix}, \quad \Phi_2 = \frac{1}{\sqrt{2}} \begin{pmatrix} 0 \\ v_2 \end{pmatrix}, \quad (1.17)$$

are constrained by $v_1^2 + v_2^2 = v^2$. Additional constraints on the 2HDM parameters can be set, like the unitarity constraints and experimental bounds [99–104].

Following the same steps presented for the SM case, it can be shown that after the spontaneous symmetry breaking $SU(2)_L \otimes U(1)_Y \rightarrow U(1)_{\text{EM}}$, 3 d.o.f. of the two doublets are eaten by the

massive bosons. However, instead of a single Higgs boson, there are five scalar Higgs bosons after the spontaneous symmetry breaking. Expressing the doublets in the unitary gauge:

$$\Phi_j = \begin{pmatrix} \phi_j^+ \\ \frac{1}{\sqrt{2}}(v_j + \rho_j + i\eta_j) \end{pmatrix}. \quad (1.18)$$

The mass terms with this new set of variables are

$$\begin{aligned} V_{2\text{HDM}}|_{\text{mass}} = & [\mu_{12}^2 - (\lambda_4 + \lambda_5)v_1v_2](\phi_1^-, \phi_2^-)M_\phi \begin{pmatrix} \phi_1^- \\ \phi_2^- \end{pmatrix} - (\rho_1, \rho_2)M_\rho \begin{pmatrix} \rho_1 \\ \rho_2 \end{pmatrix} \\ & + \left[\frac{\mu_{12}^2}{v_1v_2} - 2\lambda_5 \right] (\eta_1, \eta_2)M_\eta \begin{pmatrix} \eta_1 \\ \eta_2 \end{pmatrix} \end{aligned} \quad (1.19)$$

$$\begin{aligned} M_\phi &= \begin{pmatrix} \frac{v_2}{v_1} & -1 \\ -1 & \frac{v_1}{v_2} \end{pmatrix}, & M_\eta &= \begin{pmatrix} v_2^2 & -v_1v_2 \\ -v_1v_2 & v_1^2 \end{pmatrix}, & M_\rho &= v_1v_2M_\eta \\ M_\rho &= \begin{pmatrix} \mu_{12}^2 \frac{v_2}{v_1} + \lambda_1v_1^2 & -\mu_{12}^2 + (\lambda_3 + \lambda_4 + \lambda_5)v_1v_2 \\ -\mu_{12}^2 + (\lambda_3 + \lambda_4 + \lambda_5)v_1v_2 & \mu_{12}^2 \frac{v_1}{v_2} + \lambda_2v_2^2 \end{pmatrix}. \end{aligned}$$

The two mass matrices M_ϕ and M_η have a zero eigenvalue. The corresponding particle is the Goldstone boson eaten by the charge EW bosons and the boson Z . Therefore, we are left with a charged boson H^+ (and its antiboson), a pseudoscalar A and two neutral scalar bosons H_1 and H_2 .

The mass matrices can be diagonalized by means of two angles: α for the neutral scalar Higgs bosons and β for the charged and pseudoscalar ones. The latter is related to the doublets VEVs by

$$\tan \beta = \frac{v_2}{v_1}. \quad (1.20)$$

Assuming that there is no CP violation, both v_1 and v_2 can be assumed to be real [105]. Therefore, the physical fields of the 2HDM scalar sector are

$$\begin{aligned} H^\pm &= \phi_2^\pm \cos \beta - \phi_1^\pm \sin \beta, & m_\pm^2 &= \frac{(v_1^2 + v_2^2)}{v_1v_2} [\mu_{12}^2 - (\lambda_4 + \lambda_5)v_1v_2], \\ A &= \eta_2 \cos \beta - \eta_1 \sin \beta, & m_A^2 &= \frac{(v_1^2 + v_2^2)}{v_1v_2} [\mu_{12}^2 - (\lambda_3 + \lambda_4 + \lambda_5)v_1v_2], \\ H_1 &= \rho_2 \cos \alpha - \rho_1 \sin \alpha, & m_{H_1}^2 &= \frac{1}{2} \left[\text{Tr} [M_\rho] - \sqrt{\text{Tr} [M_\rho]^2 - 4 \det M_\rho} \right], \\ H_2 &= \rho_2 \cos \alpha + \rho_1 \sin \alpha, & m_{H_2}^2 &= \frac{1}{2} \left[\text{Tr} [M_\rho] + \sqrt{\text{Tr} [M_\rho]^2 - 4 \det M_\rho} \right]. \end{aligned} \quad (1.21)$$

The new Yukawa interactions have to be included into the 2HDM Lagrangian. The Yukawa terms for the down-type quarks is

$$\begin{aligned} -\mathcal{L}_Y^d &= Y_{ij}^1 \bar{Q}_{i,L} \Phi_1 d_{j,R} + Y_{ij}^2 \bar{Q}_{i,L} \Phi_2 d_{j,R} + h.c. \\ &\Downarrow \\ -\mathcal{L}_Y^d &\sim_{\langle \Phi_1 \rangle, \langle \Phi_2 \rangle} \left(Y_{ij}^1 \frac{v_1}{\sqrt{2}} + Y_{ij}^2 \frac{v_2}{\sqrt{2}} \right) \bar{d}_{i,L} d_{j,R} + h.c. \end{aligned} \quad (1.22)$$

The relevant Feynman rules used in thesis are depicted in Appendix I.

In general, the two Yukawa matrices cannot be diagonalized simultaneously: this fact leads to tree-level flavour-changing neutral currents (FCNC), which have never been seen by the experiments. These kind of currents can be avoided by imposing additional symmetries. Moreover, the Paschos-Glashow-Weinberg (PGW) theorem [106, 107] grants that tree level FCNC cannot occur if the fermions with same quantum numbers are coupled to the same Higgs doublet. To ensure the absence of tree level FCNCs by means of the PGW theorem, there are many possibilities:

Type I: All fermions coupled to Φ_2 only;

Type II: Down-type quark and leptons coupled to Φ_1 , up-type quark coupled to Φ_2 ;

Type X: Leptons coupled to Φ_1 , quarks coupled to Φ_2 ;

Type Y: Down-type quark coupled to Φ_1 , up-type quark and leptons coupled to Φ_2 .

Another possibility is that the Yukawa couplings involving Φ_1 and Φ_2 are proportional in the flavour space [108–110].

Type I can be induced by imposing a \mathbb{Z}_2 symmetry on Φ_1 , Type II by imposing an additional \mathbb{Z}_2 -symmetry on $d_{j,R}$. Type I has been studied in the context of dark matter [111–117], in the particular case of the inert Φ_2 doublet with $v_2 = 0$. In addition, the latter model with $\lambda_5 \rightarrow 0$ is Peccei-Quinn symmetric. On the other hand, Type II is particularly relevant since it can be treated as the effective field theory at low-energy for the Minimal Supersymmetric Standard Model with all heavy supersymmetric partners integrated out [9, 118–121].

The 2HDM has a variety of interaction vertices and four additional particles, leading to a rich phenomenology involving CP conserving and violating sources [10]. This model has been employed in the study of various BSM investigations, like composite and little Higgs models [122–124], Naturalness [125] and the origin of the neutrino masses [112].

The 125 GeV resonance discovered in 2012 compatible with a Higgs boson candidate has set another strong constraint. The possibility that it was a signal of the pseudoscalar boson A has been studied in Ref. [126], but it was discarded by the data analysis [7, 8], as well as the chance that the detection was related with a neutral heavy scalar [127]. Therefore, the most reasonable scenario is that the signal detected at the LHC comes from either a SM Higgs boson H or a neutral scalar light Higgs H_1 .

1.3 Higgs boson detection

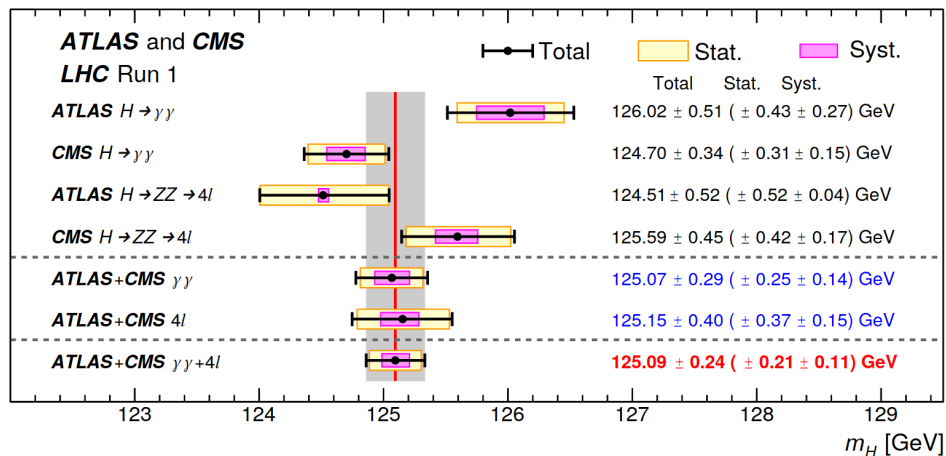


Figure 1.1: Higgs boson mass determination [128]. Combined analysis of ATLAS and CMS experiments

In 2012, the LHC experiments ATLAS [5] and CMS [6] announced the discovery of a neutral scalar boson compatible with the SM Higgs boson. The combined result of the experiments (Fig. 1.1) has fix its mass to $m_H = 125.09 \pm 0.24$ GeV [128]. It was the last unknown parameter of the SM, and it gives access to various phenomenological predictions.

The detection has been analyzed starting from two datasets recorded by ATLAS and CMS during the LHC Run 1, looking at the decays $H \rightarrow ZZ/WW \rightarrow 4l$, $H \rightarrow \gamma\gamma$, $H \rightarrow b\bar{b}$ and $H \rightarrow \tau^+\tau^-$. The two independent analyses agreed with a significant excess of events above the background, signal of the production of a neutral boson. Later on, the two datasets have been combined in a comprehensive study specific on the channels $H \rightarrow ZZ \rightarrow 4l$ and $H \rightarrow \gamma\gamma$, which gave the best mass resolution.

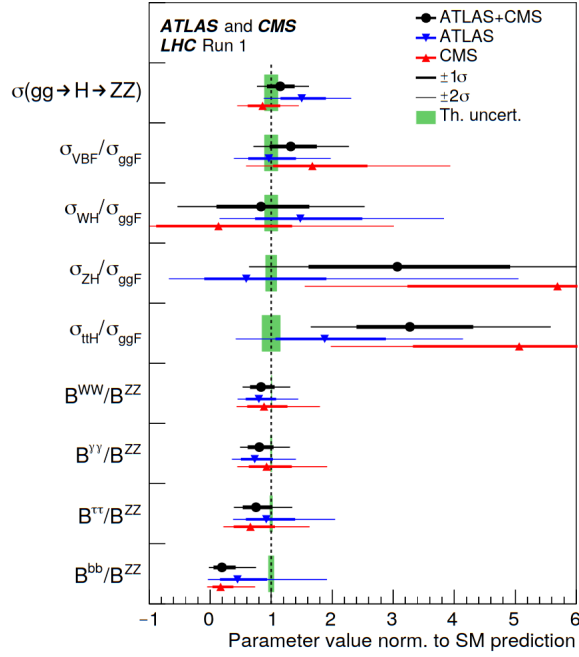


Figure 1.2: Best fit for the Higgs production and decay [128].

Knowing the Higgs mass, its production and decay can be studied. A detailed analysis of the following production processes have been done: gluon fusion, vector boson fusion and associated production with a vector boson or a top-quark pair [128]. The decay rates, that this analysis has considered, are: $H \rightarrow ZZ, WW, \gamma\gamma, \tau\tau, bb$ and $\mu\mu$. The already mentioned dataset shows compatibility with the production and decay of a SM Higgs (Fig. 1.2). Also, this analysis provided predictions on its couplings to vector bosons and fermions.

At last, the CP properties of this particle have been inferred from the angular distribution of the leptonic decays, showing complete agreement with the hypothesis $J^P = 0^+$, once again compatible with the SM Higgs [7, 8].

However, the evidence of the existence of this Higgs boson does not exclude a priori the possibility of its belonging to an extended scalar sectors, since the 2HDM scalar sector has a particle compatible with the detected one [11, 23].

1.4 Higgs boson pair production

As it has been shown before, the data analyses have checked most of the quantities related with the Higgs boson, namely its mass, CP properties and coupling to other particles with great precision, and shows compatibility with the SM prediction. However, the Higgs self-coupling is not accessible with the present LHC dataset. The upcoming high luminosity upgrade of the LHC and other future colliders will give us access to the study of the Higgs self-coupling [17–28].

The self-couplings of Higgs bosons are allowed by the constraints imposed on the SM and 2HDM Lagrangians, and they come from the Higgs potential:

$$\begin{aligned}
 V_\Phi &= -\mu^2 H^2 - \frac{\mu^2}{v} H^3 - \frac{\mu^2}{4v^2} H^4 \\
 &= \frac{m_H^2}{2} H^2 + \frac{\lambda_{3H}}{3!} H^3 + \frac{\lambda_{4H}}{4!} H^4 \\
 \lambda_{3H} &= \frac{3m_H^2}{v}, \quad \lambda_{4H} = \frac{3m_H^2}{v^2}.
 \end{aligned} \tag{1.23}$$

The parametrization of the 2HDM gives rise to more complex structures, but the trilinear-quartic

Higgs couplings can be written as follows (Appendix I)

$$V_{2\text{HDM}} = \sum_j \frac{m_{H_j}^2}{2} H_j^2 + \sum_{ijk} \frac{\lambda_{ijk}}{3!} H_i H_j H_k + \sum_{ijkl} \frac{\lambda_{ijkl}}{4!} H_i H_j H_k H_l \quad (1.24)$$

$$\lambda_{ijk} = \frac{3c_{ijk}}{v}, \quad \lambda_{ijkl} = \frac{3c_{ijkl}}{v^2}$$

Exploring the Higgs self-coupling is crucial to fully reconstruct the shape of the Higgs potential with a non-zero VEV.

This is a very challenging measurement, since the Higgs-pair production is a strongly suppressed process. With respect to single-Higgs production, it has a first suppression due to the phase space, that now has to take into account an additional final state heavy particle; moreover, it is a process of higher EW order, which gives another suppression factor. In addition, there are several irreducible background subprocesses which lead to the same final state but do not contain any Higgs self-coupling.

The quartic Higgs interaction is unreachable by the experiment due to the strong EW suppression [12–16]; the trilinear Higgs coupling instead will be accessible with the upgrade of the LHC, allowing the study of processes which involve the production of an off-shell Higgs boson that decays into two Higgs bosons [129]. These interactions may occur in the Higgs-pair production processes, which is the ingredient for a direct measurement of the trilinear Higgs coupling.

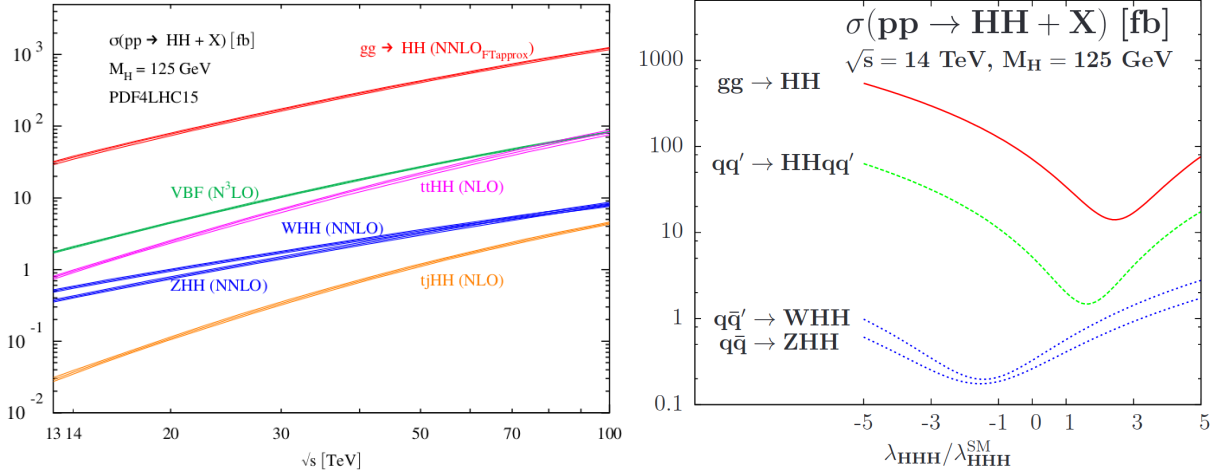


Figure 1.3: *Left plot: Cross section of the Higgs-pair production channels [29]. Right plot: sensitivity of the Higgs-pair production channels with respect to the trilinear Higgs coupling [23].*

There are four channels contributing to the Higgs-pair production process: gluon fusion [54, 130–132], vector-boson fusion [133–135], double Higgs-strahlung [131, 136] and associated production with heavy quarks [23, 137]. The gluon fusion is the dominant process (Figure 1.3), with a cross section of one order of magnitude higher with respect to the others. However, its cross section σ is still three orders of magnitude lower than the single-Higgs production [29]. In addition, for the gluon fusion channel, the relative uncertainties of its cross section are related to the relative uncertainties of the trilinear coupling in the ratio with the SM [23] with the following approximate relation

$$\frac{\Delta\sigma}{\sigma} \sim -\frac{\Delta\lambda_{3\text{H}}}{\lambda_{3\text{H}}}. \quad (1.25)$$

These facts can be inferred by the negative slope of the red curve of Figure 1.3 (right plot), and it sets the importance of investigating the gluon fusion channel of the Higgs-pair production process with high theoretical accuracy. This can only be achieved by introducing higher order corrections. Since gluon fusion is a QCD induced process, it is known that higher orders³ in QCD may introduce very large contributions to the total cross section: for single-Higgs production via gluon fusion, higher order terms introduced corrections of more than 60% [138–142].

³In the next section we will define to which order are we referring here.

Since the Higgs boson does not couple to the gluons directly, the gluon fusion channel is mediated by quark loops already at leading order. The Yukawa couplings are proportional to the quark mass: this means that the main contribution to the cross section comes from the heaviest quark, namely the top quark; lighter quark corrections are below the 1%. It has been proven that the Higgs-pair production via gluon fusion cross section behaves analogously to the single-Higgs production with respect to the perturbative order: higher order corrections are very large [32, 140]. The main reason for this is that additional QCD perturbative orders open more channels that sum to the latter ones.

The equivalent process in the 2HDM will be neutral scalar Higgs-pair production, where we allow the final state to be $H_i H_j$. If $i = j$ the process is very similar to the SM one, where the only difference lies in the Yukawa couplings to the top quark and the Higgs masses. The difference starts to be noticeable in the case where $i \neq j$, which involves two different Yukawa couplings and Higgs masses, making the actual calculation more complex. Moreover, it is important to notice that the Yukawa couplings, while in the SM are proportional only to the quark mass, in the 2HDM are proportional to $\tan \beta$ (or $\cot \beta$); this fact might strongly enhance such couplings and make the contributions of the lighter quarks in the loop relevant [10].

1.4.1 Measurement

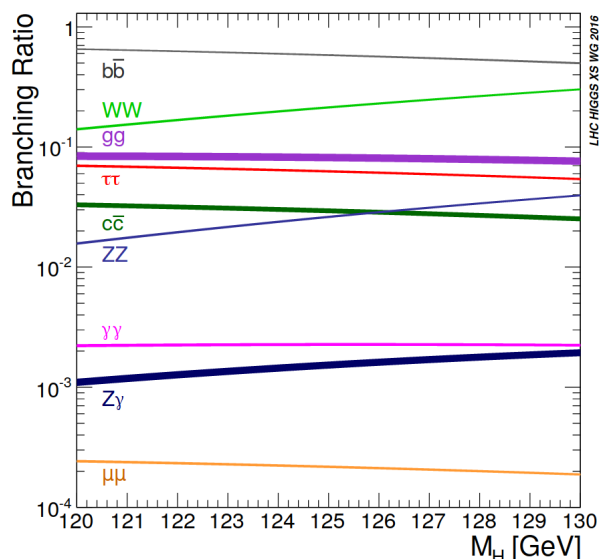


Figure 1.4: Branching ratios of the Higgs boson [30].

As shown in Fig 1.4, the Higgs mainly decays into a bottom quark pair [30]: hence it may be natural to search for the $b\bar{b}b\bar{b}$ final state. However, this final state has a huge QCD background, that makes the extraction of the signal incredibly hard. A more reliable analysis can be done by considering more rare final state like $b\bar{b}\gamma\gamma$ and $b\bar{b}\tau\tau$ [28, 29].

The $b\bar{b}\gamma\gamma$ final state constitutes a promising candidate due to its clean signal, leading to a determination of the Higgs coupling with 40% uncertainty [23, 31]. The current bounds on the trilinear Higgs coupling come from CMS analysis of the $HH \rightarrow b\bar{b}\gamma\gamma$ channel, which have set $-8\lambda_{3H}^{\text{SM}} < \lambda_{3H} < 15\lambda_{3H}^{\text{SM}}$. With the forthcoming high luminosity LHC, ATLAS can decrease the bound to $-0.8\lambda_{3H}^{\text{SM}} < \lambda_{3H} < 7.7\lambda_{3H}^{\text{SM}}$ [129].

The process $b\bar{b}\tau\tau$ has a more complex background that makes the study of this channel harder, and is strongly dependent on the capability of reconstructing the τ pairs of the experiment. However, it has been proven that, in optimistic scenarios, it represents a valid final state candidate [23].

1.5 Cross section: an overview on the calculation

The perturbative QCD provides an ideal framework to calculate the cross section of the Higgs-pair production via gluon fusion. In this work, we will consider the production of two neutral scalar Higgs bosons, namely $pp \rightarrow H_1 H_2$.

The total cross section can be written as a perturbative series with respect to the strong coupling constant: this will provide the following expansion

$$\sigma(pp \rightarrow gg \rightarrow H_1 H_2) = \sigma_{\text{LO}} + \Delta\sigma_{\text{NLO}} + \cdots + \Delta\sigma_{\text{N}^n\text{LO}} + O(\alpha_s^{n+3}). \quad (1.26)$$

The QCD factorization theorems [51] set the condition under which high energy hadrons can be described as bound states of its constituents, quark and gluons, carrying a fraction of its total momentum. Hence, in proton-proton collisions their constituents interact: we are interested in the case where a gluon carrying momentum $p_1 = x_1 P_1$ interacts with a gluon carrying momentum $p_2 = x_2 P_2$, with P_i the protons momenta. This represents a short distance interaction, that can be studied perturbatively and it is independent on the external hadron; short-distance interactions *factorize* from the long-distance one, which are encoded into the parton distribution functions (PDFs) [52]. These objects have a non-perturbative nature, and they take into account the structure of the hadrons. PDFs are interpreted as the probability that a parton inside a proton carry a certain fraction of the total momentum.

Starting from the Leading Order (LO) cross section, the factorization theorem states that

$$\sigma_{\text{LO}}(pp \rightarrow gg \rightarrow H_1 H_2) = \int_0^1 dx_1 dx_2 f_g(x_1, \mu_F) f_g(x_2, \mu_F) \hat{\sigma}_{\text{LO}}(g(p_1)g(p_2) \rightarrow H_1 H_2), \quad (1.27)$$

where $f_g(x_i, \mu_F)$ are the PDFs for the gluons, x_i is the fraction of the i proton momentum, μ_F is the *factorization scale* and $\hat{\sigma}$ is the partonic cross section; μ_F is much larger than the scale down to which the factorization theorem holds. This expression can be written in a simpler way: at the LHC the scattering is studied in the center-of-mass frame of the colliding protons \sqrt{s} ; the production of the two Higgs bosons starts above the production threshold $\hat{s} = (m_{H_1} + m_{H_2})^2$; putting together these considerations, the LO cross section becomes

$$\sigma_{\text{LO}}(pp \rightarrow gg \rightarrow H_1 H_2) = \int_{\tau_0}^1 d\tau \frac{d\mathcal{L}^{gg}}{d\tau} \hat{\sigma}(\hat{s})|_{\hat{s}=\tau s}, \quad (1.28)$$

$$\frac{d\mathcal{L}^{gg}}{d\tau} = \int_{\tau}^1 \frac{dx}{x} f_g(x, \mu_F) f_g\left(\frac{\tau}{x}, \mu_F\right), \quad \tau = \frac{\hat{s}}{s}, \quad \tau_0 = \frac{(m_{H_1} + m_{H_2})^2}{s},$$

where $\frac{d\mathcal{L}^{gg}}{d\tau}$ is the gluon luminosity.

The PDFs are determined by experimental fits of data obtained from deep inelastic scattering processes. The perturbative part is the partonic cross section $\hat{\sigma}$. The perturbative QCD approach relates it with the square of the scattering amplitude integrated over the phase space at a fixed order:

$$\hat{\sigma}_{\text{LO}}(\hat{s}) = \int d\text{PS}_2 \overline{|\mathcal{M}_{\text{LO}}|^2}, \quad (1.29)$$

where $d\text{PS}_2$ is the phase space element and \mathcal{M}_{LO} is the scattering amplitude. The line above the square amplitude stands for the polarization average. The scattering amplitude, namely the sum of the Feynman diagrams [53], can be built from the knowledge of the Lagrangian, that introduce into the game a dependence on the theory.

Since in both the 2HDM and SM there are no interaction vertices between Higgs and gluons, the amplitude of $gg \rightarrow H_1 H_2$ is loop induced already at the LO. The bulk of the amplitude is carried by the top-quark loop, due to the Yukawa interaction that enhances the heavy quark contributions. This leads us to consider only the top loops. Notice that at LO⁴, there is an additional threshold: $\hat{s} = 4m_t^2$. This corresponds to the $t\bar{t}$ production threshold.

⁴Of course, this threshold occurs at every perturbative order, but beyond LO, other thresholds arises. For the gluon rescattering diagrams at NLO, an additional threshold starts at $\sqrt{\hat{s}} = 0$ GeV, which leads to infrared singularities. This structure will be discussed in Chapter 3.

At Next-to-Leading Order (NLO), the calculation of the two-loop amplitude is required; in addition, one-loop diagrams with one radiating parton have to be considered as well. The latter belong to three new QCD channels with different initial states: the quark-antiquark $q\bar{q}$, the quark-gluon qg and the gluon-gluon gg initial states. The NLO partonic cross section can be written as

$$\begin{aligned}\Delta\hat{\sigma}_{\text{NLO}} &= \Delta\hat{\sigma}_{\text{virt}} + \Delta\hat{\sigma}_{q\bar{q}} + \Delta\hat{\sigma}_{qg} + \Delta\hat{\sigma}_{gg} \\ \Delta\hat{\sigma}_{\text{virt}} &= \int d\text{PS}_2 \, 2\text{Re} \left[\overline{\mathcal{M}}_{\text{LO}}^* \mathcal{M}_{\text{virt}} \right], \\ \Delta\hat{\sigma}_{ij} &= \int d\text{PS}_3 \, \overline{|\mathcal{M}_{ij}|^2},\end{aligned}\tag{1.30}$$

where $\mathcal{M}_{\text{virt}}$ is the *virtual amplitude* containing the two-loop diagrams, and \mathcal{M}_{ij} are the contributions of the ij initial state, called *real corrections*.

1.5.1 Divergences and their treatment

In general, higher order corrections to an observable introduce divergences. This is a general feature of the perturbative expansion of a quantum field theory. The most recognizable source of divergences are the loop corrections, which are related to the integration over the so-called *loop momentum*. An example of divergent Feynman integral is the so-called *massless tadpole*:

$$\int_{\mathbb{M}} \frac{d^4k}{(2\pi)^4} \frac{1}{(k^2)^2},\tag{1.31}$$

where k^μ is the loop momentum. Integrating over the time component and setting two cut-offs λ and Λ :

$$\int_{\mathbb{M}} \frac{d^4k}{(2\pi)^4} \frac{1}{(k^2)^2} \propto \int_{\lambda}^{\Lambda} \frac{d|\mathbf{k}|}{|\mathbf{k}|} = \log \frac{\Lambda}{\lambda}.\tag{1.32}$$

This integral is singular in both limits $\Lambda \rightarrow \infty$ and $\lambda \rightarrow 0$. The first is called *ultraviolet* (UV) *divergence*, arising at high values of the module of the loop momentum, and they come purely from the loop integration. The latter is an *infrared* (IR) *divergence*, occurring in the small momentum region, and can occur even at tree level with the phase space integration. A typical loop source of infrared divergence comes from a massless propagator connecting two external propagators that become soft. However, a physical observable must be UV and IR finite: the divergences have to be isolated and canceled.

As we are interested in the NLO QCD corrections to Higgs-pair production, the treatment of the UV and IR divergences has to be discussed. The LO of the process we are considering, even though formed by one-loop diagrams, is screened from UV divergences because of the gauge invariance; in addition, since no massless propagators occur in the loops, IR divergences do not show up.

At NLO, UV and IR divergences appear. A *regularization scheme* is needed in order to isolate them. In this calculation, *dimensional regularization* is used [55–57]: the idea is to treat the amplitude as analytic function of the space-time dimension $d = 4 - 2\epsilon$:

$$\int_{\mathbb{M}} \frac{d^4k}{(2\pi)^4} \rightarrow (\mu^2)^{\frac{4-d}{2}} \int_{\mathbb{M}} \frac{d^d k}{(2\pi)^d}\tag{1.33}$$

where the 't Hooft scale μ has the role of preserving the mass dimensionality of the amplitude. The regularization procedure makes the UV and IR divergences be poles in the ϵ analytic expansion around $\epsilon = 0$ (namely the 4-dimensional limit). At NLO, the analytic structure manifests poles up to second order.

The procedure of canceling the UV divergences is called *renormalization*. Interpreting the fields, coupling and parameters of the Lagrangian to be *bare* quantities, they develop divergences at higher orders. In order to obtain physically meaningful predictions, they have to be expressed in terms of the physical quantities (i.e. the *renormalized* ones). Their higher order terms entering the perturbative expansion are the *counterterms*. The choice of the counterterms fixes the *renormalization scheme* and

scale. The only constraint is that the counterterms have to cancel the UV poles coming from the NLO amplitude. The renormalization scheme influences the finite part of the amplitude, which introduces a renormalization scheme dependence order-by-order in the amplitude. However, this dependence completely disappears if the entire perturbation series is considered. More details on the specific renormalization scheme we have chosen can be found in Chapter 3.

The IR divergences are treated in a different way. The Kinoshita-Lee-Nauenberg (KLN) theorem [58, 59] ensures the IR safety of a sufficiently inclusive observable. The inclusiveness needed for the Higgs-pair production indicates that in addition to the virtual amplitude, which has the same final state, additional contributions have to be considered: these are the real corrections. Since they develop soft and collinear divergences, they can be combined to the virtual contribution to obtain an IR safe observable.

Since the calculation will be performed numerically, the cancellation of the IR divergences is more involved, because it takes place between terms that are integrated over different final states: this would introduce strong numerical instabilities in the single integrations. There are different ways to overcome this issue, represented by different *subtraction techniques* [60–65]. They rely on the introduction of an auxiliary differential cross section $d\sigma_A$ with the same IR pole structure of the process. This term will be added and subtracted at the level of the differential cross section in the following way:

$$\Delta\hat{\sigma}_{\text{NLO}} = \int d\text{PS}_2 \left[2\overline{|\mathcal{M}_{\text{LO}}^* \mathcal{M}_{\text{virt}}|} + \int d\text{PS}_1 d\sigma_A \right] + \int d\text{PS}_3 \left[\overline{|\mathcal{M}_{q\bar{q}}|^2} + \overline{|\mathcal{M}_{qg}|^2} + \overline{|\mathcal{M}_{gg}|^2} - d\sigma_A \right] \quad (1.34)$$

Each separated integral is now finite and the numerical integration will be stable. For this particular process, the auxiliary term has been build from the knowledge of the heavy-quark behaviour of the process. Further details will be presented in Chapter 3.

The last source of divergences comes from the collinear initial-state singularities, for which the KLN theorem does not hold, since one does not sum over the initial states. They can be absorbed by a renormalization of the PDFs, meaning that the behaviour of the collinear emission of a parton by the initial state is related to the non-perturbative parton PDFs and has been removed from the hard scattering.

1.6 Present status

The Higgs-pair production within the SM has been investigated in several approximations, valid for different phase space regions. There are three phase spaces regions of interest: the low energy region ($\hat{s} \lesssim 4m_t^2$), the $t\bar{t}$ threshold region ($\hat{s} \approx 4m_t^2$) and the high energy region ($\hat{s} \gg 4m_t^2$). Moreover, two independent NLO SM Higgs-pair production with full top-mass dependence calculations are available in the literature.

1.6.1 Low energy region

In the low energy region, the heavy top-quark limit (HTL) is valid. Many works have investigated this region up to N³LO. The first result is the *Born-improved* NLO calculation [32]: it consists in the LO with full top-mass dependence calculation in addition with the HTL NLO contribution. In this way, virtual and real corrections can be built from the effective Higgs-gluon interaction arising from the integration of the top mass, leading to a one-loop virtual amplitude and tree level real corrections. The differential K-factor, defined as

$$K = \frac{d\sigma_{\text{NLO}}}{d\sigma_{\text{LO}}}, \quad (1.35)$$

found in this approximation ranges between 1.9 and 2.

A mass refinement of the Born-improved approximation leads to the *full-theory approximation* [24, 33], obtained by considering the mass dependent NLO real contributions. They consist of the inclusion of complete one-loop five-point matrix element contributions to the real corrections. The introduction of these top-mass effects yields 10% reduction with respect to the previous approximation.

Going further in this direction, a NNLO Born-improved has been included in the previous calculations [34, 35]. This includes the virtual two-loop effective amplitude and real contributions with

five and six points one-loop and tree level matrix elements. The inclusion of the HTL NNLO effects to the full-theory approximation leads to an increase of the K-factor by 20%. The scale uncertainties reduce to $\pm 13\%$. The calculation including Next-to-Leading-Log (NNLL) decrease even more the scale uncertainties, achieving a $\pm 11\%$ [36, 37]. All the uncertainties have been found by varying the factorization and renormalization scales a factor 2 up and down from $\sqrt{\hat{s}}/2$. Recently a complete HTL N³LO calculation has been performed [38]. These refinements lead to an additional correction of the 3% to the NNLO cross section, and to scale uncertainties of about 2%.

A first attempt to include finite top-mass effects as terms of an expansion on the $1/m_t^2$ parameter has been done at NLO and NNLO. The NLO calculation considers the expansion of the integrals, making use of the optical theorem and performing the $1/m_t^2$ expansion [39]. At NNLO level, genuine top-mass expansion terms are included into the integrands, and the amplitude coefficients have been evaluated analytically. The most recent works in this direction have included eight expansion terms for the box and five for the triangle contributions, leading to a good convergence to higher Higgs-pair invariant mass values [40, 41]. The top-mass effects amount to about 10% at NLO and to 5% at NNLO. An N³LO mass refinement have been introduced by the one-particle-reducible contributions, including diagrams involving two-loop effective vertices known from the previous expansion order.

1.6.2 Threshold region

Recently, in Refs. [42, 43], a method to incorporate the large non-analytic behaviour of the differential cross section around the threshold region into the HTL expansion of the NLO differential cross section has been proposed. This strategy relies on the Padé approximant ansatz, which reads

$$[n/m](\omega) = \frac{a_0 + a_1\omega + \dots + a_n\omega^n}{1 + b_1\omega + \dots + a_m\omega^m}, \quad \frac{\hat{s}}{4m_t^2} = \frac{4\omega}{(1+\omega)^2}. \quad (1.36)$$

where the coefficients can be determined from the non-analytical part of the cross section for $\hat{s} \approx 4m_t^2$. This method can be adopted for the Higgs-pair production process within the 2HDM too, where the two final state Higgs particles may have different masses.

This method, applied to the SM, yields reliable results for the NLO cross section up to $\sqrt{\hat{s}} \lesssim 700$ GeV and provides a useful strategy to determine the top-mass effects at NNLO, currently far from a computationally viable full top-mass calculation.

1.6.3 High energy region

The high energy region can be explored by performing an expansion for $m_t^2 \ll s, |t|$ and $m_H = 0$. This approach has been explored at NLO SM in Refs. [44–46], where other refinements have been considered: eight additional terms of the top mass m_t^2/\hat{s} expansion and two terms of the finite Higgs mass expansion $m_H^2/m_t^2 \approx 0.13$. The form factors obtained in such approximation are completely analytical, based on the master integral decomposition and their analytical evaluation. It is an extremely useful result that can be exploited in cross checks with full top-mass dependent form factors. The radius of convergence of the expansion has been increased further by introducing Padé approximants for the master integrals.

The differential distribution obtained with this approach has been cross-checked with the full NLO calculation, resulting in full agreement down to 500 GeV.

1.6.4 p_T expansion and full top-mass NLO contribution

A promising method has been investigated in Ref. [143] where an expansion in terms of small transverse momentum $p_T^2 \sim 0$ has been performed. It has a very wide range of validity, that covers the low energy and threshold regions, arriving up to $\sqrt{\hat{s}} \lesssim 750$ GeV, giving an approximation at NLO SM better than per-mille.

At last, a NLO SM Higgs-pair production calculation with full top-mass dependence has been carried out in Refs. [47, 144]. The form factors have been decomposed in terms of the master integral by means of the IBP reduction, and the differential cross section has been evaluated numerically,

since not all the master integrals found were known analytically. The bottleneck of this calculation was represented by the IBP reduction. A simplification introduced to facilitate the integral reduction was fixing the numerical value for m_H and m_t . The masses have been set to $m_t = 173$ GeV and $m_H = 125$ GeV. The complete result leads to a NLO differential K-factor of 20-30% smaller w.r.t. the Born-improved method.

The other NLO SM Higgs-pair production via gluon fusion cross section calculation [67, 68] will be exhaustively discussed in Chapter 5 of this thesis, since it represents the major outcome of this work. As a remarkable difference from the first calculation, our work treats the top mass and the Higgs masses as independent variables: this allowed us to estimate the uncertainties related with the top-mass renormalization scale and scheme [69].

1.7 Topic of this thesis

We present our NLO QCD Higgs-pair production via gluon fusion calculation with full top-mass dependence. Our procedure is meant to be as general as possible, including the possibility of applying it to all possible 2HDM Higgs-pair final states.

The main difference between the two models, SM and 2HDM, applied to the process under examination is the presence of Higgs bosons of different mass. This introduces more complexity in the calculation, since the two-loop Feynman integrals contributing to the form factors will depend on five mass scales and (two kinematic invariants, two Higgs bosons and the top-quark mass). In addition, they are two-loop integrals, for which no automated strategy has been developed so far.

However, building a general framework generalizing the SM calculation can be done revisiting the Feynman rules of the 2HDM and rescaling them with respect to the SM couplings. For the neutral scalar Higgs bosons, this rescaling turns into a simple factor, depending on the Higgs boson and the model type, in particular of the angles α and β . It can be represented schematically as

$$-i\frac{m_t}{v} \rightarrow -i\frac{m_t}{v}Y_j, \quad (1.37)$$

where j refers to the light Higgs H_1 or the heavy Higgs H_2 . For the pseudoscalar A , there is an additional γ^5 , responsible of the eventual CP violation, which does not change the prescription we use:

$$-i\frac{m_t}{v} \rightarrow \frac{m_t}{v}\gamma^5Y_j. \quad (1.38)$$

The introduction of pseudoscalars requires a prescription to treat the γ^5 , since we use dimensional regularization and it is impossible to define a d -dimensional γ^5 [145]. In particular, it is not possible to have both

$$\{\gamma^5, \gamma^\mu\} = 0, \quad \mu = \{1, \dots, d\}, \quad (1.39)$$

and

$$\text{Tr} [\gamma^5 \gamma^\mu \gamma^\nu \gamma^\rho \gamma^\sigma] = 4! \epsilon^{\mu\nu\rho\sigma}. \quad (1.40)$$

A convenient choice for dealing with the AA final state is using the *naive dimensional regularization*: no definition of γ^5 will be set and the relation in Eq. (1.39) is used. The Dirac traces will be expressed in terms of metric tensors pretending that they are four dimensions, and at the end the result are interpreted in d dimensions. For mixed scalar-pseudoscalar cases, the presence of the ABJ anomaly [146, 147] makes the previous choice inconsistent. A proper way to treat the γ^5 has been proposed by 't Hooft and Veltmann [55], and systematized by Breitenlohner and Maison [148]. They define the d -dimension γ^5 from Eq. (1.40), leading to

$$\gamma^5 = \frac{1}{4!} \epsilon^{\mu\nu\rho\sigma} \gamma_\mu \gamma_\nu \gamma_\rho \gamma_\sigma, \quad (1.41)$$

and Eq. (1.39) to be

$$\begin{aligned} \{\gamma^5, \gamma^\mu\} &= 0, & \mu &= \{1, \dots, 4\}, \\ [\gamma^5, \gamma^\mu] &= 0, & \text{else,} \end{aligned} \quad (1.42)$$

such that the axial term does not vanish.

Even if different Higgs-pair final states will lead to an extremely varying phenomenology, at the level of the calculation they can be treated within the same framework, as we will explain in detail in Chapters 2 and 3. Moreover, since the charged scalar and the pseudoscalar Higgs bosons will introduce unnecessary complication into the calculation, we will restrain ourself in presenting the neutral scalars final state, meaning $gg \rightarrow H_1 H_2$ at partonic level.

Briefly, our strategy can be summarized as follows:

- Generate the LO and NLO amplitude;
- Perform the projection onto form factors and the numerator algebra;
- Isolate the UV/IR divergences by means of end-point subtractions;
- Take care of the IR divergences with a dedicated subtraction term;
- Renormalize the form factors to obtain a UV finite virtual amplitude;
- Integrate over the phase space;
- Evaluate the square amplitude of the real corrections and integrate them over the phase space;
- IR singularities from virtual corrections cancels against the real corrections ones;
- Initial state singularities are absorbed by the PDFs.

All the integrations involved in this calculation will be performed numerically, using a Monte Carlo integration. Its details will be discussed in Chapter 4. The phenomenological analyses will be presented in Chapter 5.

Chapter 2

Leading Order Cross Section

The LO cross section represents the first step of this calculation. Even though it is not the main topic of this thesis, it is essential to consider the LO matrix elements not only to settle the framework, but also because the NLO contribution is defined as the interference between the one-loop and two-loop form factors; moreover, the LO amplitude will take part in the renormalization of the NLO amplitude and in the subtraction scheme for the IR divergences. It is a very old calculation [54], but it is nonetheless instructive to present the whole calculation together with its heavy quark limit.

In this Chapter, the complete LO Higgs-pair production cross section is presented. The analytical expression of the heavy quark limit amplitude will be presented, as well as the gluon-Higgs effective vertices [32]. At last, the LO form factors will be expressed in terms of scalar Feynman integrals after having applied the Passarino-Veltmann reduction [149]. It is important to underline that such integrals have to be known up to the order $O(\epsilon^2)$, as it is required by the NLO UV, collinear and infrared divergences. The LO form factors will be implemented in a FORTRAN code, ready to be used in the context of the NLO calculation.

2.1 Preliminaries: Single-Higgs production with one off-shell gluon

The building block for our calculation is the single-Higgs production via gluon fusion amplitude:

$$\mathcal{M}_{ggH_j} = \text{1-loop} \text{---} H_j = \text{triangle}_1 + \text{triangle}_2, \quad (2.1)$$

Considering the top-quark contribution only, the amplitude \mathcal{M}_{ggH_j} can be written in terms of a single diagram:

$$\mathcal{M}_{ggH_j} = \epsilon_\mu(p)\epsilon_\nu(q)(1)\mathcal{M}_{ggH_j}^{\mu\nu,ab}(p,q), \quad (2.2)$$

where $\mathcal{M}_{ggH_j}^{\mu\nu,ab}(p,q)$ is the amputated amplitude. Let us stress that the first argument of $\mathcal{M}_{ggH_j}^{\mu\nu,ab}(p,q)$ is an on-shell momentum and the second is an off-shell one. The Feynman rules for this process are presented in Appendix I. The Casimir operator is $\text{Tr}[T^a T^b] = \frac{1}{2}\delta^{ab}$. The SM rules can be recovered by setting $\lambda_{111} = m_H$ and $Y_1 = 1$, $\lambda_{ijk} = 0$ and $Y_j = 0$ for $i, j, k \geq 2$. At the end of this calculation, we will find an effective Feynman rule about the interaction between two gluons and a Higgs boson. With these rules, the gluon fusion amplitudes becomes

$$\mathcal{M}_{ggH_j}^{\mu\nu,ab}(p,q) = (-)(2)\frac{i}{(4\pi)^2}(4\pi\mu^2)^{2-\frac{d}{2}} \times \int_k \text{Tr} \left[(-ig_s\gamma_\mu T^a) \frac{i(\not{k} - \not{p} + m_t)}{(k-p)^2 - m_t^2} \left(-i\frac{m_t}{v} Y_j \right) \frac{i(\not{k} + \not{q} + m_t)}{(k+q)^2 - m_t^2} (-ig_s\gamma_\nu T^b) \frac{i(\not{k} + m_t)}{k^2 - m_t^2} \right], \quad (2.3)$$

where¹ $\int_k = \int \frac{d^d k}{i\pi^{d/2}}$ and the factor 2 comes from the exchange of the incoming gluons. Through simple algebra passages, and by considering the amputated diagram, it follows

$$\begin{aligned}\mathcal{M}_{ggH_j}^{\mu\nu,ab}(p,q) &= -iY_j \frac{m_t}{v} \frac{g_s^2}{(4\pi)^2} 2\text{Tr}[T^a T^b] (4\pi\mu^2)^{2-\frac{d}{2}} \int_k \frac{\text{Tr}[\gamma^\mu(\not{k} - \not{p} + m_t)(\not{k} + \not{q} + m_t)\gamma^\nu(\not{k} + m_t)]}{[k^2 - m_t^2][(k-p)^2 - m_t^2][(k+q)^2 - m_t^2]} \\ &= -iY_j \left(\frac{\alpha_s m_t}{\pi v}\right) \delta^{ab} (4\pi\mu^2)^{2-\frac{d}{2}} \int_k \frac{\mathcal{N}^{\mu\nu}}{D_0 D_1 D_2}, \\ \mathcal{N}^{\mu\nu} &= \frac{1}{4} \text{Tr}[\gamma^\mu(\not{k} - \not{p} + m_t)(\not{k} + \not{q} + m_t)\gamma^\nu(\not{k} + m_t)].\end{aligned}\tag{2.4}$$

For later purposes, we consider the gluon with momentum q^μ to be off-shell, so that $q^2 \neq 0$, while $p^2 = 0$ and $(p+q)^2 = \hat{s}$. The Higgs boson is produced off-shell.

2.1.1 Projection onto the tensor basis: form factors

This rank-2 tensor can be written as

$$T^{\mu\nu}(p,q) = a_{00}g^{\mu\nu} + a_{pp}p^\mu p^\nu + a_{pq}p^\mu q^\nu + a_{qp}q^\mu p^\nu + a_{qq}q^\mu q^\nu,\tag{2.5}$$

and imposing the transversality of the external gluons:

$$\begin{cases} p_\mu T^{\mu\nu}(p,q) = 0 \\ q_\nu T^{\mu\nu}(p,q) = 0 \end{cases} \quad \text{such that} \quad \epsilon_h^\mu(p)p_\mu = 0, \quad \epsilon_h^\nu(q)q_\nu = 0 \quad \text{and} \quad p^2 = 0,\tag{2.6}$$

we find that

$$T^{\mu\nu}(p,q) = a_{00} \left(g^{\mu\nu} - \frac{q^\mu p^\nu}{(p \cdot q)} \right) = a_{00} T_1^{\mu\nu}.\tag{2.7}$$

Through $T_1^{\mu\nu}$, it is possible to define the projector

$$P^{\mu\nu} = \frac{T_1^{\mu\nu}}{(d-2)},\tag{2.8}$$

such that the amplitude becomes

$$\begin{aligned}\mathcal{M}_{ggH_j}^{\mu\nu,ab}(p,q) &= -i \left(\frac{\alpha_s m_t}{\pi v}\right) Y_j \delta^{ab} \left(\frac{4\pi\mu^2}{m_t^2}\right)^\epsilon \Gamma(1+\epsilon) T_1^{\mu\nu} \mathcal{A}_1^{(0)}, \\ \mathcal{A}_1^{(0)} &= C_\epsilon P_{\mu\nu} \int_k \frac{\mathcal{N}^{\mu\nu}}{D_0 D_1 D_2},\end{aligned}\tag{2.9}$$

where we introduce the form factor $\mathcal{A}_1^{(0)}$, and the normalization $C_\epsilon = \frac{(m_t^2)^\epsilon}{\Gamma(1+\epsilon)}$.

Coming back to the expression of the amplitude, the numerator algebra yields:

$$P_{\mu\nu} \mathcal{N}^{\mu\nu} = \frac{m_t}{(d-2)} \left(-(d-5)k^2 + (d-1)m_t^2 - (d-2)(p \cdot q) - \frac{4(k \cdot p)(k \cdot q)}{p \cdot q} \right),\tag{2.10}$$

hence the form factor becomes

$$\begin{aligned}\mathcal{A}_1^{(0)} &= C_\epsilon \frac{m_t}{(d-2)} \times \left[-(d-5) \int_k \frac{k^2}{D_0 D_1 D_2} \right. \\ &\quad \left. + [(d-1)m_t^2 - (d-2)(p \cdot q)] \int_k \frac{1}{D_0 D_1 D_2} - \frac{4}{(p \cdot q)} \int_k \frac{(k \cdot p)(k \cdot q)}{D_0 D_1 D_2} \right].\end{aligned}\tag{2.11}$$

¹Every loop contributes with the following factor: $\mu^{4-d} \int \frac{d^d k}{(2\pi)^d} = \frac{i}{(4\pi)^{d/2}} \mu^{4-d} \int \frac{d^d k}{i\pi^{d/2}} = \frac{i}{(4\pi)^2} (4\pi\mu^2)^{2-d/2} \int \frac{d^d k}{i\pi^{d/2}} = \frac{i}{(4\pi)^2} (4\pi\mu^2)^{2-d/2} \int_k$.

Using the Passarino-Veltmann reduction (see Appendix D), and defining the scalar integrals

$$\begin{aligned} B_0(0, \bar{m}_t^2) &= \int_k \frac{1}{D_0 D_1}, & B_0(q^2, \bar{m}_t^2) &= \int_k \frac{1}{D_0 D_2}, & B_0(m_{H_j}^2, \bar{m}_t^2) &= \int_k \frac{1}{D_1 D_2} \\ C_0(0, q^2, m_{H_j}^2; \bar{m}_t^2) &= \int_k \frac{1}{D_0 D_1 D_2} \end{aligned} \quad (2.12)$$

we can express all the integrals appearing in Eq. (2.11) as scalar integrals:

$$\begin{aligned} \int_k \frac{k^2}{D_0 D_1 D_2} &= m_t^2 C_0(0, q^2, m_{H_j}^2; \bar{m}_t^2) + B_0(m_{H_j}^2, \bar{m}_t^2), \\ \int_k \frac{(k \cdot p)(k \cdot q)}{D_0 D_1 D_2} &= \frac{1}{4} \left[q^2 B_0(q^2; \bar{m}_t^2) - [q^2 - (p \cdot q)] B_0(m_{H_j}^2; \bar{m}_t^2) \right], \end{aligned} \quad (2.13)$$

and replacing these integrals in the amplitude

$$\begin{aligned} \mathcal{A}_1^{(0)} &= -\frac{C_\epsilon m_t}{(d-2)} \times \left[\frac{(d-4)(p \cdot q) - q^2}{(p \cdot q)} B_0(m_{H_j}^2, \bar{m}_t^2) \right. \\ &\quad \left. + [(d-2)(p \cdot q) - 4m_t^2] C_0(0, q^2, m_{H_j}^2; \bar{m}_t^2) + \frac{q^2}{(p \cdot q)} B_0(q^2; \bar{m}_t^2) \right]. \end{aligned} \quad (2.14)$$

2.1.2 Analytic amplitude of $gg^* \rightarrow H$

Let us replace the analytical value of the scalar integrals (see Appendix D):

$$\begin{aligned} B_0(m_{H_i}^2, \bar{m}_t^2) &= \frac{\Gamma(1+\epsilon)}{(m_t^2)^\epsilon} \left[\frac{1}{\epsilon} + 2 - 2g(\tau_j) \right], \\ B_0(q^2, \bar{m}_t^2) &= \frac{\Gamma(1+\epsilon)}{(m_t^2)^\epsilon} \left[\frac{1}{\epsilon} + 2 - 2g(\lambda) \right], \\ C_0(0, q^2, m_{H_j}^2; \bar{m}_t^2) &= \frac{\Gamma(1+\epsilon)}{(m_t^2)^{1+\epsilon}} \left[\frac{\tau\lambda}{2} \frac{f(\tau) - f(\lambda)}{\tau - \lambda} \right], \\ \tau &= \frac{4m_t^2}{(p+q)^2} = \frac{4m_t^2}{\hat{s}}, \quad \lambda = \frac{4m_t^2}{q^2}, \quad \epsilon = \frac{4-d}{2}. \end{aligned} \quad (2.15)$$

Hence, replacing these analytical values into the form factor $\mathcal{A}_1^{(0)}$, we arrive at the expression

$$\begin{aligned} \mathcal{A}_1^{(0)} &= -\frac{m_t}{2(1-\epsilon)} \left\{ -\frac{2\epsilon(p \cdot q) + q^2}{(p \cdot q)} \left(\frac{1}{\epsilon} + 2 - 2g(\tau) \right) \right. \\ &\quad \left. + \left(\frac{(1-\epsilon)(p \cdot q)}{m_t^2} - 2 \right) \left[\tau\lambda \frac{f(\tau) - f(\lambda)}{\tau - \lambda} \right] + \frac{q^2}{(p \cdot q)} \left(\frac{1}{\epsilon} + 2 - 2g(\lambda) \right) \right\} \\ &= \frac{m_t}{(1-\epsilon)} \left\{ 1 - \frac{q^2}{(p \cdot q)} (g(\tau) - g(\lambda)) - \left(\frac{p \cdot q}{2m_t^2} - 1 \right) \frac{\tau\lambda}{\tau - \lambda} (f(\tau) - f(\lambda)) \right. \\ &\quad \left. + \epsilon \left[\frac{p \cdot q}{2m_t^2} \frac{\tau\lambda}{\tau - \lambda} (f(\tau) - f(\lambda)) - 2(g(\tau) - 1) \right] \right\}. \end{aligned} \quad (2.16)$$

Since the ϵ pole has been canceled through the calculation, this expression is finite. In the limit $\epsilon \rightarrow 0$, the form factor becomes:

$$\begin{aligned} \mathcal{A}_1^{(0)} &= m_t \left\{ 1 - \frac{q^2}{(p \cdot q)} [g(\tau) - g(\lambda)] - \left[\frac{p \cdot q}{2m_t^2} - 1 \right] \frac{\tau\lambda}{\tau - \lambda} [f(\tau) - f(\lambda)] \right\} \\ &= 2m_t \left\{ \frac{1}{2} + \frac{\tau}{\tau - \lambda} [g(\tau) - g(\lambda)] + \frac{1}{2} \left[1 + \frac{\tau\lambda}{\tau - \lambda} \right] [f(\tau) - f(\lambda)] \right\}. \end{aligned} \quad (2.17)$$

Using the identity:

$$2m_t = -\frac{(p \cdot q)}{m_t} \left(\frac{\tau\lambda}{\tau - \lambda} \right), \quad (2.18)$$

we can simplify the expression more, such that the form factor becomes

$$\begin{aligned}\mathcal{A}_1^{(0)} &= -\frac{(p \cdot q)}{m_t} \left\{ \frac{\tau \lambda}{2(\tau - \lambda)} + \frac{\tau^2 \lambda}{(\tau - \lambda)^2} [g(\tau) - g(\lambda)] + \frac{\tau^2 \lambda^2}{2(\tau - \lambda)^2} [f(\tau) - f(\lambda)] + \frac{\tau \lambda}{2(\tau - \lambda)} [f(\tau) - f(\lambda)] \right\} \\ &= -\frac{(p \cdot q)}{m_t} \mathcal{I}(\tau, \lambda)\end{aligned}\quad (2.19)$$

and the total amplitude becomes

$$\begin{aligned}\mathcal{M}_{ggH_j}^{\mu\nu,ab}(p, q) &= -i \left(\frac{\alpha_s m_t}{\pi v} \right) Y_j \delta^{ab} \left(\frac{4\pi\mu^2}{m_t^2} \right)^\epsilon \Gamma(1 + \epsilon) T_1^{\mu\nu} \mathcal{A}_1^{(0)}(p, q) \\ &= i \left(\frac{\alpha_s}{\pi v} \right) Y_j \delta^{ab} \left(\frac{4\pi\mu^2}{m_t^2} \right)^\epsilon \Gamma(1 + \epsilon) \mathcal{I}(\tau, \lambda) [(p \cdot q)g^{\mu\nu} - q^\mu p^\nu].\end{aligned}\quad (2.20)$$

This form factor is independent on the neutral scalar Higgs boson taken into account: this fact will be useful later when we will build the amplitude for the Higgs-pair production matrix elements.

The heavy top-quark limit and the gluon in the on-shell limit will define a gluon-Higgs effective vertex. It can be done by taking the simultaneous limits $\lambda \rightarrow \infty$ and $\tau \rightarrow \infty$. Since the off-shellness of the incoming gluon and the leading dependence on the top mass are encoded into the $\mathcal{I}(\tau, \lambda)$ factor, it will be the only term affected by this limit:

$$\mathcal{M}_{ggH_j}^{\mu\nu,ab}(p, q) \xrightarrow{\text{HTL}} -i \left(\frac{\alpha_s}{3\pi v} \right) Y_j \delta^{ab} \left(\frac{4\pi\mu^2}{m_t^2} \right)^\epsilon \Gamma(1 + \epsilon) [(p \cdot q)g^{\mu\nu} - q^\mu p^\nu]. \quad (2.21)$$

2.2 Leading Order amplitude for $H_1 H_2$ production

The LO amplitude for the Higgs-pair production channels gets contributions from one-loop diagrams. For the moment, we will only consider the case where the Higgs bosons in the final state are CP-even;

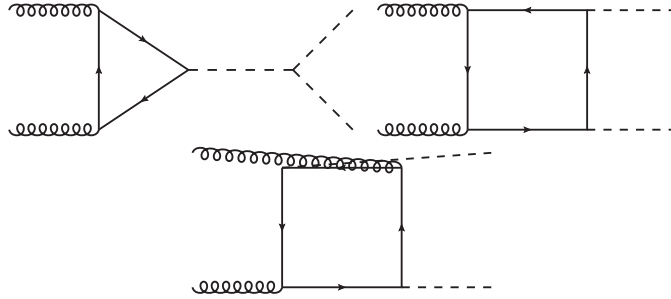


Figure 2.1: Sample of the Feynman diagrams contributing at LO.

the same calculation strategy can be exploited for the CP-odd Higgs final state.

The process under investigation is $gg \rightarrow H_1 H_2$. The LO amplitude \mathcal{M}_{LO} can be written as

$$\mathcal{M}_{LO} = \epsilon_\mu(p_1) \epsilon_\nu(p_2) (\mathcal{M}_\Delta^{\mu\nu,ab} + \mathcal{M}_\square^{\mu\nu,ab}), \quad (2.22)$$

where we have separated the two gauge-invariant subsets of diagrams.

2.2.1 Triangle contribution

The triangle-like contribution $\mathcal{M}_\Delta^{\mu\nu}$ can be built by composing the $gg^* \rightarrow H_j$ matrix element with a tree-level factor as follows:

$$\begin{aligned}\mathcal{M}_\Delta^{\mu\nu,ab} &= \sum_j^2 \mathcal{M}_{ggH_j}^{\mu\nu,ab}(p_1, p_2) \Big|_{p_2^2=0} \left(\frac{i}{(p_1 + p_2)^2 - m_{H_j}^2 - im_{H_j} \Gamma(m_{H_j}^2)} \right) \left(-i3 \frac{\lambda_{j12}}{v} \right) \\ &= \tilde{F}_\Delta^{(0)} T_1^{\mu\nu},\end{aligned}\quad (2.23)$$

where in the last step, we have defined the triangle form factor $F_{\Delta}^{(0)}$. Collecting all our expressions, we obtain

$$\begin{aligned}\tilde{F}_{\Delta}^{(0)} &= \frac{i\alpha_s}{(4\pi)} \frac{m_t^2}{v^2} \delta^{ab} \left(\frac{4\pi\mu^2}{m_t^2} \right)^{\epsilon} \Gamma(1+\epsilon) \tilde{\mathcal{A}}_1^{(0)}, \\ \tilde{\mathcal{A}}_1^{(0)} &= \sum_j^2 \left(\frac{6Y_j \lambda_{j12}}{\hat{s} - m_{H_j}^2 - im_{H_j} \Gamma(m_{H_j}^2)} \right) \frac{\hat{s}}{m_t^2} \mathcal{I}(\tau, \infty).\end{aligned}\quad (2.24)$$

The on-shell limit for the $gg^* \rightarrow H_j$ amplitude leads to the following expression:

$$\mathcal{I}(\tau, \infty) = \lim_{\lambda \rightarrow \infty} \mathcal{I}(\tau, \lambda) = -\frac{\tau}{2} [1 - \tau f(\tau) + f(\tau)]. \quad (2.25)$$

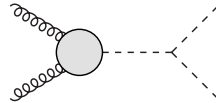
Since the form factor $\tilde{F}_{\Delta}^{(0)}$ has a factorizable dependence on the type of virtual Higgs boson which propagates from the top-loop. This leads to an important factorization:

$$\begin{aligned}\tilde{F}_{\Delta}^{(0)} &= C_{\Delta} F_{\Delta}^{(0)}, \\ C_{\Delta} &= \sum_j^2 \frac{6Y_j \lambda_{j12}}{\hat{s} - m_{H_j}^2 - im_{H_j} \Gamma(m_{H_j}^2)}.\end{aligned}\quad (2.26)$$

The form factor $F_{\Delta}^{(0)}$ is common to the one of the LO QCD single-Higgs production. This factorization is extremely important: it will turn to be useful later since the same structure of $\tilde{F}_{\Delta}^{(0)}$ holds at NLO. Single-Higgs production form factors are already known at NLO, and we can implement them in our calculation as a simple factor.

Heavy top limit

The HTL triangle amplitude can be built as a tree-level amplitude where the vertex contribution is replaced by the ggH_j effective vertex, found in the previous section, leading to



$$= -i \left(\frac{\alpha_s}{3\pi v^2} \right) \delta^{ab} \left(\frac{4\pi\mu^2}{m_t^2} \right)^{\epsilon} \Gamma(1+\epsilon) \frac{C_{\Delta}}{2} [(p \cdot q) g^{\mu\nu} - q^{\mu} p^{\nu}]. \quad (2.27)$$

2.2.2 Box diagrams

There are three box diagrams contributing at LO (Fig. 2.2). The corresponding ones with reversed fermion flow, due to Furry's theorem, contribute with an additional factor 2.

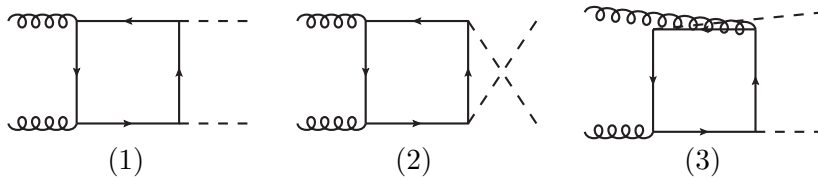


Figure 2.2: LO box diagrams.

To approach this calculation, a theoretical common framework can be useful. In general, each of these diagrams can be expressed as follows:

$$\begin{aligned}\mathcal{M}_{\square}^{\mu\nu, ab} &= -(-ig_s)^2 \left(-i \frac{m_t}{v} \right)^2 Y_1 Y_2 (i)^4 \text{Tr}[T^a T^b] \frac{i}{(4\pi)^2} (4\pi\mu^2)^{2-\frac{d}{2}} \int_k \frac{N^{\mu\nu}(k, \mathbf{p})}{D_0 D_1 D_2 D_3} \\ &= -\frac{i\alpha_s}{(4\pi)} \frac{m_t^2}{v^2} Y_1 Y_2 \text{Tr}[T^a T^b] (4\pi\mu^2)^{\epsilon} \int_k \frac{N^{\mu\nu}(k, \mathbf{p})}{D_0 D_1 D_2 D_3},\end{aligned}\quad (2.28)$$

where $\mathbf{p} = \{p_1, p_2, p_3\}$ and k the loop momenta. Here there is a general tensor $N^{\mu\nu}$ depending on the momenta which is unique for each box diagram. The Feynman parametrization procedure allows one to write an integral of n denominators as a tadpole-like integral:

$$\begin{aligned} \frac{1}{D_0^{a_0} \cdots D_n^{a_n}} &= \frac{\Gamma(a_1 + \cdots + a_n)}{\Gamma(a_1) \cdots \Gamma(a_n)} \int_0^1 dx_0 d^n \mathbf{x} \frac{x_0^{a_0-1} \cdots x_n^{a_n-1} \delta(1 - \sum_j x_j)}{[D_0 x_0 + \cdots + D_n x_n]^{\sum_j a_j}} \\ &= \frac{\Gamma(a_1 + \cdots + a_n)}{\Gamma(a_1) \cdots \Gamma(a_n)} \int_{\mathcal{C}} d^n \mathbf{x} \frac{(1 - \sum_j x_j)^{a_0-1} \cdots x_n^{a_n-1}}{[D_0(1 - \sum_j x_j) + \cdots + D_n x_n]^{\sum_j a_j}}, \end{aligned} \quad (2.29)$$

$$\mathcal{C} = \left\{ \mathbf{x} = (x_1, \dots, x_n) \in [0, 1]^n \mid x_2 < 1 - x_1 \wedge x_3 < 1 - x_1 - x_2 \wedge \cdots \wedge x_n < 1 - \sum_{j=1}^{n-1} x_j \right\}.$$

Applying the Feynman parameterization to the box integral, the integrand takes the form:

$$\begin{aligned} \mathcal{M}_{\square}^{\mu\nu, ab} &= -\frac{i\alpha_s}{(4\pi)} \frac{m_t^2}{v^2} Y_1 Y_2 \text{Tr}[T^a T^b] (4\pi\mu^2)^{2-\frac{d}{2}} \times \\ &\quad \times \Gamma(4) \int_{\mathcal{C}} d\mathbf{x} \int_k \frac{N^{\mu\nu}(k, \mathbf{p})}{[D_0(1 - x_1 - x_2 - x_3) + D_1 x_1 + D_2 x_2 + D_3 x_3]^4}, \end{aligned} \quad (2.30)$$

where $\mathcal{C} = \{\mathbf{x} = (x_1, x_2, x_3) \in [0, 1] \times [0, 1] \times [0, 1] \mid x_2 < 1 - x_1 \wedge x_3 < 1 - x_1 - x_2\}$. All the internal lines are massive, and the Feynman parametrization yields a "tadpole-like" denominator

$$\begin{aligned} \mathcal{M}_{\square}^{\mu\nu, ab} &= -\frac{i\alpha_s}{(4\pi)} \frac{m_t^2}{v^2} Y_1 Y_2 \text{Tr}[T^a T^b] (4\pi\mu^2)^{2-\frac{d}{2}} \Gamma(4) \int_{\mathcal{C}} d\mathbf{x} \int_k \frac{N^{\mu\nu}(k, \mathbf{p})}{[k^2 + 2k \cdot q - M^2]^4} \\ q^\mu &= \sum_{i=1}^3 a_i(\mathbf{x}) p_i^\mu, \quad M^2 = m_t^2 - \sum_{i,j=1}^3 b_{ij}(\mathbf{x}) (p_i \cdot p_j). \end{aligned} \quad (2.31)$$

Then, by shifting $k \rightarrow k - q$, it is possible to complete the square into the denominator:

$$\mathcal{M}_{\square}^{\mu\nu, ab} = -\frac{i\alpha_s}{(4\pi)} \frac{m_t^2}{v^2} Y_1 Y_2 \text{Tr}[T^a T^b] (4\pi\mu^2)^{2-\frac{d}{2}} \Gamma(4) \int_{\mathcal{C}} d\mathbf{x} \int_k \frac{N^{\mu\nu}(k - q, \mathbf{p})}{[k^2 - q^2 - M^2]^4}. \quad (2.32)$$

With this shift, the integrand becomes even with respect to k^μ ; hence, odd powers of k^μ vanish after the integration.

The numerator $N^{\mu\nu}$ is a tensor of rank up to 4 in the loop momentum. We can replace rank-2 and rank-4 tensors with the following tensor structures

$$\begin{aligned} k^\mu k^\nu &\rightarrow \frac{k^2}{d} g^{\mu\nu}, \\ k^\mu k^\nu k^\rho k^\sigma &\rightarrow (k^2)^2 \frac{g^{\mu\nu} g^{\rho\sigma} + g^{\mu\rho} g^{\nu\sigma} + g^{\mu\sigma} g^{\nu\rho}}{d(d+2)}, \end{aligned} \quad (2.33)$$

since the tensors depending only on the loop momentum can not depend on any other dimensionful quantities. Therefore, we can single out every (2α) -rank factor:

$$\begin{aligned} \mathcal{M}_{\square}^{\mu\nu, ab} &= -\frac{i\alpha_s}{(4\pi)} \frac{m_t^2}{v^2} Y_1 Y_2 \text{Tr}[T^a T^b] (4\pi\mu^2)^{2-\frac{d}{2}} \Gamma(4) \int_{\mathcal{C}} d\mathbf{x} \left[A^{\mu\nu}(\mathbf{p}, \mathbf{x}) \int_k \frac{1}{[k^2 - q^2 - M^2]^4} + \right. \\ &\quad B^{\mu\nu}(\mathbf{p}, \mathbf{x}) \int_k \frac{k^2}{[k^2 - q^2 - M^2]^4} + \\ &\quad \left. C^{\mu\nu}(\mathbf{p}, \mathbf{x}) \int_k \frac{(k^2)^2}{[k^2 - q^2 - M^2]^4} \right] \end{aligned} \quad (2.34)$$

The loop integrals can be now integrated. After a Wick rotation and the integration in d -dimensional spherical coordinates, we obtain the following close form

$$\int_k \frac{(k^2)^\alpha}{[k^2 - q^2 - M^2]^n} = (-1)^{(n-\alpha)} \frac{\Gamma(n - \alpha - \frac{d}{2}) \Gamma(\alpha + \frac{d}{2})}{\Gamma(n) \Gamma(\frac{d}{2})} \frac{1}{[q^2 + M^2]^{n-\alpha-\frac{d}{2}}}, \quad (2.35)$$

which brings the amplitude into the following form

$$\begin{aligned} \mathcal{M}_{\square}^{\mu\nu,ab} = & -\frac{i\alpha_s}{(4\pi)} \frac{m_t^2}{v^2} Y_1 Y_2 \text{Tr}[T^a T^b] (4\pi\mu^2)^{2-\frac{d}{2}} \int_{\mathcal{C}} d\mathbf{x} \left[\Gamma\left(4 - \frac{d}{2}\right) \frac{A^{\mu\nu}(\mathbf{p}, \mathbf{x})}{[q^2 + M^2]^{4-\frac{d}{2}}} - \right. \\ & -\Gamma\left(3 - \frac{d}{2}\right) \frac{d}{2} \frac{B^{\mu\nu}(\mathbf{p}, \mathbf{x})}{[q^2 + M^2]^{3-\frac{d}{2}}} + \\ & \left. +\Gamma\left(2 - \frac{d}{2}\right) \frac{d}{2} \left(1 + \frac{d}{2}\right) \frac{C^{\mu\nu}(\mathbf{p}, \mathbf{x})}{[q^2 + M^2]^{2-\frac{d}{2}}} \right]. \end{aligned} \quad (2.36)$$

Using $\epsilon = \frac{4-d}{2}$ and extracting the dependence on the Gamma function, we obtain:

$$\begin{aligned} \mathcal{M}_{\square}^{\mu\nu,ab} = & -\frac{i\alpha_s}{(4\pi)} \frac{m_t^2}{v^2} Y_1 Y_2 \text{Tr}[T^a T^b] \left(\frac{4\pi\mu^2}{m_t^2}\right)^\epsilon \Gamma(1 + \epsilon) \int_{\mathcal{C}} d\mathbf{x} \left[\frac{(1 + \epsilon)}{(m_t^2)^2} \frac{A^{\mu\nu}(\mathbf{p}, \mathbf{x})}{\left[\frac{q^2 + M^2}{m_t^2}\right]^{2+\epsilon}} - \right. \\ & -\frac{(2 - \epsilon)}{m_t^2} \frac{B^{\mu\nu}(\mathbf{p}, \mathbf{x})}{\left[\frac{q^2 + M^2}{m_t^2}\right]^{1+\epsilon}} + \\ & \left. +\frac{(2 - \epsilon)(3 - \epsilon)}{\epsilon} \frac{C^{\mu\nu}(\mathbf{p}, \mathbf{x})}{\left[\frac{q^2 + M^2}{m_t^2}\right]^\epsilon} \right] \end{aligned} \quad (2.37)$$

The denominators are now dimensionless, and they can be expressed as

$$\Delta(\mathbf{p}, \mathbf{x}) = \frac{q^2 + M^2}{m_t^2} = \frac{m_t^2 + \sum_{ij}^3 a_i a_j (p_i \cdot p_j) - \sum_{ij}^3 b_{ij} (p_i \cdot p_j)}{m_t^2} = 1 - \sum_{i,j=1}^3 c_{ij}(\mathbf{x}) \frac{p_i \cdot p_j}{m_t^2}. \quad (2.38)$$

A change of variables $g : \mathcal{C} \rightarrow [0, 1]^3$ transforms the integration variables into the unit 3-cube²

$$\begin{aligned} \mathcal{M}_{\square}^{\mu\nu,ab} = & -\frac{i\alpha_s}{(4\pi)} \frac{m_t^2}{v^2} Y_1 Y_2 \text{Tr}[T^a T^b] \left(\frac{4\pi\mu^2}{m_t^2}\right)^\epsilon \Gamma(1 + \epsilon) \int_0^1 d\mathbf{x} \det[J(g)] \left[\frac{(1 + \epsilon)}{(m_t^2)^2} \frac{A^{\mu\nu}(\mathbf{p}, \mathbf{x})}{\Delta^{2+\epsilon}} - \right. \\ & -\frac{(2 - \epsilon)}{m_t^2} \frac{B^{\mu\nu}(\mathbf{p}, \mathbf{x})}{\Delta^{1+\epsilon}} + \\ & \left. +\frac{(2 - \epsilon)(3 - \epsilon)}{\epsilon} \frac{C^{\mu\nu}(\mathbf{p}, \mathbf{x})}{\Delta^\epsilon} \right], \end{aligned} \quad (2.39)$$

where $J(g)$ is the Jacobian of the change of variables g . The integral is regular below the threshold $s = 4m_t^2$. The singular behaviour for $\epsilon = 0$ is proportional to the tensor $C^{\mu\nu}(\mathbf{p}, \mathbf{x})$, coming from the rank-4 tensor integral:

$$\mathcal{M}_{\square}^{\mu\nu,ab} \sim_{\epsilon \rightarrow 0} -\frac{i\alpha_s}{(4\pi)} \frac{m_t^2}{v^2} Y_1 Y_2 \text{Tr}[T^a T^b] \frac{6}{\epsilon} \int_0^1 d\mathbf{x} \det[J(g)] C^{\mu\nu}(\mathbf{p}, \mathbf{x}). \quad (2.40)$$

Due to the renormalizability of the theory, this term has to vanish after the box sum. By only looking at the tensor structure:

$$\begin{aligned} 2\text{Tr}[\gamma^\mu \not{k} \not{k} \not{k} \gamma^\nu \not{k}] + \text{Tr}[\not{k} \gamma^\mu \not{k} \not{k} \gamma^\nu \not{k}] &= 8k^2(2k^\mu k^\nu - k^2 g^{\mu\nu}) + 4(k^2)^2 g^{\mu\nu} \\ &\rightarrow 4(k^2)^2 g^{\mu\nu} \frac{4-d}{d} = (k^2)^2 C^{\mu\nu}(\mathbf{p}, \mathbf{x}) \\ &\implies C^{\mu\nu}(\mathbf{p}, \mathbf{x}) \propto \epsilon, \end{aligned} \quad (2.41)$$

where we neglected the presence of the denominator since they contribute like $1 + O(\epsilon)$.

Hence, the single pole coefficient is zero, and the total amplitude is finite as expected.

²With a little abuse of notation, we use the same symbols \mathbf{x} for the new variables: $\mathbf{x} \rightarrow \mathbf{X} = g(\mathbf{x}) \equiv \mathbf{x}$

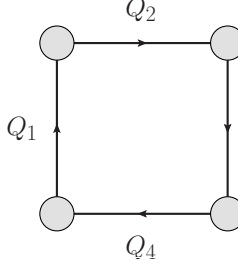
External momenta vs. internal momenta

Going towards the actual calculation, we start fixing our convention for the external legs (all incoming):



$$(2.42)$$

and a single way to identify the topology in terms of the "internal" momenta:



$$\sim \frac{1}{D_1 D_2 D_3 D_4}, \quad \begin{cases} D_1 = (k + Q_1)^2 - m_t^2 \\ D_2 = (k + Q_2)^2 - m_t^2 \\ D_3 = (k + Q_3)^2 - m_t^2 \\ D_4 = (k + Q_4)^2 - m_t^2 \end{cases} . \quad (2.43)$$

Using momentum conservation, we can express the external momenta in terms of the internal

$$P_i = P_i(Q) = A_{ij} Q_j. \quad (2.44)$$

This is what we call *internal momenta convention*.

The kinematics is defined as follows:

$$\begin{aligned} P_1^2 &= P_4^2 = 0, \\ P_2^2 &= m_{H_1}^2, \\ P_3^2 &= m_{H_2}^2, \\ (P_1 + P_4)^2 &= (P_2 + P_3)^2 = \hat{s}, \\ (P_1 + P_2)^2 &= (P_3 + P_4)^2 = \hat{t}, \\ (P_1 + P_3)^2 &= (P_2 + P_4)^2 = \hat{u}, \\ P_4 &= -P_1 - P_2 - P_3, \end{aligned} \quad (2.45)$$

and the tensors defined with the external momenta become

$$\begin{aligned} T_1 &= g^{\mu\nu} - \frac{P_1^\nu P_4^\mu}{(P_1 \cdot P_4)}, \\ T_2 &= g^{\mu\nu} + \frac{(P_2^2) P_1^\nu P_4^\mu - 2(P_1 \cdot P_4) P_2^\nu P_4^\mu - 2(P_2 \cdot P_4) P_1^\nu P_2^\mu + 2(P_1 \cdot P_4) P_2^\nu P_2^\mu}{(P_1 \cdot P_4) p_T^2} \\ p_T^2 &= \frac{2(P_2 \cdot P_4)(P_1 \cdot P_2)}{(P_1 \cdot P_4)} - P_2^2. \end{aligned} \quad (2.46)$$

With this convention, we can express each of these diagrams in terms of the same integral, containing the shortest possible internal momenta. On the other hand, the invariants expressed in terms of the internal momenta can have an involved dependence on them, and some cancellation may not occur.

The *external momenta convention* is the most common, meaning that we express the internal momenta with respect to the external ones:

$$Q_i = Q_i(P) = A_{ij} P_j. \quad (2.47)$$

While the two conventions will lead to the same result (of course), at higher number of loops, the internal momenta convention might help the computation of the Feynman integrals with many propagators, leading to more compact integrals expressions suitable for numerical calculations.

2.2.3 Applying the procedure

Feynman parametrization

Consider the box diagram (1) in Figure (2.2), and let us adapt our conventions:

$$\begin{cases} Q_1 = p_4 \\ Q_2 = p_1 \\ Q_3 = p_2 \\ Q_4 = p_3 \end{cases} \implies \begin{cases} P_1 = p_1 - p_4 \\ P_2 = p_2 - p_1 \\ P_3 = p_3 - p_2 \\ P_4 = p_4 - p_1 \end{cases} \quad (2.48)$$

as it can be seen in Figure (2.3). The box diagram (2) can be found by crossing $t \leftrightarrow u$ ($P_2 \leftrightarrow P_3$) from the box (1).

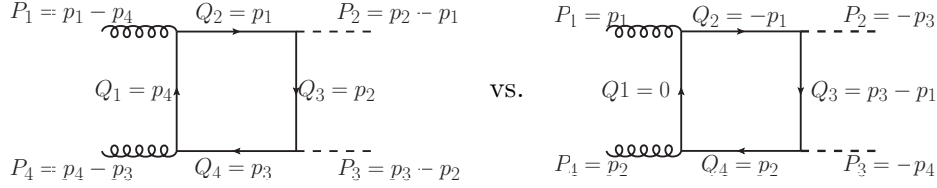


Figure 2.3: *Internal vs. external momenta convention.*

At one-loop, we can always shift the loop-momentum, such that we can absorb one of the internal momenta. This is equivalent to set one internal momentum to zero. We choose $p_4 = 0$, therefore

$$\begin{aligned} p_1^2 = p_3^2 = 0, \quad p_2^2 = \hat{t}, \\ (p_1 \cdot p_2) = -\frac{\hat{t} - m_{H_1}^2}{2}, \quad (p_2 \cdot p_3) = -\frac{\hat{t} - m_{H_2}^2}{2}, \quad (p_1 \cdot p_3) = -\frac{\hat{s}}{2}. \end{aligned} \quad (2.49)$$

Instead of using the standard Feynman parametrization of the whole denominator, we can notice that if we parametrize only two propagators:

$$\frac{1}{D_0 D_1^n} = \int_0^1 dx \frac{x^{n-1}}{[D_0 x + D_1(1-x)]^{n+1}}, \quad (2.50)$$

the integration boundary already is the interval $[0, 1]$. Exploiting this relation, we can recursively apply this parametrization to avoid the explicit change of variables with maps the general boundaries into the unit 3-cube. Applying this knowledge to the planar box diagram, we obtain the following integral:

$$\begin{aligned} D'_0 = D_0, \quad D'_{i+1} = D_{i+1}(1-x_i) + D'_i x_i \\ \implies \int_k \frac{1}{D_0 D_1 D_2 D_3} = \Gamma(4) \int_0^1 d\mathbf{x} (x_2 x_3^2) \int_k \frac{1}{[D'_3]^4}. \end{aligned} \quad (2.51)$$

The D'_3 is quadratic in the loop momentum, and it can be expressed in terms of the general variables defined in the previous section:

$$\begin{aligned} \det[J(g)] = x_2 x_3^2, \quad q_1^\mu = p_1^\mu x_1 x_2 x_3 + p_2^\mu x_3(1-x_2) + p_3^\mu(1-x_3) \\ M_1^2 = m_t^2 - p_2^2(1-x_2)x_3, \end{aligned} \quad (2.52)$$

and

$$\Delta_1 = 1 - \frac{p_2^2}{m_t^2}(1-x_2)x_3 + \frac{q_1^2}{m_t^2}. \quad (2.53)$$

Of course, this procedure is equivalent to the standard parametrization where a particular change of variable $g : \mathcal{C} \rightarrow [0, 1]^3$ with Jacobian $\det[J(g_1)] = x_2 x_3^2$ is performed: applying the parametrization to all four propagators, we arrive at the following structure

$$\begin{aligned} \det[J(g_1)] = x_2 x_3^2, \quad q_1^\mu = p_1^\mu x_1 x_2 x_3 + p_2^\mu x_2(1-x_1) + p_3^\mu(1-x_2) \\ M_1^2 = m_t^2 - p_2^2(1-x_1)x_2, \end{aligned} \quad (2.54)$$

where we used the following transformation

$$g_1 : \mathcal{C} \rightarrow [0, 1]^3, \quad g_1(\mathbf{x}) = \begin{pmatrix} x_2(1-x_1) \\ (1-x_2) \\ x_1x_2x_3 \end{pmatrix}, \quad \det[J(g_1)] = x_2^2x_1. \quad (2.55)$$

Of course, it is exactly the previous transformation with the exchange of the variables names $x_1 \rightarrow x_2$, $x_2 \rightarrow x_3$ and $x_3 \rightarrow x_1$.

A simpler option will be using the external momenta conventions. This will bring the integrals in a more compact form:

$$\begin{cases} P_1 = p_1 \\ P_2 = -p_3 \\ P_3 = -p_4 \\ P_4 = p_2 \end{cases} \implies \begin{cases} Q_1 = 0 \\ Q_2 = -p_1 \\ Q_3 = p_3 - p_1 \\ Q_4 = p_2 \end{cases}, \quad (2.56)$$

$$p_1^2 = p_2^2 = 0, \quad p_3^2 = m_{H_1}^2, \quad p_4^2 = m_{H_2}^2 \\ p_1 \cdot p_2 = \frac{\hat{s}}{2}, \quad p_1 \cdot p_3 = -\frac{\hat{t} - m_{H_1}^2}{2}, \quad p_2 \cdot p_3 = -\frac{\hat{u} - m_{H_1}^2}{2}.$$

The momentum conservation implies the following kinematic relation:

$$2p_1 \cdot p_2 - 2p_1 \cdot p_3 - 2p_2 \cdot p_3 = m_{H_2}^2 - m_{H_1}^2. \quad (2.57)$$

The new momentum flow yields a different expression for the (corresponding) integrals. Of course, the diagram is completely parametrization-independent, hence it will lead to the same final result.

We define the dimensionless variables:

$$\begin{aligned} \rho_s &= \frac{\hat{s}}{m_t^2} = \frac{2(p_1 \cdot p_2)}{m_t^2}, & \rho_t &= \frac{\hat{t}}{m_t^2} = \frac{p_3^2 - 2(p_1 \cdot p_3)}{m_t^2}, \\ \rho_u &= \frac{\hat{u}}{m_t^2} = \frac{p_3^2 - 2(p_2 \cdot p_3)}{m_t^2}, & \rho_1 &= \frac{m_{H_1}^2}{m_t^2} = \frac{p_3^2}{m_t^2}, & \rho_2 &= \frac{m_{H_2}^2}{m_t^2} = \frac{p_4^2}{m_t^2} \\ \hat{\rho}_t &= -\frac{2(p_1 \cdot p_3)}{m_t^2}, & \hat{\rho}_u &= -\frac{2(p_2 \cdot p_3)}{m_t^2}. \end{aligned} \quad (2.58)$$

The general variables defined in the previous section in the external momentum convention are:

$$g_1 : \mathcal{C} \rightarrow [0, 1]^3, \quad g_1(\mathbf{x}) = \begin{pmatrix} (1-x_1)(1-x_3) \\ x_1x_2 \\ x_1(1-x_3) \end{pmatrix}, \quad \det[J(g_1)] = x_1(1-x_1), \quad (2.59) \\ q_1^\mu = -(1-x_1)p_1^\mu + x_1x_2p_2^\mu + (1-x_1)x_3p_3^\mu, \\ M_1^2 = m_t^2 + (1-x_1)x_32(p_1 \cdot p_3) - (1-x_1)x_3m_{H_1}^2, \\ \Delta_1 = 1 - (1-x_1)x_1x_2\rho_s - (1-x_1)x_1x_3\hat{\rho}_t - (1-x_1)x_1x_2x_3\hat{\rho}_u - [1 - (1-x_1)x_3](1-x_1)x_3\rho_1$$

Numerator algebra

The Dirac algebra is needed to extract the tensor structure from the diagram. The numerator of the Feynman diagram is:

$$N_1^{\mu\nu} = \text{Tr} \left[\gamma^\nu (\not{k} + m_t) \gamma^\mu (\not{k} - \not{p}_1 + m_t) (\not{k} + \not{p}_3 - \not{p}_1 + m_t) (\not{k} + \not{p}_2 + m_t) \right] \quad (2.60)$$

We are interested in the tensors $A^{\mu\nu}(\mathbf{p}, \mathbf{x})$, $B^{\mu\nu}(\mathbf{p}, \mathbf{x})$ and $C^{\mu\nu}(\mathbf{p}, \mathbf{x})$ defined in the previous section. Hence, after the evaluation of the Dirac trace, the shift of the loop-momentum and the integration over the odd powers of the integrating momentum, we obtain:

$$\begin{aligned}
C_1^{\mu\nu} &= -\frac{4(d-2)g^{\mu\nu}}{d} \\
B_1^{\mu\nu} &= \frac{4g^{\mu\nu}}{d} \left[6m_t^2 - 2d(p_1 \cdot q_1) + d(p_2 \cdot q_1) + d(p_3 \cdot q_1) + (d-2)(p_1 \cdot p_3) - d(p_2 \cdot p_3) - \right. \\
&\quad \left. - 2(d+1)q_1^2 + 2(p_2 \cdot q_1) - 2(p_3 \cdot q_1) + 2(p_1 \cdot p_2) + 2(p_2 \cdot p_3) \right] - \\
&\quad - \frac{8p_2^\mu p_1^\nu}{d} + \left(4 - \frac{8}{d}\right) p_2^\mu p_3^\nu + \left(\frac{8}{d} - 4\right) p_3^\mu p_1^\nu - \frac{4(d+2)}{d} p_2^\mu q_1^\nu + \frac{16}{d} p_1^\nu q_1^\mu + \\
&\quad + \left(4 - \frac{8}{d}\right) p_3^\nu q_1^\mu + \left(4 - \frac{8}{d}\right) p_3^\mu q_1^\nu + \frac{8(d+4)}{d} q_1^\mu q_1^\nu \\
A_1^{\mu\nu} &= 4g^{\mu\nu} \left[m_t^4 + 2m_t^2(p_1 \cdot q_1) - m_t^2(p_2 \cdot q_1) - m_t^2(p_3 \cdot q_1) + (p_1 \cdot p_2)(p_3 \cdot q_1 - 2m_t^2) - \right. \\
&\quad \left. - (p_1 \cdot p_3)(m_t^2 + p_2 \cdot q_1 - q_1^2) + m_t^2(p_2 \cdot p_3) - (p_2 \cdot p_3)(p_1 \cdot q_1) + \right. \\
&\quad \left. + 2(p_1 \cdot q_1)(p_2 \cdot q_1) + q_1^2(-2(p_1 \cdot q_1) + p_2 \cdot q_1 + p_3 \cdot q_1 - p_2 \cdot p_3) - (q_1^2)^2 \right] + \\
&\quad + p_2^\mu p_1^\nu (8m_t^2 - 4(p_3 \cdot q_1)) - 4p_3^\mu q_1^\nu (m_t^2 - 2(p_1 \cdot q_1) + p_1 \cdot p_2 - q_1^2) + \\
&\quad + 4p_2^\mu q_1^\nu (m_t^2 - 2(p_1 \cdot q_1) + p_1 \cdot p_3 - q_1^2) + 4p_3^\mu p_1^\nu (m_t^2 + p_2 \cdot q_1 - q_1^2) - \\
&\quad - 4p_3^\nu q_1^\mu (m_t^2 + 2(p_2 \cdot q_1) + p_1 \cdot p_2 - q_1^2) + 4p_2^\mu p_3^\nu (-m_t^2 + p_1 \cdot q_1 + q_1^2) + \\
&\quad + 8q_1^\mu q_1^\nu (3m_t^2 + 2(p_1 \cdot q_1) - 2(p_3 \cdot q_1) - p_1 \cdot p_3 + p_2 \cdot p_3 + q_1^2) + 4(p_2 \cdot p_3)p_1^\nu q_1^\mu.
\end{aligned} \tag{2.61}$$

Notice that these tensors do not depend on the four-vectors p_1^μ and p_2^ν , since they are contracted with the on-shell polarizations $\epsilon_\mu(p_1)$ and $\epsilon_\nu(p_2)$, which are orthogonal with respect to their momenta:

$$\epsilon(p_j) \cdot p_j = 0. \tag{2.62}$$

Moreover, after the calculation of the missing box diagram, the complete tensor coefficient $C^{\mu\nu}(\mathbf{p}, \mathbf{x})$ will turn to be proportional to ϵ .

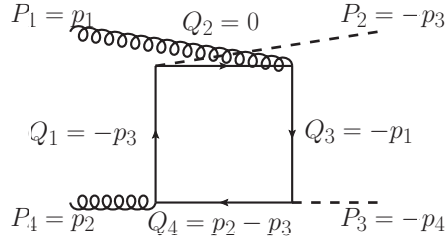


Figure 2.4: External momenta convention

Applying the same procedure for the box (3) (see Fig. (2.2)), the external momentum convention (Fig. (2.4)) yields

$$\begin{cases} P_1 = p_1 \\ P_2 = -p_3 \\ P_3 = -p_4 \\ P_4 = p_2 \end{cases} \implies \begin{cases} Q_1 = -p_3 \\ Q_2 = 0 \\ Q_3 = -p_1 \\ Q_4 = p_2 - p_3 \end{cases}. \tag{2.63}$$

The change of variables required with this setting is

$$g_2 : \mathcal{C} \rightarrow [0, 1]^3, \quad g_2(\mathbf{x}) = \begin{pmatrix} (1-x_1)(1-x_3) \\ x_1 x_2 \\ x_1(1-x_3) \end{pmatrix}, \quad \det[J(g_2)] = x_1(1-x_1), \tag{2.64}$$

and completing the square, we obtain the shift q_2^μ and the tadpole-mass term Δ_2 :

$$\begin{aligned} q_2^\mu &= -x_1 x_2 p_1^\mu + x_3(1-x_1)p_2^\mu - p_3^\mu(1-x_1) \\ M_2^2 &= m_t^2 + x_3(1-x_1)(2p_2 \cdot p_3) - (1-x_1)m_{H_1}^2 \\ \Delta_2 &= 1 - x_1(1-x_1)[x_2 \hat{\rho}_t + x_3 \hat{\rho}_u + x_2 x_3 \rho_s + \rho_{H_1}]. \end{aligned} \quad (2.65)$$

Finally, the numerator algebra will provide the tensor coefficients needed by the master formula Eq. (2.39).

$$N_2^\mu = \text{Tr} \left[\gamma^\nu (\not{k} - \not{p}_3 + m_t) (\not{k} + m_t) \gamma^\mu (\not{k} - \not{p}_1 + m_t) (\not{k} + \not{p}_2 - \not{p}_3 + m_t) \right] \quad (2.66)$$

$$\begin{aligned} C_2^{\mu\nu} &= 4g^{\mu\nu} \\ B_2^{\mu\nu} &= \frac{4g^{\mu\nu}}{d} \left[-2 \left[(d-4)m^2 + p_2 \cdot q_3 - 2(p_3 \cdot q_3) + p_3^2 - p_2 \cdot p_3 - 2q_3^2 \right] + (d+2)(p_1 \cdot q_3) + \right. \\ &\quad \left. + d(-p_2 \cdot q_3 + 2(p_3 \cdot q_3 + q_3^2)) + p_3^2 - (p_2 \cdot p_3) - d(p_1 \cdot p_2) + 4(p_1 \cdot p_3) \right] + \\ &\quad + \left(4 - \frac{8}{d} \right) p_2^\mu p_3^\nu - \frac{16}{d} p_3^\mu p_1^\nu + \left(\frac{16}{d} - 8 \right) p_3^\mu p_3^\nu + \left(\frac{8}{d} + 4 \right) p_2^\mu q_3^\nu - \frac{4(d+2)}{d} p_1^\nu q_3^\mu + \\ &\quad + \frac{8(d+2)}{d} p_3^\nu q_3^\mu - \frac{8(d+2)}{d} p_3^\mu q_3^\nu + 4p_2^\mu p_1^\nu \\ A_2^{\mu\nu} &= 4g^{\mu\nu} \left[m_t^4 + m_t^2(p_2 \cdot q_3) - 2m_t^2(p_3 \cdot q_3) - q_3^2(2m_t^2 + p_2 \cdot q_3 - 2(p_3 \cdot q_3) - p_3^2 + p_2 \cdot p_3) - \right. \\ &\quad \left. - (p_1 \cdot p_2)(m_t^2 + p_3 \cdot q_3 + q_3^2) + (p_1 \cdot q_3)(-m_t^2 + 2(p_3 \cdot q_3) + p_3^2 - p_2 \cdot p_3 + q_3^2) - \right. \\ &\quad \left. - m_t^2 p_3^2 + m_t^2(p_2 \cdot p_3) + (p_1 \cdot p_3)(p_2 \cdot q_3) + (q_3^2)^2 \right] + \\ &\quad + 8q_3^\mu q_3^\nu (4m_t^2 - p_3^2 + p_1 \cdot p_3 + p_2 \cdot p_3) + 4p_3^\mu q_3^\nu (2m_t^2 - 2(p_1 \cdot q_3) + p_1 \cdot p_2 - 2q_3^2) - \\ &\quad - 4p_2^\mu q_3^\nu (m_t^2 + p_1 \cdot p_3 - q_3^2) + 8p_3^\mu p_3^\nu (m_t^2 - p_1 \cdot q_3 - q_3^2) + 4p_2^\mu p_1^\nu (m_t^2 + p_3 \cdot q_3 + q_3^2) + \\ &\quad + 4p_1^\nu q_3^\mu (m_t^2 - 2(p_3 \cdot q_3) - p_3^2 + p_2 \cdot p_3 - q_3^2) + 4p_2^\mu p_3^\nu (-m_t^2 + p_1 \cdot q_3 + q_3^2) + \\ &\quad + p_3^\nu q_3^\mu [8(3m_t^2 - p_2 \cdot q_3 + 2(p_3 \cdot q_3) + p_1 \cdot p_3 + q_3^2) - 4(p_1 \cdot p_2)] - 4p_3^\mu p_1^\nu (p_2 \cdot q_3). \end{aligned} \quad (2.67)$$

Summing the diagrams

The box-like contribution to the leading order cross section is the sum of the box diagrams considered in the previous subsection:

$$\mathcal{M}_\square^{\mu\nu, ab} = 2 \left(\begin{array}{c} \text{diagram 1} \\ \text{diagram 2} \\ \text{diagram 3} \end{array} \right), \quad (2.68)$$

which lead to the following d -dimensional tensor-structure:

$$\begin{aligned} \mathcal{M}_\square^{\mu\nu, ab} &= -2 \frac{i\alpha_s}{(4\pi)} \frac{m_t^2}{v^2} Y_1 Y_2 \text{Tr}[T^a T^b] \left(\frac{4\pi\mu^2}{m_t^2} \right)^\epsilon \Gamma(1+\epsilon) \times \\ &\quad \times \int_0^1 dx \left\{ \det[J(g_1)] \left[\frac{(1+\epsilon) A_1^{\mu\nu}}{(m_t^2)^2 \Delta_1^{2+\epsilon}} - \frac{(2-\epsilon) B_1^{\mu\nu}}{m_t^2 \Delta_1^{1+\epsilon}} + \frac{(2-\epsilon)(3-\epsilon) C_1^{\mu\nu}}{\epsilon \Delta_1^\epsilon} \right] + \right. \\ &\quad \left. \det[J(g_1)] \left[\frac{(1+\epsilon) A_1^{\mu\nu}}{(m_t^2)^2 \Delta_1^{2+\epsilon}} - \frac{(2-\epsilon) B_1^{\mu\nu}}{m_t^2 \Delta_1^{1+\epsilon}} + \frac{(2-\epsilon)(3-\epsilon) C_1^{\mu\nu}}{\epsilon \Delta_1^\epsilon} \right] \Big|_{t \leftrightarrow u} + \right. \\ &\quad \left. \det[J(g_2)] \left[\frac{(1+\epsilon) A_2^{\mu\nu}}{(m_t^2)^2 \Delta_2^{2+\epsilon}} - \frac{(2-\epsilon) B_2^{\mu\nu}}{m_t^2 \Delta_2^{1+\epsilon}} + \frac{(2-\epsilon)(3-\epsilon) C_2^{\mu\nu}}{\epsilon \Delta_2^\epsilon} \right] \right\}. \end{aligned} \quad (2.69)$$

A first check on its finiteness is needed, such that the ϵ -expansion may lead to a meaningful physical quantity. The ϵ divergent part is proportional to the tensor $C^{\mu\nu}(\mathbf{p}, \mathbf{x})$:

$$\begin{aligned} \mathcal{M}_{\square}^{\mu\nu,ab}|_{A,B=0} &= -2 \frac{i\alpha_s}{(4\pi)} \frac{m_t^2}{v^2} Y_1 Y_2 \text{Tr}[T^a T^b] \left(\frac{4\pi\mu^2}{m_t^2} \right)^\epsilon \Gamma(1+\epsilon) \times \\ &\int_0^1 d\mathbf{x} \det[J(g)] \frac{(2-\epsilon)(3-\epsilon)}{\epsilon} \left\{ \frac{C_1^{\mu\nu}}{\Delta_1^\epsilon} + \frac{C_1^{\mu\nu}}{\Delta_1^\epsilon} \Big|_{t \leftrightarrow u} + \frac{C_2^{\mu\nu}}{\Delta_2^\epsilon} \right\}. \end{aligned} \quad (2.70)$$

since $g_1 = g_2 = g$, as noticeable from the calculation of the single diagrams. The expansion of the integrand up to its finite term yields:

$$\begin{aligned} \mathcal{M}_{\square}^{\mu\nu,ab}|_{A,B=0} &\propto g^{\mu\nu} \int_0^1 d\mathbf{x} \det[J(g)] \left(\frac{6}{\epsilon} - 5 + \epsilon \right) \times \\ &\times \left\{ -\frac{4(1-\epsilon)}{2-\epsilon} [2 - \epsilon \log(\Delta_1 \tilde{\Delta}_1) + O(\epsilon^2)] + 4[1 - \epsilon \log(\Delta_2) + O(\epsilon^2)] \right\} \\ &= g^{\mu\nu} \int_0^1 d\mathbf{x} \det[J(g)] \left(\frac{6}{\epsilon} - 5 + \epsilon \right) \times \\ &\times \left\{ -2(1-\epsilon) \left(1 + \frac{\epsilon}{2} \right) [2 - \epsilon \log(\Delta_1 \tilde{\Delta}_1)] + 4[1 - \epsilon \log(\Delta_2)] + O(\epsilon^2) \right\} \\ &= g^{\mu\nu} \int_0^1 d\mathbf{x} \det[J(g)] \left(\frac{6}{\epsilon} - 5 + \epsilon \right) 2\epsilon \left[1 + \log \left(\frac{\Delta_1 \tilde{\Delta}_1}{\Delta_2^2} \right) \right] + O(\epsilon^2) \\ &= g^{\mu\nu} \int_0^1 d\mathbf{x} \det[J(g)] \left(\frac{6}{\epsilon} - 5 + \epsilon \right) \left[2\epsilon \left(1 + \log \left(\frac{\Delta_1 \tilde{\Delta}_1}{\Delta_2^2} \right) \right) + O(\epsilon^2) \right] \\ &= 12g^{\mu\nu} \int_0^1 d\mathbf{x} \det[J(g)] \left[1 + \log \left(\frac{\Delta_1 \tilde{\Delta}_1}{\Delta_2^2} \right) \right] + O(\epsilon), \end{aligned} \quad (2.71)$$

which is finite in ϵ , as expected. Here, $\tilde{\Delta}_1 = \Delta_1|_{t \leftrightarrow u}$ and from now on, the tilde variables will denote the switch $t \leftrightarrow u$, which implies $p_3 \rightarrow p_1 + p_2 - p_3$.

Hence, since the contributions proportional to $A^{\mu\nu}(\mathbf{p}, \mathbf{x})$ and $B^{\mu\nu}(\mathbf{p}, \mathbf{x})$ are already finite in ϵ , the complete expansion will be finite, and it reads:

$$\begin{aligned} \mathcal{M}_{\square}^{\mu\nu,ab} &= -2 \frac{i\alpha_s}{(4\pi)} \frac{m_t^2}{v^2} Y_1 Y_2 \text{Tr}[T^a T^b] \left(\frac{4\pi\mu^2}{m_t^2} \right)^\epsilon \Gamma(1+\epsilon) \times \\ &\times \int_0^1 d\mathbf{x} \det[J(g)] \left\{ 12g^{\mu\nu} \left[1 + \log \left(\frac{\Delta_1 \tilde{\Delta}_1}{\Delta_2} \right) \right] + \frac{1}{(m_t^2)^2} \left(\frac{A_1^{\mu\nu}}{\Delta_1^2} + \frac{\tilde{A}_1^{\mu\nu}}{\tilde{\Delta}_1^2} + \frac{A_2^{\mu\nu}}{\Delta_2^2} \right) \Big|_{\epsilon=0} + \right. \\ &\left. - \frac{2}{m_t^2} \left(\frac{B_1^{\mu\nu}}{\Delta_1} + \frac{\tilde{B}_1^{\mu\nu}}{\tilde{\Delta}_1} + \frac{B_2^{\mu\nu}}{\Delta_2} \right) \Big|_{\epsilon=0} \right\} + O(\epsilon). \end{aligned} \quad (2.72)$$

We first present the case where the top-quark mass is considered to be heavy ($m_t \rightarrow \infty$), which can be solved analytically in a very compact form. Later, we show how a numerical approach for the LO amplitude can be exploited.

Heavy top limit

The heavy top limit $m_t \rightarrow \infty$ provides us with a first analytical expression to handle. Before writing explicitly the top-mass expansion of tadpole masses and tensors, we can express these expansions symbolically:

$$\begin{aligned} \frac{1}{\Delta_i} &\sim_{m_t \rightarrow \infty} 1 + \frac{\delta_i}{m_t^2} + O\left(\frac{1}{m_t^4}\right), \\ A_i^{\mu\nu} &\sim_{m_t \rightarrow \infty} a_{i,(-2)}^{\mu\nu} m_t^4 + a_{i,(-1)}^{\mu\nu} m_t^2 + O(1), \\ B_i^{\mu\nu} &\sim_{m_t \rightarrow \infty} b_{i,(-1)}^{\mu\nu} m_t^2 + b_{i,(0)}^{\mu\nu} + O\left(\frac{1}{m_t^2}\right). \end{aligned} \quad (2.73)$$

Therefore, the Eq. (2.72) reads:

$$\begin{aligned}
\mathcal{M}_{\square}^{\mu\nu,ab} &= -2 \frac{i\alpha_s}{(4\pi)} \frac{m_t^2}{v^2} Y_1 Y_2 \text{Tr}[T^a T^b] \left(\frac{4\pi\mu^2}{m_t^2} \right)^\epsilon \Gamma(1+\epsilon) \times \\
&\quad \times \int_0^1 d\mathbf{x} \det[J(g)] \left\{ 12g^{\mu\nu} \left[1 + \frac{2\delta_2 - \delta_1 - \tilde{\delta}_1}{m_t^2} + O\left(\frac{1}{m_t^4}\right) \right] + \right. \\
&\quad \left. + \frac{1}{(m_t^2)^2} \left(\left[a_{1,(-2)}^{\mu\nu} + \tilde{a}_{1,(-2)}^{\mu\nu} + a_{2,(-2)}^{\mu\nu} \right] m_t^4 + \right. \right. \\
&\quad \left. \left. + \left[a_{1,(-1)}^{\mu\nu} + \tilde{a}_{1,(-1)}^{\mu\nu} + a_{2,(-1)}^{\mu\nu} + \right. \right. \right. \\
&\quad \left. \left. \left. + 2a_{1,(-2)}^{\mu\nu} \delta_1 + 2\tilde{a}_{1,(-2)}^{\mu\nu} \tilde{\delta}_1 + 2a_{2,(-2)}^{\mu\nu} \delta_2 \right] m_t^2 + O(1) \right) - \right. \\
&\quad \left. - \frac{2}{m_t^2} \left(\left[b_{1,(-1)}^{\mu\nu} + \tilde{b}_{1,(-1)}^{\mu\nu} + b_{2,(-1)}^{\mu\nu} \right] m_t^2 + \right. \right. \\
&\quad \left. \left. + \left[b_{1,(0)}^{\mu\nu} + \tilde{b}_{1,(0)}^{\mu\nu} + b_{2,(0)}^{\mu\nu} + \right. \right. \right. \\
&\quad \left. \left. \left. + \tilde{b}_{1,(-1)}^{\mu\nu} \tilde{\delta}_1 + b_{1,(-1)}^{\mu\nu} \delta_1 + b_{2,(-1)}^{\mu\nu} \delta_2 \right] + O\left(\frac{1}{m_t^2}\right) \right) \right\} + O(\epsilon) = \tag{2.74}
\end{aligned}$$

$$\begin{aligned}
&= -2 \frac{i\alpha_s}{(4\pi)} \frac{m_t^2}{v^2} Y_1 Y_2 \text{Tr}[T^a T^b] \left(\frac{4\pi\mu^2}{m_t^2} \right)^\epsilon \Gamma(1+\epsilon) \times \\
&\quad \times \int_0^1 d\mathbf{x} \det[J(g)] \left\{ 12g^{\mu\nu} + \left[a_{1,(-2)}^{\mu\nu} + \tilde{a}_{1,(-2)}^{\mu\nu} + a_{2,(-2)}^{\mu\nu} \right] - \right. \\
&\quad \left. - 2 \left[b_{1,(-1)}^{\mu\nu} + \tilde{b}_{1,(-1)}^{\mu\nu} + b_{1,(-1)}^{\mu\nu} \right] + \right. \\
&\quad \left. + \frac{1}{(m_t^2)} \left(12g^{\mu\nu} (2\delta_2 - \delta_1 - \tilde{\delta}_1) + \right. \right. \\
&\quad \left. \left. + \left[a_{1,(-1)}^{\mu\nu} + \tilde{a}_{1,(-1)}^{\mu\nu} + a_{2,(-1)}^{\mu\nu} + \right. \right. \right. \\
&\quad \left. \left. \left. + 2a_{1,(-2)}^{\mu\nu} \delta_1 + 2\tilde{a}_{1,(-2)}^{\mu\nu} \tilde{\delta}_1 + 2a_{2,(-2)}^{\mu\nu} \delta_2 \right] \right. \right. \\
&\quad \left. \left. - 2 \left[b_{1,(0)}^{\mu\nu} + \tilde{b}_{1,(0)}^{\mu\nu} + b_{2,(0)}^{\mu\nu} + \right. \right. \right. \\
&\quad \left. \left. \left. + \tilde{b}_{1,(-1)}^{\mu\nu} \tilde{\delta}_1 + b_{1,(-1)}^{\mu\nu} \delta_1 + b_{2,(-1)}^{\mu\nu} \delta_2 \right] \right) \right\} + O\left(\epsilon, \frac{1}{m_t^2}\right).
\end{aligned}$$

Since the Yukawa vertices contributes with an m_t^2 , the integrand has to scale with $\frac{1}{m_t^2}$ to ensure the finiteness of the heavy top-quark limit. The implication of this is that the sum of the leading term of each expanded quantity has to vanish:

$$12g^{\mu\nu} + \left[a_{1,(-2)}^{\mu\nu} + \tilde{a}_{1,(-2)}^{\mu\nu} + a_{2,(-2)}^{\mu\nu} \right] - 2 \left[b_{1,(-1)}^{\mu\nu} + \tilde{b}_{1,(-1)}^{\mu\nu} + b_{1,(-1)}^{\mu\nu} \right] = 0. \tag{2.75}$$

From the explicit mass expansion, we obtain

$$\begin{aligned}
a_{1,(-2)}^{\mu\nu} &= \tilde{a}_{1,(-2)}^{\mu\nu} = a_{2,(-2)}^{\mu\nu} = 4g^{\mu\nu} \\
b_{1,(-1)}^{\mu\nu} &= \tilde{b}_{1,(-1)}^{\mu\nu} = 6g^{\mu\nu}, \quad b_{2,(-1)}^{\mu\nu} = 0,
\end{aligned} \tag{2.76}$$

which satisfies the Eq. (2.75). Hence:

$$\begin{aligned} \mathcal{M}_{\square}^{\mu\nu,ab} = & -2 \frac{i\alpha_s}{(4\pi)} \frac{Y_1 Y_2}{v^2} \text{Tr}[T^a T^b] \left(\frac{4\pi\mu^2}{m_t^2} \right)^\epsilon \Gamma(1+\epsilon) \times \\ & \times \int_0^1 d\mathbf{x} \det[J(g)] \left\{ 16g^{\mu\nu}(2\delta_2 - \delta_1 - \tilde{\delta}_1) + \right. \\ & \quad \left. + \left[a_{1,(-1)}^{\mu\nu} + \tilde{a}_{1,(-1)}^{\mu\nu} + a_{2,(-1)}^{\mu\nu} \right] \right. \\ & \quad \left. - 2 \left[b_{1,(0)}^{\mu\nu} + \tilde{b}_{1,(0)}^{\mu\nu} + b_{2,(0)}^{\mu\nu} \right] \right\} + O\left(\epsilon, \frac{1}{m_t^2}\right). \end{aligned} \quad (2.77)$$

The explicit expressions for the subleading terms needed are:

$$\begin{aligned} b_{1,(0)}^{\mu\nu} = & 2g^{\mu\nu} \left[-4(p_1 \cdot q_1) + 3(p_2 \cdot q_1) + (p_3 \cdot q_1) + (p_1 \cdot p_2) - \right. \\ & \quad \left. + (p_1 \cdot p_3) - (p_2 \cdot p_3) - 5q_1^2 \right] - \\ & - 2p_2^\mu p_1^\nu + 2p_2^\mu p_3^\nu - 2p_3^\mu p_1^\nu - 6p_2^\mu q_1^\nu + \\ & + 4p_1^\nu q_1^\mu + 2p_3^\nu q_1^\mu + 2p_3^\mu q_1^\nu + 16q_1^\mu q_1^\nu, \\ b_{2,(0)}^{\mu\nu} = & 2g^{\mu\nu} \left[3(p_1 \cdot q_3) - 3(p_2 \cdot q_3) + 6(p_3 \cdot q_3 + q_3^2) + \right. \\ & \quad \left. + p_3^2 - 2(p_1 \cdot p_2) + 2(p_1 \cdot p_3) - p_2 \cdot p_3 \right] + \\ & + 4p_2^\mu p_1^\nu + 2p_2^\mu p_3^\nu - 4p_3^\mu p_1^\nu - 4p_3^\mu p_3^\nu + \\ & + 6p_2^\mu q_3^\nu - 6p_1^\nu q_3^\mu + 12p_3^\nu q_3^\mu - 12p_3^\mu q_3^\nu, \\ a_{1,(-1)}^{\mu\nu} = & -4g^{\mu\nu} \left[-2(p_1 \cdot q_1) + p_2 \cdot q_1 + p_3 \cdot q_1 + \right. \\ & \quad \left. + 2(p_1 \cdot p_2) + p_1 \cdot p_3 - p_2 \cdot p_3 \right] + \\ & + 8p_2^\mu p_1^\nu - 4p_2^\mu p_3^\nu + 4p_3^\mu p_1^\nu + 4p_2^\mu q_1^\nu - \\ & - 4p_3^\nu q_1^\mu - 4p_3^\mu q_1^\nu + 24q_1^\mu q_1^\nu, \\ a_{2,(-1)}^{\mu\nu} = & -4g^{\mu\nu} \left[(p_1 \cdot q_3) - (p_2 \cdot q_3) + 2(p_3 \cdot q_3 + q_3^2) + \right. \\ & \quad \left. + p_3^2 + p_1 \cdot p_2 - p_2 \cdot p_3 \right] + \\ & + 4p_2^\mu p_1^\nu - 4p_2^\mu p_3^\nu + 8p_3^\mu p_3^\nu - 4p_2^\mu q_3^\nu + \\ & + 4p_1^\nu q_3^\mu + 24p_3^\nu q_3^\mu + 8p_3^\mu q_3^\nu + 32q_3^\mu q_3^\nu. \end{aligned} \quad (2.78)$$

The complete analytical expression for the heavy top-quark limit is obtained by integrating w.r.t. the Feynman parameters (x_1, x_2, x_3). After doing this, the final expression is very compact:

$$\begin{aligned} \mathcal{M}_{\square}^{\mu\nu,ab} = & -2 \frac{i\alpha_s}{(4\pi)} \frac{Y_1 Y_2}{v^2} \text{Tr}[T^a T^b] \left(\frac{4\pi\mu^2}{m_t^2} \right)^\epsilon \Gamma(1+\epsilon) \frac{4}{3} \left[p_2^\mu p_1^\nu - (p_1 \cdot p_2) g^{\mu\nu} \right] \\ = & i \frac{\alpha_s}{3\pi v^2} Y_1 Y_2 \delta^{ab} C_\epsilon \left[(p_1 \cdot p_2) g^{\mu\nu} - p_2^\mu p_1^\nu \right]. \end{aligned} \quad (2.79)$$

This last result can also be interpreted as a $ggH_i H_j$ effective vertex for the low-energy lagrangian:

$$\begin{aligned} \text{Diagram} & = i \frac{\alpha_s}{3\pi v^2} Y_1 Y_2 \delta^{ab} \left(\frac{4\pi\mu^2}{m_t^2} \right)^\epsilon \Gamma(1+\epsilon) \left[(p_1 \cdot p_2) g^{\mu\nu} - p_2^\mu p_1^\nu \right]. \end{aligned} \quad (2.80)$$

2.2.4 LO amplitude in the Heavy top limit

The sum of Eq. (2.27) and Eq. (2.80) leads to the HTL LO amplitude. It has a very simple expression:

$$\begin{aligned} \mathcal{M}_{\text{LO}}^{\text{HTL}} = & -i \frac{\alpha_s}{3\pi v^2} \delta^{ab} \sqrt{\kappa} \left(\frac{4\pi\mu^2}{m_t^2} \right)^\epsilon \Gamma(1+\epsilon) \left[(p_1 \cdot p_2) g^{\mu\nu} - p_2^\mu p_1^\nu \right], \\ \sqrt{\kappa} = & \sum_j \left(\frac{3Y_j \lambda_{j12}}{\hat{s} - m_{H_j}^2 + im_{H_j} \Gamma(m_{H_j}^2)} \right) - Y_1 Y_2, \end{aligned} \quad (2.81)$$

where the factor κ encodes the explicit dependence on the parameters of the model.

The averaged square amplitude will depend only on the Higgs-pair invariant mass $\sqrt{\hat{s}}$, and it takes the following form:

$$\frac{1}{256} \sum_{\text{pol}} |\overline{\mathcal{M}_{\text{LO}}}|^2 = \frac{\alpha_s^2}{(4\pi)^2 v^4} \frac{\kappa}{64} \frac{4}{9} \hat{s}^2. \quad (2.82)$$

This result is in complete agreement with the literature [32, 54].

2.3 Projecting onto the Lorentz structure

The necessity of knowing ϵ -expansion terms up to the second order leads to consider a different strategy for the finite top-mass calculation.

Following the same spirit of the calculation of the $gg^* \rightarrow H$ amplitude, we can infer the Lorentz structure behind the process and project the amplitude onto them. The form factors thus generated can be expressed in terms of scalar integrals by means of the Passarino-Veltmann decomposition [149].

A process involving two gluons and two scalar particles can be decomposed following the tensor structure

$$T^{\mu\nu} = a_{00} g^{\mu\nu} + \sum_{i,j=1}^3 a_{ij} p_i^\mu p_j^\nu. \quad (2.83)$$

A relation between the coefficients a_{ij} can be found by imposing the transversality of the on-shell gluons and the Ward identities (Appendix B):

$$\begin{aligned} p_{1,\mu} \epsilon^\mu(p_1) &= p_{2,\nu} \epsilon^\nu(p_1) = 0, \\ p_{1,\mu} T^{\mu\nu} &= p_{2,\nu} T^{\mu\nu} = 0. \end{aligned} \quad (2.84)$$

These conditions will fix the tensor structure to be generated by two tensors $T_1^{\mu\nu}$ and $T_2^{\mu\nu}$:

$$\begin{aligned} T_1^{\mu\nu} &= g^{\mu\nu} - \frac{p_2^\mu p_1^\nu}{p_1 \cdot p_2}, \\ T_2^{\mu\nu} &= g^{\mu\nu} + \frac{p_3^2 p_2^\mu p_1^\nu - 2(p_2 \cdot p_3) p_1^\mu p_3^\nu - 2(p_1 \cdot p_3) p_2^\mu p_3^\nu + 2(p_1 \cdot p_2) p_3^\mu p_3^\nu}{(p_1 \cdot p_2) p_T^2} \\ p_T^2 &= \frac{2(p_1 \cdot p_3)(p_2 \cdot p_3)}{(p_1 \cdot p_2)} - p_3^2, \end{aligned} \quad (2.85)$$

which are orthogonal in $d = 4$. However, in d -dimensions the contraction over the tensor indices is

$$T_i^{\mu\nu} T_{i,\mu\nu} = d - 2, \quad T_{1,\mu\nu} T_2^{\mu\nu} = d - 4 \quad (2.86)$$

The projectors $P_i^{\mu\nu}$ on a tensor $T_i^{\mu\nu}$ can be found by imposing the following conditions:

$$P_i^{\mu\nu} T_{j,\mu\nu} = \delta_{ij} \quad \Longrightarrow \quad \begin{cases} P_1 = \frac{(d-2)T_1^{\mu\nu} - (d-4)T_2^{\mu\nu}}{4(d-3)} \\ P_2 = \frac{(d-2)T_2^{\mu\nu} - (d-4)T_1^{\mu\nu}}{4(d-3)} \end{cases} \quad (2.87)$$

The expression of the complete LO amplitude of Eq. (2.22) projected onto form factors is:

$$\begin{aligned} \mathcal{M}_{LO} &= \epsilon_\mu(p_1) \epsilon_\nu(p_2) (\mathcal{M}_\Delta^{\mu\nu,ab} + \mathcal{M}_\square^{\mu\nu,ab}) \\ &= \epsilon_\mu(p_1) \epsilon_\nu(p_2) \left[\left(F_\Delta^{(0)} + F_1^{(0)} \right) T_1^{\mu\nu} + F_2^{(0)} T_2^{\mu\nu} \right], \end{aligned} \quad (2.88)$$

which can be expressed in terms of scalar integrals. The Passarino-Veltmann decomposition for the

triangles will lead to:

$$\begin{aligned}
F_{\Delta}^{(0)} &= -(-ig_s)^2(i)^4 \left(2\text{Tr} \left[T^a T^b\right]\right) \frac{i}{(4\pi)^2} \left(\frac{4\pi\mu^2}{m_t^2}\right)^\epsilon \Gamma(1+\epsilon) \times \\
&\quad \times \sum_j^3 \left(-iY_j \frac{m_t}{v}\right) \left(-i3\frac{\lambda_{j12}}{v}\right) \left(\frac{1}{\hat{s} - m_{H_j}^2 - im_{H_j}\Gamma(m_{H_j}^2)}\right) (m_t \mathcal{A}_{\Delta}^{(0)}) \\
&= -\frac{i\alpha_s}{(4\pi)} \frac{m_t^2}{v^2} \delta^{ab} \left(\frac{4\pi\mu^2}{m_t^2}\right)^\epsilon \Gamma(1+\epsilon) \left[\sum_j^3 \left(\frac{3Y_j \lambda_{j12}}{\hat{s} - m_{H_j}^2 - im_{H_j}\Gamma(m_{H_j}^2)}\right)\right] \mathcal{A}_{\Delta}^{(0)}, \\
&= -\frac{i\alpha_s}{(4\pi)} \frac{m_t^2}{v^2} \delta^{ab} \left(\frac{4\pi\mu^2}{m_t^2}\right)^\epsilon \Gamma(1+\epsilon) C_{\Delta} \mathcal{A}_{\Delta}^{(0)},
\end{aligned} \tag{2.89}$$

$$\mathcal{A}_{\Delta}^{(0)} = P_1^{\mu\nu} \int_k \frac{\mathcal{N}_{\mu\nu}}{\mathcal{D}}, \quad C_{\Delta} = \sum_j^3 \frac{3Y_j \lambda_{j12}}{\hat{s} - m_{H_j}^2 - im_{H_j}\Gamma(m_{H_j}^2)}$$

where the explicit expression for $\mathcal{A}_{\Delta}^{(0)}$ is

$$\mathcal{A}_{\Delta}^{(0)} = 4C_{\epsilon} \left[\frac{(d-4)}{(d-2)} B_0(\hat{s}, \bar{m}_t^2) - \left(\frac{4m_t^2}{d-2} - \frac{\hat{s}}{2}\right) C_0(0, 0, \hat{s}, \bar{m}_t^2) \right]. \tag{2.90}$$

where

$$C_{\epsilon} = \frac{(m_t^2)^\epsilon}{\Gamma(1+\epsilon)}. \tag{2.91}$$

The Passarino-Veltmann decomposition of the box form factors leads to more complex expressions:

$$\begin{aligned}
F_j^{(0)} &= -(-ig_s)^2(i)^4 \left(2\text{Tr} \left[T^a T^b\right]\right) \frac{i}{(4\pi)^2} \left(\frac{4\pi\mu^2}{m_t^2}\right)^\epsilon \Gamma(1+\epsilon) \left(-i\frac{m_t}{v}\right)^2 Y_1 Y_2 \mathcal{A}_j^{(0)} \\
&= -\frac{i\alpha_s}{(4\pi)} \frac{m_t^2}{v^2} Y_1 Y_2 \delta^{ab} \left(\frac{4\pi\mu^2}{m_t^2}\right)^\epsilon \Gamma(1+\epsilon) \mathcal{A}_j^{(0)}, \\
\mathcal{A}_j^{(0)} &= \sum_{l=1}^3 P_j^{\mu\nu} \int_k \frac{\mathcal{N}_{jl, \mu\nu}}{\mathcal{D}_{jl}}, \quad j \in (1, 2),
\end{aligned} \tag{2.92}$$

where the index j runs over the three independent box diagrams (Figure 2.2).

$$\begin{aligned}
\mathcal{A}_1^{(0)} = & - \left\{ 4 \frac{(d-4)}{(d-2)} B_0(\hat{s}, \overline{m}_t^2) - \frac{1}{2(d-3)(m_{H_1}^2 m_{H_2}^2 - \hat{t}\hat{u})} \right. \\
& \frac{C_0(0, 0, \hat{s}, \overline{m}_t^2)}{(d-2)} [8m_t^2 4(d-3)(m_{H_1}^2 m_{H_2}^2 - \hat{t}\hat{u}) + (d-4)(d-2)\hat{s}(\hat{t} + \hat{u})(\hat{t} + \hat{u} - 8m_t^2)] + \\
& + C_0(0, m_{H_1}^2, \hat{t}, \overline{m}_t^2) \frac{(\hat{t} - m_{H_1}^2)}{\hat{s}} \left[(d-2)(m_{H_1}^2 m_{H_2}^2 - \hat{t}\hat{u})(m_{H_1}^2 + m_{H_2}^2 - 8m_t^2) + \right. \\
& \quad \left. + \hat{s}(d-4)(\hat{t}^2 - 8m_t^2 \hat{t} + m_{H_1}^2 m_{H_2}^2) \right] + \\
& + C_0(0, m_{H_1}^2, \hat{u}, \overline{m}_t^2) \frac{(\hat{u} - m_{H_1}^2)}{\hat{s}} \left[(d-2)(m_{H_1}^2 m_{H_2}^2 - \hat{t}\hat{u})(m_{H_1}^2 + m_{H_2}^2 - 8m_t^2) + \right. \\
& \quad \left. + \hat{s}(d-4)(\hat{u}^2 - 8m_t^2 \hat{u} + m_{H_1}^2 m_{H_2}^2) \right] + \\
& + C_0(0, \hat{t}, m_{H_2}^2, \overline{m}_t^2) \frac{(\hat{t} - m_{H_2}^2)}{\hat{s}} \left[(d-2)(m_{H_1}^2 m_{H_2}^2 - \hat{t}\hat{u})(m_{H_1}^2 + m_{H_2}^2 - 8m_t^2) + \right. \\
& \quad \left. + \hat{s}(d-4)(\hat{t}^2 - 8m_t^2 \hat{t} + m_{H_1}^2 m_{H_2}^2) \right] + \\
& + C_0(0, \hat{u}, m_{H_2}^2, \overline{m}_t^2) \frac{(\hat{u} - m_{H_2}^2)}{\hat{s}} \left[(d-2)(m_{H_1}^2 m_{H_2}^2 - \hat{t}\hat{u})(m_{H_1}^2 + m_{H_2}^2 - 8m_t^2) + \right. \\
& \quad \left. + \hat{s}(d-4)(\hat{u}^2 - 8m_t^2 \hat{u} + m_{H_1}^2 m_{H_2}^2) \right] + \\
& - C_0(\hat{s}, m_{H_1}^2, m_{H_2}^2, \overline{m}_t^2) (d-4) (\hat{t} + \hat{u} - 8m_t^2) ((\hat{t} + \hat{u})^2 - 4m_{H_1}^2 m_{H_2}^2) + \\
& - D_0(0, 0, m_{H_1}^2, m_{H_2}^2, \hat{s}, \hat{t}, \overline{m}_t^2) \left[4m_t^2 [2(d-3)\hat{s} + \hat{t} + \hat{u} - 8m_t^2] (m_{H_1}^2 m_{H_2}^2 - \hat{t}\hat{u}) + \right. \\
& \quad \left. + (d-4)\hat{s}\hat{t}^2(\hat{t} + \hat{u} - 8m_t^2) \right] + \\
& - D_0(0, 0, m_{H_1}^2, m_{H_2}^2, \hat{s}, \hat{u}, \overline{m}_t^2) \left[4m_t^2 [2(d-3)\hat{s} + \hat{t} + \hat{u} - 8m_t^2] (m_{H_1}^2 m_{H_2}^2 - \hat{t}\hat{u}) + \right. \\
& \quad \left. + (d-4)\hat{s}\hat{u}^2(\hat{t} + \hat{u} - 8m_t^2) \right] + \\
& - D_0(0, m_{H_1}^2, 0, m_{H_2}^2, \hat{t}, \hat{u}, \overline{m}_t^2) \left[4m_t^2 (2(d-3)\hat{s} + \hat{t} + \hat{u} - 8m_t^2) (m_{H_1}^2 m_{H_2}^2 - \hat{t}\hat{u}) - \right. \\
& \quad - (d-2) \left(\frac{m_{H_1}^2 + m_{H_2}^2 - 8m_t^2}{\hat{s}} \right) (m_{H_1}^2 m_{H_2}^2 - \hat{t}\hat{u})^2 - \\
& \quad \left. - (d-4) (m_{H_1}^2 m_{H_2}^2 - \hat{t}\hat{u})^2 \right] \left. \right\}, \tag{2.93}
\end{aligned}$$

$$\begin{aligned}
\mathcal{A}_2^{(0)} = & -\frac{1}{2(d-3)(m_{H_1}^2 m_{H_2}^2 - \hat{t}\hat{u})} \left\{ \right. \\
& - C_0(0, 0, \hat{s}, \overline{m_t^2}) \hat{s} [4(d-3)(m_{H_1}^2 m_{H_2}^2 - \hat{t}\hat{u}) + (d-2)(\hat{t} + \hat{u})(\hat{t} + \hat{u} - 8m_t^2)] + \\
& - C_0(0, m_{H_1}^2, \hat{t}, \overline{m_t^2}) \frac{(\hat{t} - m_{H_1}^2)}{\hat{s}} [(d-4)(m_{H_1}^2 m_{H_2}^2 - \hat{t}\hat{u})(m_{H_1}^2 + m_{H_2}^2 - 8m_t^2) + \\
& \quad + \hat{s}(d-2)(\hat{t}^2 - 8m_t^2 \hat{t} + m_{H_1}^2 m_{H_2}^2)] + \\
& - C_0(0, m_{H_1}^2, \hat{u}, \overline{m_t^2}) \frac{(\hat{u} - m_{H_1}^2)}{\hat{s}} [(d-4)(m_{H_1}^2 m_{H_2}^2 - \hat{t}\hat{u})(m_{H_1}^2 + m_{H_2}^2 - 8m_t^2) - \\
& \quad + \hat{s}(d-2)(\hat{u}^2 - 8m_t^2 \hat{u} + m_{H_1}^2 m_{H_2}^2)] + \\
& - C_0(0, \hat{t}, m_{H_2}^2, \overline{m_t^2}) \frac{(\hat{t} - m_{H_2}^2)}{\hat{s}} [(d-4)(m_{H_1}^2 m_{H_2}^2 - \hat{t}\hat{u})(m_{H_1}^2 + m_{H_2}^2 - 8m_t^2) + \\
& \quad + \hat{s}(d-2)(\hat{t}^2 - 8m_t^2 \hat{t} + m_{H_1}^2 m_{H_2}^2)] + \\
& - C_0(0, \hat{u}, m_{H_2}^2, \overline{m_t^2}) \frac{(\hat{u} - m_{H_2}^2)}{\hat{s}} [(d-4)(m_{H_1}^2 m_{H_2}^2 - \hat{t}\hat{u})(m_{H_1}^2 + m_{H_2}^2 - 8m_t^2) - \\
& \quad + \hat{s}(d-2)(\hat{u}^2 - 8m_t^2 \hat{u} + m_{H_1}^2 m_{H_2}^2)] + \\
& + C_0(\hat{s}, m_{H_1}^2, m_{H_2}^2, \overline{m_t^2}) (4-d) (\hat{t} + \hat{u} - 8m_t^2) [(\hat{t} + \hat{u})^2 - 4(m_{H_1}^2 m_{H_2}^2 - \hat{t}\hat{u})] + \\
& + D_0(0, 0, m_{H_1}^2, m_{H_2}^2, \hat{s}, \hat{t}, \overline{m_t^2}) \left[-4m_t^2(\hat{t} + \hat{u} - 8m_t^2)(m_{H_1}^2 m_{H_2}^2 - \hat{t}\hat{u}) + \right. \\
& \quad + (d-4)\hat{s}\hat{t}(m_{H_1}^2 m_{H_2}^2 - \hat{t}\hat{u}) + \\
& \quad \left. + (d-2)\hat{s}\hat{t}(\hat{t}^2 - 8m_t^2 \hat{t} + m_{H_1}^2 m_{H_2}^2) \right] \\
& - D_0(0, 0, m_{H_1}^2, m_{H_2}^2, \hat{s}, \hat{u}, \overline{m_t^2}) \left[-4m_t^2(\hat{t} + \hat{u} - 8m_t^2)(m_{H_1}^2 m_{H_2}^2 - \hat{t}\hat{u}) + \right. \\
& \quad + (d-4)\hat{s}\hat{u}(m_{H_1}^2 m_{H_2}^2 - \hat{t}\hat{u}) + \\
& \quad \left. + (d-2)\hat{s}\hat{u}(\hat{u}^2 - 8m_t^2 \hat{u} + m_{H_1}^2 m_{H_2}^2) \right] \\
& \left. - D_0(0, m_{H_1}^2, 0, m_{H_2}^2, \hat{t}, \hat{u}, \overline{m_t^2}) (\hat{t} + \hat{u} - 8m_t^2) \left[(d-4) \frac{(m_{H_1}^2 m_{H_2}^2 - \hat{t}\hat{u})}{\hat{s}} + 4m_t^2 \right] \right\}. \tag{2.94}
\end{aligned}$$

These expressions are finite in the physical limit $d \rightarrow 4$. Details on the notation of these integrals can be found in Appendix E. It is important to keep the d dependence since the divergences at NLO develop second order poles, for which terms of the LO form factors up to $O(\epsilon^2)$ are needed.

2.4 Leading-Order Cross section

As anticipated in the previous chapter, the total LO cross section is obtained by integrating the partonic cross section along with the gluon luminosity:

$$\begin{aligned}
\sigma_{LO}(pp \rightarrow gg \rightarrow H_1 H_2) &= \int_{\tau_0}^1 d\tau \frac{d\mathcal{L}_{gg}}{d\tau} \hat{\sigma}_{LO}(\hat{s} = \tau s), \quad \tau_0 = \frac{(m_{H_1} + m_{H_2})^2}{s} \\
\frac{d\mathcal{L}_{gg}}{d\tau} &= \int_{\tau}^1 \frac{dx}{x} f_g(x, \mu_F) f_g\left(\frac{\tau}{x}, \mu_F\right). \tag{2.95}
\end{aligned}$$

Notice that the Higgs-pair invariant mass $Q^2 = (m_{H_1} + m_{H_2})^2$, for the LO amplitude is equal to the partonic center-of-mass, namely $Q^2 = \hat{s}$. Same identity occurs for the virtual correction at NLO; this fact is not true for the real corrections, for which $Q^2 = \hat{s} + \hat{t} + \hat{u}$ (see Chapter 3).

The explicit partonic cross section can be found by squaring Eq. (2.88), summing over the polar-

ization vectors and integrating over the phase space:

$$\begin{aligned}\hat{\sigma}_{LO}(\hat{s}) &= C_{\text{flux}}C_{\text{sym}} \int d\text{PS}_2 \overline{|\mathcal{M}_{LO}|^2} \\ &= C_{\text{flux}}C_{\text{sym}}C_{\text{av}} \int d\text{PS}_2 \left[\left| F_{\Delta}^{(0)} + F_1^{(0)} \right|^2 + \left| F_2^{(0)} \right|^2 \right],\end{aligned}\tag{2.96}$$

where C_{av} takes into account the polarization average. More details on the phase space integration can be found in Appendix C. Here, $C_{\text{sym}} = 1$, since no identical particles lie in the final state, and $C_{\text{flux}} = \frac{1}{2\hat{s}}$.

$$\begin{aligned}\hat{\sigma}_{LO}(\hat{s}) &= \frac{1}{(2\hat{s})(256)} \int d\text{PS}_2 \left[\left| F_{\Delta}^{(0)} + F_1^{(0)} \right|^2 + \left| F_2^{(0)} \right|^2 \right] \\ &= \frac{\alpha_s^2}{(4\pi)^2} \frac{G_F^2 m_t^4}{512\pi\hat{s}^2} \int_{t^-}^{t^+} dt \left[\left| C_{\Delta}\mathcal{A}_{\Delta}^{(0)} + Y_1 Y_2 \mathcal{A}_1^{(0)} \right|^2 + \left| Y_1 Y_2 \mathcal{A}_2^{(0)} \right|^2 \right].\end{aligned}\tag{2.97}$$

The partonic transferred momentum square \hat{t} is related to the scattering angle θ in the following way:

$$\begin{aligned}\hat{t} &= -\frac{\hat{s}}{2}(1 - \Sigma - \beta \cos \theta), \quad \beta = \sqrt{1 - 2\Sigma + \Delta^2} \\ \Sigma &= \frac{m_{H_1}^2 + m_{H_2}^2}{\hat{s}}, \quad \Delta = \frac{m_{H_2}^2 - m_{H_1}^2}{\hat{s}} \\ \hat{t}^{\pm} &= -\frac{\hat{s}}{2}(1 - \Sigma \mp \beta)\end{aligned}\tag{2.98}$$

The LO cross section has been extensively studied in the past decades [54, 130, 131], providing a total cross section of the order of $\sigma_{LO} \approx 10$ fb at $\sqrt{s} = 14$ TeV. As we will see later, the NLO contributions are significant: HTL NLO is known to increase the total cross section of around a factor 2. Finite top-mass effects will decrease those contributions, as discussed in this thesis in Chapter 5.

Chapter 3

NLO Cross Section

In this section, we describe in detail the complete calculation for the virtual cross section $\Delta\hat{\sigma}_{\text{virt}}$ and real cross section $\Delta\hat{\sigma}_{\text{real}}$ for the NLO Higgs-pair production via gluon fusion process. All the diagrams under investigation are represented in Appendix H.

The virtual amplitude is made of two-loop Feynman diagrams, and it gets contributions from three classes of diagrams: box diagrams, one-particle-reducible diagrams and triangle diagrams. The 47 box diagrams are grouped into six topologies: topology 1 consists of top-quark self-energy corrections to the LO boxes; topologies 2 and 3 are the vertex corrections to the LO boxes, containing abelian and non-abelian corrections respectively; topology 4 and 5 are respectively the planar and non-planar double-boxes; topology 6 contains the genuine IR divergent two-loop boxes, both planar and non-planar. The one-particle reducible diagrams can be constructed from the QCD Higgs production via gluon fusion process where an external gluon is off-shell. For this amplitude, the analytical expression has been found in Chapter 2. The triangle diagrams are the ones that contain the trilinear Higgs coupling: they represent the diagrams carrying the signal of the detection of a Higgs-pair final state produced by a Higgs-decay, while the other virtual amplitudes represent an irreducible background. The 24 triangle diagrams can be grouped in the same way shown for the boxes: 6 top-quark propagator self-energies corrections to the LO triangle diagrams; 10 vertex corrections to the LO triangle diagrams, both abelian and non-abelian; 4 non-planar triangles and 4 genuine IR contributions. It is important to notice that the number of triangle diagrams of the 2HDM is doubled with respect to the SM, since the off-shell Higgs can be either light (H_1) or heavy (H_2).

The real contributions are made of 43 one-loop diagrams where an additional parton is emitted in the final state. There are three channels that contribute to the real cross section: $q\bar{q} \rightarrow H_1 H_2 g$, $qg \rightarrow H_1 H_2 q$ and $gg \rightarrow H_1 H_2 g$. Most of the diagrams of the real amplitude can be built from the LO amplitude where one external gluon is put off-shell. This feature will be relevant in the integration over the phase space, where such subprocess can be integrated separately from the whole process explicitly. The latter channel contains contributions coming from pentagon diagrams.

The calculation of the box diagrams represents the most challenging part of this thesis, and a dedicated strategy to approach this part of the virtual amplitude will be presented.

3.1 Virtual contributions

Following the same form factor decomposition exploited to calculate the LO diagrams, we can conveniently project the amplitude on the Lorentz structure.

$$\begin{aligned}\mathcal{M}_{\text{NLO}} &= \epsilon_\mu(p_1)\epsilon_\nu(p_2)(1)(1)(\mathcal{M}_\Delta^{\mu\nu,ab} + \mathcal{M}_\square^{\mu\nu,ab}) \\ &= \epsilon_\mu(p_1)\epsilon_\nu(p_2) \left[\left(F_\Delta^{(1)} + F_1^{(1)} \right) T_1^{\mu\nu} + F_2^{(1)} T_2^{\mu\nu} \right]\end{aligned}\tag{3.1}$$

We are interested in the form factors $F_j^{(1)}$ and $F_\Delta^{(1)}$, that represent the core of the square amplitude: the interference of these form factor with the LO ones are the NLO virtual contributions needed for the partonic cross section.

Since we already know the analytical expression of the LO QCD single-Higgs production via gluon fusion amplitude, we can use it to infer the form factor of $\mathcal{M}_{1\text{-PR}}$. To simplify the expression, we can make use of the kinematic variables and the momentum conservation:

$$\begin{aligned}
 \mathcal{M}_{1\text{-PR}} &= -\frac{i\alpha_s^2}{(4\pi)^2} \frac{m_t^2}{v^2} Y_1 Y_2 \delta^{ab} \frac{16\mathcal{I}(\tau_1, \lambda_t)\mathcal{I}(\tau_2, \lambda_t)}{m_t^2(p_1 - p_3)^2} [(p_1 \cdot q_{31})g^{\mu\sigma} - q_{31}^\mu p_1^\sigma] [p_2 \cdot q_{31}g^\nu{}_\sigma - q_{31}^\nu p_{2,\sigma}] \\
 &= -\frac{i\alpha_s^2}{(4\pi)^2} \frac{m_t^2}{v^2} Y_1 Y_2 \delta^{ab} \frac{16\mathcal{I}(\tau_1, \lambda_t)\mathcal{I}(\tau_2, \lambda_t)}{m_t^2(p_1 - p_3)^2} [(p_1 \cdot p_3)g^{\mu\sigma} - p_3^\mu p_1^\sigma] [(p_2 \cdot p_4)g^\nu{}_\sigma - p_4^\nu p_{2,\sigma}] \\
 &= -\frac{i\alpha_s^2}{(4\pi)^2} \frac{m_t^2}{v^2} Y_1 Y_2 \delta^{ab} \frac{16\mathcal{I}(\tau_1, \lambda_t)\mathcal{I}(\tau_2, \lambda_t)}{m_t^2(p_1 - p_3)^2} M^{\mu\nu}, \quad \text{with}
 \end{aligned} \tag{3.6}$$

$$M^{\mu\nu} = [(p_1 \cdot p_3)(p_2 \cdot p_4)g^{\mu\nu} - (p_2 \cdot p_4)p_3^\mu p_1^\nu - (p_1 \cdot p_3)p_4^\nu p_2^\mu + (p_1 \cdot p_2)p_4^\nu p_3^\mu],$$

where we exploited momentum conservation $p_1 + p_2 = p_3 + p_4$ to obtain a more compact expression.

Note that $\mathcal{I}(\tau_2, \lambda)$ is the function that contains the loop-integrals, and it is already finite: the projection of $\mathcal{M}_{1\text{-PR}}$ onto the Lorentz tensors can be performed in $d = 4$. The explicit expressions for the tensors have been shown in Eq. (2.85). Then, we have

$$P_j^{\mu\nu} = \frac{1}{2} T_j^{\mu\nu}. \tag{3.7}$$

The projection of $M_{\mu\nu}$ onto the tensor $T_1^{\mu\nu}$ yields

$$\begin{aligned}
 P_1^{\mu\nu} M_{\mu\nu} &= \frac{1}{2} [(p_1 \cdot p_3)(p_2 \cdot p_4) + (p_1 \cdot p_2)(p_3 \cdot p_4) - (p_1 \cdot p_4)(p_2 \cdot p_3)] \\
 &= -\frac{1}{2}(p_1 - p_3)^2(p_1 \cdot p_2),
 \end{aligned} \tag{3.8}$$

and, recalling the structure of the amplitude given in Eq. (3.3), the first form factor for the one-particle-reducible graphs is:

$$\tilde{\mathcal{A}}_{1,\text{IPR}}^{(1)} = -i [4\mathcal{I}(\tau_1, \lambda_t)\mathcal{I}(\tau_2, \lambda_t) + 4\mathcal{I}(\tau_1, \lambda_u)\mathcal{I}(\tau_2, \lambda_u)] \rho_s, \tag{3.9}$$

where we have taken into account the $\hat{t} \rightarrow \hat{u}$ crossed diagram as well.

The second projection of $M_{\mu\nu}$ gives us:

$$\begin{aligned}
 P_2^{\mu\nu} M_{\mu\nu} &= \frac{1}{2} [(p_1 \cdot p_3)(p_2 \cdot p_4) - (p_1 \cdot p_2)(p_3 \cdot p_4) + (p_1 \cdot p_4)(p_2 \cdot p_3)] \\
 &= -\frac{1}{2} p_T^2(p_1 \cdot p_2)
 \end{aligned} \tag{3.10}$$

and the second form factor is:

$$\tilde{\mathcal{A}}_{2,\text{IPR}}^{(1)} = -i \left[4\mathcal{I}(\tau_1, \lambda_t)\mathcal{I}(\tau_2, \lambda_t) \left(\frac{\rho_t \rho_u - \rho_1 \rho_2}{\rho_t} \right) + 4\mathcal{I}(\tau_1, \lambda_u)\mathcal{I}(\tau_2, \lambda_u) \left(\frac{\rho_t \rho_u - \rho_1 \rho_2}{\rho_u} \right) \right]. \tag{3.11}$$

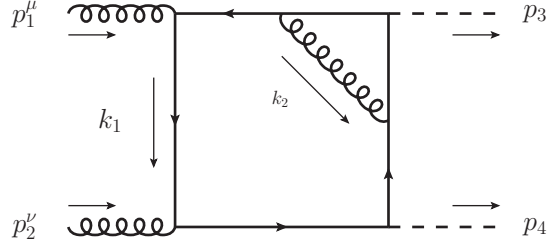
These form factors represent the total contribution of the one-particle-reducible diagrams, which is thus known analytically.

3.1.2 Two-loop box diagrams

The two-loop box diagrams represent the challenging part of this calculation. It involves two-loop diagrams with five scale parameters. Since a reduction strategy is prohibitive for such process, we will approach the calculation with the same spirit we have presented the LO amplitude. In order to show the calculation algorithm we have used, we present its application on two specific boxes.

Consider the Box 15 (Fig. 3.1). We fix the external momentum convention and a specific change of variables for the Feynman parameters suited on this particular diagram¹. Of course, Box 15

¹It is possible to extend this setup for the whole set of diagrams belonging to the same topology, by mixing the internal and external momentum approaches. We can fix a routing for the whole topology and modify the external momenta according to it.

Figure 3.1: *External momentum convention for Box 15.*

contributes both to $F_1^{(1)}$ and $F_2^{(1)}$, but the approach is unified for both projections. The explicit expression for the j -th form factor contribution of Box 15 is:

$$\begin{aligned}
 \tilde{\mathcal{A}}_{j,15} &= (i)^6(-i)I_{j,15} \\
 &= iI_{j,15}, \\
 I_{j,15} &= P_j^{\mu\nu} \int_{k_1, k_2} \frac{1}{k_2^2} \text{Tr}[\Delta_t(k_1)\gamma_\mu\Delta_t(k_1-p_1)\gamma^\sigma\Delta_t(k_1+k_2-p_1)\Delta_t(k_1+k_2-p_1+p_3) \times \\
 &\quad \times \gamma_\sigma\Delta_t(k_1-p_1+p_3)\Delta_t(k_1+p_2)\gamma_\nu], \\
 \Delta_t(q) &= \frac{(\not{q} + m_t)}{q^2 - m_t^2}
 \end{aligned} \tag{3.12}$$

From now on, we will call $I_{j,15}$ a form factor, since it differs from $\hat{\mathcal{A}}_{j,15}^{(1)}$ only by a constant term.

The $I_{j,15}$ has the usual structure of a Feynman integral, but this time we do not apply a reduction algorithm, since the complexity of the process with the full top-mass dependence makes the reduction a prohibitive task. At the state-of-the-art, the IBP reduction has been made possible by considering the Standard Model Higgs-pair production with fixed ratio between top and Higgs mass. Our aim is to keep the full- m_t dependence along the whole calculation. Hence, we follow a numerical strategy, applying the same procedure we have shown in Section (2.2.2).

After expanding the numerator of Eq. (3.12), it can be written as:

$$I_{j,15} = \int_{k_1, k_2} \frac{N_{j,15}(k_1, k_2)}{D_1 D_2 D_3 D_4 D_5 D_6 D_7} \tag{3.13}$$

where

$$\begin{aligned}
 D_1 &= k_1^2 - m_t^2, & D_5 &= (k_1 - p_1)^2 - m_t^2, \\
 D_2 &= (k_1 + k_2 - p_1 + p_3)^2 - m_t^2, & D_6 &= (k_1 + p_2)^2 - m_t^2, \\
 D_3 &= (k_1 + k_2 - p_1)^2 - m_t^2, & D_7 &= k_2^2. \\
 D_4 &= (k_1 - p_1 + p_3)^2 - m_t^2,
 \end{aligned} \tag{3.14}$$

The Feynman parametrization of $I_{j,15}^{\mu\nu}$ has to be applied on each subset of propagators depending

on k_1 and k_2 subsequently. The quantities involved in the Feynman parametrization are given by

$$I_{j,15} = \Gamma(6) \int_{k_2} \frac{1}{D_7} \int_0^1 d\mathbf{x}_5 \det[J(g_{15})] \int_{k_1} \frac{N_{j,15}(k_1 - q_{15,1}, k_2)}{(k_1^2 - q_{15,1}^2 - M_{15,1}^2)^6},$$

$$g_{15} : \mathcal{C} \rightarrow [0, 1]^5, \quad g_{15}(\mathbf{x}) = \begin{pmatrix} x_2(1-x_1) \\ (1-x_1)(1-x_2) \\ x_1(1-x_3)x_4 \\ x_1(1-x_3)(1-x_4) \\ x_1x_3x_5 \end{pmatrix}, \quad \det[J(g_{15})] = x_1^3(1-x_1)x_3(1-x_3),$$

$$q_{15,1} = (1-x_1)k_2 - (1-x_1x_3)p_1 + p_2x_1x_3x_5 + [(1-x_1)x_2 + x_1(1-x_3)x_4]p_3,$$

$$M_{15,1}^2 = m_t^2 + 2(1-x_1)(k_2 \cdot p_1) - 2(1-x_1)x_2(k_2 \cdot p_3) - k_2^2(1-x_1) +$$

$$- \hat{t}[(1-x_1)x_2 + x_1(1-x_3)x_4],$$

$$q_{15,1}^2 + M_{15,1}^2 = m_t^2 - k_2^2(1-x_1)x_1 + 2x_1(1-x_1)k_2 \cdot \{x_3p_1 - x_3x_5p_2 + [x_2 - (1-x_3)x_4]p_3\} -$$

$$- \hat{t}x_1x_3[(1-x_1)x_2 + x_1(1-x_3)x_4] - \hat{u}x_1x_3x_5[(1-x_1)x_2 + x_1(1-x_3)x_4] -$$

$$- sx_1x_3x_5(1-x_1x_3) - m_{H_1}^2[(1-x_1)x_2 + x_1(1-x_3)x_4][1 - (1-x_1)x_2 - x_1(1-x_3)x_4]. \quad (3.15)$$

The integration over k_1 involves rank-6 tensors, and the following identities are needed for factorizing the tensor structures of solely loop momenta:

$$\int_k \frac{k^\mu k^\nu (k^2)^\alpha}{k^2 - M^2} = \frac{g^{\mu\nu}}{d} \int_k \frac{(k^2)^{\alpha+1}}{k^2 - M^2}, \quad (3.16)$$

$$\int_k \frac{k^\mu k^\nu k^\rho k^\sigma (k^2)^\alpha}{k^2 - M^2} = \frac{g^{\mu\nu} g^{\rho\sigma} + g^{\mu\rho} g^{\nu\sigma} + g^{\mu\sigma} g^{\nu\rho}}{d(d+2)} \int_k \frac{(k^2)^{\alpha+2}}{k^2 - M^2}.$$

The general rank- α tadpole integral has the analytical solution written in Eq. (2.35), and it allows to express the integral in terms of a sum of its rank terms:

$$I_{j,15} = \sum_{\alpha=0}^3 (-1)^{(6-\alpha)} \frac{\Gamma(6-\alpha-\frac{d}{2})\Gamma(\alpha+\frac{d}{2})}{\Gamma(\frac{d}{2})} \int_0^1 d\mathbf{x}_5 \det[J(g_{15})] \int_{k_2} \frac{\tilde{B}_{j,15}^{(\alpha)}(k_2)}{(q_{15,1}^2 + M_{15,1}^2)^{6-\alpha-\frac{d}{2}} D_7} \quad (3.17)$$

The integral must be parametrized one additional time. Before applying the parametrization, the denominators have to be slightly rearranged, such that they assume the desired form:

$$q_{15,1}^2 + M_{15,1}^2 = -x_1(1-x_1)D_8. \quad (3.18)$$

Hence, the integral we are considering is

$$\int_{k_2} \frac{\tilde{B}_{j,15}^{(\alpha)}(k_2)}{D_7 D_8^{6-\alpha-\frac{d}{2}}} = \frac{\Gamma(7-\alpha-\frac{d}{2})}{\Gamma(6-\alpha-\frac{d}{2})} \int_0^1 dx_6 \int_{k_2} \frac{x_6^{5-\alpha-\frac{d}{2}} \tilde{B}_{j,15}^{(\alpha)}(k_2)}{(k_2^2 - q_{15,2}^2 - M_{15,2}^2)^{7-\alpha-\frac{d}{2}}}, \quad (3.19)$$

where

$$\begin{aligned}
g : \mathcal{C} &\rightarrow [0, 1], \quad g(x_6) = \mathbf{1}, \quad \det[J(g)] = 1, \\
q_{15,2} &= -x_6 \{p_1 x_3 + p_2 x_3 x_5 - p_3 [x_2 - (1 - x_3)x_4]\}, \\
M_{15,2}^2 &= \frac{x_6}{x_1(1-x_1)} \{m_t^2 - \hat{t} x_1 x_3 [(1-x_1)x_2 + x_1(1-x_3)x_4] - \hat{u} x_1 x_3 x_5 [(1-x_1)x_2 + x_1(1-x_3)x_4] - \\
&\quad - s x_1 x_3 x_5 (1-x_1 x_3) - m_{H_1}^2 [(1-x_1)x_2 + x_1(1-x_3)x_4] [1 - (1-x_1)x_2 - x_1(1-x_3)x_4]\}, \\
\tilde{\Delta}_{15} &= \frac{x_6}{x_1(1-x_1)} \left\{ 1 + \rho_s x_1 x_3 x_5 (1-x_1 x_3 - (1-x_1)x_3 x_6) - \right. \\
&\quad - x_1 x_3 \hat{\rho}_t [(1-x_1)x_2(1-x_6) + (1-x_3)x_4(x_1 + (1-x_1)x_6)] - \\
&\quad - x_1 x_3 x_5 \hat{\rho}_u [(1-x_1)x_2(1-x_6) + (1-x_3)x_4(x_1 + (1-x_1)x_6)] - \\
&\quad \left. - \rho_1 \{x_2(1-x_2) - x_1(1-2x_2)[x_2 - (1-x_3)x_5] - x_1[x_1 + (1-x_1)x_6][x_2 - (1-x_3)x_5]^2\} \right\}, \\
\tilde{\Delta}_{15} &= \frac{x_6}{x_1(1-x_1)} \Delta_{15}.
\end{aligned} \tag{3.20}$$

Finally, after the integration over the loop momentum k_2 , the integral $I_{j,15}$ gets the following form:

$$\begin{aligned}
I_{j,15} &= \sum_{\alpha, \beta=0}^3 (-1)^{(7-\alpha-\beta)} \frac{\Gamma(7-\alpha-\beta-d)\Gamma(\alpha+\frac{d}{2})\Gamma(\beta+\frac{d}{2})}{\Gamma(\frac{d}{2})\Gamma(\frac{d}{2})} \times \\
&\quad \times \int_0^1 d\mathbf{x}_6 \frac{[x_1(1-x_1)]^{1-\beta-\frac{d}{2}} \det[J(g_{15})] B_{j,15}^{(\alpha,\beta)}(\mathbf{x})}{x_6^{2-\beta-\frac{d}{2}} \Delta_{15}^{7-\alpha-\beta-d}} \\
&= \sum_{\alpha, \beta=0}^3 (-1)^{(7-\alpha-\beta)} \frac{\Gamma(3-\alpha-\beta+2\epsilon)\Gamma(\alpha+\frac{d}{2})\Gamma(\beta+\frac{d}{2})}{\Gamma(\frac{d}{2})\Gamma(\frac{d}{2})} \times \\
&\quad \times \int_0^1 d\mathbf{x}_6 \frac{x_3(1-x_3)x_6^{\beta-\epsilon} B_{j,15}^{(\alpha,\beta)}(\mathbf{x})}{x_1^{\beta-2-\epsilon}(1-x_1)^{\beta-\epsilon} \Delta_{15}^{3-\alpha-\beta+2\epsilon}}.
\end{aligned} \tag{3.21}$$

The Δ_{15} is always positive for $\mathbf{x} \in [0, 1]^6 \wedge \rho_i < 4$, hence below the top-mass threshold the tadpole-like mass term is well-defined. Moreover, no further divergences do arise from the numerator.

There is still the possibility that $I_{j,15}$ develops a singular behaviour on the boundaries of the integration region. Such terms are the source of the ultraviolet divergences. Since the aim is to arrive at an expression which can be integrated numerically, a particular treatment is needed to single them out.

3.1.3 Extracting the singularities

The singularities of the form factor under consideration come from an interplay between the integration over the Feynman parameters and the β -rank integrals. The highest possible rank for $I_{j,15}$ is 6, from which follows the constraint $\alpha + \beta \leq 3$.

Divergences arising from the integral come from the following terms:

$$I_{j,15}|_{\text{div}} \subset \int_0^1 dx_1 \frac{B_{j,15}^{(\alpha,\beta)}(x_1)}{x_1^{\beta-2-\epsilon}(1-x_1)^{\beta-\epsilon}} \quad \text{for some } \beta. \tag{3.22}$$

The numerator $B_{j,15}^{(\alpha,\beta)}(x_1)$ has a polynomial dependence on x_1 that may influence the divergency, so it must be taken into account. Hence, $I_{j,15}$ diverges in $x_1 = 0$ for $\beta = 3$ and in $x_1 = 1$ for $\beta \geq 1$.

An additional constraint on diverging β -rank tensors can be set by taking into account the numerator. Purely k_2 tensor integrals have at most $\beta \leq 1$: higher β -rank tensor integrals comes from the shift of the first loop momenta $k_1 \rightarrow k_1 - q_{15,1}$. Each shift introduces a $(1-x_1)$ on the numerator,

which cancels against the denominator $(1 - x_1)^{\beta - \epsilon}$. This fact implies that the divergences have the following form:

$$I_{j,15}|_{\text{div}} \subset \left\{ \int_0^1 dx_1 \frac{f(x_1)}{x_1^{1-\epsilon}}, \int_0^1 dx_1 \frac{f(x_1)}{(1-x_1)^{1-\epsilon}} \right\}. \quad (3.23)$$

and it also ensures that there can not be simultaneous divergences in both the integration boundaries.

The idea for extracting the singular behaviour of the integrals is the so-called *end-point subtraction*: manipulating the numerator, it can be arranged such that it converges faster than the denominator on the boundaries. The strategy is to add a clever zero in the numerator:

$$\begin{aligned} \int_0^1 dx_1 \frac{f(x_1)}{x_1^{1-\epsilon}} &= \int_0^1 dx_1 \frac{f(0)}{x_1^{1-\epsilon}} + \int_0^1 dx_1 \frac{f(x_1) - f(0)}{x_1^{1-\epsilon}} \\ &= \frac{f(0)}{\epsilon} + \int_0^1 dx_1 \frac{f(x_1) - f(0)}{x_1^{1-\epsilon}} \\ \int_0^1 dx_1 \frac{f(x_1)}{(1-x_1)^{1-\epsilon}} &= \frac{f(1)}{\epsilon} + \int_0^1 dx_1 \frac{f(x_1) - f(1)}{x_1^{1-\epsilon}} \end{aligned} \quad (3.24)$$

The convergence is facilitated by noticing that $f(x_1) - f(0)$ is the Taylor series of $f(x_1)$ starting from the second term, proportional to x_1 .

An additional source of ultraviolet singularities comes from the Gamma function which multiplies Eq. (3.21) when $\alpha + \beta = 3$:

$$\Gamma(2\epsilon) = \frac{1}{2} \frac{\Gamma(1+2\epsilon)}{\epsilon}. \quad (3.25)$$

This is a completely independent behaviour, which can happen simultaneously to the poles coming from the integrals $I_{j,15}|_{\text{div}}$. Therefore, $I_{j,15}$ develops second order poles in ϵ , that have to cancel against the real corrections. For later purposes, notice that

$$\Gamma(1+2\epsilon) = \frac{\Gamma(1+\epsilon)\Gamma(1-\epsilon)}{\Gamma(1-2\epsilon)} + O(\epsilon^2). \quad (3.26)$$

Once that every ultraviolet divergence has been singled out, the form factor $I_{j,15}$ can be ϵ -expanded and its coefficient will be suitable for a numerical integration.

For the kinematic regions above the top-pair production threshold ($\rho_i > 4$), threshold singularities enter the game. These kinds of divergences can be prevented by introducing an imaginary mass regulator to the top-mass, which acts as a parameter for the analytical continuation of the form factor:

$$m_t^2 \rightarrow m_t^2(1 - i\epsilon_t). \quad (3.27)$$

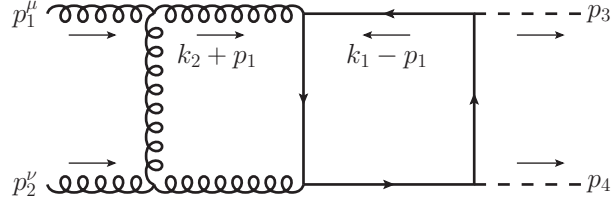
For small values of ϵ_t , the dependence of the form factor on ϵ_t is completely negligible, and it ensures the finiteness of its real (and imaginary) part. But, as we can expect, the numerical stability gets lower when ϵ_t decreases. To avoid integrations with high statistic, integration-by-parts represents an useful tool to decrease the power of the denominator, at the price of increasing the number of integrands. A single integral with $\alpha = \beta = 0$ occurring in the form factor can be written as:

$$I_{j,15}^{(n)} = -2 \int_0^1 d\mathbf{x}_6 \frac{x_1^2 x_3 (1-x_3) B_{j,15}^{(0,0),(n)}(\mathbf{x})}{\Delta_{15}^3}. \quad (3.28)$$

Focusing on a single parameter, Δ_{15} has at most a quadratic dependence on a Feynman parameter and a linear dependence on x_5 and x_6 . Integration by parts on such parameter yields:

$$I_{j,15}^{(n)} \propto \int_0^1 dx_5 \frac{f(x_5)}{(ax_5 + b)^3} = \frac{f(0)}{2ab^2} - \frac{f(1)}{2a(a+b)^2} + \frac{1}{2a} \int_0^1 dx_5 \frac{f'(x_5)}{(ax_5 + b)^2}. \quad (3.29)$$

Therefore, when a denominator of an integrand is linearly dependent on a Feynman parameter, it is convenient to apply integration-by-parts such that the power of the denominator decreases. The numerical stability will be significantly increased.

Figure 3.2: *External momentum convention for Box 45.*

3.1.4 Infrared divergences

Infrared divergences come from a particular set of diagrams, belonging to topology 6. They are characterized by the rescattering of a virtual gluon emitted and reabsorbed by the initial state gluons (Fig. 3.2). The explicit expression for the j -th form factor is

$$\begin{aligned}\tilde{\mathcal{A}}_{j,45} &= - \left(-\frac{3}{2} \delta^{ab} \right) (i)^4 (-i)^3 \left(-i \frac{m_t}{v} \right)^2 Y_1 Y_2 I_{j,45} \\ &= -i \frac{3}{2} \frac{m_t^2}{v^2} \delta^{ab} Y_1 Y_2 I_{j,45},\end{aligned}$$

$$\begin{aligned}I_{j,45} &= P_j^{\mu\nu} \int_{k_1, k_2} \frac{\lambda_3^{\mu\eta}(p_1, -k_2 - p_1, k_2) \lambda_3^{\nu\sigma}(p_2, -k_2, k_2 - p_2)}{k_2^2 (k_2 + p_1)^2 (k_2 - p_2)^2} \times \\ &\quad \times \text{Tr} [\gamma_\rho \Delta_t(k_1 - p_1) \Delta_t(k_1 - p_1 + p_3) \Delta_t(k_1 + p_2) \gamma_\sigma \Delta_t(k_1 + k_2)],\end{aligned}\quad (3.30)$$

$$\lambda_3^{\mu_1 \mu_2 \mu_3}(p_1, p_2, p_3) = g^{\mu_1 \mu_2} (p_1 - p_2)^{\mu_3} + g^{\mu_2 \mu_3} (p_2 - p_3)^{\mu_1} + g^{\mu_1 \mu_3} (p_3 - p_1)^{\mu_2}$$

Expanding the form factor, it assumes the usual structure of a Feynman integral:

$$I_{j,45} = \int_{k_1, k_2} \frac{N_{j,45}(k_1, k_2)}{D_1 D_2 D_3 D_4 D_5 D_6 D_7} \quad (3.31)$$

where

$$\begin{aligned}D_1 &= (k_1 - p_1)^2 - m_t^2, & D_5 &= k_2^2, \\ D_2 &= (k_1 - p_2)^2 - m_t^2, & D_6 &= (k_2 + p_1)^2, \\ D_3 &= (k_1 - p_1 + p_3)^2 - m_t^2, & D_7 &= (k_2 - p_2)^2. \\ D_4 &= (k_1 + k_2)^2 - m_t^2,\end{aligned}\quad (3.32)$$

Below, we summarize the quantities coming from the Feynman parametrization of $I_{j,45}$:

First integration

$$g_{45,1} : \mathcal{C} \rightarrow [0, 1]^3, \quad g_{45,1}(\mathbf{x}) = \begin{pmatrix} (1 - x_1) \\ x_1(1 - x_2) \\ x_1 x_2 x_3 \end{pmatrix}, \quad \det[J(g_{45,1})] = x_1^2 x_2,$$

$$\begin{aligned}q_{45,1} &= (1 - x_1)k_2 - x_1 x_2 p_1 + x_1(1 - x_2)p_2 + x_1 x_2 x_3 p_3, \\ M_{45,1}^2 &= m_t^2 - (1 - x_1)k_2^2 - x_1 x_2 x_3 t,\end{aligned}\quad (3.33)$$

$$\begin{aligned}q_{45,1}^2 + M_{45,1}^2 &= m_t^2 - x_1(1 - x_1)k_2^2 - 2x_1(1 - x_1)k_2 \cdot \{x_2 p_1 - (1 - x_2)p_2 - x_2 x_3 p_3\} - s x_1^2 x_2(1 - x_2) - \\ &\quad - \hat{t} x_1 x_2 x_3(1 - x_1 x_2) - \hat{u} x_1^2 x_2 x_3(1 - x_2) - m_{H_1}^2 x_1 x_2 x_3(1 - x_1 x_2 x_3) \\ q_{45,1}^2 + M_{45,1}^2 &= -x_1(1 - x_1),\end{aligned}$$

hence

$$I_{j,45} = \sum_{\alpha=0}^3 (-1)^{\frac{d}{2}} \frac{\Gamma(4 - \alpha - \frac{d}{2}) \Gamma(\alpha + \frac{d}{2})}{\Gamma(\frac{d}{2})} \int_0^1 d\mathbf{x}_3 \frac{\det[J(g_{45,1})]}{[x_1(1 - x_1)]^{4 - \alpha - \frac{d}{2}}} \int_{k_2} \frac{\tilde{B}_{j,45}^{(\alpha)}(k_2)}{D_5 D_8^{4 - \alpha - \frac{d}{2}} D_6 D_7}. \quad (3.34)$$

Second integration

$$g_{45,2} : \mathcal{C} \rightarrow [0, 1]^3, \quad g_{45,1}(\mathbf{x}) = \begin{pmatrix} x_4 x_5 \\ 1 - x_5 \\ (1 - x_4) x_5 x_6 \end{pmatrix}, \quad \det[J(g_{45,2})] = (1 - x_4) x_5^2,$$

$$q_{45,2} = (1 - x_5 + x_2 x_4 x_5) p_1 - [x_4 x_5 (1 - x_2) + (1 - x_4) x_5 x_6] p_2 + x_2 x_3 x_4 x_5 p_3,$$

$$M_{45,2}^2 = \frac{x_4 x_5 m_t^2}{x_1 (1 - x_1)} - s \frac{x_1 x_2 x_4 x_5 (1 - x_2)}{(1 - x_1)} - \hat{t} \frac{x_2 x_3 x_4 x_5 (1 - x_1 x_2)}{(1 - x_1)} - \hat{u} \frac{x_1 x_2 x_3 x_4 x_5 (1 - x_2)}{(1 - x_1)} - m_{H_1}^2 \frac{x_2 x_3 x_4 x_5 (1 - x_1 x_2 x_3)}{(1 - x_1)},$$

$$\begin{aligned} \tilde{\Delta}_{45} = \frac{x_5}{x_1 (1 - x_1)} & \left\{ x_4 - x_1 [x_1 x_2 x_4 (1 - x_2) + (1 - x_1) (1 - x_5 + x_2 x_4 x_5) \{x_6 (1 - x_4) + x_4 (1 - x_2)\}] \rho_s - \right. \\ & - x_1 x_2 x_3 x_4 [1 - x_1 x_2 - (1 - x_1) (1 - x_5 + x_2 x_4 x_5)] \hat{\rho}_t - \\ & - x_1 x_2 x_3 x_4 [x_1 (1 - x_2) + (1 - x_1) x_5 \{(1 - x_4) x_6 + x_4 (1 - x_2)\}] \hat{\rho}_u \\ & \left. - x_1 x_2 x_3 x_4 [1 - x_1 x_2 x_3 - (1 - x_1) x_2 x_3 x_4 x_5] \rho_1 \right\}, \end{aligned}$$

$$\tilde{\Delta}_{45} = \frac{x_5}{x_1 (1 - x_1)} \Delta_{45},$$

(3.35)

hence

$$\begin{aligned} I_{j,45} = \sum_{\alpha, \beta=0}^2 (-1)^{7-\alpha-\beta} \frac{\Gamma(3-\alpha-\beta+2\epsilon) \Gamma(\alpha+\frac{d}{2}) \Gamma(\beta+\frac{d}{2})}{\Gamma(\frac{d}{2}) \Gamma(\frac{d}{2})} \times \\ \times \int_0^1 d\mathbf{x}_6 \left[x_1^{3-\beta+\epsilon} (1-x_1)^{1-\beta+\epsilon} x_2 (1-x_4) x_4^{1-\alpha+\epsilon} x_5^{\beta-\epsilon} \right] \frac{B_{j,45}^{(\alpha, \beta)}(\mathbf{x})}{\Delta_{45}^{3-\alpha-\beta+2\epsilon}}. \end{aligned}$$

(3.36)

Even if it can develop UV divergences, their treatment is completely analogous to how it has been presented before. Hence, in order to focus on the analysis of the IR divergences, we set $\alpha = 0$, $\beta = 0$ and factorize the x_4 from $B_{j,45}^{(0,0)}(\mathbf{x})$:

$$I_{j,45} \propto \int_0^1 dx_4 \frac{(1-x_4) x_4^{1+\eta+\epsilon} B_{j,45}^{(0,0)}(\hat{\mathbf{x}}_4, x_4)}{(ax_4^2 + bx_4 + c)^{3+2\epsilon}}.$$

(3.37)

where the new index η has been introduced to take into account a potential x_4 factor coming from the numerator. Moreover, the quadratic dependence on x_4 has been made explicit. Its roots for $c \neq 0$ fall outside the integration domain, so we focus on the case where $x_4 = 0$ and $c = 0$. At last, $\hat{\mathbf{x}}_4$ is the set of Feynman parameters with x_4 excluded.

The quadratic formula can be rewritten as

$$\begin{aligned} \Delta_{45} = ax_4^2 + bx_4 + c & = c(1+r_-x_4)(1+r_+x_4) \\ r_{\pm} = \frac{b}{2c} & \left[1 \pm \sqrt{1 - \frac{4ac}{b^2}} \right], \end{aligned}$$

(3.38)

where a, b, c are generic coefficients of a polynomial of the second degree in x_4 . In the limit of $c \rightarrow 0$:

$$\begin{aligned} r_+(c) \sim_0 \frac{b}{c} \left(1 + \frac{ac}{b^2} \right) \sim_0 \frac{b}{c} & \implies \lim_{c \rightarrow 0} r_+ = \infty, \\ r_-(c) \sim_0 \frac{b}{c} \left(\frac{ac}{b^2} \right) \sim_0 \frac{a}{b} & \implies \lim_{c \rightarrow 0} r_- = \frac{a}{b}. \end{aligned}$$

(3.39)

The behaviour of Δ_{45} in the limit of $x_4, c \rightarrow 0$ is exactly what we can expect from the heavy-top limit of this amplitude. The reason behind this lies in the *universality of the infrared singular structure*. From the heavy-top limit of the form factor, it is known that only the coefficients b and c give contribution to

the IR structure. Therefore, by subtracting the limit, we have found for Δ_{45} is equivalent to subtract the heavy-top limit form factor from it.

The explicit subtraction yields:

$$I_{j,45} \propto \int_0^1 dx_4 (1-x_4)x_4^{1+\eta+\epsilon} \left[\frac{B_{j,45}^{(0,0)}(\hat{\mathbf{x}}_4, x_4)}{(ax_4^2 + bx_4 + c)^{3+2\epsilon}} - \frac{B_{j,45}^{(0,0)}(\hat{\mathbf{x}}_4, 0)}{[c(1 + \frac{b}{c}x_4)]^{3+2\epsilon}} \right] + \frac{B_{j,45}^{(0,0)}(\hat{\mathbf{x}}_4, 0)}{c^{3+2\epsilon}} \int_0^1 dx_4 x_4^{1+\eta+\epsilon} (1-x_4) \left(1 + \frac{b}{c}x_4\right)^{-3-2\epsilon}. \quad (3.40)$$

The latter integral can be integrated analytically, involving the integral representation of the hypergeometric function

$${}_2F_1(a, b; c; z) = \frac{\Gamma(c)}{\Gamma(b)\Gamma(c-b)} \int_0^1 dt t^{b-1} (1-t)^{c-b-1} (1-zt)^{-a}. \quad (3.41)$$

Therefore:

$$\int_0^1 dx_4 x_4^{1+\eta+\epsilon} (1-x_4) \left(1 + \frac{b}{c}x_4\right)^{-3-2\epsilon} = \frac{\Gamma(2+\eta+\epsilon)}{\Gamma(3+\eta+\epsilon)} {}_2F_1\left(3+2\epsilon, 2+\eta+\epsilon; 3+\eta+\epsilon; -\frac{b}{c}\right). \quad (3.42)$$

By exploiting the properties of the hypergeometric functions, the divergence can be factorized from ${}_2F_1$:

$$\begin{aligned} {}_2F_1(a, b; c; z) &= \frac{\Gamma(c)\Gamma(b-a)}{\Gamma(b)\Gamma(c-a)} (-z)^{-a} {}_2F_1(a, 1-c+a; 1-b+a; z^{-1}) \\ &\quad + \frac{\Gamma(c)\Gamma(a-b)}{\Gamma(a)\Gamma(c-b)} (-z)^{-b} {}_2F_1(b, 1-c+b; 1-a+b; z^{-1}) \\ &\quad \downarrow \\ \frac{\Gamma(2+\eta+\epsilon)}{\Gamma(3+\eta+\epsilon)} {}_2F_1\left(3+2\epsilon, 2+\eta+\epsilon; 3+\eta+\epsilon; -\frac{b}{c}\right) &= \\ &= \frac{\Gamma(-1+\eta-\epsilon)}{\Gamma(\eta-\epsilon)} \left(\frac{c}{b}\right)^{3+2\epsilon} {}_2F_1\left(3+2\epsilon, 1-\eta+\epsilon; 2-\eta+\epsilon; -\frac{c}{b}\right) \\ &\quad + \frac{\Gamma(2+\eta+\epsilon)\Gamma(1-\eta+\epsilon)}{\Gamma(3+2\epsilon)} \left(\frac{c}{b}\right)^{2+\eta+\epsilon} {}_2F_1\left(2+\eta+\epsilon, 0; \eta-\epsilon; -\frac{c}{b}\right) \\ &= \frac{\Gamma(\eta-1-\epsilon)}{\Gamma(\eta-\epsilon)} \left(\frac{c}{b}\right)^{3+2\epsilon} {}_2F_1\left(3+2\epsilon, 1-\eta+\epsilon; 2-\eta+\epsilon; -\frac{c}{b}\right) \\ &\quad + \frac{\Gamma(2+\eta+\epsilon)\Gamma(1-\eta+\epsilon)}{\Gamma(3+2\epsilon)} \left(\frac{c}{b}\right)^{2+\eta+\epsilon} \end{aligned} \quad (3.43)$$

where ${}_2F_1(a, 0; c; z) = 1$. The latter expression is suitable for an analysis of the pole structure. Plugging Eq. (3.43) in Eq. (3.40):

$$I_{j,45}|_{\text{poles}} \propto B_{j,45}^{(0,0)}(\hat{\mathbf{x}}_4, 0) \left\{ \frac{\Gamma(\eta-1-\epsilon)}{\Gamma(\eta-\epsilon)} \frac{{}_2F_1\left(3+2\epsilon, 1-\eta+\epsilon; 2-\eta+\epsilon; -\frac{c}{b}\right)}{b^{3+2\epsilon}} + \frac{\Gamma(2+\eta+\epsilon)\Gamma(1-\eta+\epsilon)}{\Gamma(3+2\epsilon)} \left(\frac{1}{b^{2+\eta+\epsilon}c^{1-\eta+\epsilon}}\right) \right\}. \quad (3.44)$$

While the hypergeometric and Gamma functions in Eq. (3.44) are regular for every other η , the singular behaviour of the form factor shows up for $\eta = 0$ and $\eta = 1$. The latter case is a pole generated by a gamma function, for which no subtraction is needed. The $\eta = 0$ divergence originates from the term $c^{-1-\epsilon}$, for which an end-point subtraction is needed. For this, we need the explicit expression of c , which is

$$c = -\rho_s x_1 (1-x_1)(1-x_5)x_6. \quad (3.45)$$

The divergent part of $\alpha = \beta = 0$ added of the form factor $I_{j,45}$ is:

$$I_{j,45}|_{\text{poles}} \subset (-1)^{-\epsilon} \Gamma(2+\epsilon)\Gamma(1+\epsilon) \int_0^1 d\hat{\mathbf{x}}_4 \left(\frac{x_1^2 x_2 x_5^{-\epsilon} \rho_s^{-1-\epsilon}}{(1-x_5)^{1+\epsilon} x_6^{1+\epsilon}} \right) \frac{B_{j,45}^{(0,0)}(\hat{\mathbf{x}}_4, 0)}{b^{2+\epsilon}}, \quad (3.46)$$

which develops poles for $x_5 = 1$ and $x_6 = 0$. Since these two divergent behaviours can happen simultaneously, a proper subtraction term is needed:

$$\int_0^1 dx_5 dx_6 \frac{f(x_5, x_6)}{(1-x_5)^{1+\epsilon} x_6^{1+\epsilon}} = \int_0^1 dx_5 dx_6 \frac{f(x_5, x_6) - f(1, x_6) - f(x_5, 0) + f(1, 0)}{(1-x_5)^{1+\epsilon} x_6^{1+\epsilon}} + \frac{f(1, 0)}{\epsilon^2} - \frac{1}{\epsilon} \left[\int_0^1 dx_6 \frac{f(1, x_6) - f(1, 0)}{x_6^{1+\epsilon}} + \int_0^1 dx_5 \frac{f(x_5, 0) - f(1, 0)}{(1-x_5)^{1+\epsilon}} \right]. \quad (3.47)$$

Therefore, Box 45 can have ϵ^{-2} and ϵ^{-1} poles. It can be shown that an additional pole can arise from the remaining dependence on x_1 , x_2 or x_3 , but it is properly canceled after summing all the diagrams belonging to topology 6.

Finally, after the end-point subtraction of all the divergences arising from the loop integrals, the finite part is numerically integrable. However, the presence of a threshold at $\sqrt{\hat{s}} = 0$ GeV makes the integration-by-parts technique an essential requirement to achieve a stable numerical integration.

3.2 Renormalization

The NLO form factors have a divergent behaviour for the physical limit $\epsilon \rightarrow 0$. From the previous section we know that both ultraviolet and infrared divergence appear in the amplitude, leading to a definite pole structure that we have singled out explicitly.

Infrared divergences cancel against the real corrections. Ultraviolet divergences have to be renormalized by choosing a renormalization scale and scheme and adding the proper counterterms. Different choices of renormalization would not affect the physically relevant quantities if we were able to perform the calculation at every order of the perturbative expansion. Since we truncate the series at NLO, we end up with a renormalization-dependent result. The variation of the renormalization scales and schemes is useful to estimate the theoretical uncertainties arising from the truncation of the perturbative series expansion.

Every parameter involved in this calculation possesses a running with respect to the energy of the process. These quantities are the strong coupling constant $\alpha_s = \alpha_s(\mu_R)$ and the top-quark mass $m_t = m_t(\mu_R)$.

In the whole calculation, we have considered these parameters as bare quantities ($\alpha_{s,0}$ and $m_{t,0}$), which lead to the usual divergent behaviour of higher order contributions. A UV finite result can be achieved by considering the renormalized quantities:

$$\begin{aligned} m_{t,0} &= m_t - \delta m_t + O(\delta m_t^2) \\ \alpha_{s,0} &= \alpha_s + \delta \alpha_s + O(\delta \alpha_s^2). \end{aligned} \quad (3.48)$$

The counterterms δm_t and $\delta \alpha_s$ have a scheme and a scale dependence. All the renormalization schemes are designed to cancel the UV poles coming from the NLO amplitude against the counterterms. Different scheme choices will only lead to different finite parts.

We start by considering the *on-shell (OS) renormalization scheme* for δm_t : the quark propagator can be written as

$$iG_{2,0}(\not{p}) = \frac{i}{\not{p} - m_{t,0} - \Sigma_2(\not{p})} = iZ_2 G_{2,R}(\not{p}). \quad (3.49)$$

The term $\Sigma_2(\not{p})$ contains all the one-loop contributions to the quark propagator. We also have explicitly shown the relation between the bare and renormalized propagator.

Expanding the renormalization constant up to the first order:

$$\begin{aligned} iG_{2,R}(\not{p}) &= \frac{i}{\not{p} - m_{t,0} - \Sigma_2(\not{p}) + \delta_2 \not{p} - \delta_2 m_{t,0}} \\ &= \frac{i}{\not{p} - m_t + \delta m_t - \Sigma_2(\not{p}) + \delta_2 \not{p} - \delta_2 m_t} \\ &= \frac{i}{\not{p} - m_t - \Sigma_R(\not{p})}. \end{aligned} \quad (3.50)$$

The on-shell condition for the top mass is translated into the two following conditions:

$$\Sigma_R(m_t) = 0, \quad \left. \frac{\partial}{\partial \not{p}} \Sigma_R(\not{p}) \right|_{\not{p}=m_t} = 0 \quad (3.51)$$

which fix the conditions on δm_t and δ_2 . Since we are only interested in the mass counterterm, its explicit expression in the OS scheme is

$$\frac{\delta m_t}{m_t} = \frac{\alpha_s}{(4\pi)} \Gamma(1 + \epsilon) \left(\frac{4\pi\mu^2}{m_t^2} \right)^\epsilon \left(\frac{1}{\epsilon} + \frac{4}{3} \right), \quad (3.52)$$

which has a non-vanishing finite part. Alternatively, the $\overline{\text{MS}}$ counterterm has the following explicit expression

$$\frac{\delta \overline{m}_t}{\overline{m}_t(\mu_t)} = \frac{\alpha_s}{(4\pi)} \Gamma(1 + \epsilon) \left(\frac{4\pi\mu^2}{\mu_t^2} \right)^\epsilon \frac{1}{\epsilon}. \quad (3.53)$$

where μ_t denotes the scale of the running top-quark mass.

For the α_s counterterm we will use the $\overline{\text{MS}}$ scheme. It is designed to cancel only the poles and universal finite constants. The expression for the five active massless flavour QCD is ($N_f = 5$):

$$\frac{\delta \alpha_s}{\alpha_s} = \frac{\alpha_s}{(4\pi)} \left(\frac{4\pi\mu^2}{\mu_R^2} \right)^\epsilon \Gamma(1 + \epsilon) \left[-\frac{11C_A - 2N_f}{3\epsilon} \right]. \quad (3.54)$$

Since we have to add the divergences due to the top-quark involved in the calculation, the $\overline{\text{MS}}$ scheme is modified by adding the missing pole:

$$\frac{\delta \alpha_s}{\alpha_s} = \frac{\alpha_s}{(4\pi)} \left(\frac{4\pi\mu^2}{\mu_R^2} \right)^\epsilon \Gamma(1 + \epsilon) \left[-\frac{11C_A - 2(N_f + 1)}{3\epsilon} \right]. \quad (3.55)$$

The $\overline{\text{MS}}$ scheme is mass-independent scheme. The remaining top-mass dependent term depends logarithmically on μ_R , namely it is proportional to $\log \frac{m_t^2}{\mu_R^2}$. The presence of such terms might break the perturbative expansion, since these logarithms can be large depending on the energy region. The way to avoid such terms is to *decouple the top-quark from the running of α_s* . This procedure leads to the following counterterm:

$$\frac{\delta \alpha_s}{\alpha_s} = \frac{\alpha_s}{(4\pi)} \left(\frac{4\pi\mu^2}{\mu_R^2} \right)^\epsilon \Gamma(1 + \epsilon) \left[-\left(\frac{11C_A - 2(N_f + 1)}{3} \right) \frac{1}{\epsilon} + \frac{2}{3} \log \left(\frac{\mu_R^2}{m_t^2} \right) \right]. \quad (3.56)$$

where the finite term tames the logarithmic behaviour introduced by the $\overline{\text{MS}}$ scheme.

Since we have considered the input parameters of the calculation to be "bare", we have to express the form factors in terms of the running parameters:

$$\begin{aligned} F_j(\alpha_{s,0}, m_{t,0}) &= F_j^{(0)}(\alpha_s + \delta\alpha_s, m_t - \delta m_t) + F_j^{(1)}(\alpha_s, m_t) \\ &\simeq F_j^{(0)}(\alpha_s, m_t) + \delta\alpha_s \frac{\partial F_j^{(0)}}{\partial \alpha_s}(\alpha_s, m_t) - \delta m_t \frac{\partial F_j^{(0)}}{\partial m_t}(\alpha_s, m_t) + F_j^{(1)}(\alpha_s, m_t) \\ &= F_j^{(0)}(\alpha_s, m_t) + \frac{\delta\alpha_s}{\alpha_s} F_j^{(0)}(\alpha_s, m_t) - 2 \frac{\delta m_t}{m_t} m_t^2 \frac{\partial F_j^{(0)}}{\partial m_t^2}(\alpha_s, m_t) + F_j^{(1)}(\alpha_s, m_t) \\ &= F_j^{(0)}(\alpha_s, m_t) + F_j^{(CT,1)}(\alpha_s, m_t) + F_j^{(1)}(\alpha_s, m_t) \\ &= F_j^{(0)}(\alpha_s, m_t) + \overline{F}_j^{(1)}(\alpha_s, m_t) \end{aligned} \quad (3.57)$$

where the linearity of $F_j^{(0)}(\alpha_s)$ with respect to α_s has been exploited. The terms proportional to $\delta\alpha_s$ and δm_t contribute to the NLO form factors, and they correspond exactly to the UV counterterms that cancel the UV divergences of the NLO form factor shown in the previous section.

The $\delta\alpha_s$ counterterm has been prepared to cancel the divergences that appear as external vacuum polarization diagrams. This contribution can be found by considering the massive vacuum polarization diagram (Appendix G) in the on-shell limit. It provides the following contribution

$$\Pi_{m_t}(0)F_j^{(0)}(\alpha_s) = -\frac{\alpha_s}{(4\pi)} \left(\frac{4\pi\mu^2}{m_t^2}\right)^\epsilon \Gamma(1+\epsilon) \frac{2}{3} \frac{1}{\epsilon} F_j, \quad (3.58)$$

and calling $\delta\alpha_s = \Pi_{m_t}(0) + \frac{\delta\alpha_s}{\alpha_s}$, the complete counterterm plus external self-energy contribution for α_s is

$$\begin{aligned} \delta\alpha_s F_j^{(0)}(\alpha_s, m_t) &= -\frac{\alpha_s}{(4\pi)} \left(\frac{4\pi\mu^2}{\mu_R^2}\right)^\epsilon \Gamma(1+\epsilon) \left(\frac{11C_A - 2N_f}{3}\right) \frac{1}{\epsilon} F_j^{(0)}(\alpha_s, m_t) \\ &\quad \downarrow \\ \delta\alpha_s F_j^{(0)}(\alpha_s, m_t) &= \frac{i\alpha_s^2}{(4\pi)^2} \frac{m_t^2}{v^2} \left(\frac{4\pi\mu^2}{m_t^2}\right)^{2\epsilon} \Gamma^2(1+\epsilon) \left(\frac{11C_A - 2N_f}{3}\right) \left[\frac{1}{\epsilon} - \log\left(\frac{\mu_R^2}{m_t^2}\right)\right] \mathcal{A}_j. \end{aligned} \quad (3.59)$$

Moving the discussion to the top-mass counterterm, we set

$$\delta_{m_t} F_j^{(0)}(\alpha_s, m_t) = -2 \frac{\delta m_t}{m_t} m_t^2 \frac{\partial F_j^{(0)}}{\partial m_t^2}(\alpha_s, m_t). \quad (3.60)$$

Therefore:

$$\delta_{m_t} F_j^{(0)}(\alpha_s, m_t) = 2 \frac{i\alpha_s^2}{(4\pi)^2} \frac{m_t^2}{v^2} Y_1 Y_2 \Gamma^2(1+\epsilon) \left(\frac{4\pi\mu^2}{m_t^2}\right)^{2\epsilon} \left(\frac{1}{\epsilon} + \frac{4}{3}\right) \left[(1-\epsilon)\mathcal{A}_j + \frac{\partial \mathcal{A}_j}{\partial m_t^2}\right], \quad (3.61)$$

and

$$F_j^{(CT,1)}(\alpha_s, m_t) = \delta\alpha_s F_j^{(0)}(\alpha_s, m_t) + \delta_{m_t} F_j^{(0)}(\alpha_s, m_t). \quad (3.62)$$

Notice that the form factor of the $\overline{\text{MS}}$ counterterm is the same, but without the factor $4/3$ coming from the OS part.

Since we know the heavy-top limit behaviour of the form factors at NLO, we can exploit the universality of the infrared structure to build a term containing the infrared singularities. The NLO form factor in the heavy-top limit can be written as,

$$F_{\text{HTL},j}^{(1)}(\alpha_s) = \frac{\alpha_s}{(4\pi)} \frac{\Gamma(1-\epsilon)}{\Gamma(1-2\epsilon)} \left(\frac{4\pi\mu^2}{-\hat{s}}\right)^\epsilon \left[\frac{6}{\epsilon^2} + \frac{11C_A - 2N_f}{3\epsilon} \left(\frac{\mu^2}{-\hat{s}}\right)^{-\epsilon} - 11 + \pi^2 \right] F_j^{(0)}(\alpha_s), \quad (3.63)$$

and summing it with the α_s counterterm, we get

$$\begin{aligned} \delta_{\text{IR}} F_j(\alpha_s, m_t) &= -\frac{i\alpha_s^2}{(4\pi)^2} \frac{m_t^2}{v^2} Y_1 Y_2 \frac{\Gamma(1-\epsilon)\Gamma(1+\epsilon)}{\Gamma(1-2\epsilon)} \left(\frac{4\pi\mu^2}{-\hat{s}}\right)^{2\epsilon} \times \\ &\quad \times \left[\frac{12}{\epsilon^2} - \frac{6}{\epsilon} \log\left(\frac{-\hat{s}}{m_t^2}\right) + 3 \log^2\left(\frac{-\hat{s}}{m_t^2}\right) - 22 + 2\pi^2 \right] \mathcal{A}_j^{(0)}, \end{aligned} \quad (3.64)$$

where we used the following replacement:

$$\Gamma^2(1+\epsilon) \rightarrow \frac{\Gamma(1-\epsilon)\Gamma(1+\epsilon)}{\Gamma(1-2\epsilon)}. \quad (3.65)$$

This term encodes the infrared behaviour that is common both for the HTL form factor and the full m_t dependent one.

This last term, once added to the virtual form factor $F_j^{(1)}$, will lead to a finite result which can be integrated without numerical issues, like instability or diverging behaviour.

3.3 Virtual cross-section

The form factors of the partonic process $gg \rightarrow H_1 H_2$ at NLO QCD get contributions from the box diagrams, one-particle-reducible diagrams and triangle diagrams. Each diagram has been processed

by the calculation strategy presented in the previous section, and the form factors $F_j^{(1)}$ are found by summing the whole set of diagrams.

The UV finite virtual contributions to the cross section $\overline{F}_j^{(1)}$ is still IR divergent. However, the IR divergent part of the form factor with the full m_t dependence is the same as the HTL one. This fact implies the following:

$$\frac{\overline{F}_j^{(1)}}{F_j^{(0)}} - \frac{\overline{F}_{\text{HTL},j}^{(1)}}{F_{\text{HTL},j}^{(0)}} \sim O(\epsilon^0), \quad (3.66)$$

which means that they have the same IR pole structure. Hence, we define

$$R_j^{(1)} = \frac{\overline{F}_j^{(1)}}{F_j^{(0)}} - \frac{\overline{F}_{\text{HTL},j}^{(1)}}{F_{\text{HTL},j}^{(0)}} \propto \frac{\overline{\mathcal{A}}_j^{(1)}}{\mathcal{A}_j^{(0)}} - \frac{\overline{\mathcal{A}}_{\text{HTL},j}^{(1)}}{\mathcal{A}_{\text{HTL},j}^{(0)}}, \quad (3.67)$$

such that the virtual cross section split into a finite part $d\hat{\sigma}_{\text{virt}}^{\text{fin}}$ and divergent one $d\hat{\sigma}_{\text{HTL}}$:

$$\hat{\sigma}_{\text{virt}} = \hat{\sigma}_{\text{virt}}^{\text{fin}} + \hat{\sigma}_{\text{HTL}}. \quad (3.68)$$

Therefore, the virtual cross section is:

$$\begin{aligned} \hat{\sigma}_{\text{virt}} &= C_{\text{sym}} C_{\text{flux}} 2\text{Re} \int d\text{PS}_2 C_{\text{av}} \left[\left(C_{\Delta} F_{\Delta}^{(0)} + F_1^{(0)} \right)^* \left(C_{\Delta} F_{\Delta}^{(1)} + F_1^{(1)} \right) + F_2^{*(0)} F_2^{(1)} \right], \\ \hat{\sigma}_{\text{virt}}^{\text{fin}} &= \frac{\alpha_s^3}{(4\pi)^3} \frac{G_F^2 m_t^4}{32\pi \hat{s}^2} \int_{t^-}^{t^+} dt \left[\left| C_{\Delta} \mathcal{A}_{\Delta}^{(0)} \right|^2 R_{\Delta}^{(1)} + Y_1^2 Y_2^2 \left| \mathcal{A}_1^{(0)} \right|^2 R_1^{(1)} + Y_1^2 Y_2^2 \left| \mathcal{A}_2^{(0)} \right|^2 R_2^{(1)} \right. \\ &\quad \left. + Y_1 Y_2 C_{\Delta} \mathcal{A}_{\Delta}^{*(0)} \mathcal{A}_1^{(0)} \left(R_{\Delta}^{(1)} + R_1^{(1)} \right) \right], \\ \hat{\sigma}_{\text{HTL}} &= \frac{\alpha_s^3}{(4\pi)^3} \frac{G_F^2 m_t^4}{32\pi \hat{s}^2} \int_{t^-}^{t^+} dt \left[\left| C_{\Delta} \mathcal{A}_{\Delta}^{(0)} \right|^2 \frac{\overline{\mathcal{A}}_{\text{HTL},\Delta}^{(1)}}{\mathcal{A}_{\text{HTL},\Delta}^{(0)}} + Y_1^2 Y_2^2 \left| \mathcal{A}_1^{(0)} \right|^2 \frac{\overline{\mathcal{A}}_{\text{HTL},1}^{(1)}}{\mathcal{A}_{\text{HTL},1}^{(0)}} + Y_1^2 Y_2^2 \left| \mathcal{A}_2^{(0)} \right|^2 \frac{\overline{\mathcal{A}}_{\text{HTL},2}^{(1)}}{\mathcal{A}_{\text{HTL},2}^{(0)}} \right. \\ &\quad \left. + Y_1 Y_2 C_{\Delta} \mathcal{A}_{\Delta}^{*(0)} \mathcal{A}_1^{(0)} \left(\frac{\overline{\mathcal{A}}_{\text{HTL},\Delta}^{(1)}}{\mathcal{A}_{\text{HTL},\Delta}^{(0)}} + \frac{\overline{\mathcal{A}}_{\text{HTL},1}^{(1)}}{\mathcal{A}_{\text{HTL},1}^{(0)}} \right) \right]. \end{aligned} \quad (3.69)$$

It is useful to define the ratio between the NLO mass effects and LO partonic cross section:

$$C_{\text{mass}} = 2\text{Re} \left[\frac{\hat{\sigma}_{\text{virt}}^{\text{fin}}}{\hat{\sigma}_{\text{LO}}} \right], \quad (3.70)$$

such that the virtual mass effects to the NLO cross section become:

$$\Delta\sigma_{\text{virt}} = \frac{\alpha_s}{4\pi} \int_{\tau_0}^1 \frac{d\mathcal{L}_{gg}}{d\tau} \hat{\sigma}_{\text{LO}}(\tau s) C_{\text{mass}}. \quad (3.71)$$

Let us stress that $\hat{\sigma}_{\text{HTL}}$ contains IR divergences, but they will cancel against the real corrections, once that the phase space integration is performed.

3.4 Real corrections

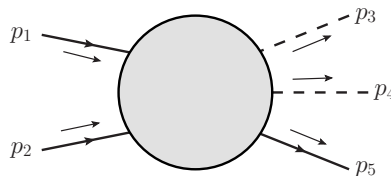


Figure 3.3: *Kinematic conventions for the real amplitude*

The missing piece to complete the calculation is the real corrections to the cross section. They consist of one-loop diagrams with an additional emission of a massless parton in the final state. The integration over the phase space will lead to IR divergences which will cancel against σ_{HTL} coming from the virtual correction.

There are three channels for the real corrections: $q\bar{q} \rightarrow H_1 H_2 g$, $qg \rightarrow H_1 H_2 q$ and $gg \rightarrow H_1 H_2 g$. The number of generic diagrams amounts to 43, plus the reversion of the fermion flow. For the first two channels, only triangle and box integrals are needed. For the last channel, there are pentagon integrals involved.

Finding the Lorentz projector is not an easy task: for the $gg \rightarrow H_1 H_2 g$ there are 14 form factors, and building 14 orthogonal tensors and projector can introduce overcomplexity into this calculation. The approach exploited is to immediately square the total amplitude, without performing any projection onto their tensor structure.

Let us introduce the actual calculation by considering the following kinematics (Figure 3.3):

$$\begin{aligned}\hat{s} &= 2p_1 \cdot p_2, & \hat{t} &= -2p_1 \cdot p_5, & \hat{u} &= -2p_2 \cdot p_5 \\ \hat{s} + \hat{t} + \hat{u} &= (p_3 + p_4)^2 = Q^2\end{aligned}\quad (3.72)$$

3.4.1 Heavy-top limit

To illustrate how the procedure has been done, let us focus on the $q\bar{q} \rightarrow H_1 H_2 g$ process in the heavy-top limit. This process can be built from the effective vertices we have calculated in the Chapter 2.

The triangle contributions are:

$$\begin{aligned}\mathcal{M}_\Delta &= \bar{v}(p_2)\gamma^\sigma u(p_1)\epsilon_\mu^*(p_5)(-ig_s)\frac{ig_{\sigma\rho}}{(p_1+p_2)^2}\sum_j Y_j \frac{i}{(p_1+p_2-p_5)^2 - m_{H_j}^2} \left(-i3\frac{\lambda_{j12}}{v}\right) \times \\ &\quad \times \left[\frac{i\alpha_s}{3\pi v}\delta^{ab}\left(\frac{4\pi\mu^2}{m_t^2}\right)^\epsilon \Gamma(1+\epsilon)[p_5 \cdot (p_1+p_2)g^{\mu\rho} - p_5^\rho(p_1+p_2)^\mu]\right]\end{aligned}\quad (3.73)$$

$$= \bar{v}(p_2)\gamma_\rho u(p_1)\epsilon_\mu^*(p_5)\frac{i\alpha_s g_s}{3\pi v^2}\delta^{ab}\sum_j \frac{3Y_j\lambda_{j12}}{Q^2 - m_{H_j}^2} \left(\frac{4\pi\mu^2}{m_t^2}\right)^\epsilon \Gamma(1+\epsilon) \left[\frac{1}{2}\frac{(\hat{t}+\hat{u})}{\hat{s}}g^{\mu\rho} + \frac{p_5^\rho(p_1+p_2)^\mu}{\hat{s}}\right],$$

and the box one is

$$\begin{aligned}\mathcal{M}_\square &= \bar{v}(p_2)\gamma^\sigma u(p_1)\epsilon_\mu^*(p_5)(-ig_s)\frac{ig_{\sigma\rho}}{(p_1+p_2)^2} \times \\ &\quad \times \left[-i\frac{\alpha_s}{3\pi v^2}Y_1 Y_2 \delta^{ab}\left(\frac{4\pi\mu^2}{m_t^2}\right)^\epsilon \Gamma(1+\epsilon)[p_5 \cdot (p_1+p_2)g^{\mu\rho} - p_5^\rho(p_1+p_2)^\mu]\right] \\ &= -\bar{v}(p_2)\gamma_\rho u(p_1)\epsilon_\mu^*(p_5)\frac{i\alpha_s g_s}{3\pi v^2}\delta^{ab}\left(\frac{4\pi\mu^2}{m_t^2}\right)^\epsilon \Gamma(1+\epsilon) \left[\frac{1}{2}\frac{(\hat{t}+\hat{u})}{\hat{s}}g^{\mu\rho} + \frac{p_5^\rho(p_1+p_2)^\mu}{\hat{s}}\right].\end{aligned}\quad (3.74)$$

This contribution already shows a feature that occurs in all the channels: there is a common factor dependent on the couplings that can be factorized. Hence, we define

$$\sqrt{\kappa} = \sum_j \left(\frac{3Y_j\lambda_{j12}}{Q^2 - m_{H_j}^2}\right) - Y_1 Y_2. \quad (3.75)$$

The sum of all the diagrams leads to the following amplitude:

$$\mathcal{M}_{q\bar{q}} = \bar{v}(p_2)\gamma_\rho u(p_1)\epsilon_\mu^*(p_5)\sqrt{\kappa}\frac{i\alpha_s g_s}{3\pi v^2}\delta^{ab}\left(\frac{4\pi\mu^2}{m_t^2}\right)^\epsilon \Gamma(1+\epsilon) \left[\frac{1}{2}\frac{(\hat{t}+\hat{u})}{\hat{s}}g^{\mu\rho} + \frac{p_5^\rho(p_1+p_2)^\mu}{\hat{s}}\right], \quad (3.76)$$

Let us evaluate the square amplitude explicitly. Since the polarization sum gives a factor² $\epsilon_\mu(p_5)\epsilon_\nu(p_5) \rightarrow -g_{\mu\nu}$, and the spin sum gives us

$$\sum_{\text{spins}} \bar{u}(p_1)\gamma_\sigma v(p_2)\bar{v}(p_2)\gamma_\rho u(p_1) = \text{Tr} \left[\not{p}_2\gamma_\rho\not{p}_1\gamma_\sigma\right] \quad (3.77)$$

²Since there is only one external on-shell gluon, the Ward identities grant that we can work in the pure Lorenz gauge.

the square of the tensor structure yields:

$$\begin{aligned}
& -\text{Tr} \left[\not{p}_2 \gamma_\rho \not{p}_1 \gamma_\sigma \right] \left[\frac{1}{2} \frac{(\hat{t} + \hat{u})}{\hat{s}} g^{\mu\rho} + \frac{p_5^\rho (p_1 + p_2)^\mu}{\hat{s}} \right] \left[\frac{1}{2} \frac{(\hat{t} + \hat{u})}{\hat{s}} g_\mu^\sigma + \frac{p_5^\sigma (p_1 + p_2)_\mu}{\hat{s}} \right] = \\
& - \left[\frac{1}{4} \frac{(\hat{t} + \hat{u})^2}{\hat{s}^2} \text{Tr} \left[\not{p}_2 \gamma^\sigma \not{p}_1 \gamma_\sigma \right] + \text{Tr} \left[\not{p}_2 \not{p}_5 \not{p}_1 \not{p}_5 \right] \right] = \frac{(d-2)(\hat{t} + \hat{u})^2}{2\hat{s}} - 2\hat{t}\hat{u} = \\
& = \frac{\hat{t}^2 + \hat{u}^2}{\hat{s}} - \epsilon \frac{(\hat{t} + \hat{u})^2}{\hat{s}}.
\end{aligned} \tag{3.78}$$

Therefore, the averaged square amplitude is

$$\sum_{\text{pol,spin}} \overline{|\mathcal{M}_{q\bar{q}}^{\text{HTL}}|^2} = \kappa \frac{8\alpha_s^3 G_F^2}{81\pi} \left(\frac{4\pi\mu^2}{m_t^2} \right)^{2\epsilon} \Gamma^2(1+\epsilon) \left[\frac{\hat{t}^2 + \hat{u}^2}{\hat{s}} - \epsilon \frac{(\hat{t} + \hat{u})^2}{\hat{s}} \right], \tag{3.79}$$

For completeness, the HTL square amplitudes for the other channels are

$$\begin{aligned}
\sum_{\text{pol,spin}} \overline{|\mathcal{M}_{qg}^{\text{HTL}}|^2} &= \kappa \frac{\alpha_s^3 G_F^2}{27\pi} \left(\frac{4\pi\mu^2}{m_t^2} \right)^{2\epsilon} \frac{\Gamma^2(1+\epsilon)}{(1-\epsilon)} \left[\frac{\hat{s}^2 + \hat{u}^2}{-\hat{t}} + \epsilon \frac{(\hat{s} + \hat{u})^2}{\hat{t}} \right], \\
\sum_{\text{pol,spin}} \overline{|\mathcal{M}_{gg}^{\text{HTL}}|^2} &= \kappa \frac{\alpha_s^3 G_F^2}{12\pi} \left(\frac{4\pi\mu^2}{m_t^2} \right)^{2\epsilon} \frac{\Gamma^2(1+\epsilon)}{(1-\epsilon)^2} \left[(1-\epsilon) \frac{\hat{s}^4 + \hat{t}^4 + \hat{u}^4 + Q^8}{\hat{s}\hat{t}\hat{u}} - 4\epsilon Q^2 \right].
\end{aligned} \tag{3.80}$$

A little side note on the gluon-gluon channel. The sum over the polarization must be done on the *physical* polarization states: the QED Ward identities do not hold for QCD contributions with triple gluon interaction. Therefore, the sum has to be restricted on the physical polarization, namely

$$\sum_{\text{pol}} \epsilon_\mu^*(p_1) \epsilon_\mu(p_1) = -g^{\mu\nu} + \frac{p_1^\mu p_r^\nu + p_1^\nu p_r^\mu}{p_1 \cdot p_r}, \quad (p_r^2 = 0) \tag{3.81}$$

where p_r is an auxiliary momentum such that $p_1 \cdot p_r \neq 0$. If one would like to not introduce these additional tensors, the external ghost contributions have to be considered. The square amplitude of these contribution will cancel the unphysical degrees of freedom contributions from the gluon-gluon amplitude. We have chosen to sum over the physical polarization by introducing the additional tensor of Eq. (3.81). Further details for the polarization sum are presented in Appendix C.

3.4.2 Full m_t dependence

The full top-mass dependence contribution requires the evaluation of one-loop Feynman integrals. Since the Feynman integrals appearing into the real correction are at most of rank-5, we have applied the Passarino-Veltmann reduction to the amplitude and, in a second step, we have prepared the square amplitude to be integrated over the phase space.

We chose to not reduce the tensor integrals down to scalar ones. This strategy is aimed at obtaining manageable expressions and localize the possible numerical instabilities due to small Gram determinants. Such instabilities are more severe in the gluon-gluon channel because of the presence of the pentagon integrals involving many Gram determinants. We have preferred to decompose the integrals in the internal momentum basis (see Chapter 2) in order to keep the length of the expressions under control. The coefficients of the Lorentz tensors are Feynman integrals of rank up to 4, and they depend only on the scale parameters, i.e. the kinematic invariants and the masses. We will not present the calculation in details, since it has been completely automated, and the procedure we exploited is in the end completely analogous to the LO amplitude one. We present the strategy with the $q\bar{q}$ channel as an example:

$$\mathcal{M}_{q\bar{q},j} = \frac{ig_s^3}{(4\pi)^2} \frac{m_t^2}{v^2} \delta^{ab} \left(\frac{4\pi\mu^2}{m_t^2} \right)^\epsilon \Gamma(1+\epsilon) \bar{v}(p_2) \gamma_\nu u(p_1) \epsilon_\mu^*(p_5) K_j \mathcal{A}_j^{\mu\nu}, \tag{3.82}$$

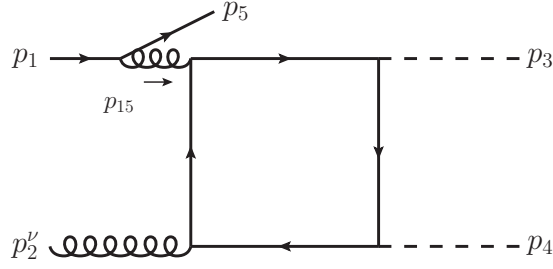


Figure 3.4: *Infrared divergent diagram belonging to the qq channel.*

where K_j encodes the normalization, remaining factors and the dependence on λ_{j12} , Y_1 and $\mathcal{A}_j^{\mu\nu}$ is the j -th Feynman integral. Taking the gauge-invariant triangle subprocesses as an example, the internal momenta basis for $\mathcal{A}_j^{\mu\nu}$ reads

$$\begin{aligned} \mathcal{A}_j^{\mu\nu} = & \sum_{ik} C_{00i} g^{(\mu\nu} q_i^{\rho)} q_{k,\rho} + \sum_{iklm} q_i^\mu q_k^\nu (q_l \cdot q_m) C_{ikl} \\ & + C_{00} g^{\mu\nu} + \sum_{ik} q_i^\mu q_k^\nu C_{ik} + \sum_{ik} q_i^\mu q_k^\nu C_i \\ & + g^{\mu\nu} \sum_i B_{00}^{(i)} + \sum_{ik} q_i^\mu q_k^\nu B_{ij} + g^{\mu\nu} A_{00}, \end{aligned} \quad (3.83)$$

where q_j are linear combinations of the external momenta. More details on the structure of the coefficients of Eq. (3.83) can be found in Appendix D.

In the actual calculation, the Eq. (3.83) drastically simplifies thanks to the presence of massless particles, Ward identities, same propagator mass in the loops, and in general with low number of scales. The coefficients of the tensors are known by means of standard recursion relations. Once that the projection of the amplitude on the internal momentum basis has been applied, we take the modulus square of the result and the spin, polarization and color average. This constitutes the building block for the real cross section.

The generation of the amplitude and the PV reduction has been performed within `Mathematica`. We have used the libraries `FeynArts` [151] and `FeynCalc` [152] to perform the algebra and the square amplitude function, that later on has been exported in `Fortran` subroutines. The evaluation of the tensor integrals has been committed to the package `LoopTools` [151], which has a `Mathematica` interface that has been extremely useful for internal crosschecks.

3.5 Real cross section

The square amplitude is now ready to be integrated over the 3-particle phase space. As for the virtual correction, we split the real corrections in a finite term and an IR divergent part:

$$\frac{|\mathcal{M}_{ij}|^2}{|\mathcal{M}_{\text{LO}}|^2} - \frac{|\mathcal{M}_{ij}^{\text{HTL}}|^2}{|\mathcal{M}_{\text{LO}}^{\text{HTL}}|^2} = (\text{IR finite}). \quad (3.84)$$

which expresses the fact that the ratio between the matrix elements and the Born term of the square amplitude and its heavy top-quark limit possess the same IR structure.

Defining the IR safe quantity

$$R^{(r)} = \frac{|\mathcal{M}_{ij}|^2}{|\mathcal{M}_{\text{LO}}|^2} - \frac{|\mathcal{M}_{ij}^{\text{HTL}}|^2}{|\mathcal{M}_{\text{LO}}^{\text{HTL}}|^2}, \quad (3.85)$$

it is possible to express the cross section as the sum of IR divergent and IR safe terms. Therefore,

the partonic real cross section $\hat{\sigma}_{ij}(\hat{s})$ reads:

$$\begin{aligned}\hat{\sigma}_{ij}(Q^2) &= \int d\text{PS}_3 \left[|\mathcal{M}_{\text{LO}}|^2 R^{(r)} + |\mathcal{M}_{\text{LO}}|^2 \frac{|\mathcal{M}_{ij}^{\text{HTL}}|^2}{|\mathcal{M}_{\text{LO}}^{\text{HTL}}|^2} \right] \\ &= \int d\text{PS}_3 \left[|\mathcal{M}_{\text{LO}}|^2 R^{(r)} \right] + \hat{\sigma}_{ij}^{\text{HTL}}\end{aligned}\quad (3.86)$$

The $\hat{\sigma}_{ij}^{\text{HTL}}$ will cancel against the $\hat{\sigma}_{\text{HTL}}$ coming from the calculation of the virtual cross section.

A clarification on the meaning of the ratio $R^{(r)}$ is necessary. Since the two processes do not share the same number of external legs (and so the kinematic invariants), the 3-particle phase space has to be projected on the 2-particle one. The IR behaviour comes from the soft and collinear limits related to the emission of the additional parton since each parton is massless. From this simple argument follows that the pentagon topologies can not generate IR divergences: the massive loop prevents both limits to occur.

Therefore, we can give an explicit example by looking at the diagram in Figure 3.4. The structure of this diagram shows an explicit factorization into a quark-flow and a LO box diagram with an off-shell gluon. The LO box represents the $2 \rightarrow 2$ subprocess onto which the 3-particle phase space needs to be projected. The factorization reads

$$\mathcal{M}_{qg} \supset \frac{f^\mu(p_1; p_5)}{p_{15}^2} \mathcal{M}_{\text{LO}}^{\mu\nu}(\tilde{p}_{15}, \tilde{p}_2; \tilde{p}_3, \tilde{p}_4), \quad (3.87)$$

where the tilded momenta have to be defined, according to the embedding we are aiming at. They will be linear combinations of the external on-shell momenta with the coefficients depending on the kinematics.

For the incoming particles, the transformed momenta are

$$\begin{aligned}\tilde{p}_{15}^\mu &= \frac{p_1 \cdot p_2 - p_1 \cdot p_5 - p_2 \cdot p_5}{p_1 \cdot p_2} p_1^\mu = \frac{Q^2}{\hat{s}} p_1^\mu, \\ \tilde{p}_2^\nu &= p_2^\nu,\end{aligned}\quad (3.88)$$

and the outgoing ones are

$$\begin{aligned}\tilde{p}_{3,4}^\mu &= p_{3,4}^\mu - \frac{2p_{3,4} \cdot (K + \tilde{K})}{(K + \tilde{K})^2} (K + \tilde{K})^\mu + \frac{2p_{3,4} \cdot K}{K^2} \tilde{K}^\mu, \\ K^\mu &= p_1^\mu + p_2^\mu - p_5^\mu, \quad \tilde{K}^\mu = \tilde{p}_{12}^\mu + \tilde{p}_2^\mu.\end{aligned}\quad (3.89)$$

Further details on the factorization of the $2 \rightarrow 2$ phase space out of the $2 \rightarrow 3$ can be found in Ref. [60].

The phase space integral has been built such that the LO factor factorizes (Appendix C.2), and the integration over the 2-particle phase space factor can be performed, obtaining the following result

$$\begin{aligned}\hat{\sigma}_{ij}(Q^2) &= \int d\text{PS}_3 \left[|\mathcal{M}_{\text{LO}}|^2 R^{(r)} \right] + \hat{\sigma}_{ij}^{\text{HTL}} \\ &= \frac{\alpha_s}{(4\pi)} \int_{\frac{\tau_0}{\tau}}^1 \frac{dz}{z} \hat{\sigma}_{\text{LO}}(z\hat{s}) D_{ij}(z).\end{aligned}\quad (3.90)$$

The coefficients D_{ij} have the following structure:

$$\begin{aligned}D_{q\bar{q}}(z) &= d_{q\bar{q}}(z), \\ D_{qg}(z) &= d_{qg}(z) - \frac{z}{2\epsilon} \frac{\Gamma(1-\epsilon)}{\Gamma(1-2\epsilon)} \left(\frac{4\pi\mu^2}{\mu_F^2} \right)^\epsilon P_{qg}(z), \\ D_{gg}(z) &= d_{gg}(z) - \frac{z}{\epsilon} \frac{\Gamma(1-\epsilon)}{\Gamma(1-2\epsilon)} \left(\frac{4\pi\mu^2}{\mu_F^2} \right)^\epsilon P_{gg}(z) + 6[1 - z^4 + (1-z)^4] \left[\frac{\log(1-z)}{1-z} \right]_+.\end{aligned}\quad (3.91)$$

The coefficients $d_{ij}(z)$ contain the top-mass dependence of the partonic cross section, and they have an already-known heavy-top limit:

$$\begin{aligned} d_{q\bar{q}}(z) &\xrightarrow{m_t \rightarrow \infty} \frac{32}{27}(1-z)^3, \\ d_{qg}(z) &\xrightarrow{m_t \rightarrow \infty} \frac{2}{3}z^2 - (1-z)^2, \\ d_{gg}(z) &\xrightarrow{m_t \rightarrow \infty} -\frac{11}{2}(1-z)^3. \end{aligned} \quad (3.92)$$

The functions $P_{ij}(z)$ are the Altarelli-Parisi splitting functions:

$$\begin{aligned} P_{qq} &= \frac{4}{3} \frac{1 + (1-z)^2}{z}, \\ P_{gg} &= 6 \left\{ \left[\frac{1}{1-z} \right]_+ + \frac{1}{z} - 2 + z(1-z) \right\} + \delta(1-z) \frac{33 - 2N_f}{6}, \end{aligned} \quad (3.93)$$

and

$$[f(z)]_+ = f(z) - \delta(1-z) \int_0^1 dz' f(z') \quad (3.94)$$

is the plus prescription.

Notice that there are still some residual collinear initial-state singularities located in the coefficients of the splitting functions. These divergences can be absorbed in a redefinition of the *bare* NLO gluon densities located in the gluon luminosity.

We would require a term that cancels against the initial-state singularities, acting as:

$$\hat{\sigma}_{R,ij}(\mu_F) = \hat{\sigma}_{ij} - \frac{\alpha_s}{(4\pi)} \int dz \left[-\frac{1}{2\epsilon} \frac{\Gamma(1-\epsilon)}{\Gamma(1-2\epsilon)} \left(\frac{4\pi\mu_R^2}{\mu_F^2} \right)^\epsilon P_{ij}(z) + K_{ij,\text{FS}}(z) \right] \hat{\sigma}_{\text{LO}}(z\hat{s}), \quad (3.95)$$

where $K_{ij,\text{FS}}(z)$ are arbitrary functions of z that fulfill the momentum sum rule. It is possible to show that such term arises from the renormalization of the partonic distribution functions. Recalling that

$$\sigma_{ij} = \int_0^1 dx_1 dx_2 f_{g,0}(x_1) f_{g,0}(x_2) \hat{\sigma}_{ij}(x_1 x_2 z \hat{s}), \quad (3.96)$$

the bare gluon densities can be renormalized in the following way

$$\begin{aligned} f_{g,0}(x) &= f_g(x, \mu_F) + \frac{\alpha_s}{(4\pi)} \left[-\frac{1}{2\epsilon} \frac{\Gamma(1-\epsilon)}{\Gamma(1-2\epsilon)} \left(\frac{4\pi\mu^2}{\mu_F^2} \right)^\epsilon P_{gg} + K_{gg,\text{FS}} \right] \otimes f_g(x, \mu_F) \\ &+ \frac{\alpha_s}{(4\pi)} \left[-\frac{1}{2\epsilon} \frac{\Gamma(1-\epsilon)}{\Gamma(1-2\epsilon)} \left(\frac{4\pi\mu^2}{\mu_F^2} \right)^\epsilon P_{gq} + K_{gq,\text{FS}} \right] \otimes f_q(x, \mu_F), \end{aligned} \quad (3.97)$$

where

$$f \otimes g(x, \mu_F) = \int_x^1 \frac{dz}{z} f(z, \mu_F) g\left(\frac{x}{z}, \mu_F\right). \quad (3.98)$$

The functions $K_{ij,\text{FS}}(z)$ can be fixed by choosing a factorization scheme. The simplest choice is the $\overline{\text{MS}}$ scheme, which sets these functions to zero everywhere: $K_{ij,\text{FS}} = 0$. Therefore,

$$f_{g,0}(x) = f_g(x, \mu_F) + \frac{\alpha_s}{(4\pi)} \frac{1}{2\epsilon} \frac{\Gamma(1-\epsilon)}{\Gamma(1-2\epsilon)} \left(\frac{4\pi\mu^2}{\mu_F^2} \right)^\epsilon [P_{gg} \otimes f_g(x, \mu_F) + P_{gq} \otimes f_q(x, \mu_F)]. \quad (3.99)$$

In conclusion, the finite parts of the real contributions to the cross section are

$$\begin{aligned} \Delta\sigma_{gg} &= \frac{\alpha_s}{(4\pi)} \int_{\tau_0}^1 d\tau \sum_q \frac{d\mathcal{L}_{gg}}{d\tau} \int_{\frac{\tau_0}{\tau}}^1 \frac{dz}{z} \hat{\sigma}_{\text{LO}}(z\tau s) C_{q\bar{q}}(z), \\ \Delta\sigma_{gq} &= \frac{\alpha_s}{(4\pi)} \int_{\tau_0}^1 d\tau \sum_{q,\bar{q}} \frac{d\mathcal{L}_{gg}}{d\tau} \int_{\frac{\tau_0}{\tau}}^1 \frac{dz}{z} \hat{\sigma}_{\text{LO}}(z\tau s) C_{gq}(z), \\ \Delta\sigma_{gg} &= \frac{\alpha_s}{(4\pi)} \int_{\tau_0}^1 d\tau \frac{d\mathcal{L}_{gg}}{d\tau} \int_{\frac{\tau_0}{\tau}}^1 \frac{dz}{z} \hat{\sigma}_{\text{LO}}(z\tau s) C_{gg}(z), \end{aligned} \quad (3.100)$$

where

$$\begin{aligned}
 C_{q\bar{q}}(z) &= d_{q\bar{q}}(z), \\
 C_{gq}(z) &= d_{gq}(z) - \frac{z}{2} P_{gq}(z) \log \left(\frac{\mu_F^2}{\tau_S(1-z)^2} \right), \\
 C_{gg}(z) &= d_{gg}(z) - z P_{gg}(z) \log \left(\frac{\mu_F^2}{\tau_S} \right) + 6[1+z^4+(1-z)^4] \left[\frac{\log(1-z)}{1-z} \right]_+.
 \end{aligned} \tag{3.101}$$

Chapter 4

Numerical integration

In this Chapter, the technicalities related to the numerical integration of the quantities found in Chapter 3 are presented. The main ingredients are: the Vegas algorithm [66] for Monte Carlo integrations and the Richardson extrapolation [153]. The Vegas algorithm is an adaptive method to drastically decrease the numerical error on the integration, keeping the statistics under control, based on the importance sampling. For each form factor, a relative statistical error of 10^{-5} has been required.

The Richardson extrapolation is a method to obtain the value of a function in a specific point by a proper linear combination of its values on a set of points. It will be employed in the extraction of the differential cross section with narrow width top quark from non-zero widths differential distributions, intended as the "limit" $\epsilon_t \rightarrow 0$ (defined in the previous Chapter). In this context, it can be seen as the analytical continuation of the differential distribution in $\epsilon_t = 0$. The convergence of the Richardson extrapolation will be discussed in detail, and some explicit examples will be presented.

The Richardson extrapolation, together with the trapezoidal rule, will be also exploited to integrate the differential distribution in order to obtain the total NLO cross section.

4.1 Integrating the Box form factors

The procedure described in Section (3.1) provides form factors depending on the Feynman parameters, the Higgs-pair invariant mass \hat{s} and the transferred momentum square \hat{t} , the top-quark mass m_t and the two Higgs masses m_{H_1} and m_{H_2} . The threshold singularities corresponding to the production of two on-shell top quarks have been regularized by introducing the regulator ϵ_t .

In the context of this work, the virtual differential cross section is the sum of the interferences of the LO and NLO form factors:

$$\tau \frac{d\sigma}{ds}(\tau s) = \hat{\sigma}_{\text{virt}}^{\text{fin}}(\hat{s}) = \hat{\sigma}_{\Delta\Delta} + \hat{\sigma}_{1\Delta} + \sum_k^{\text{diags}} \hat{\sigma}_{\Delta 1}^{(k)} + \sum_k^{\text{diags}} \hat{\sigma}_{11}^{(k)} + \sum_k^{\text{diags}} \hat{\sigma}_{22}^{(k)}, \quad (4.1)$$

where $\hat{\sigma}_{ij}^{(k)}$ is the partial partonic cross section constituted by the interference of the (total) LO form factor i with the NLO form factor j belonging to the diagram k . We recall that for the virtual contributions, $\hat{s} = Q^2$. Each term has the following structure

$$\hat{\sigma}_{ij}^{(k)}(\hat{s}, \epsilon_t) = \int_{\hat{t}^-}^{\hat{t}^+} d\hat{t} \int_0^1 d^6 \mathbf{x} I_{ij}^{(k)}(\hat{t}, \mathbf{x}), \quad (4.2)$$

where \mathbf{x} are the Feynman parameters and t^\pm is defined in Appendix C. Each integral depends on at most 6 parameters.

The integration leads to logarithmic divergences which only cancel in the total sum; this will lead to strong numerical instabilities. It is possible to tame the behaviour of the integral on the boundaries.

Notice first that

$$\begin{aligned} \frac{d\hat{t}}{\hat{s}p_T^2} &= \frac{d\hat{t}}{(\hat{t}^+ - \hat{t}^-)} \left[\frac{1}{(\hat{t} - \hat{t}^-)} + \frac{1}{(\hat{u} - \hat{t}^-)} \right] \\ &\quad \Downarrow \\ \int_{\hat{t}^-}^{\hat{t}^+} d\hat{t} I_{ij}^{(k)}(\hat{t}, \mathbf{x}) &= \hat{s}p_T^2 \int_{\hat{t}^-}^{\hat{t}^+} \frac{d\hat{t}}{(\hat{t} - \hat{t}^-)} \frac{I_{ij}^{(k)}(\hat{t}, \mathbf{x}) + I_{ij}^{(k)}(\hat{u}, \mathbf{x})}{(\hat{t}^+ - \hat{t}^-)}, \end{aligned} \quad (4.3)$$

where we exploited the relation between the kinematic variables $\hat{s} + \hat{t} + \hat{u} = m_{H_1}^2 + m_{H_2}^2$ (see Appendix F). To avoid numerical instabilities, the following change of variable will smooth the convergence of the integral:

$$y = \log \frac{\hat{t} - \hat{t}^-}{m_t^2}, \quad dy = \frac{d\hat{t}}{\hat{t} - \hat{t}^-} \quad (4.4)$$

and the integral becomes

$$\int_{\hat{t}^-}^{\hat{t}^+} d\hat{t} I_{ij}^{(k)}(\hat{t}, \mathbf{x}) = \hat{s}p_T^2 \int_{y^-}^{y^+} \frac{dy}{(\hat{t}^+ - \hat{t}^-)} \left[I_{ij}^{(k)}(\hat{t}(y), \mathbf{x}) + I_{ij}^{(k)}(\hat{u}(y), \mathbf{x}) \right]. \quad (4.5)$$

We have to regulate the behaviour of the boundaries since the change of variables of Eq. (4.4) moves the lower boundary to $y^- = -\infty$. Introducing a technical cut-off $\bar{\epsilon}$ it reads

$$\hat{t}^- \rightarrow \hat{t}^- + (\hat{t}^+ - \hat{t}^-)\bar{\epsilon}, \quad \hat{t}^+ \rightarrow \hat{t}^+ - (\hat{t}^+ - \hat{t}^-)\bar{\epsilon}. \quad (4.6)$$

After the change of variable $\hat{t} = \hat{t}(y)$, the integration boundaries becomes

$$y^- = \log \frac{(\hat{t}^+ - \hat{t}^-)\bar{\epsilon}}{m_t^2}, \quad y^+ = \log \frac{(\hat{t}^+ - \hat{t}^-)(1 - \bar{\epsilon})}{m_t^2}. \quad (4.7)$$

A last change of variable will turn the integration domain into the unit segment:

$$y = y^- + (y^+ - y^-)x_7, \quad dy = \log \frac{1 - \bar{\epsilon}}{\bar{\epsilon}} dx_7 \quad (4.8)$$

so that it can be treated like an additional Feynman parameter. The integral becomes:

$$\hat{\sigma}_{ij}^{(k)}(\hat{s}, \epsilon_t) = sp_T^2 \left(\log \frac{1 - \bar{\epsilon}}{\bar{\epsilon}} \right) \int_0^1 d^6 \mathbf{x} dx_7 \left[I_{ij}^{(k)}(\hat{t}(x_7), \mathbf{x}) + I_{ij}^{(k)}(\hat{u}(x_7), \mathbf{x}) \right], \quad (4.9)$$

A regulator can be introduced for each Feynman parameter, in the same manner as depicted in Eq. (4.6), and by introducing a cut-off regulator $\bar{\epsilon}_i$ for each parameter x_i , the convergence is even better. This brings the contribution to the total cross section to become

$$\begin{aligned} x_i &\rightarrow \bar{\epsilon}_i + (1 - 2\bar{\epsilon}_i)x_i, & dx_i &\rightarrow (1 - 2\bar{\epsilon}_i)x_i \\ &\quad \Downarrow \\ \hat{\sigma}_{ij}^{(k)}(\hat{s}, \epsilon_t) &= sp_T^2 \left(\log \frac{1 - \bar{\epsilon}}{\bar{\epsilon}} \right) \prod_i^6 (1 - 2\bar{\epsilon}_i) \int_0^1 d\mathbf{x} dx_7 \left[I_{ij}^{(k)}(\hat{t}(x_7), \mathbf{x}) + I_{ij}^{(k)}(\hat{u}(x_7), \mathbf{x}) \right]. \end{aligned} \quad (4.10)$$

The numerical integration of each $\hat{\sigma}_{ij}^{(k)}(\hat{s})$ has been performed using a Monte Carlo integration method based on the VEGAS algorithm: it reduces the integration error through the *importance sampling*, aimed at optimizing the sampling in the integration region that contributes the most to the integral. Consider a function $f(x)$ that has to be integrated between 0 and 1. The numerical integration can be written as

$$\int_0^1 f(x) dx \approx \frac{1}{N} \sum_n^N f(x_n) = \mathbf{E}(f), \quad (4.11)$$

where x_n comes from a uniform distribution. If x_n comes from a distribution $g(x)$ instead, it is possible to show that

$$\int_0^1 f(x)dx \approx \frac{1}{N} \sum_n \frac{f(x_n)}{g(x_n)} = E_g(f), \quad \text{Var}_g(f) = E\left(\frac{f^2}{g^2}\right) - E^2\left(\frac{f}{g}\right), \quad (4.12)$$

where g must respect the following requirement

$$E(f) = E_g(f). \quad (4.13)$$

It is easy to show that:

$$g(x) = \frac{f(x)}{\int_0^1 f(x)dx} \implies \text{Var}_g(f) = 0. \quad (4.14)$$

Since it is not possible to choose this distribution at numerical level, it will provide a simple way to reduce drastically the error by concentrating the distribution around the bulk of $f(x)$. Therefore, a preliminary integration of $f(x)$ with uniform distribution will provide an estimation of the distribution $g(x)$ that will be used to integrate $f(x)$ with an increased precision. The process can be iterated as far as the aimed precision has not been reached.

The VEGAS algorithm has been implemented in the `Fortran` code `XVEGAS`, and it has been run on the computer cluster, which granted us access to 4000 CPUs for a maximum runtime of individual jobs of 96 hours.

The energy bins chosen for the integration run from 270 GeV and 2500 GeV, with a scan of 25 GeV around the threshold region ($Q = 245$ GeV for $m_t = 172.5$ GeV in the OS scheme), 50 in the region 500 – 1500 GeV and two additional bins in the tails at 2000 GeV and 2500 GeV. For all integrations, the Feynman parameter regulator has been set to $\bar{\epsilon} = \bar{\epsilon}_i = 10^{-8}$. The top-mass regulators have been set to the values $\epsilon_t = 0.1 \cdot 2^k$ with $k = \{1, \dots, 8\}$, with two additional values ($k = -1, -2$) for the bins around the threshold. The reason for this will become clear later.

For each integral, a number of 10 preliminary samplings with lower statistics have been generated, and this leads to an optimization of the integration method. The number of sampling points has been adapted for each form factor to reach the ideal statistical error $\delta\sigma_{ij}^{(k)} \sim 10^{-5}$. Due to limitations related with the size of the calculation, we choose to split the integration on multiple random number seeds, and combining the single estimates for each seed afterwards. For the majority of the form factors, for the regulators set to $\epsilon_t > 0.4$ and $\bar{\epsilon} = \bar{\epsilon}_i = 10^{-8}$, two runs with number of sampling points $N \sim 10^8$ can be combined to obtain the aimed precision. The lower ϵ_t and the higher invariant Higgs-pair mass Q^2 , the lower is the convergence of the integration and the numerical stability: for $\epsilon_t = 0.1$ and $Q > 1000$ GeV and for the whole tail the differential cross section distribution, 50 runs were needed to achieve $\delta\sigma_{ij}^{(k)} \sim 10^{-5}$ for topologies 1, 2, 3 and 4 and up to 1000 for topologies 5 and 6 (diagrams depicted in Appendix H).

All the runs have been performed a total of 4 times: one with the top-mass in the OS scheme, setting its value to 172.5 GeV; the other 3 times considering the top-mass in the $\overline{\text{MS}}$ scheme. For these last runs, we performed the calculation with $\overline{m}_t(\overline{m}_t) = 163.0$ GeV, $\overline{m}_t(Q)$ and $\overline{m}_t(Q/4)$. Since these last three runs have a role into the estimation of the uncertainties related with the top mass scheme, a simplified energy scan has been chosen, keeping the same energy range but, with half the number of bins.

As it is clear from this picture, the integration of the virtual form factors represented the bottleneck of this calculation, with a total running time of around 9 months in more than 2000 CPUs.

4.2 Richardson Extrapolation

The imaginary part ϵ_t introduced in the top mass as $m_t^2 \rightarrow m_t^2(1 - i\epsilon_t)$ plays the role of a finite width of the top quark. In accordance with the literature, we consider the top quark in the narrow width approximation, which induces us to take the limit $\epsilon_t \rightarrow 0$. Since we build a numerical setup, the "limit" is not a viable option, and the numerical integration for $\epsilon_t < 10^{-2}$ becomes highly unstable.

The way to take this "limit" in our numerical framework is provided by the *Richardson extrapolation method*. Consider a function $f(h)$ depending *polynomially*¹ on h . We are interested in its value for $h = 0$ knowing it for $h = h_0$ and $h = 2h_0$. Expanding f around $h = 0$:

$$\begin{cases} f(h_0) = f(0) + h_0 f'(0) + O(h_0^2) \\ f(2h_0) = f(0) + 2h_0 f'(0) + O(h_0^2) \end{cases} \quad (4.15)$$

Combining the two expressions:

$$\begin{aligned} f(0) &= 2f(h_0) - f(2h_0) + O(h_0^2) \\ &\Downarrow \\ \text{RiEx}_{2,h_0}[f(0)] &= 2f(h_0) - f(2h_0) \end{aligned} \quad (4.16)$$

where we have introduced the $\text{RiEx}_{n,h_0}[f(0)]$ to be the Richardson extrapolation of $f(0)$ with n nodes and pivot node h_0 . One more example with three node yields

$$\begin{aligned} f(0) &= \frac{1}{3}[8f(h_0) - 6f(2h_0) + f(4h_0)] + O(h_0^3) \\ &\Downarrow \\ \text{RiEx}_{3,h_0}[f(0)] &= \frac{1}{3}[8f(h_0) - 6f(2h_0) + f(4h_0)] \end{aligned} \quad (4.17)$$

The key feature of the Richardson extrapolation is that the error is inversely proportional to the number of nodes. Beyond a certain number of nodes, the extrapolation reaches a plateau where the approximation can not be improved further.

Coming back to the virtual differential cross section $\hat{\sigma}_{\text{virt}}^{\text{fin}}(\hat{s})$, the role of the variable h is played by the top-mass regulator ϵ_t . The pivot value for ϵ_t has been set to different values depending on the energy region: for Q between 300 GeV and 350 GeV, we set $\epsilon_t = 0.025$; for Q between 375 GeV and 475 GeV, we set $\epsilon_t = 0.05$; for all the other energies $\epsilon_t = 0.1$. The reason for choosing different pivot with respect to the energy region will become clear later.

For each of the energy bins, a 9-nodes Richardson extrapolation for each form factor contribution $\hat{\sigma}_{ij}^{(k)}(\hat{s}, \epsilon_t)$ has been performed:

$$\text{RiEx}_{9,2^m \cdot 0.025}[\hat{\sigma}_{ij}^{(k)}(\hat{s}, 0)] = \sum_{n=m}^{m+8} c_n \hat{\sigma}_{ij}^{(k)}(\hat{s}, 2^n \cdot 0.025), \quad m = \{0, 1, 2\}. \quad (4.18)$$

Since the plateau region is reached already for 4 of 5 nodes for almost all form factors, increasing the number of the nodes may lead to an underestimation of the error, which decreases with the number of nodes. In order to obtain a conservative extrapolation, the error associated to each extrapolation has been chosen to be the difference of the extrapolations with 4 and 5 nodes. To conclude, the Richardson extrapolation leads to the following narrow width approximation of the differential cross section

$$\hat{\sigma}_{ij}^{(k)}(\hat{s}, 0) = \text{RiEx}_{9,2^m \cdot 0.025}[\hat{\sigma}_{ij}^{(k)}(\hat{s}, 0)] \pm 2^{\Theta(m)} \left| \text{RiEx}_{5,2^m \cdot 0.025}[\hat{\sigma}_{ij}^{(k)}(\hat{s}, 0)] - \text{RiEx}_{4,2^m \cdot 0.025}[\hat{\sigma}_{ij}^{(k)}(\hat{s}, 0)] \right|, \quad (4.19)$$

where

$$\Theta(m) = \begin{cases} 1 & \text{for } m = \{0, 1\} \\ 0 & \text{otherwise} \end{cases}. \quad (4.20)$$

It is designed to include a factor two when lower regulators are considered, in order to obtain a conservative estimate of the error around the $t\bar{t}$ -production threshold. The Richardson extrapolation error will be quadratically summed with the statistical error coming from the Monte Carlo integration. These errors represent the complete statistical uncertainties introduced by the numerical setup at the differential cross section level. An additional Richardson extrapolation will be applied to obtain the integrated total cross section.

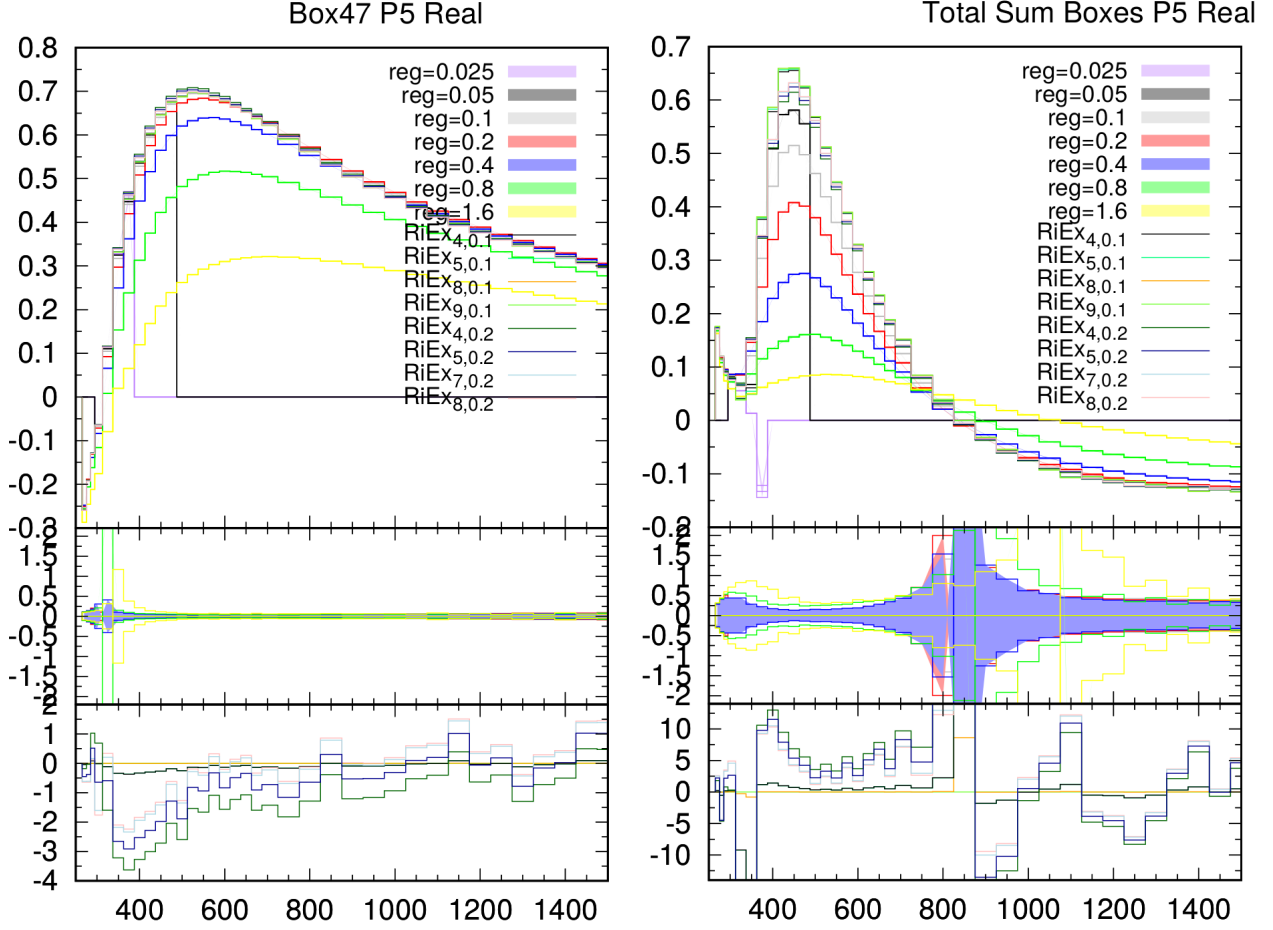


Figure 4.1: *Richardson extrapolation of the narrow width m_t of the NLO 2HDM H_1H_2 production differential cross section of the Box 47 (left panel) and the total contribution of the boxes (right). P_5 is the contribution $\hat{\sigma}_{\Delta 1}^{(j)} + \hat{\sigma}_{11}^{(j)} + \hat{\sigma}_{22}^{(j)}$. Upper panels: Richardson extrapolation of the narrow width approximation of $\text{RiEx}_{n,h_0}[\hat{\sigma}_{ij}^{(47)}(\hat{s}, 0)]$ for different pivots and number of nodes; middle panels: relative errors for each bin; lower panels: deviation (in per-cent) between $\text{RiEx}_{9,0.1}[\hat{\sigma}_{ij}^{(47)}(\hat{s}, 0)]$ and all the other extrapolations.*

4.2.1 Convergence of the Richardson extrapolation: two examples

An analysis of the Richardson extrapolation for specific cases will clarify its convergence behaviour. The notion of convergence will be identified with considering the following sequence and convergence ratio:

$$(\text{RiEx}_{n,h_0})_{n \leq 9}, \quad \delta_n = \frac{|\text{RiEx}_{n,h_0} - \text{RiEx}_{n-1,h_0}|}{\text{RiEx}_{n-1,h_0}}. \quad (4.21)$$

The sequence will be considered "quickly" convergent if $\delta_n \lesssim 1\%$ for $n > 5$ and $\delta_n \lesssim 0.1\%$ for $n > 8$: in other words, if the estimated error is below the percent level and the plateau of the extrapolation is reached starting from the 7-nodes².

It can be shown that an 8-nodes Richardson extrapolation with pivot value $\epsilon_t = 0.2$ does not satisfy the criteria expressed in Eq. (4.21) for many box diagrams and energy bins, i.e. its convergence is not sufficiently good. This fact brought us to consider the 9-nodes one with pivot $\epsilon_t = 0.1$. The $\text{RiEx}_{8,0.2}$ is anyhow useful for two reasons: at first instance, its computational requirements are small compared to the $\text{RiEx}_{9,0.1}$, of about one order of magnitude less in runtime; in addition, $\text{RiEx}_{8,0.2}$ can be used as a test of compatibility with $\text{RiEx}_{9,0.1}$ since the 8-nodes Richardson extrapolation is affected by a

¹The polynomial requirement is demanded for having a good convergence of the method.

²These criteria are mostly empiric.

larger statistical error, and the central value of the 9-nodes one will likely falls within its error band.

The box 47 (Appendix H) is an infrared divergent diagram that has been extensively run such that the statistical error is negligible for this purpose (around the per-mille level). The convergence of the Richardson extrapolation for the complete contribution of this box to the differential cross section can be better understood in Figure 4.1. The upper panel shows the differential distributions with different widths and the Richardson extrapolations of the narrow width approximation with different nodes; in particular, it shows how good the convergence of the extrapolations becomes once more nodes are considered. In the lower panel it is shown the convergence of the extrapolations around $\text{RiEx}_{9,0.1}[\hat{\sigma}_{ij}^{(47)}(\hat{s}, 0)]$, which has been taken as central value.

In more detail, the behavior of the Richardson extrapolation can be better understood by looking at the single curves. The yellow curve represents the partonic cross section evaluated with regulator $\epsilon_t = 1.6$, the green represents the one with regulator $\epsilon_t = 0.8$, the blue represents the one with regulator $\epsilon_t = 0.4$. It is visible how the different partonic cross sections tend to approach a "limit" distribution, until the red curve starts to be indistinguishable from the upper curves. The latter ones are the partonic cross section with regulator $\epsilon_t = 0.1$ and various Richardson extrapolations with different nodes and pivot. The Richardson extrapolation that takes into account all the curves we have described here is the $\text{RiEx}_{5,0.1}$ (light green curve in the left plot in Figure 4.1). In this case, the difference between the Richardson extrapolation and the pivot value $\epsilon_t = 0.1$ (grey curve) is about the per-cent level, and its robustness has been checked by varying the pivot and the number of nodes. The lower panel in the left plot shows that, setting $\text{RiEx}_{9,0.1}$ as expectation value, a 4-nodes extrapolation already introduces deviations of around the per-mille level, and an 8-nodes Richardson extrapolated falls within the statistical error of the estimated value (including its Richardson extrapolation error), and it is completely indistinguishable from $\text{RiEx}_{9,0.1}$. For the majority of the bins, the $\text{RiEx}_{9,0.1}$ has a sufficient fast convergence such that it can be considered the most robust estimate of the differential cross section.

The right plot in Figure 4.1 shows a case where the pivot $\epsilon_t = 0.1$ may be not enough for a reliable extrapolation. The differential distributions for different regulators do not show a manifest convergent behaviour on the $\text{RiEx}_{9,0.1}$, since its deviation from the pivot value $\epsilon_t = 0.1$ (grey curve of the right plot) in the threshold region is more than 25% in the peak. In addition, $\text{RiEx}_{8,0.2}$ and $\text{RiEx}_{9,0.1}$ are not compatible within a standard deviation, a hint that pivots closer to $\epsilon_t = 0$ have to be taken into account. Therefore, to test the reliability of the Richardson extrapolation, additional regulators have been introduced: $\epsilon_t = 0.05$ and $\epsilon_t = 0.025$. The addition of these new regulators is very expensive from the computational point of view since Monte Carlo integrations with many sample points have to be considered³. However, the $\epsilon = 0.1$ curve still offers a reliable Richardson extrapolation for $Q > 500$ GeV and $Q < 300$ GeV. The black curve, namely the distribution with $\epsilon_t = 0.05$ (right plot of Figure 4.1) adds a 10% to the grey curve in the peak region, which attests the beginning of a convergence to some curve. There can be shown that $\text{RiEx}_{9,0.05}$ and $\text{RiEx}_{9,0.025}$ reach their plateau value and the deviation between them is lower than their respective errors. Therefore, the $\text{RiEx}_{9,0.025}$ has been chosen to be the expectation value for the bins $Q = \{300, 325, 350\}$ GeV, $\text{RiEx}_{9,0.05}$ the one for $Q = \{375, \dots, 475\}$ GeV, $\text{RiEx}_{9,0.1}$ for all the other bins.

4.3 Total Cross Section

The total cross section is found by integrating the differential distribution built with the partonic cross section $\hat{\sigma}_{ij}^{(k)}(\hat{s}, 0)$. The numerical framework that has been setup in the previous section is suitable

³For our setup, the number of sampling points were the same; to accomplish the aimed precision, the multi-seeds structure of the code has been exploited. For problematic boxes, hundreds of seeds have been combined.

for the trapezoidal rule:

$$\begin{aligned} \Delta\sigma_{\text{NLO}} &= 2 \int_{Q_-}^{Q_+} Q \frac{d\Delta\sigma_{\text{NLO}}}{dQ^2} dQ = \delta Q \left[Q_- \frac{d\Delta\sigma_{\text{NLO}}}{dQ^2}(Q_-^2) + 2 \sum_{j=1}^{n-1} (Q_- + j\delta Q) \frac{d\Delta\sigma_{\text{NLO}}}{dQ^2}((Q_- + j\delta Q)^2) + \right. \\ &\quad \left. Q_+ \frac{d\Delta\sigma_{\text{NLO}}}{dQ^2}(Q_+^2) \right] + O(\delta Q^2) \\ &= \Delta\sigma_{\text{NLO}}(\delta Q) + O(\delta Q^2), \end{aligned} \tag{4.22}$$

where δQ is the step size of the energy bins. The trapezoidal rule introduces a dependence on δQ , and an error proportional to δQ^2 . The analytical integration, in the spirit of the Riemann integral, is reached in the limit when the width of the steps δQ goes to 0 and their number goes to infinity simultaneously. Since the two quantities are related, the limit $\delta Q \rightarrow 0$ is sufficient to describe the continuum limit.

We can assume a polynomial dependence ansatz on δQ , such that the limit $\delta Q \rightarrow 0$ can be extrapolated by the Richardson extrapolation:

$$\sigma_{\text{NLO}} = \text{RiEx}_{n,\delta Q}[\Delta\sigma_{\text{NLO}}(0)] + O(\delta Q^{n+2}), \tag{4.23}$$

Different pivot values have been selected depending on the region. Empirical arguments have shown that for the threshold region, namely for $300 \text{ GeV} < Q < 700 \text{ GeV}$, a 25 GeV energy scan must be considered in order to achieve a Richardson extrapolation which converges sufficiently quick; for the remaining energy bins, a 50 GeV scan has been chosen. This energy scan grants a Richardson extrapolation of the NLO total cross section with an error below the per-mille level. The remaining region $260 \text{ GeV} < Q < 300 \text{ GeV}$ can be integrated by using the Boole's rule with 5-points, achieving an error comparable with the other method.

Chapter 5

Results and Discussion

The method presented in the previous Chapters has been applied and studied extensively in Refs. [68, 69] for the SM case, where $m_{H_1} = m_{H_2} = 125$ GeV and $Y_1 = Y_2 = 1$. The 2HDM neutral scalar Higgs-pair production will be treated in a future work. However, the arguments presented in this Chapter can be generalized to the analysis of the 2HDM case.

In this last Chapter, the major outcomes of the works discussed in this thesis are presented. The PDFs considered in the calculation are the PDF4LHC and MMHT2014 sets [154, 155]. The NLO differential cross section in the HTL [32] will be compared with the full- m_t dependent one, and cross-checked with the first calculation [47, 144]. The mass effects become sizable for increasing values of the Higgs-pair invariant mass.

Three main topics will be discussed in detail: the size of the uncertainties due to the top-mass renormalization scale and scheme, the proper top-mass renormalization scale choice for the main Higgs-pair invariant mass regions and how to combine the top-mass uncertainties with the state-of-the-art calculation [156].

5.1 SM Differential and Total cross section

The addition of the virtual and real contributions constitutes the differential cross section, which reads

$$Q^2 \frac{d\Delta\sigma_{\text{NLO}}}{dQ^2} = \frac{\alpha_s(\mu_R)}{4\pi} \left[\frac{d\mathcal{L}_{gg}}{d\tau} \hat{\sigma}_{\text{LO}} C_{\text{mass}}(\hat{s}) \Big|_{\tau=\frac{\hat{s}}{s}} + \int \frac{dz}{z^2} \frac{d\mathcal{L}_{ij}}{d\tau} \hat{\sigma}_{\text{LO}} C_{ij}(\hat{s}, z) \Big|_{\tau=\frac{\hat{s}}{zs}} \right]. \quad (5.1)$$

For the SM calculation, we have set $m_{H_1} = m_{H_2} = m_H = 125$ GeV and $m_t = 172.5$ GeV.

As discussed in the previous Chapter, we provided the result for Higgs-pair invariant mass from 250 GeV to 1500 GeV with steps of 5 GeV for 250-300 GeV, of 25 GeV from 300 GeV to 700 GeV, and 50 GeV for the rest. To have control on the tail of the distribution, additional bins at 2000 GeV and 2500 GeV have been included. The Richardson extrapolation has been performed with 9 nodes with pivot node $\epsilon_t = 0.025$ from 300 GeV to 375 GeV, since the presence of the OS top-mass threshold had bad impact on the stability of the integration, making the convergence slow. For higher energies, we choose the pivot at $\epsilon_t = 0.05$ up to 475 GeV and pivot $\epsilon_t = 0.1$ up to 1500 GeV with 9 nodes. The multi-seeds approach has been extremely useful to obtain the total statistical and Richardson extrapolation error at per-mille level.

The NLO partonic cross section has been implemented into the program `Hpair` [32], already used to derive the NLO HTL cross section. The PDF4LHC and MMHT2014 PDFs are used to obtain the numerical results [154, 155]. The distributions we provide are built for centre-of-mass energy of $\sqrt{s} = 14, 27, 100$ TeV. The renormalization and factorization scales have been set to $\mu_R = \mu_F = \frac{Q}{2}$. We present the comparison between the NLO distribution of the full top-mass dependence against the LO and HTL calculations, which has been studied in previous works [32].

In Figure 5.1 the differential distribution of the invariant mass of the Higgs-pair system is shown. The finite top-mass effects introduced by the virtual contributions (the green line) have a huge impact on the differential distributions, leading to a -20% deviation with respect to the HTL starting from

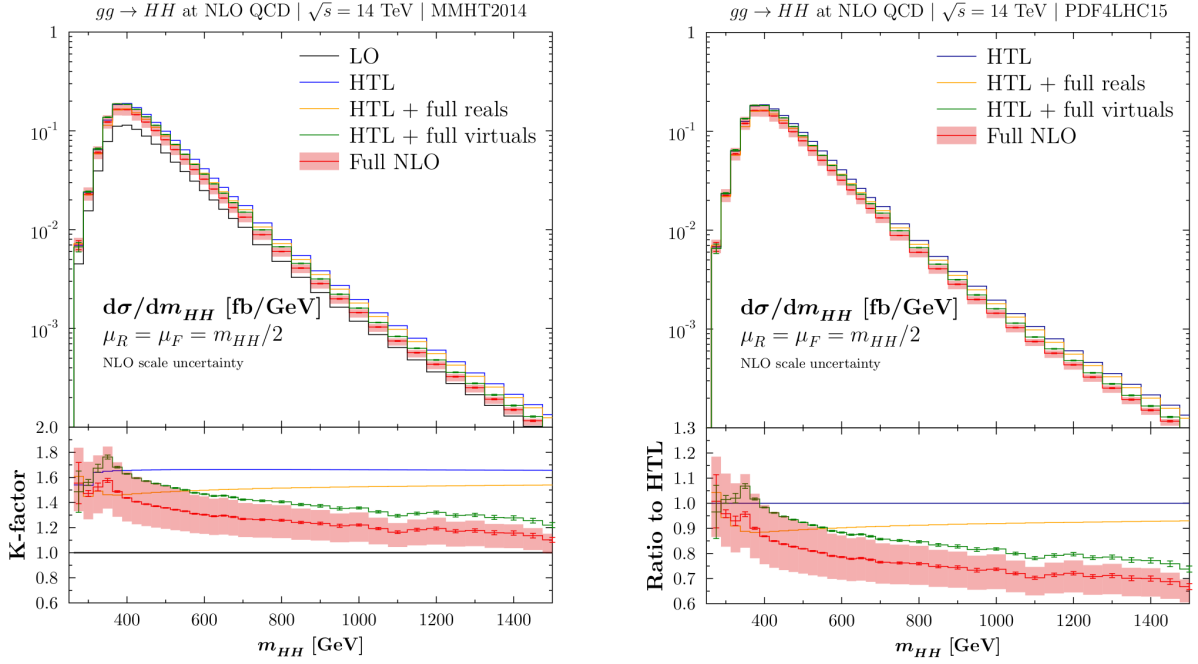


Figure 5.1: *Differential cross section distribution for the NLO SM Higgs-pair production at 14 TeV. Left panels: result with MMHT2014 and bin-by-bin K-factor; right panel: result with PDF4LHC PDF and bin-by-bin ratio to the HTL. Black line: LO calculation; blue line: NLO HTL calculation; yellow line: NLO HTL + reals with full m_t dependence; green line: NLO HTL + virtuals with full m_t dependence; red line: full NLO calculation, with renormalization and factorization uncertainties included as red band. Here $m_{HH} = \sqrt{\hat{s}}$ is the Higgs-pair invariant mass.*

$Q = 1000$ GeV. This deviation becomes even larger at centre-of-mass energies of $\sqrt{s} = 100$ TeV, with a decreasing of -40% when the real corrections are taken into account (red line). This behaviour does not show up for Higgs-pair invariant masses around the threshold region, since this is the region of validity of the HTL approximation. The red band represents the scale and scheme uncertainties, estimated as an envelope of the differential distributions evaluated at $\mu_R = \mu_F = Q$ and $\mu_R = \mu_F = \frac{Q}{4}$. They amount to around 15% from the central value at low Higgs-pair invariant mass, and decrease to around 10% in the tails. It can be shown that the bulk of the mass effect to the NLO K-factor is carried by the continuum diagrams (the ones that do not contain the triple Higgs interaction), that can be used to describe this process within a deviation of at most 5% .

\sqrt{s} (TeV)	σ_{NLO} (fb)	\sqrt{s} (TeV)	σ_{HTL} (fb)
13	$27.73^{+13.8\%}_{-12.8\%}$	13	$32.51^{+18\%}_{-15\%}$
14	$32.81^{+13.5\%}_{-12.5\%}$	14	$38.65^{+18\%}_{-15\%}$
27	$127.0^{+11.7\%}_{-10.7\%}$	27	$156.2^{+17\%}_{-13\%}$
100	$1140^{+10.7\%}_{-10.0\%}$	100	$1521^{+16\%}_{-13\%}$

Table 5.1: *Total cross section for SM Higgs-pair production. On the left, the full top-mass dependence, on the right, the HTL calculation. The numbers in the brackets are the numerical errors.*

The total cross section has been calculated by means of a numerical integration. The Richardson extrapolation of the trapezoidal method offered a reliable numerical integration: as already mentioned in Chapter 4, the numerical integral of the differential distribution can be treated as a function of the bin size, and its value at vanishing bin size can be extrapolated with the Richardson extrapolation. This strategy has been adopted for $Q > 300$ GeV. For lower value the Boole's rule with five nodes

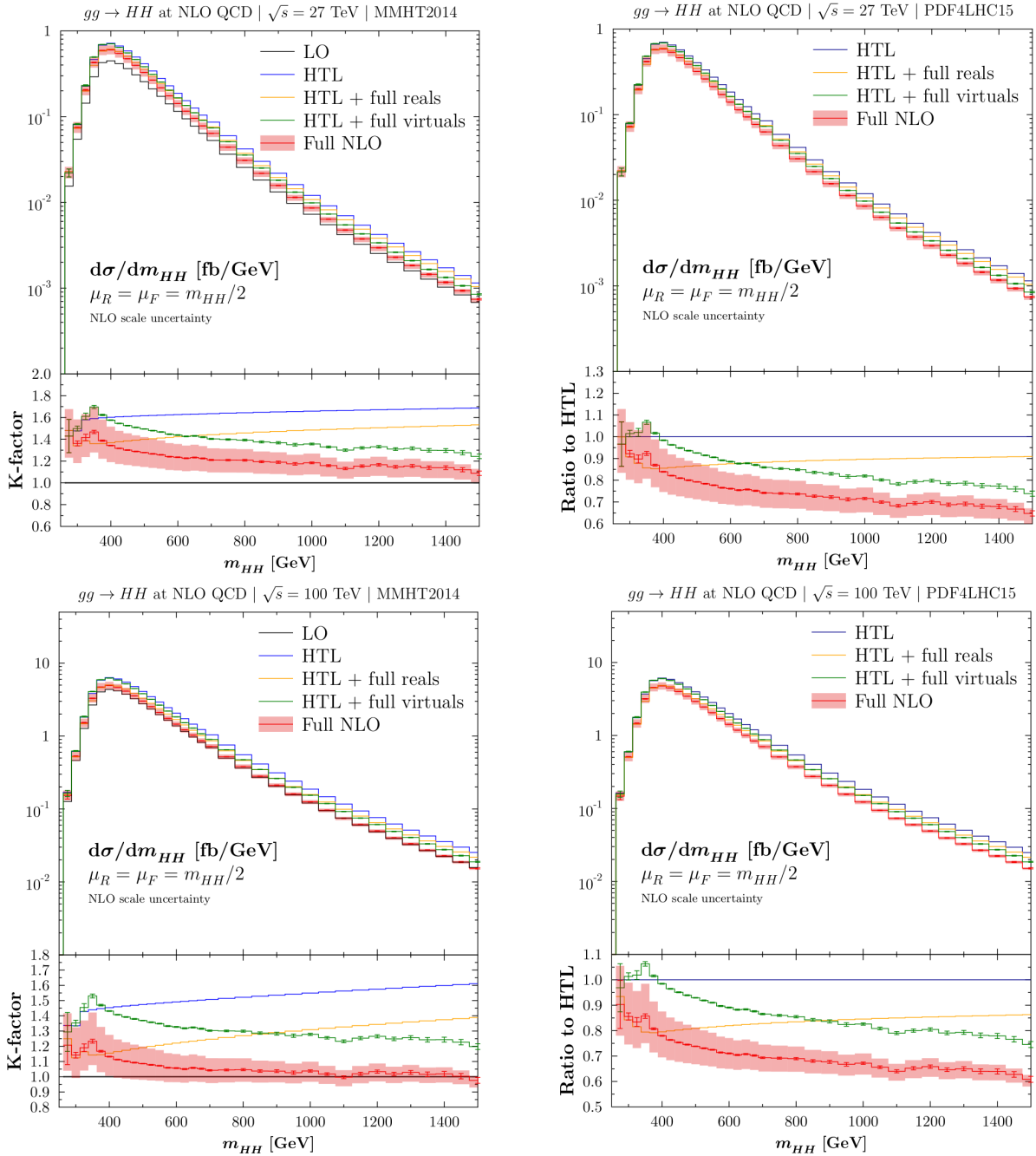


Figure 5.2: Same description of Figure 5.1, with $\sqrt{s} = 27$ TeV and $\sqrt{s} = 100$ TeV

has been considered.

The procedures yield the total cross section depicted in Table 5.1, together with renormalization and factorization scale uncertainties. As we can infer from the comparison between the left and right tables, the top-mass effects have decreased the total cross section with respect to the NLO HTL approximation of around 15% [68]; the inclusion of the top-mass effects has reduced the scale uncertainties too. These cross sections show complete agreement with the literature [144].

5.1.1 Dependence on the trilinear Higgs coupling

The NLO total cross section of the Higgs-boson pair production is the key to access the trilinear Higgs coupling λ_{3H} . We recall [23] that the total cross section has a proportionality relation to the trilinear

Higgs coupling close to the SM value

$$\frac{\Delta\sigma}{\sigma} \sim -\frac{\Delta\lambda_{3H}}{\lambda_{SM}}. \quad (5.2)$$

Therefore, the sensitivity of the Higgs-pair production total cross section can be probed by varying the trilinear Higgs coupling. The study of these variations can be also interpreted as due to BSM effects to the trilinear Higgs coupling. They can be treated systematically by considering the SM Lagrangian with dimension-6 operators in the scalar sector only [157]. A more general approach including all dimension-6 operators has been studied up to the NNLO HTL [158–160].

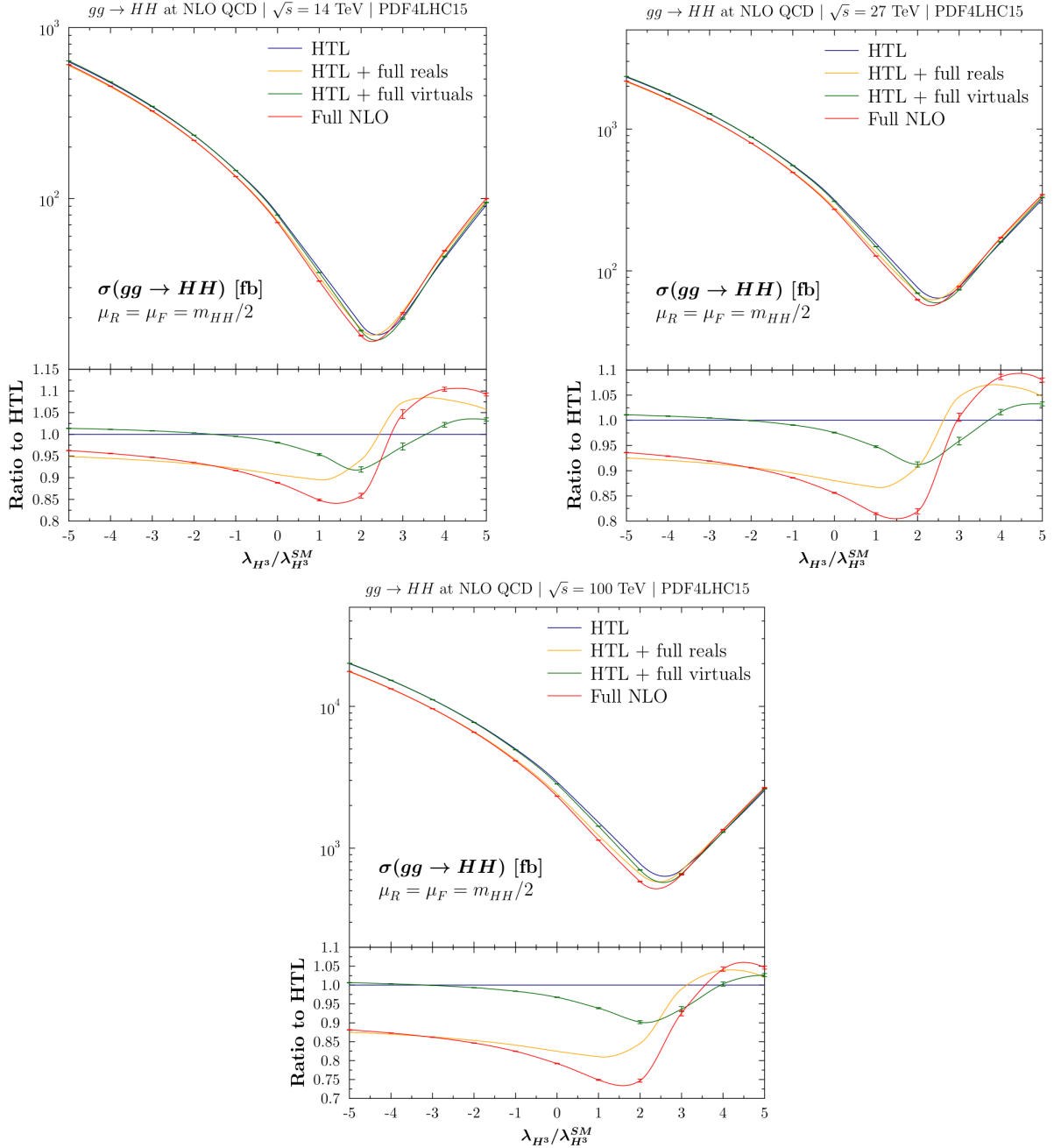


Figure 5.3: Total Higgs-pair production as function of the trilinear Higgs coupling in units of SM coupling. The centre-of-mass energy is fixed to $\sqrt{s} = 14$ TeV (left), $\sqrt{s} = 27$ TeV (right) and $\sqrt{s} = 100$ TeV (down). The PDF4LHC15 PDFs have been used and the renormalization scale is fixed to $Q/2$. The error bars are statistical uncertainties combined with the Richardson extrapolation error.

We have studied the behaviour of the NLO total cross section of the Higgs-pair production process

with respect to λ_{3H} in units of SM coupling λ_{SM} . It can be expressed as follows

$$\sigma_{\text{NLO}} = \sigma_1 + \sigma_2 \frac{\lambda_{3H}}{\lambda_{SM}} + \sigma_3 \left(\frac{\lambda_{3H}}{\lambda_{SM}} \right)^2 \quad (5.3)$$

In Figure 5.3, the dependence of the integrated Higgs-pair production cross section with respect to the Higgs self-coupling is presented. The parabolic behaviour of the curves in the upper panels is distorted by the logarithmic scale of the y -axis. The minimum of the full NLO total cross section is shifted from 2.4 to 2.3 SM units w.r.t. the HTL calculation [23, 32, 161]. The NLO mass effects amount to 10-15% with respect to the HTL. The sign of the correction changes in correspondence to the passage from constructive to destructive interference between the box and triangle diagrams in the form factor $F_1^{(i)}$. The meaning of constructive and destructive interference for $F_1^{(i)}$ is manifest in the HTL [54, 130, 162], and it can be seen in Eq. (3.79) and (3.80).

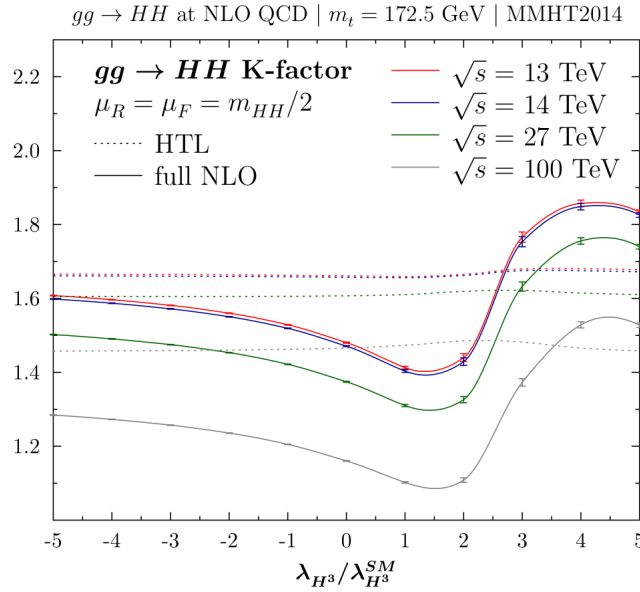


Figure 5.4: *K-factor comparison between the different full NLO cross sections and the HTL one as function of the trilinear Higgs coupling in SM units. The error bars represent the statistical uncertainties.*

The Figure 5.4 gathers all the NLO K-factors for different collider energies. The dotted lines correspond to the HTL K-factors, the solid ones to the full top-mass dependence NLO K-factors. The top-mass effects increase with the collider energy in the constructive interference region ($\lambda_{3H} < 0$), ranging from 10% to 15%. As it is clear from the behaviour of the solid curves, the top-mass effects introduce a strong dependence on the trilinear Higgs coupling, including a change of slope for $\lambda_{3H} > 1$, where the interference between box and triangles becomes destructive. At last, using Eq. (5.3), the expressions for the curves represented in Figure 5.3 are

$$\begin{aligned} \sigma_{\text{NLO}}|_{14\text{TeV}} &= \left(72.27(7) - 50.70(6) \frac{\lambda_{3H}}{\lambda_{SM}} + 11.23(9) \left(\frac{\lambda_{3H}}{\lambda_{SM}} \right)^2 \right) \text{fb}, \\ \sigma_{\text{NLO}}|_{27\text{TeV}} &= \left(270.9(3) - 183.1(2) \frac{\lambda_{3H}}{\lambda_{SM}} + 39.5(4) \left(\frac{\lambda_{3H}}{\lambda_{SM}} \right)^2 \right) \text{fb}, \\ \sigma_{\text{NLO}}|_{100\text{TeV}} &= \left(2323(2) - 1496(2) \frac{\lambda_{3H}}{\lambda_{SM}} + 313(3) \left(\frac{\lambda_{3H}}{\lambda_{SM}} \right)^2 \right) \text{fb}, \end{aligned} \quad (5.4)$$

where the PDF4LHC PDFs have been used and the central scales $\mu_R = \mu_F = Q/2$ have been chosen.

5.2 Top-mass uncertainties

A consequence of the truncation of the perturbative QCD series is the introduction of theoretical uncertainties due to the choice of the renormalization scheme and scale. The uncertainties due to the renormalization μ_R and factorization μ_F scales have already been taken into account in previous studies [67, 144] and they have been represented in the previous Section in Figure 5.1 and Figure 5.2 as a red band around the central value (red curve). The top-quark mass is a renormalization scheme and scale dependent variable as well. Different choices of the renormalization scheme and scale will lead to a different running of the top mass and introduce an additional source of theoretical uncertainties. Such uncertainties and the ones coming from the renormalization of the strong coupling and the PDFs have to be combined.

In single-Higgs production, the finite top-mass effects were negligible due to the small Higgs mass. This is also the reason why the HTL approximation works very well for that process. Since it has been shown that the finite top-mass effects on the Higgs-pair production are sizable, a dedicated study of the uncertainties due to the choice of different mass renormalization scheme and scales have been performed.

We have evaluated the top-mass uncertainties by evaluating the whole differential cross section by choosing four different top-mass scenarios: $m_t = 172.5$ GeV in the on-shell renormalization scheme and $\overline{m}_t(\overline{m}_t) = 163.01516101$ GeV, $\overline{m}(Q)$ and $\overline{m}(Q/4)$ in the $\overline{\text{MS}}$ renormalization scheme¹. The running of the $\overline{\text{MS}}$ top mass has been considered at N³LL:

$$\overline{m}_t(\mu_t) = \overline{m}_t(m_t) \frac{c(\alpha_s(\mu_t)/\pi)}{c(\alpha_s(m_t)/\pi)}, \quad (5.5)$$

$$c(x) = \left(\frac{7}{2}\right)^{\frac{4}{7}} [1 + 1.398x + 1.793x^2 - 0.6834x^3],$$

and $\overline{m}_t(m_t)$ has been calculated using the relation between the top pole mass and $\overline{\text{MS}}$ top mass at N³LO [163–167]. The integration of the partonic cross section has been repeated for every mass configuration taking into account the running of Eq. (5.5) with the same setup used for the OS scheme calculation shown in the previous section. Since the role of these runs is to estimate the top-mass uncertainties, a rougher energy scan has been chosen: 25 GeV scan between $Q = 300$ GeV and $Q = 400$ GeV and 100 GeV for $Q > 400$ GeV.

Figure 5.5 shows the distributions obtained for the four top-mass schemes chosen. For $Q > 400$ GeV the maximum value for each bin is the OS scheme and the minimum is the distribution for $\overline{m}_t(Q)$.

Choosing the OS scheme as central value, we have estimated the mass uncertainties by taking the envelope of the different mass distributions bin-by-bin. This procedure makes the top-mass uncertainties strongly asymmetric at the differential cross section level (Table 5.2): for $Q > 400$ GeV the upper uncertainty vanishes, since the OS distribution provides the maximum for each bin. As it is clear from the Table 5.2, the mass uncertainties are very large: going from LO to NLO, they decrease by about a factor two, being of order 30% at 600 GeV. This same behaviour has been seen for off-shell single-Higgs production, where the top-mass effects are noticeable.

5.2.1 Preferred scale choice

An appropriate choice of the top-mass renormalization scheme is mandatory to avoid that large logarithms involving the Higgs-pair invariant mass Q do not spoil the convergence of the QCD perturbative expansion.

In Figure 5.6 the differential distributions for different choices of the top-mass scale and scheme are presented, and important information can be inferred from them. The OS scheme and the $\overline{\text{MS}}$ scheme with $\overline{m}_t(\overline{m}_t)$ in the ratio with the NLO HTL are shown respectively in red and blue. These ratios are decreasing with respect of the Higgs-pair invariant mass. The $\overline{\text{MS}}$ scheme with $\overline{m}_t(Q)$ and $\overline{m}_t(Q/4)$,

¹Note that since different top-quark masses have to be used, this study can only be performed nowadays with the method presented in this thesis so far.

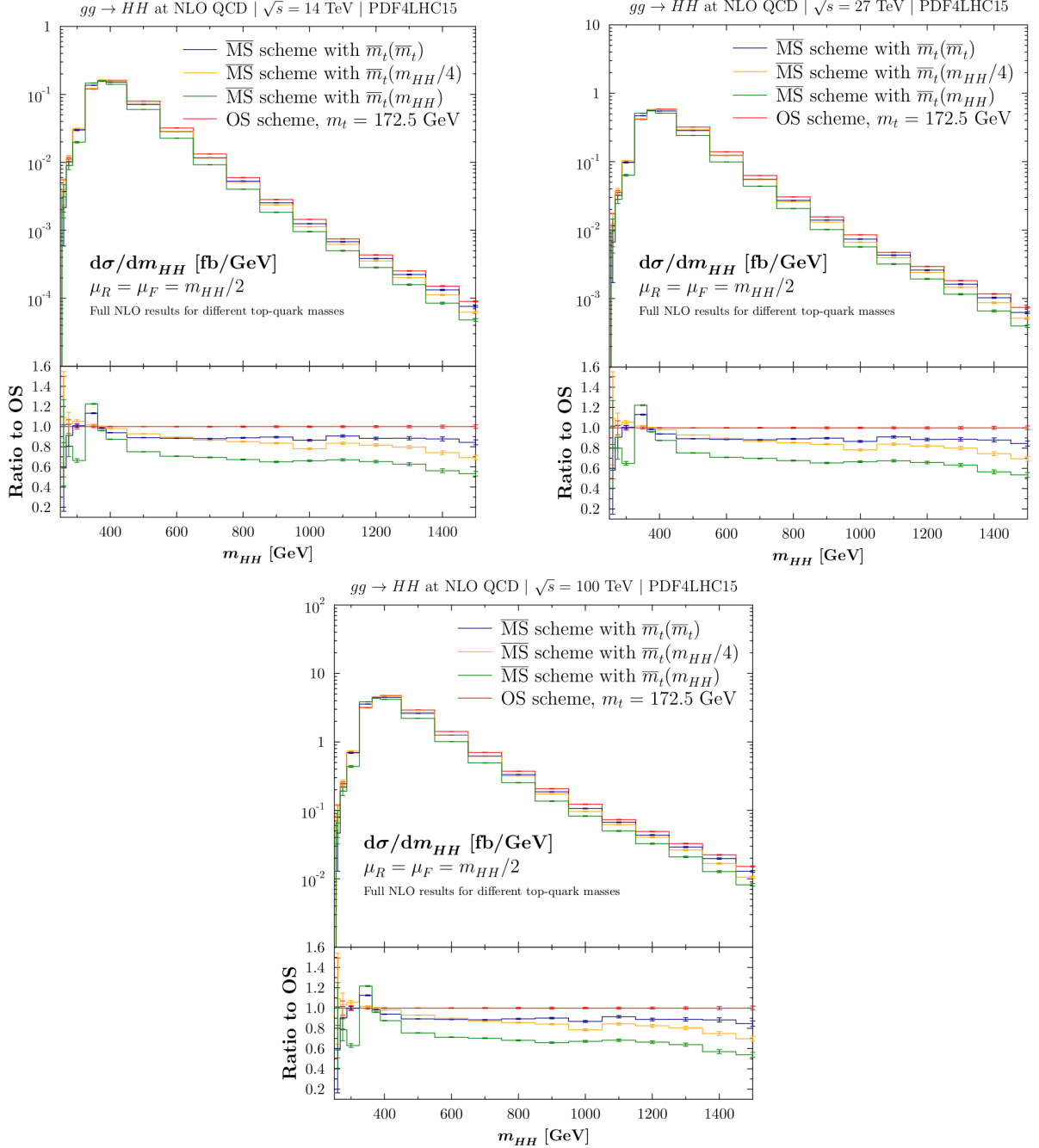


Figure 5.5: *Differential cross section of NLO SM Higgs-pair production for different values of the top mass at $\sqrt{s} = 14$ TeV, $\sqrt{s} = 27$ TeV and $\sqrt{s} = 100$ TeV. The PDF4LHC15 PDFs have been used.*

respectively in green and blue, are rather constant for Higgs-pair invariant mass $Q > 500$ GeV. This behaviour of the ratios reflects the two distinct effects of the scale choice:

1. *decreasing top-mass effects* for the choice of fixed value of the mass renormalization scale;
2. *constant top-mass effects* for dynamical scale choice.

These trends can be clearly understood from the theory, by looking at the low and high energy limits of the process. For energies below the double Higgs production threshold, the HTL is a good approximation of the process. We notice that the HTL can be described by the SM effective field theory where the top quark has been integrated out [32, 35, 168, 169], which manifests as an effective vertex between gluons and Higgs bosons:

$$\mathcal{L}_{\text{eff}} = \frac{\alpha_s}{12\pi} \text{Tr} [G^{\mu\nu} G_{\mu\nu}] \left(\frac{C_1}{v} H - \frac{C_2}{2v^2} H^2 \right). \quad (5.6)$$

Q (GeV)	$\frac{d\sigma_{\text{LO}}}{dQ}$ (fb/GeV)	$\frac{d\sigma_{\text{NLO}}}{dQ}$ (fb/GeV)	\sqrt{s} (TeV)	σ_{NLO} (fb)
300	$0.01656^{+62\%}_{-2.4\%}$	$0.02978(7)^{+6\%}_{-34\%}$	13	$27.73^{+4\%}_{-18\%}$
400	$0.09391^{+0\%}_{-20\%}$	$0.1609(4)^{+0\%}_{-13\%}$	14	$32.81^{+4\%}_{-18\%}$
600	$0.02132^{+0\%}_{-48\%}$	$0.03204(9)^{+0\%}_{-30\%}$	27	$127.0^{+4\%}_{-18\%}$
1200	$0.0003223^{+0\%}_{-56\%}$	$0.000435(4)^{+0\%}_{-35\%}$	100	$1140^{+3\%}_{-18\%}$

↓

$\sigma_{\text{NLO}} = 32.81(7)^{+4\%}_{-18\%}$ fb

Table 5.2: *Left table: Differential cross section values for $\sqrt{s} = 14$ TeV at LO and NLO. The NLO corrections make the mass uncertainties decrease by a factor 2. The total cross section is shown below. Right table: total cross sections including top mass scheme and scale uncertainties for $\sqrt{s} = 13, 24, 27, 100$ TeV.*

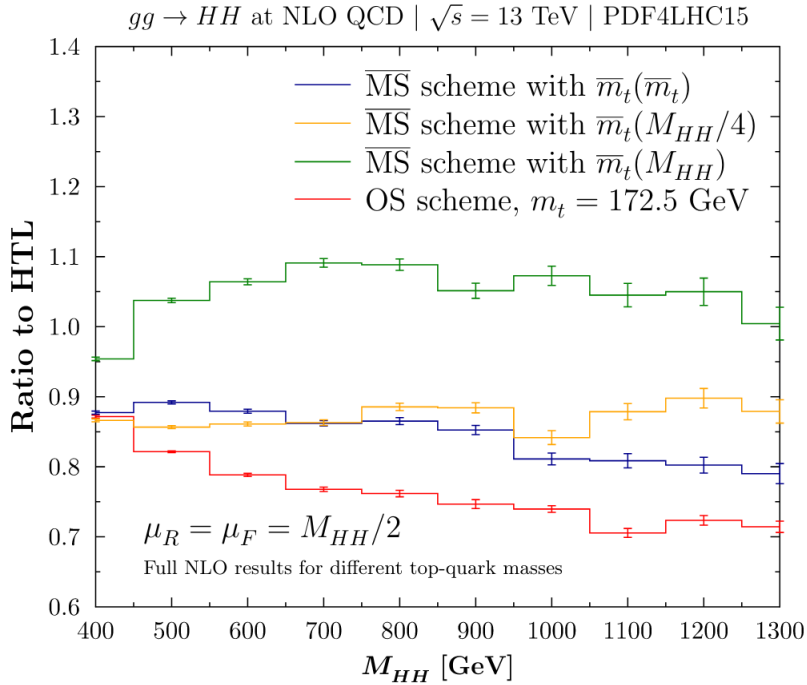


Figure 5.6: *Ratio of the NLO differential cross section to the HTL NLO one for the mass schemes considered for $\sqrt{s} = 13$ TeV.*

The Wilson coefficients C_i of the HTL Lagrangian, independent of the scattering process, are determined by the matching to the SM Lagrangian. These coefficients at NLO are

$$\begin{aligned}
 C_1 &= 1 + \frac{11}{4} \left(\frac{\alpha_s}{\pi} \right) + \left\{ \frac{2777}{288} + \frac{19}{16} \log \left(\frac{\mu_R^2}{m_t^2} \right) + N_f \left[\frac{1}{2} \log \left(\frac{\mu_R^2}{m_t^2} \right) - \frac{67}{96} \right] \right\} \left(\frac{\alpha_s}{\pi} \right)^2 + O(\alpha_s^3), \\
 C_2 &= C_1 + \left(\frac{35}{24} + \frac{2}{3} N_f \right) \left(\frac{\alpha_s}{\pi} \right)^2 + O(\alpha_s^3).
 \end{aligned} \tag{5.7}$$

Therefore, the natural choice of the matching scale is the top pole mass $\mu_R = m_t$. This fact shows why at low Higgs-pair invariant mass the OS scheme offers a good scheme choice.

The large Q behaviour of the form factors can be understood by considering their analytical high energy expansion [45, 46]. Foremost, the triangle contributions are strongly suppressed, because of the off-shell Higgs propagator, so the dominant contribution comes from the virtual boxes. The analytical

expressions of the form factors in terms of the top pole mass are

$$F_i^{(1)} \sim \frac{\alpha_s}{\pi} \left\{ 2F_i^{(0)} \log \left(\frac{m_t^2}{\hat{s}} \right) + \frac{m_t^2}{\hat{s}} G_i(\hat{s}, \hat{t}) \right\}, \quad (5.8)$$

where G_i are complicated functions of the partonic kinematic invariants. Notice that the dependence of $F_i^{(1)}$ on the top mass is completely isolated. However, the logarithms involving the top mass introduce large contributions proportional to the LO. A different behaviour shows up when the form factors are expanded in term of the $\overline{\text{MS}}$ mass:

$$F_i^{(1)} \sim \frac{\alpha_s}{\pi} \left\{ 2F_i^{(0)} \left[\log \left(\frac{\mu_t^2}{\hat{s}} \right) + \frac{4}{3} \right] + \frac{\overline{m}_t^2(\mu_t)}{\hat{s}} G_i(\hat{s}, \hat{t}) \right\}. \quad (5.9)$$

Setting $\mu_t = \kappa \hat{s}$ the logarithm is under control and behaves good at high $\sqrt{\hat{s}}$. This provides the explanation of why a dynamical scale choice of the $\overline{\text{MS}}$ mass renormalization scale provides a good scale choice for the high energy regime. Notice that Figure 5.6 shows in particular that a proper choice of the mass renormalization scale makes the NLO finite top-mass effects to be independent on the Higgs-pair invariant mass, and their size settle to around 10-15% for $\mu_t = \sqrt{\hat{s}}/4$.

5.2.2 Combining the uncertainties

Collecting all the results found in our analysis, the uncertainties of the NLO SM total cross section are summarized in Table 5.3. It shows NLO cross sections at different centre-of-mass energies with theoretical uncertainties. The left table displays the uncertainties related to the renormalization and factorization scale choice; the central one shows the uncertainties related to the top-mass renormalization scale and scheme choice; the right table shows the combination of the two uncertainties. Since both sources of uncertainties have been estimated from the envelope, their interplay is an envelope too, leading to the linear sum of the uncertainties. Additional corrections to the Higgs-pair produc-

\sqrt{s} (TeV)	σ_{NLO} (fb)		\sqrt{s} (TeV)	σ_{NLO} (fb)		\sqrt{s} (TeV)	σ_{NLO} (fb)
13	$27.73^{+13.8\%}_{-12.8\%}$		13	$27.73^{+4\%}_{-18\%}$		13	$27.73^{+18\%}_{-31\%}$
14	$32.81^{+13.5\%}_{-12.5\%}$	\oplus	14	$32.81^{+4\%}_{-18\%}$	$=$	14	$32.81^{+18\%}_{-31\%}$
27	$127.0^{+11.7\%}_{-10.7\%}$		27	$127.0^{+4\%}_{-18\%}$		27	$127.0^{+16\%}_{-29\%}$
100	$1140^{+10.7\%}_{-10.0\%}$		100	$1140^{+3\%}_{-18\%}$		100	$1140^{+14\%}_{-28\%}$
Ren.+fac. uncertainties			top-mass uncertainties			Combined uncertainties	

Table 5.3: *Left table: NLO SM total cross sections with renormalization and factorization scheme uncertainties. Central table: NLO SM total cross section with top-mass uncertainties. Right table: NLO SM total cross section with combined uncertainties.*

tion have been studied. The recommended prediction is the NNLO QCD corrections in the full-theory approximation (FTapprox), i.e. LO and NLO with full top-mass dependence, HTL virtual and real-virtual contributions and full top-mass dependence for the double real contributions [29, 156]. This calculation estimates a renormalization and factorization scale uncertainties up to 5%.

To analyze how to combine the top-mass uncertainties with the state-of-the-art calculation, a comment of the structure of the n -th order of the total cross section is useful:

$$d\sigma_n = d\sigma_{n-1} \left(K_{\text{SV}}^{(n)} + K_{\text{rem}}^{(n)} \right), \quad (5.10)$$

where $K_{\text{SV}}^{(n)}$ is the soft+virtual contribution in the HTL (independent on the top mass) and $K_{\text{rem}}^{(n)}$ is the top mass contribution to the differential cross section in the ratio with the previous perturbative order [39, 69].

\sqrt{s} (TeV)	$\sigma_{\text{NNLO}}^{\text{FTapprox}}$ (fb)		\sqrt{s} (TeV)	σ_{NLO} (fb)		\sqrt{s} (TeV)	$\sigma_{\text{NNLO}}^{\text{FTapprox}}$ (fb)
13	$31.05^{+2.2\%}_{-5.0\%}$		13	$27.73^{+4\%}_{-18\%}$		13	$31.05^{+6\%}_{-23\%}$
14	$36.69^{+2.1\%}_{-4.9\%}$	\oplus	14	$32.81^{+4\%}_{-18\%}$	$=$	14	$36.69^{+6\%}_{-23\%}$
27	$139.9^{+1.3\%}_{-3.9\%}$		27	$127.0^{+4\%}_{-18\%}$		27	$139.9^{+5\%}_{-22\%}$
100	$1224^{+0.9\%}_{-3.2\%}$		100	$1140^{+3\%}_{-18\%}$		100	$1224^{+4\%}_{-21\%}$
Ren.+fac. uncertainties			top-mass uncertainties			Combined uncertainties	

Table 5.4: *Left table: Recommended NNLO FTapprox SM total cross sections with renormalization and factorization scheme uncertainties. Central table: NLO SM total cross section with top-mass uncertainties. Right table: NNLO FTapprox SM total cross section with combined uncertainties.*

Both the soft+virtual and remainder terms are multiplied by the same factor and $K_{\text{SV}}^{(n)}$ is dominant. The $K_{\text{rem}}^{(n)}$ provides a correction of 10-15% of the $K_{\text{SV}}^{(n)}$ contribution. The latter term occurs both in the HTL approximation and the FTapprox, which is why these approximations are reliable. These statements have been tested at NLO and NNLO [156]. The explicit form of the NLO differential cross section shown in Eq. (3.69) and (3.100) are provided such that the factorization of Eqs. (5.10) is explicit. Since the SV part of the NNLO differential cross section, which is known in literature, scales with the full NLO contribution, and the top-mass uncertainties are independent of the renormalization and factorization scale choice, we are legitimate to consider the combined uncertainties to be the *envelope* of the two *relative* ones, leading to a linear sum of the uncertainties. Therefore, the NNLO QCD total cross section for Higgs-pair production are recommended to be considered affected by the theoretical uncertainties in Table 5.4.

Chapter 6

Conclusions

In this thesis, a framework for the NLO QCD Higgs-pair production via gluon fusion cross section with full top-mass dependence has been described. It is suitable for BSM extensions of the scalar sector, such as the 2HDM. In particular, in Chapter 1 it has been explained how the different final states can be implemented into the calculation and how to deal with the dimensional regularization in the presence of pseudoscalar and charged Higgs bosons.

The building blocks of the NLO contributions are the amplitudes built with up to four-point two-loop Feynman diagrams with five mass scales and five-point one-loop ones. The first are the virtual contributions, the latter are the real ones. Since there is no systematic strategy for two-loop diagrams, a specific calculation method for such amplitude is presented. No tensor reduction methods has been performed during the calculation. For each of the 47 box diagrams belonging to the virtual amplitude, the projection into their form factors has been performed, and a topology-wise Feynman parametrization has been chosen, allowing the isolation of UV and IR divergences by means of end-point subtractions. Particular care has been dedicated to the subtraction of the divergences coming from the diagrams belonging to the topology 6: the universality of the IR divergences has been exploited to build a subtraction term analogous to the heavy-top limit of the form factors. The addition of the renormalization counterterms to the virtual amplitude yields UV finite quantities. The $\overline{\text{MS}}$ scheme with five active flavours and the on-shell top quark decoupled from the running has been used to renormalize the strong coupling. Finally, after the UV renormalization and the end-point subtraction of the IR divergences, the box form factors are ready to be integrated over the Feynman parameters and the two-particle phase space. The one-particle-reducible diagrams have been obtained by combining two Higgs decay into on-shell and off-shell gluon LO amplitudes, employed as effective vertices. At last, the NLO triangle contributions have been built from the single-Higgs production form factors.

The numerical setup has involved the VEGAS algorithm for Monte Carlo integration [66], implemented into a *Fortran* code built with a multi-seed approach. Numerical instabilities arise for energies lying above the virtual thresholds, which can be $t\bar{t}$ or gg production thresholds. A small imaginary parameter ϵ_t introduced as a finite top-quark width increases the stability of the Monte Carlo, and it can be used for an analytical continuation of the cross section to extract the narrow top-quark width. Moreover, integration-by-parts has been performed to decrease the power of the denominators, and the numerical stability has been improved further. The narrow width of the top quark has been extracted from combining linear evaluations of the differential cross section for different ϵ_t regulator values. This is the core of the Richardson extrapolation method, whose extrapolation error is inversely proportional to the number of nodes. Nine nodes for each energy bin have been combined to obtain the final differential distribution for each interference terms, leading to a complete virtual differential cross section contribution.

The real corrections have been obtained through standard algorithms, involving the decomposition of the real amplitude into the Passarino-Veltmann tensor basis, and by taking its analytical square average. Every analytical step has been implemented in a MATHEMATICA code that provides the square amplitude of every real correction channel. The IR divergences have been subtracted by the same term used for subtracting the virtual IR singularities. The integration over the three-particle

phase space has led to the real differential cross section.

The SM case has been studied in detail. The finite top-mass effects to the NLO total cross section introduce a 15% correction to the NLO HTL calculation. More noticeable effects can be seen at the level of the differential distribution, where the finite top mass introduces a deviation in its tail down to -40% . The results for the central values at different centre-of-mass energies are in complete agreement with the literature, as well as the reduction of the renormalization and factorization scale uncertainties. The total cross section as a function of the trilinear Higgs coupling shows significant deviation from the HTL due to top-mass effects, leading to a noticeable shift of its minimum.

The framework built for this calculation allows the choice of different top-mass renormalization scheme and scales, suitable for the first estimation the uncertainties they introduce. The $\overline{\text{MS}}$ top mass at different scale choices has underlined the importance of these uncertainties, that amounts to -15% at the total cross section level and to -35% at the differential cross section level. The behaviour of the differential cross section at different renormalization scales has been discussed, and it has been shown how a dynamical renormalization scale is the most natural choice for large Higgs-pair invariant mass. The quasi-independence of the relative top-mass uncertainties from the renormalization and factorization scheme leads to a linear addition of the uncertainties since they have been defined as envelopes of multiple distributions. The combination of the NLO top-mass uncertainties and the NNLO renormalization and factorization uncertainties has been discussed, and from a factorization of the cross section argument, the most conservative treatment of the uncertainties has been identified as their linear sum.

The framework described in this thesis has already been applied successfully to the 2HDM; some results regarding the neutral scalar Higgs-pair production has been shown in Chapter 4. Further future applications will involve final states containing pseudoscalars. Moreover, the dependence on the β angle of the Yukawa couplings in the 2HDM may lead to non-negligible contributions from bottom quark loops, for which additional treatments on the form factors are needed to increase the numerical stability, like bottom-quark mass expansions and integration by parts.

Appendix A

HTL gluon-Higgs effective vertex

The low-energy Higgs effective Lagrangian contains the effective gluon-Higgs interaction vertices. Such interactions can be obtained from the SM Lagrangian by taking the heavy-top limit of the QCD induced Higgs production via gluon fusion. This amplitude has been calculated in Chapter 2 in the case where an incoming gluon is off-shell. Starting from that expression, the analytical limit can be calculated.

For both the HTL limit and the on-shell limit, the parameters λ and τ behave in the same way:

$$\lambda, \tau \xrightarrow[m_t^2 \rightarrow \infty]{p_t^2 \rightarrow 0} \infty, \quad (\text{A.1})$$

therefore the functions $f(\lambda)$ and $g(\lambda)$ have the same behaviour in both limits. The functions $f(\lambda)$ and $g(\lambda)$ are defined as follows:

$$f(\lambda) = -\frac{1}{4} \log^2 \left(-\frac{\alpha_+}{\alpha_-} \right), \quad g(\lambda) = \frac{\sqrt{1-\lambda}}{2} \log \left(-\frac{\alpha_+}{\alpha_-} \right), \quad (\text{A.2})$$

$$\alpha_{\pm} = 1 \pm \sqrt{1-\lambda},$$

The limit of α_{\pm} for $\lambda \rightarrow \infty$ is

$$\alpha_{\pm} \sim_{\lambda \rightarrow \infty} 1 \pm i\sqrt{\lambda} \left(1 - \frac{1}{2\lambda} \right) = 1 \mp \frac{i}{2\sqrt{\lambda}} \pm i\sqrt{\lambda}, \quad (\text{A.3})$$

and the inverse of α_- has the following behaviour:

$$\begin{aligned} \frac{1}{\alpha_-} \sim_{\lambda \rightarrow \infty} \frac{1}{1 + \frac{i}{2\sqrt{\lambda}} - i\sqrt{\lambda}} &= \frac{i}{\sqrt{\lambda}} \frac{1}{1 + \frac{i}{\sqrt{\lambda}} - \frac{1}{2\lambda}} \sim_{\lambda \rightarrow \infty} \frac{i}{\sqrt{\lambda}} \left(1 - \frac{i}{\sqrt{\lambda}} - \frac{1}{2\lambda} \right) \\ &= \frac{i}{\sqrt{\lambda}} + \frac{1}{\lambda} - \frac{i}{2\lambda\sqrt{\lambda}}. \end{aligned} \quad (\text{A.4})$$

Hence

$$\begin{aligned} -\frac{\alpha_+}{\alpha_-} &= - \left(1 - \frac{i}{2\sqrt{\lambda}} + i\sqrt{\lambda} \right) \left(\frac{i}{\sqrt{\lambda}} + \frac{1}{\lambda} - \frac{i}{2\lambda\sqrt{\lambda}} \right) \\ &= 1 - \frac{2i}{\sqrt{\lambda}} - \frac{2}{\lambda} + \frac{i}{\lambda\sqrt{\lambda}}, \end{aligned} \quad (\text{A.5})$$

and from

$$\begin{aligned} \log(1 + ax + bx^2 + cx^3) \sim_{x \rightarrow 0} (ax + bx^2 + cx^3) - \frac{1}{2}(ax + bx^2)^2 + \frac{1}{3}(ax)^3 \\ \sim ax + \left(b - \frac{1}{2}a^2 \right) x^2 + \left(c - ab + \frac{1}{3}a^3 \right) x^3, \end{aligned} \quad (\text{A.6})$$

the logarithm occurring into the definitions of $f(\lambda)$ and $g(\lambda)$ is

$$\begin{aligned} \log \left[-\frac{\alpha_+}{\alpha_-} \right] &\sim_{\lambda \rightarrow \infty} \log \left[1 - 2i \frac{1}{\sqrt{\lambda}} - 2 \left(\frac{1}{\sqrt{\lambda}} \right)^2 + i \left(\frac{1}{\sqrt{\lambda}} \right)^3 \right] \\ &\sim_{\lambda \rightarrow \infty} -\frac{2i}{\sqrt{\lambda}} + (-2 + 2) \left(\frac{1}{\sqrt{\lambda}} \right)^2 + \left(i - 4i + \frac{8}{3}i \right) \left(\frac{1}{\sqrt{\lambda}} \right)^3 \\ &\sim_{\lambda \rightarrow \infty} -i \left(2 \frac{1}{\sqrt{\lambda}} + \frac{1}{3} \frac{1}{\lambda \sqrt{\lambda}} \right). \end{aligned} \quad (\text{A.7})$$

Therefore, $f(\lambda)$ in the limit $\lambda \rightarrow \infty$ has the following series expansion:

$$\begin{aligned} f(\lambda) &= -\frac{1}{4} \log^2 \left[-\frac{\alpha_+}{\alpha_-} \right] = \left(\frac{1}{\sqrt{\lambda}} + \frac{1}{6} \frac{1}{\lambda \sqrt{\lambda}} \right)^2 + O \left(\frac{1}{\lambda^3} \right) \\ &= \frac{1}{\lambda} + \frac{1}{3\lambda^2} + O \left(\frac{1}{\lambda^3} \right) \end{aligned} \quad (\text{A.8})$$

Going further with the expansion, the third expansion term is

$$f(\lambda) = \frac{1}{\lambda} + \frac{1}{3\lambda^2} + \frac{8}{45\lambda^3} + O \left(\frac{1}{\lambda^4} \right) \quad (\text{A.9})$$

Moving the discussion to the function $g(\lambda)$:

$$\begin{aligned} g(\lambda) &= \frac{\sqrt{1-\lambda}}{2} \log \left(-\frac{\alpha_+}{\alpha_-} \right) = \sqrt{1-\frac{1}{\lambda}} \left(1 + \frac{1}{6\lambda} \right) + O \left(\frac{1}{\lambda^2} \right) \\ &= \left(1 - \frac{1}{2\lambda} \right) \left(1 + \frac{1}{6\lambda} \right) + O \left(\frac{1}{\lambda^3} \right) \\ &= 1 - \frac{1}{3\lambda} + O \left(\frac{1}{\lambda^2} \right) \end{aligned} \quad (\text{A.10})$$

and, adding an additional order to $g(\lambda)$:

$$g(\lambda) \sim_{\lambda \rightarrow \infty} 1 - \frac{1}{3\lambda} - \frac{2}{15\lambda^2} \quad (\text{A.11})$$

A.1 ggH_j effective vertex

From the result of Chapter 2, the gluon-Higgs effective vertex is the on-shell and heavy-top limit of the $gg \rightarrow H_j$ amplitude:

$$\begin{aligned} \text{Diagram} &= \lim_{\tau, \lambda \rightarrow \infty} \mathcal{M}_{\Delta}^{\mu\nu, ab} = i \left(\frac{\alpha_s}{\pi v} \right) \delta^{ab} \left(\frac{4\pi\mu^2}{m_t^2} \right)^{\epsilon} \Gamma(1 + \epsilon) [(p \cdot q)g^{\mu\nu} - q^{\mu}p^{\nu}] \lim_{\tau, \lambda \rightarrow \infty} \mathcal{I}(\tau, \lambda), \end{aligned} \quad (\text{A.12})$$

where

$$\mathcal{I}(\tau, \lambda) = \frac{\tau\lambda}{2(\tau-\lambda)} + \frac{\tau^2\lambda}{(\tau-\lambda)^2} [g(\tau) - g(\lambda)] + \frac{\tau^2\lambda^2}{2(\tau-\lambda)^2} [f(\tau) - f(\lambda)] + \frac{\tau\lambda}{2(\tau-\lambda)} [f(\tau) - f(\lambda)]. \quad (\text{A.13})$$

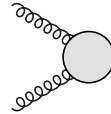
The on-shell limit $\lambda \rightarrow \infty$ yields:

$$\begin{aligned}
\frac{\tau\lambda}{2(\tau-\lambda)} &\sim -\frac{\tau}{2} - \frac{\tau^2}{2\lambda} \\
\frac{\tau^2\lambda}{(\tau-\lambda)^2} [g(\tau) - g(\lambda)] &\sim -\frac{\tau^2}{\lambda} + \frac{\tau^2}{\lambda} g(\tau) \\
\frac{\tau^2\lambda^2}{2(\tau-\lambda)^2} [f(\tau) - f(\lambda)] &\sim \frac{\tau^2}{2} f(\tau) + \frac{\tau^2}{\lambda} \frac{(2\tau f(\tau) - 1)}{2} \\
\frac{\tau\lambda}{2(\tau-\lambda)} [f(\tau) - f(\lambda)] &\sim -\frac{\tau}{2} f(\tau) - \frac{\tau}{\lambda} \frac{(\tau f(\tau) - 1)}{2} \\
&\Downarrow \\
\mathcal{I}(\tau, \infty) = \lim_{\lambda \rightarrow \infty} \mathcal{I}(\tau, \lambda) &= -\frac{\tau}{2} [1 - \tau f(\tau) + f(\tau)],
\end{aligned} \tag{A.14}$$

and the HTL:

$$\begin{aligned}
\mathcal{I}(\tau, \infty) &\sim -\frac{\tau}{2} \left[-\frac{1}{3\tau} + \frac{1}{\tau} \right] \\
&\Downarrow \\
\lim_{\lambda, \tau \rightarrow \infty} \mathcal{I}(\tau, \lambda) &= -\frac{1}{3}.
\end{aligned} \tag{A.15}$$

Therefore, the gluon-Higgs effective vertex is

$$
= -i \left(\frac{\alpha_s}{3\pi v} \right) \delta^{ab} \left(\frac{4\pi\mu^2}{m_t^2} \right)^\epsilon \Gamma(1 + \epsilon) [(p \cdot q)g^{\mu\nu} - q^\mu p^\nu]. \tag{A.16}$$

Notice that the two limits do commute.

Appendix B

General tensors for the $gg \rightarrow H_1 H_2$ process

The amplitude of $gg \rightarrow H_1 H_2$ is a rank-2 tensor depending on the external momenta p_1, p_2, p_3 :

$$\mathcal{M}^{\mu\nu} = a_{00}g^{\mu\nu} + \sum_{i,j=1}^3 a_{ij}p_i^\mu p_j^\nu \quad (\text{B.1})$$

where a_{00} and a_{ij} are the coefficients of the tensor basis, which will depend on the process. First of all, the incoming gluons are physical, i.e. transverse with respect to their momenta:

$$p_i^\sigma \epsilon_\sigma(p_i) = 0. \quad (\text{B.2})$$

Consider the gluon with momentum p_1 contracted with the first index μ , and the gluon with momentum p_2 contracted with the second index ν of $\mathcal{M}^{\mu\nu}$. With this consideration, since $p_1^\mu \epsilon_\mu(p_1) = p_2^\nu \epsilon_\nu(p_2) = 0$, the general tensor $\mathcal{M}^{\mu\nu}$ reads:

$$\mathcal{M}^{\mu\nu} = a_{00}g^{\mu\nu} + a_{21}p_2^\mu p_1^\nu + a_{31}p_3^\mu p_1^\nu + a_{23}p_2^\mu p_3^\nu + a_{33}p_3^\mu p_3^\nu \quad (\text{B.3})$$

If one performs the calculation in the axial gauge, in general, there will be complicated tensor structures for propagators and polarization sum. However, it allows to use the QED-like Ward identities for on-shell gluons:

$$p_{1\mu}\mathcal{M}^{\mu\nu} = 0, \quad p_{2\nu}\mathcal{M}^{\mu\nu} = 0. \quad (\text{B.4})$$

The Ward identities provide the following conditions

$$\begin{cases} p_{1\mu}p_{1\nu}T^{\mu\nu} = 0 \\ p_{1\mu}p_{2\nu}T^{\mu\nu} = 0 \\ p_{2\mu}p_{2\nu}T^{\mu\nu} = 0 \end{cases}, \quad (\text{B.5})$$

$$\begin{cases} a_{23}(p_1 \cdot p_2) + a_{33}(p_1 \cdot p_3) = 0 \\ a_{00}(p_1 \cdot p_2) + a_{21}(p_1 \cdot p_2)^2 + a_{31}(p_1 \cdot p_3)(p_1 \cdot p_2) + a_{23}(p_1 \cdot p_2)(p_2 \cdot p_3) + a_{33}(p_1 \cdot p_3)(p_2 \cdot p_3) = 0 \\ a_{31}(p_1 \cdot p_2) + a_{33}(p_2 \cdot p_3) = 0 \end{cases}.$$

The first and the last equation give

$$a_{23} = -\frac{(p_1 \cdot p_3)}{(p_1 \cdot p_2)}a_{33}, \quad a_{31} = -\frac{(p_2 \cdot p_3)}{(p_1 \cdot p_2)}a_{33}, \quad (\text{B.6})$$

and replacing these results in the second equation it follows that

$$a_{00} = \frac{a_{33}(p_1 \cdot p_3)(p_2 \cdot p_3) - a_{21}(p_1 \cdot p_2)^2}{(p_1 \cdot p_2)}. \quad (\text{B.7})$$

The amplitude becomes

$$T^{\mu\nu} = a_{12} [-(p_1 \cdot p_2)g^{\mu\nu} + p_2^\mu p_1^\nu] + a_{33} \left(\frac{(p_1 \cdot p_3)(p_2 \cdot p_3)}{(p_1 \cdot p_2)} g^{\mu\nu} - \frac{(p_2 \cdot p_3)}{(p_1 \cdot p_2)} p_1^\mu p_3^\nu - \frac{(p_1 \cdot p_3)}{(p_1 \cdot p_2)} p_2^\mu p_3^\nu + p_3^\mu p_3^\nu \right), \quad (\text{B.8})$$

and factoring out the terms proportional to $g^{\mu\nu}$, the tensor reads:

$$\begin{aligned} a_{12} &\rightarrow -\frac{a_{21}}{(p_1 \cdot p_2)}, & a_{33} &\rightarrow \frac{(p_1 \cdot p_2)}{(p_1 \cdot p_3)(p_2 \cdot p_3)} a_{33} \\ \mathcal{M}^{\mu\nu} &= a_{12} \left(g^{\mu\nu} - \frac{p_2^\mu p_1^\nu}{(p_1 \cdot p_2)} \right) + a_{33} \left(g^{\mu\nu} - \frac{(p_2 \cdot p_3)p_1^\mu p_3^\nu + (p_1 \cdot p_3)p_2^\mu p_3^\nu - (p_1 \cdot p_2)p_3^\mu p_3^\nu}{(p_1 \cdot p_3)(p_2 \cdot p_3)} \right) \\ &= a_{12} \tilde{T}_1^{\mu\nu} + a_{33} \tilde{T}_2^{\mu\nu} \end{aligned} \quad (\text{B.9})$$

The tensors $\tilde{T}_1^{\mu\nu}$ and $\tilde{T}_2^{\mu\nu}$ are not orthogonal in four dimensions. Using $\tilde{T}_1^{\mu\nu}$ as reference, the Gram-Schmidt orthogonalization yields:

$$\begin{aligned} T_1^{\mu\nu} &= \tilde{T}_1^{\mu\nu} \\ T_2^{\mu\nu} &= \tilde{T}_2^{\mu\nu} - \frac{(\tilde{T}_2^{\mu\nu} T_{1\mu\nu})}{(T_1^{\mu\nu} T_{1\mu\nu})} T_{1\mu\nu} \end{aligned} \quad (\text{B.10})$$

that can be enforced by the shift

$$a_{12} = F_1 - \frac{(\tilde{T}_2^{\mu\nu} T_{1\mu\nu})}{(T_1^{\mu\nu} T_{1\mu\nu})} = F_1 - \frac{1}{2} \frac{(p_1 \cdot p_2)p_3^2}{(p_1 \cdot p_3)(p_2 \cdot p_3)}. \quad (\text{B.11})$$

Therefore, the amplitude is

$$\begin{aligned} \mathcal{M}^{\mu\nu} &= F_1 T_1^{\mu\nu} + a_{33} \left(\frac{2(p_1 \cdot p_3)(p_2 \cdot p_3) - (p_1 \cdot p_2)p_3^2}{2(p_1 \cdot p_3)(p_2 \cdot p_3)} g^{\mu\nu} \right. \\ &\quad \left. + \frac{p_3^2 p_2^\mu p_1^\nu - 2(p_2 \cdot p_3)p_1^\mu p_3^\nu - 2(p_1 \cdot p_3)p_2^\mu p_3^\nu + 2(p_1 \cdot p_2)p_3^\mu p_3^\nu}{2(p_1 \cdot p_3)(p_2 \cdot p_3)} \right) \end{aligned} \quad (\text{B.12})$$

and defining the transverse momentum by

$$p_T^2 = \frac{2(p_1 \cdot p_3)(p_2 \cdot p_3)}{(p_1 \cdot p_2)} - p_3^2, \quad (\text{B.13})$$

it becomes

$$\begin{aligned} a_{33} &= \frac{2(p_1 \cdot p_3)(p_2 \cdot p_3)}{(p_1 \cdot p_2)p_T^2} F_2 \\ \mathcal{M}^{\mu\nu} &= F_1 T_1^{\mu\nu} + F_2 \left(g^{\mu\nu} + \frac{p_3^2 p_2^\mu p_1^\nu - 2(p_2 \cdot p_3)p_1^\mu p_3^\nu - 2(p_1 \cdot p_3)p_2^\mu p_3^\nu + 2(p_1 \cdot p_2)p_3^\mu p_3^\nu}{(p_1 \cdot p_2)p_T^2} \right) \\ &= F_1 T_1^{\mu\nu} + F_2 T_2^{\mu\nu} \end{aligned} \quad (\text{B.14})$$

and

$$\begin{aligned} T_1^{\mu\nu} &= g^{\mu\nu} - \frac{p_2^\mu p_1^\nu}{(p_1 \cdot p_2)}, \\ T_2^{\mu\nu} &= g^{\mu\nu} + \frac{p_3^2 p_2^\mu p_1^\nu - 2(p_2 \cdot p_3)p_1^\mu p_3^\nu - 2(p_1 \cdot p_3)p_2^\mu p_3^\nu + 2(p_1 \cdot p_2)p_3^\mu p_3^\nu}{(p_1 \cdot p_2)p_T^2}. \end{aligned} \quad (\text{B.15})$$

It is easy to show that in d dimensions, the tensor basis satisfies $T_1^{\mu\nu} T_{1\mu\nu} = T_2^{\mu\nu} T_{2\mu\nu} = d - 2$ and $T_1^{\mu\nu} T_{2\mu\nu} = d - 4$. The projectors onto $T_1^{\mu\nu}$ and $T_2^{\mu\nu}$ can be defined by the following relations:

$$P_i^{\mu\nu} T_{j\mu\nu} = \delta_{ij}, \quad P_i^{\mu\nu} = a_{i1} T_{1\mu\nu} + a_{i2} T_{2\mu\nu}, \quad (\text{B.16})$$

and the solution of this system yields

$$P_1^{\mu\nu} = \frac{(d-2)T_1^{\mu\nu} + (d-4)T_2^{\mu\nu}}{4(d-3)}, \quad P_2^{\mu\nu} = \frac{(d-4)T_1^{\mu\nu} + (d-2)T_2^{\mu\nu}}{4(d-3)}. \quad (\text{B.17})$$

The projection of the amplitude onto the tensor basis $T_{1,2\mu\nu}$ is done by contracting $\mathcal{M}^{\mu\nu}$ with the projectors of Eq. (B.17); they give the form factors F_1 and F_2 which depend only on the kinematical variables and the space-time dimension d .

Appendix C

Phase space integral

The total cross section for a $2 \rightarrow n$ scattering process is the integral over the phase space of its square amplitude. The number of dimensions of the phase space depends on the number of particles involved in the process, and increases quickly with n . In this Appendix the phase space elements for the $2 \rightarrow 2$ and $2 \rightarrow 3$ particles will be presented. In particular, the treatment of the $2 \rightarrow 3$ phase space involves a factorization, of crucial importance to define the infrared subtraction terms needed for isolating the soft and collinear divergences.

C.1 $2 \rightarrow 2$ process

C.1.1 Kinematics

Consider the process

$$g(p_1) + g(p_2) \rightarrow H_1(p_3) + H_2(p_4). \quad (\text{C.1})$$

The definitions of the four-momenta (omitting the transpose notation) are: $p_1 = (E_1, E_1 \hat{a})$, $p_2 = (E_2, E_2 \hat{b})$ for the gluons and $p_3 = (\omega_3, \bar{p}_3 = |\bar{p}_3| \hat{c})$ and $p_4 = (\omega_4, \bar{p}_4 = |\bar{p}_4| \hat{d})$ for the two Higgs bosons, where we defined $\hat{a}, \hat{b}, \hat{c}, \hat{d}$ to be unit length vectors. In the center-of-mass frame, we have

$$\begin{aligned} p_1 + p_2 = p_3 + p_4 &= (\sqrt{\hat{s}}, \vec{0}) \\ \implies \begin{cases} (E_1 + E_2, E_1 \hat{a} + E_2 \hat{b}) = (\sqrt{\hat{s}}, \vec{0}) \\ (\omega_1 + \omega_2, |\bar{p}_3| \hat{c} + |\bar{p}_4| \hat{d}) = (\sqrt{\hat{s}}, \vec{0}) \end{cases} \end{aligned} \quad (\text{C.2})$$

From the 3-momentum components, we obtain:

$$\begin{aligned} E_1 \hat{a} = -E_2 \hat{b} &\implies E_1 = E_2 \quad \wedge \quad \hat{a} = -\hat{b} \\ |\bar{p}_3| \hat{c} = -|\bar{p}_4| \hat{d} &\implies |\bar{p}_3| = |\bar{p}_4| \quad \wedge \quad \hat{c} = -\hat{d}, \end{aligned} \quad (\text{C.3})$$

and from the conservation of the energy:

$$E_1 + E_2 = 2E_1 = \sqrt{\hat{s}} \implies E_1 = \frac{\sqrt{\hat{s}}}{2}. \quad (\text{C.4})$$

Therefore, incoming and outgoing particles lie on two different straight lines respectively. We chose the reference frame such that the incoming particles lie on the \hat{z} axis, and the outgoing ones lie on a straight line generated by the unit vector \hat{v} . Moreover, by momentum conservation, we set $|\bar{p}_3| = |\bar{p}_4| = p_{\text{cm}}$. The kinematics of the process become

$$\begin{aligned} p_1 &= \frac{\sqrt{\hat{s}}}{2}(1, \hat{z}), & p_2 &= \frac{\sqrt{\hat{s}}}{2}(1, -\hat{z}) \\ p_3 &= (\omega_3, p_{\text{cm}} \hat{v}), & p_4 &= (\omega_4, -p_{\text{cm}} \hat{v}) \\ \omega_3 + \omega_4 &= \sqrt{\hat{s}}. \end{aligned} \quad (\text{C.5})$$

The on-shell conditions state that $\omega_i^2 = p_{\text{cm}}^2 + m_{H_i}^2$, so that

$$\begin{aligned} \omega_3^2 - m_{H_1}^2 &= \omega_4^2 - m_{H_2}^2 \\ \omega_3^2 - m_{H_1}^2 &= (\sqrt{\hat{s}} - \omega_3)^2 - m_{H_2}^2, & (\sqrt{\hat{s}} - \omega_2)^2 - m_{H_1}^2 &= \omega_4^2 - m_{H_2}^2 \\ \omega_3 &= \frac{\hat{s} + m_{H_1}^2 - m_{H_2}^2}{2\sqrt{\hat{s}}}, & \omega_4 &= \frac{\hat{s} - m_{H_1}^2 + m_{H_2}^2}{2\sqrt{\hat{s}}}, \end{aligned} \quad (\text{C.6})$$

and defining $\Delta = \frac{m_{H_2}^2 - m_{H_1}^2}{\hat{s}}$, we get

$$\omega_3 = \frac{\sqrt{\hat{s}}}{2}(1 - \Delta), \quad \omega_4 = \frac{\sqrt{\hat{s}}}{2}(1 + \Delta). \quad (\text{C.7})$$

The Higgs boson momentum p_{cm} in the CM frame is

$$\begin{aligned} p_{\text{cm}}^2 &= \frac{\hat{s}}{4}(1 - \Delta)^2 - m_{H_1}^2 \\ &= \frac{\hat{s}}{4} \left(1 + \Delta^2 - 2 \left(\Delta + \frac{2m_{H_1}^2}{\hat{s}} \right) \right) \\ &= \frac{\hat{s}}{4} (1 + \Delta^2 - 2\Sigma) \\ \implies p_{\text{cm}} &= \frac{\sqrt{\hat{s}}}{2} \sqrt{1 + \Delta^2 - 2\Sigma} = \frac{\sqrt{\hat{s}}}{2} \beta, \end{aligned} \quad (\text{C.8})$$

where we defined

$$\Sigma = \frac{m_{H_1}^2 + m_{H_2}^2}{\hat{s}}. \quad (\text{C.9})$$

With these constraints, the transferred momentum square \hat{t} is

$$\begin{aligned} \hat{t} &= (p_3 - p_1)^2 = -2(p_1 \cdot p_3) + p_3^2 \\ &= m_{H_1}^2 + p_{\text{cm}} \sqrt{\hat{s}} (\hat{z} \cdot \hat{v}) - \sqrt{\hat{s}} \omega_1 \\ &= m_{H_1}^2 + \frac{\hat{s}}{2} \beta \cos \theta - \frac{\hat{s}}{2} (1 - \Delta) \\ &= m_{H_1}^2 - \frac{\hat{s}}{2} (1 - \Delta - \beta \cos \theta) \\ &= -\frac{\hat{s}}{2} (1 - \Sigma - \beta \cos \theta). \end{aligned} \quad (\text{C.10})$$

Using momentum conservation, the missing kinematical variable is \hat{u} , which is

$$\hat{u} = -\frac{\hat{s}}{2} (1 - \Sigma + \beta \cos \theta). \quad (\text{C.11})$$

The independent variables are \hat{s} and \hat{t} . Since the total cross section at fixed \hat{s} is of interest, the phase space element will be integrated over \hat{t} .

C.1.2 d -dimensional Phase space integrals

The $a + b \rightarrow 1 + \dots + n$ differential cross section is

$$d\sigma \propto (\mu^2)^{\frac{4-d}{2}} \int \frac{d^{d-1}\mathbf{p}_1}{(2\pi)^{d-1}} \dots \frac{d^{d-1}\mathbf{p}_n}{(2\pi)^{d-1}} \frac{1}{(2\omega_1)} \dots \frac{1}{(2\omega_n)} (2\pi)^d \delta^d(P - p_1 - \dots - p_n) \overline{|\mathcal{M}|^2}, \quad (\text{C.12})$$

where the integration is performed over the d.o.f. for which the amplitude does not depend on and \hat{t} , $\overline{|\mathcal{M}|^2}$ is the square amplitude averaged over the polarizations and $P = p_a + p_b$ is the total incoming momentum. Hence, we can define

$$dR_n = (\mu^2)^{\frac{4-d}{2}} \int \frac{d^{d-1}\mathbf{p}_1}{(2\pi)^{d-1}} \dots \frac{d^{d-1}\mathbf{p}_n}{(2\pi)^{d-1}} \frac{1}{(2\omega_1)} \dots \frac{1}{(2\omega_n)} (2\pi)^d \delta^d(P - p_1 - \dots - p_n). \quad (\text{C.13})$$

We are interested in dR_2 i.e. the phase space element of the $2 \rightarrow 2$ scattering process:

$$dR_2 = (\mu^2)^{\frac{4-d}{2}} \int \frac{d^{d-1}\mathbf{p}_3}{(2\pi)^{d-1}} \frac{d^{d-1}\mathbf{p}_4}{(2\pi)^{d-1}} \frac{1}{(2\omega_3)} \frac{1}{(2\omega_4)} (2\pi)^d \delta^d(P - p_3 - p_4), \quad (\text{C.14})$$

where $P = p_1 + p_2 = (\sqrt{\hat{s}}, \bar{0}_{d-1})$ and p_3, p_4 are the two Higgs boson momenta. Using the identity

$$\int \frac{d^{d-1}\mathbf{p}_4}{(2\pi)^{d-1}} \frac{1}{2\omega_4} = \int \frac{d^d p_4}{(2\pi)^{d-1}} \delta(p_4^2 - m_{H_2}^2) \Theta(\omega_4), \quad (\text{C.15})$$

we obtain

$$\begin{aligned} dR_2 &= (\mu^2)^{\frac{4-d}{2}} \int \frac{d^{d-1}\mathbf{p}_3}{(2\pi)^{d-1}} \frac{d^d p_4}{(2\pi)^{d-1}} \frac{1}{2\omega_3} \delta(p_4^2 - m_{H_2}^2) \Theta(\omega_4) (2\pi)^d \delta^d(P - p_3 - p_4) \\ &= \frac{(\mu^2)^{\frac{4-d}{2}}}{(2\pi)^{d-2}} \int \frac{d^{d-1}\mathbf{p}_3}{2\omega_3} \delta((P - p_3)^2 - m_{H_2}^2) \Theta(\sqrt{\hat{s}} - \omega_3). \end{aligned} \quad (\text{C.16})$$

The delta function can be transformed as follows

$$\begin{aligned} (P - p_3)^2 - m_{H_2}^2 &= s - 2\sqrt{\hat{s}}\omega_3 + m_{H_1}^2 - m_{H_2}^2, \\ \delta((P - p_3)^2 - m_{H_2}^2) &= \frac{1}{2\sqrt{\hat{s}}} \delta\left(\omega_3 - \frac{\sqrt{\hat{s}}}{2}(1 - \Delta)\right). \end{aligned} \quad (\text{C.17})$$

The integration of the momenta in d -dimensional spherical coordinates reads

$$d^{d-1}\mathbf{p}_3 = p_{\text{cm}}^{d-2} dp_{\text{cm}} d\Omega = p_{\text{cm}}^{d-3} \omega_3 d\omega_3 d\Omega_{d-2}, \quad (\text{C.18})$$

the integral reads as

$$\begin{aligned} dR_2 &= \frac{(\mu^2)^{\frac{4-d}{2}}}{4(2\pi)^{d-2}} \int \frac{d\omega_3 d\Omega_{d-2}}{\sqrt{\hat{s}}} p_{\text{cm}}^{d-3} \delta\left(\omega_3 - \frac{\sqrt{\hat{s}}}{2}(1 - \Delta)\right) \Theta(\sqrt{\hat{s}} - \omega_3) \\ &= (\mu^2)^{\frac{4-d}{2}} \frac{p_{\text{cm}}^{d-3}}{4(2\pi)^{d-2} \sqrt{\hat{s}}} \int d\Omega_{d-2} \Theta\left(\frac{\sqrt{\hat{s}}}{2}(1 + \Delta)\right) \\ &= (\mu^2)^{\frac{4-d}{2}} \frac{\hat{s}^{\frac{d-4}{2}} \beta^{d-3}}{2^{2d-3} \pi^{d-2}} \int d\Omega_{d-2}. \end{aligned} \quad (\text{C.19})$$

The condition on the Heaviside function is always satisfied ($\Delta > 0$).

The $(d-2)$ -dimensional sphere can be integrated over $(d-3)$ angles since they do not play any role in the scattering, and can be integrated out directly. The integration yields:

$$\begin{aligned} \int d\Omega_{d-2} &= d\theta \sin^{d-3} \theta \left[\int_0^\pi d\phi_2 \sin^{d-4} \phi_2 \right] \cdots \left[\int_0^\pi d\phi_{d-3} \sin \phi_{d-3} \right] \left[\int_0^{2\pi} d\phi_{d-2} \right] \\ &= d\theta \sin^{d-3} \theta \int d\Omega_{d-3}, \end{aligned} \quad (\text{C.20})$$

The angle element $d\theta$ has been factorized since the integrand will depend explicitly on it.

Using the following identity

$$\int_0^\pi d\phi_j \sin^n \phi_j \cos^m \phi_j = \frac{1}{2} \frac{\Gamma(\frac{1}{2}(n+1)) \Gamma(\frac{1}{2}(m+1))}{\Gamma(\frac{1}{2}(n+m)+1)}, \quad (\text{C.21})$$

for $m = 0$, the volume element becomes

$$\begin{aligned} \int d\Omega_{d-2} &= \left[\frac{\Gamma(\frac{d-3}{2}) \Gamma(\frac{1}{2})}{\Gamma(\frac{d-2}{2})} \right] \left[\frac{\Gamma(\frac{d-4}{2}) \Gamma(\frac{1}{2})}{\Gamma(\frac{d-3}{2})} \right] \cdots \left[\frac{\Gamma(1) \Gamma(\frac{1}{2})}{\Gamma(\frac{3}{2})} \right] \left[\int_0^{2\pi} d\phi_{d-2} \right] \sin^{d-3} \theta d\theta \\ &= \left[\frac{\Gamma^{d-4}(\frac{1}{2})}{\Gamma(\frac{d-2}{2})} \right] \left[\int_0^{2\pi} d\phi_{d-2} \right] \sin^{d-3} \theta d\theta, \end{aligned} \quad (\text{C.22})$$

which contains a remarkable value of the Gamma function, such as

$$\Gamma\left(\frac{1}{2}\right) = \pi^{\frac{1}{2}}. \quad (\text{C.23})$$

Therefore, we get

$$\int d\Omega_{d-2} = \frac{2\pi^{1-\epsilon}}{\Gamma(1-\epsilon)} \sin^{d-3} \theta d\theta, \quad (\text{C.24})$$

where we have integrated over the ϕ_{d-2} angle since the scattering occurs on the \widehat{xz} plane. We will see that we are not legitimate to integrate over this variable for the calculation of dR_3 since the $2 \rightarrow 3$ scattering does not happen on a single plane. An important result of this integration states that:

$$d\Omega_{n-1} = \frac{2\pi^{\frac{n}{2}}}{\Gamma\left(\frac{n}{2}\right)} = \frac{2\pi^{\frac{n-1}{2}}}{\Gamma\left(\frac{n-1}{2}\right)} \sin^{n-2} \theta d\theta \quad (\text{C.25})$$

We can first present the result of the integration over the whole phase space:

$$\begin{aligned} \int dR_2 &= \left(\frac{\mu^2}{\hat{s}}\right)^\epsilon \frac{\beta^{1-2\epsilon}}{4^{2-2\epsilon}\pi^{1-\epsilon}} \frac{1}{\Gamma(1-\epsilon)} \int \sin^{d-3} \theta d\theta \\ &= \left(\frac{\mu^2}{\hat{s}}\right)^\epsilon \frac{\beta^{1-2\epsilon}}{4^{2-2\epsilon}\pi^{1-\epsilon}} \frac{1}{\Gamma(1-\epsilon)} \left[\frac{\Gamma(1-\epsilon)\Gamma\left(\frac{1}{2}\right)}{\Gamma\left(\frac{1}{2}+1-\epsilon\right)} \right]. \end{aligned} \quad (\text{C.26})$$

A useful identity involving the Gamma function is:

$$\Gamma(2n) = \frac{4^n}{\sqrt{4\pi}} \Gamma(n) \Gamma\left(\frac{1}{2} + n\right), \quad (\text{C.27})$$

which brings the phase space integral to the following form

$$\int dR_2 = \left(\frac{4\pi\mu^2}{\hat{s}}\right)^\epsilon \frac{\beta^{1-2\epsilon}}{8\pi} \frac{\Gamma(1-\epsilon)}{\Gamma(2-2\epsilon)}. \quad (\text{C.28})$$

If we keep the dependence on the θ angle, the expression is more involved

$$dR_2 = \left(\frac{4\pi\mu^2}{\hat{s}}\right)^\epsilon \frac{\beta^{1-2\epsilon}}{16\pi} \frac{1}{\Gamma(1-\epsilon)} \left(\frac{1-\cos^2\theta}{4}\right)^{-\epsilon} d\cos\theta, \quad (\text{C.29})$$

but the factor involving the cosine square can be simplified by using the explicit expression of $\cos\theta$ in Eq. (C.10) and the relations contained in Appendix F:

$$\begin{aligned} \frac{1-\cos^2\theta}{4} &= -\frac{1}{\beta^2} \left[\frac{(\hat{t}-m_{H_1}^2)(\hat{t}-m_{H_2}^2)+\hat{s}\hat{t}}{\hat{s}^2} \right] = \frac{1}{\beta^2} \frac{p_T^2}{\hat{s}} \\ &\Downarrow \\ dR_2 &= \left(\frac{4\pi\mu^2}{p_T^2}\right)^\epsilon \frac{\beta}{16\pi} \frac{1}{\Gamma(1-\epsilon)} d\cos\theta. \end{aligned} \quad (\text{C.30})$$

The integral over the θ angle is related to the transferred momentum square \hat{t} :

$$\hat{t} = -\frac{\hat{s}}{2}(1-\Sigma-\beta\cos\theta) \implies d\hat{t} = \frac{\hat{s}\beta}{2} d\cos\theta, \quad (\text{C.31})$$

hence we get the following final expression:

$$dR_2 = \left(\frac{4\pi\mu^2}{p_T^2}\right)^\epsilon \frac{1}{\Gamma(1-\epsilon)} \frac{d\hat{t}}{8\pi\hat{s}}. \quad (\text{C.32})$$

where p_T^2 depends on \hat{t} .

In general, the d -dimensional dependence of dR_2 can not be neglected, since it generates non-trivial finite terms once that the (IR divergent) renormalized square matrix element is considered. However, the matrix elements built in Chapter 3 are IR finite. Thus, the (finite) top-mass effects at LO and (virtual contributions at) NLO can be integrated safely over the four-dimensional phase space:

$$dR_2 = \frac{d\hat{t}}{8\pi\hat{s}} + O(\epsilon). \quad (\text{C.33})$$

C.1.3 Differential partonic cross section: setup

The differential cross section for the partonic scattering under investigation is

$$d\hat{\sigma} = C_{\text{flux}} C_{\text{sym}} \int d\text{PS}_2 \overline{|\mathcal{M}_{\text{LO}}|^2} \quad (\text{C.34})$$

where C_{flux} is the flux factor and C_{sym} is the symmetry factor. The flux coefficient C_{flux} for the QCD Higgs-pair production via gluon fusion process is

$$C_{\text{flux}} = \frac{1}{4\sqrt{(p_1 \cdot p_2)^2 - p_1^2 p_2^2}} = \frac{1}{4|p_1 \cdot p_2|} = \frac{1}{2\hat{s}} \quad (\text{C.35})$$

and the differential cross section becomes

$$\begin{aligned} d\hat{\sigma} &= C_{\text{sym}} \frac{dR_2}{2\hat{s}} \overline{|\mathcal{M}|^2} \\ &= \frac{C_{\text{sym}}}{2\hat{s}} \left(\frac{4\pi\mu^2}{p_T^2} \right)^\epsilon \frac{1}{\Gamma(1-\epsilon)} \frac{d\hat{t}}{8\pi\hat{s}} \overline{|\mathcal{M}|^2}. \end{aligned} \quad (\text{C.36})$$

We now extract the factor coming from the averaged square amplitude: each gluon in the initial state can have $(d-2)$ polarizations and $(N_c^2 - 1)$ colors. Therefore

$$\begin{aligned} d\hat{\sigma} &= \left(\frac{4\pi\mu^2}{p_T^2} \right)^\epsilon \frac{1}{\Gamma(1-\epsilon)} \frac{1}{(d-2)^2} \frac{C_{\text{sym}}}{(N_c^2 - 1)^2} \frac{d\hat{t}}{16\pi\hat{s}^2} \sum_{a,b} \sum_{h_1, h_2} |\mathcal{M}|^2 \\ &= \left(\frac{4\pi\mu^2}{p_T^2} \right)^\epsilon \frac{1}{\Gamma(1-\epsilon)} \frac{1}{(1-\epsilon)^2} \frac{C_{\text{sym}}}{4(N_c^2 - 1)^2} \frac{d\hat{t}}{16\pi\hat{s}^2} \sum_{a,b} \sum_{h_1, h_2} |\mathcal{M}|^2 \\ &= \left(\frac{4\pi\mu^2}{p_T^2} \right)^\epsilon \frac{1}{\Gamma(1-\epsilon)} \frac{1}{(1-\epsilon)^2} \frac{C_{\text{sym}}}{256} \frac{d\hat{t}}{16\pi\hat{s}^2} \sum_{a,b} \sum_{h_1, h_2} |\mathcal{M}|^2, \end{aligned} \quad (\text{C.37})$$

where C_{sym} is the factor which takes into account the permutation of the external legs. We can permute the initial state gluon but not the Higgs in the final state. Moreover, the final state Higgs bosons are different: no identical final state factor is needed. This implies $C_{\text{sym}} = 2$ and

$$\begin{aligned} d\hat{\sigma} &= \left(\frac{4\pi\mu^2}{p_T^2} \right)^\epsilon \frac{1}{\Gamma(1-\epsilon)} \frac{1}{(1-\epsilon)^2} \frac{2}{256} \frac{d\hat{t}}{16\pi\hat{s}^2} \sum_{a,b} \sum_{h_1, h_2} |\mathcal{M}|^2 \\ &= \left(\frac{4\pi\mu^2}{p_T^2} \right)^\epsilon \frac{1}{\Gamma(1-\epsilon)} \frac{1}{(1-\epsilon)^2} \frac{1}{128} \frac{d\hat{t}}{16\pi\hat{s}^2} \sum_{a,b} \sum_{h_1, h_2} |\mathcal{M}|^2 \\ &= \frac{d\hat{t}}{16\pi\hat{s}^2} \frac{1}{128} \sum_{a,b} \sum_{h_1, h_2} |\mathcal{M}|^2 + O(\epsilon). \end{aligned} \quad (\text{C.38})$$

C.1.4 Polarization sum

Assuming that a gluon is moving along the \hat{z} axis with momentum $p_1^\mu = \omega_1(1, \hat{z})$, its two physical polarization vectors can be written as¹

$$\epsilon_\mu^+(p_1) = \frac{1}{\sqrt{2}}(0, 1, i, 0), \quad \epsilon_\mu^-(p_1) = \frac{1}{\sqrt{2}}(0, 1, -i, 0). \quad (\text{C.39})$$

The polarization vectors satisfy the following relations:

$$p_1^\mu \epsilon_\mu^\pm(p_1) = 0, \quad \epsilon_\mu^{h_1}(p_1) \epsilon^{*h_2\mu}(p_1) = -\delta^{h_1 h_2}. \quad (\text{C.40})$$

¹The Lorenz gauge is implicitly assumed.

These relations are valid in d dimension as well. The basis can be completed by adding the longitudinal polarization and an additional light-like polarization vector:

$$\epsilon_L^\mu(p_1) = \frac{1}{\sqrt{2}}(1, \hat{z}) = \frac{p_1^\mu}{\sqrt{2}\omega_1}, \quad \tilde{\epsilon}_L^\mu(q) = \frac{1}{\sqrt{2}}(1, -\hat{z}) = \frac{q^\mu}{\sqrt{2}\omega_q}, \quad q^\mu = \omega_q(1, -\hat{z}), \quad (\text{C.41})$$

where q^μ is a *reference momentum*, whose 3-momentum is anti-parallel to the gluon 3-momentum. The completeness relation of this basis reads

$$-\epsilon_\mu^+(p_1)\epsilon_\nu^{*+}(p_1) - \epsilon_\mu^-(p_1)\epsilon_\nu^{*-}(p_1) + \epsilon_{L\mu}(p_1)\tilde{\epsilon}_{L\nu}^*(q) + \tilde{\epsilon}_{L\mu}(q)\epsilon_{L\nu}^*(p_1) = g_{\mu\nu}, \quad (\text{C.42})$$

and using the explicit expressions for the longitudinal four-vectors, the polarization sum takes the following form:

$$\sum_{h=\pm} \epsilon_\mu^h(p_1)\epsilon_\nu^{*h}(p_1) = -g_{\mu\nu} + \frac{p_{1\mu}q_\nu + q_\mu p_{1\nu}}{p_1 \cdot q} = -g_{\mu\nu} + \frac{p_{1\{\mu}q_{\nu\}}}{p_1 \cdot q}, \quad (\text{C.43})$$

where the $\{\dots\}$ is the symmetrization of the tensor with respect to the indices they wrap.

For QCD processes, if one wants to perform the QED-like polarization sum, namely

$$\sum_{h=\pm} \epsilon_\mu^h(p_1)\epsilon_\nu^{*h}(p_1) = -g_{\mu\nu} \quad (\text{C.44})$$

the ghost contributions are needed, otherwise the general polarization sum of Eq. (C.43) is mandatory in order to avoid the sum over the unphysical degrees of freedom. To make this point clear, the amplitude of the process under consideration can be written as

$$\mathcal{M} = \epsilon_\mu(p_1)\epsilon_\nu(p_2)\mathcal{M}^{\mu\nu}. \quad (\text{C.45})$$

The sum of over the physical polarization yields:

$$\begin{aligned} \sum_{h_1, h_2=\pm} |\mathcal{M}|^2 &= \sum_{h_1, h_2=\pm} \epsilon_\mu^{h_1}(p_1)\epsilon_\rho^{*h_1}(p_1)\epsilon_\nu^{h_2}(p_2)\epsilon_\sigma^{*h_2}(p_2)\mathcal{M}^{\mu\nu}\mathcal{M}^{\rho\sigma}, \\ \sum_{h_1, h_2=\pm} |\mathcal{M}|^2 &= \sum_{h_1=\pm} \epsilon_\mu^{h_1}(p_1)\epsilon_\rho^{*h_1}(p_1) \left[-g_{\nu\sigma} + \frac{p_{2\{\nu}q'_{\sigma\}}}{p_2 \cdot q'} \right] \mathcal{M}^{\mu\nu}\mathcal{M}^{*\rho\sigma} \\ &= \left[-\sum_{h_1=\pm} \epsilon_\mu^{h_1}(p_1)\epsilon_\rho^{*h_1}(p_1)g_{\nu\sigma} + \sum_{h_1=\pm} \epsilon_\mu^{h_1}(p_1)\epsilon_\rho^{*h_1}(p_1)\frac{p_{2\{\nu}q'_{\sigma\}}}{p_2 \cdot q'} \right] \mathcal{M}^{\mu\nu}\mathcal{M}^{*\rho\sigma}, \end{aligned} \quad (\text{C.46})$$

The polarization sum depicted in Eq. (C.46) is rather complex, but it can be simplified. It can be shown that

$$p_{1\mu}\epsilon_\nu^h(p_2)\mathcal{M}^{\mu\nu} \propto p_2^\nu\epsilon_\nu^h(p_2), \quad (\text{C.47})$$

which implies that, for a longitudinal polarization:

$$p_{1\mu}\epsilon_{L\nu}(p_2)\mathcal{M}^{\mu\nu} \propto p_2^\nu\epsilon_{L\nu}(p_2) = 0, \quad p_2^2 = 0, \quad (\text{C.48})$$

therefore

$$p_{1\mu}p_{2\nu}\mathcal{M}^{\mu\nu} = 0. \quad (\text{C.49})$$

In particular, it means that $p_{2\mu}\epsilon_\nu^h(p_2)\mathcal{M}^{\mu\nu} = 0$ if $\epsilon_\nu^h(p_2)p_2^\nu = 0$ for $h = \pm$ (meaning that such gluon is transverse).

Therefore, the second term in the parenthesis of Eq. (C.46) vanishes because of Eq. (C.47) for physical gluons:

$$\begin{aligned}
\sum_{h_1, h_2 = \pm} |\mathcal{M}|^2 &= \left[- \sum_{h_1 = \pm} \epsilon_\mu^{h_1}(p_1) \epsilon_\rho^{*h_1}(p_1) g_{\nu\sigma} \right] \mathcal{M}^{*\rho\sigma} \mathcal{M}^{\mu\nu} \\
&= \left[g_{\mu\rho} g_{\nu\sigma} - g_{\nu\sigma} \frac{p_{1\{\mu} q_{\rho\}}}{p_1 \cdot q} \right] \mathcal{M}^{*\rho\sigma} \mathcal{M}^{\mu\nu} \\
&= \left[g_{\mu\rho} g_{\nu\sigma} + \left(\sum_{h_2 = \pm} \epsilon_\nu^{h_2}(p_2) \epsilon_\sigma^{*h_2}(p_2) \right) \frac{p_{1\{\mu} q_{\rho\}}}{p_1 \cdot q} - \frac{p_{1\{\mu} q_{\rho\}}}{p_1 \cdot q} \frac{p_{2\{\nu} q'_{\sigma\}}}{p_2 \cdot q'} \right] \mathcal{M}^{*\rho\sigma} \mathcal{M}^{\mu\nu} \\
&= \left[g_{\mu\rho} g_{\nu\sigma} - \frac{p_{1\{\mu} q_{\rho\}}}{p_1 \cdot q} \frac{p_{2\{\nu} q'_{\sigma\}}}{p_2 \cdot q'} \right] \mathcal{M}^{*\rho\sigma} \mathcal{M}^{\mu\nu},
\end{aligned} \tag{C.50}$$

where again the transversality of $\epsilon^\nu(p_2)$ has been exploited. Finally, expanding the symmetrical combination in the parenthesis, the square amplitude reads:

$$\sum_{h_1, h_2 = \pm} |\mathcal{M}|^2 = \left[g_{\mu\rho} g_{\nu\sigma} - \frac{p_{1\rho} q_\mu p_{2\nu} q'_\sigma + p_{1\mu} q_\rho p_{2\sigma} q'_\nu}{(p_1 \cdot q)(p_2 \cdot q')} \right] \mathcal{M}^{*\rho\sigma} \mathcal{M}^{\mu\nu}. \tag{C.51}$$

A convenient choice of the reference momenta will introduce a further simplification: setting $q = p_2$ and $q' = p_1$, Eq. (C.46) becomes

$$\sum_{h_1, h_2 = \pm} |\mathcal{M}|^2 = \left[g_{\mu\rho} g_{\nu\sigma} - \frac{p_{2\mu} p_{2\nu} p_{1\rho} p_{1\sigma} + p_{1\mu} p_{1\nu} p_{2\rho} p_{2\sigma}}{(p_1 \cdot p_2)^2} \right] \mathcal{M}^{*\rho\sigma} \mathcal{M}^{\mu\nu}. \tag{C.52}$$

In general, the second term of Eq. (C.52) yields non-vanishing contribution of the polarization sum. However, in Appendix B the axial gauge has been used to extract the form factors; the expression of the amputated amplitude is

$$\mathcal{M}^{\mu\nu} = \delta_{ab} (F_1 T_1^{\mu\nu} + F_2 T_2^{\mu\nu}). \tag{C.53}$$

It is possible to show that

$$p_{1\mu} p_{1\nu} T_j^{\mu\nu} = p_{2\mu} p_{2\nu} T_j^{\mu\nu} = 0, \tag{C.54}$$

as expected from the tensors written in the axial gauge. Therefore, the second term of Eq. (C.52) will always lead to a vanishing contribution, and therefore it can be neglected:

$$\sum_{h_1, h_2 = \pm} |\mathcal{M}|^2 = g_{\mu\rho} g_{\nu\sigma} \mathcal{M}^{*\rho\sigma} \mathcal{M}^{\mu\nu}. \tag{C.55}$$

It is important to underline that Eq. (C.55) is a direct consequence of considering the polarization vectors in the axial gauge for the $2 \rightarrow 2$ process. For the $2 \rightarrow 3$ process no axial gauge form factors will be provided, and the general polarization sum of Eq. (C.43) have to be used.

C.1.5 Differential partonic cross section: Virtual corrections

At LO, the square amplitude (in $d = 4$) is

$$\begin{aligned}
|\mathcal{M}_{\text{LO}}|^2 &= g_{\mu\rho} g_{\nu\sigma} \mathcal{M}_{\text{LO}}^{*\rho\sigma} \mathcal{M}_{\text{LO}}^{\mu\nu} \\
&= \delta_{ab} \delta_{ba} \left[F_1^{(0)} T_1^{\mu\nu} + F_2^{(0)} T_2^{\mu\nu} \right]^* \left[F_1^{(0)} T_{1\mu\nu} + F_2^{(0)} T_{2\mu\nu} \right] \\
&= 2\delta_{ab} \delta_{ba} \left(|F_1^{(0)}|^2 + |F_2^{(0)}|^2 \right).
\end{aligned} \tag{C.56}$$

Putting all the ingredients together, the LO partonic cross sections reads

$$\begin{aligned}
d\hat{\sigma}_{\text{LO}} &= \frac{d\hat{t}}{16\pi\hat{s}^2} \frac{1}{128} \sum_{a,b} \sum_{h_1, h_2} |\mathcal{M}_{\text{LO}}|^2 \\
&= \frac{d\hat{t}}{16\pi\hat{s}^2} \frac{1}{64} \left(\sum_{a,b} \delta_{ab}\delta_{ba} \right) \left(|F_1^{(0)}|^2 + |F_2^{(0)}|^2 \right) \\
&= \frac{d\hat{t}}{16\pi\hat{s}^2} \frac{\text{Tr} [\text{id}_{N_c^2-1}]}{64} \left(|F_1^{(0)}|^2 + |F_2^{(0)}|^2 \right) \\
&= \frac{d\hat{t}}{128\pi\hat{s}^2} \left(|F_1^{(0)}|^2 + |F_2^{(0)}|^2 \right),
\end{aligned} \tag{C.57}$$

where $N_c = 3$.

At NLO, the interference between the one-loop and two-loop virtual amplitude have to be considered:

$$\begin{aligned}
\sum_{h_1, h_2 = \pm} 2\text{Re}\mathcal{M}_{\text{LO}}^* \mathcal{M}_{\text{NLO}} &= 2g_{\mu\rho}g_{\nu\sigma} \text{Re}\mathcal{M}_{\text{LO}}^{\mu\nu} \mathcal{M}_{\text{NLO}}^{*\rho\sigma} \\
&= 2\delta_{ab}\delta_{ba} \text{Re} \left[F_1^{(0)} T_1^{\mu\nu} + F_2^{(0)} T_2^{\mu\nu} \right]^* \left[F_1^{(1)} T_{1\mu\nu} + F_2^{(1)} T_{2\mu\nu} \right] \\
&= 4\delta_{ab}\delta_{ba} \text{Re} \left(F_1^{*(0)} F_1^{(1)} + F_2^{*(0)} F_2^{(1)} \right)
\end{aligned} \tag{C.58}$$

which leads to

$$d\Delta\hat{\sigma}_{\text{NLO}} = \frac{d\hat{t}}{64\pi\hat{s}^2} \text{Re} \left(F_1^{*(0)} F_1^{(1)} + F_2^{*(0)} F_2^{(1)} \right). \tag{C.59}$$

C.2 2 → 3 process

The 5-point kinematics are more involved than the 4-point one. Consider the 2 → 3 process

$$g(p_1) + g(p_2) \rightarrow H_1(p_3) + H_1(p_4) + g(p_5), \tag{C.60}$$

where an additional outgoing particle with four-momentum

$$p_5 = (E_5, \vec{p}_5), \tag{C.61}$$

has been considered. After applying the conservation of the four-momenta, the kinematics of the process can be written as

$$\begin{aligned}
p_1 + p_2 &= p_3 + p_4 + p_5 \\
&\Downarrow \\
\begin{cases} (E_1 + E_2, E_1\hat{a} + E_2\hat{b}) = (\sqrt{\hat{s}}, \vec{0}) \\ (E_3 + E_4 + E_5, E_3\hat{c} + E_4\hat{d} + E_5\hat{e}) = (\sqrt{\hat{s}}, \vec{0}) \end{cases} \\
&\Downarrow \\
E_1\hat{a} + E_2\hat{b} = 0 &\implies E_1\hat{a} = -E_2\hat{b} \implies E_1 = E_2 = \frac{\sqrt{\hat{s}}}{2}, \\
E_3 + E_4 + E_5 = \sqrt{\hat{s}} &\implies x_3 + x_4 + x_5 = 2, \quad E_i = x_i \frac{\sqrt{\hat{s}}}{2},
\end{aligned} \tag{C.62}$$

where x_i is the fraction of centre-of-mass energy \hat{s} . The momentum p_3 is parametrized such that it lies on the \hat{z} axis. Before explaining the details of the phase space, we introduce the relevant kinematical variables

$$2p_1 \cdot p_2 = \hat{s}, \quad -2p_1 \cdot p_5 = \hat{t}, \quad -2p_2 \cdot p_5 = \hat{u}, \quad (p_3 + p_4)^2 = \hat{s} + \hat{t} + \hat{u} = Q^2. \tag{C.63}$$

The incoming-particle four-momenta can be parametrized as follows

$$p_1 = \frac{\sqrt{\hat{s}}}{2}(1, \sin \theta_{15}, 0, \cos \theta_{15}), \quad p_2 = \frac{\sqrt{\hat{s}}}{2}(1, -\sin \theta_{15}, 0, -\cos \theta_{15}), \quad (\text{C.64})$$

where the scattering occurs in the $\hat{x}\hat{z}$ plane and the radiating parton p_5 lies on the \hat{z} axis; θ_{15} is the angle between p_1 and p_5 on the $\hat{x}\hat{z}$ plane:

$$p_5 = \frac{\sqrt{\hat{s}}}{2}x_5(1, 0, 0, 1). \quad (\text{C.65})$$

At last, we define the angle θ_{35} and φ_{35} that in spherical coordinates parametrize the direction of p_3 ; due to momentum conservation, these directions are sufficient to parametrize the scattering. Note that the same setup can be applied by choosing any of the outgoing momentum, and we can define the angles θ_{ij} and φ_{ij} for every couple of momenta.

Therefore, the kinematics of the process are:

$$\begin{aligned} p_3 &= \frac{\sqrt{\hat{s}}}{2}x_3(1, \beta_3 \cos \varphi_{35} \sin \theta_{35}, \beta_3 \sin \varphi_{35} \sin \theta_{35}, \beta_3 \cos \theta_{35}), \\ p_4 &= \frac{\sqrt{\hat{s}}}{2}(x_4, -x_3\beta_3 \cos \varphi_{35} \sin \theta_{35}, -x_3\beta_3 \sin \varphi_{35} \sin \theta_{35}, -x_5 - x_3\beta_3 \cos \theta_{35}), \end{aligned} \quad (\text{C.66})$$

$$\begin{aligned} \mu_i &= \frac{m_i}{\sqrt{\hat{s}}}, \\ \beta_i &= \sqrt{1 - 4\frac{\mu_i^2}{x_i^2}}, \quad \cos \theta_{ij} = \frac{2}{x_i x_j \beta_i \beta_j} \left(1 - x_i - x_j + \frac{x_i x_j}{2} + \mu_i + \mu_j - \mu_k \right). \end{aligned}$$

These definitions set boundaries on the parameters we have chosen. The particle production thresholds state that $(p_i + p_j)^2 \geq (m_i + m_j)^2$. For x_5 , we have

$$\begin{aligned} &\begin{cases} p_5^0 \geq 0 \\ (p_3 + p_4)^2 = (p_1 + p_2 - p_5)^2 \geq (m_{H_1} + m_{H_2})^2 \end{cases} \\ &\quad \downarrow \\ &0 \leq x_5 \leq 1 - (\mu_{H_1} + \mu_{H_2})^2. \end{aligned} \quad (\text{C.67})$$

The constraint on x_3 comes from the image of $\cos \theta_{35}$, meaning that it can be read from

$$\begin{aligned} -1 \leq \cos \theta_{35} \leq 1 &\implies \cos^2 \theta_{35} \leq 1 \\ &\downarrow \\ x_3^2(1 - x_5) - x_3(2 - x_5)(1 - x_5 - \Delta) + (1 - x_5 - \Delta)^2 + \mu_{H_1}^2 x_5^2 &\leq 0, \end{aligned} \quad (\text{C.68})$$

and solving for x_3 , we obtain the following condition:

$$\begin{aligned} x_3^- \leq x_3 \leq x_3^+ \\ x_3^\pm &= \frac{(2 - x_5)(1 - x_5 - \Delta) \pm x_5(1 - x_5)\beta_{x_5}}{2(1 - x_5)} \\ \beta_{x_5} &= \sqrt{\left[1 - \frac{(\mu_{H_2} + \mu_{H_1})^2}{(1 - x_5)} \right] \left[1 - \frac{(\mu_{H_2} - \mu_{H_1})^2}{(1 - x_5)} \right]}. \end{aligned} \quad (\text{C.69})$$

C.2.1 d -dimensional Phase space integrals

Recalling the definition presented in Section C.1.2, the phase space element dR_3 is

$$dR_3 = (\mu^2)^{\frac{4-d}{2}} \int \frac{d^{d-1}\mathbf{p}_3}{(2\pi)^{d-1}} \frac{d^{d-1}\mathbf{p}_4}{(2\pi)^{d-1}} \frac{d^{d-1}\mathbf{p}_5}{(2\pi)^{d-1}} \frac{1}{(2\omega_3)} \frac{1}{(2\omega_4)} \frac{1}{(2\omega_5)} (2\pi)^d \delta^d(P - p_3 - p_4 - p_5), \quad (\text{C.70})$$

where $P = p_1 + p_2 = (\sqrt{\hat{s}}, \bar{0}_{d-1})$ and p_3, p_4, p_5 are the two Higgs boson momenta and the additional parton. Similarly to the steps described for the 2-particle phase space, the integration over p_4 yields

$$\begin{aligned} dR_3 &= \frac{(\mu^2)^{4-d}}{(2\pi)^{2d-3}} \int \frac{d^{d-1}\mathbf{p}_3}{(2\omega_3)} \frac{d^{d-1}\mathbf{p}_5}{(2\omega_5)} d^d p_4 \delta(p_4^2 - m_{H_2}^2) \Theta(p_4^0) \delta^d(P - p_3 - p_4 - p_5) \\ &= \frac{(\mu^2)^{4-d}}{4(2\pi)^{2d-3}} \int \frac{d^{d-1}\mathbf{p}_3}{\omega_3} \frac{d^{d-1}\mathbf{p}_5}{\omega_5} \delta((P - p_3 - p_5)^2 - m_{H_2}^2). \end{aligned} \quad (\text{C.71})$$

The argument of the Dirac delta distribution is

$$\begin{aligned} (P - p_3 - p_5)^2 - m_{H_2}^2 &= \hat{s} - \hat{s}(x_3 + x_5) + \frac{\hat{s}}{2} x_3 x_5 (1 - \beta_3 \cos \theta_{35}) + m_{H_1}^2 - m_{H_2}^2 \\ &= \hat{s} \left[1 - x_3 - x_5 + \frac{x_3 x_5}{2} (1 - \beta_3 \cos \theta_{35}) - \Delta \right], \end{aligned} \quad (\text{C.72})$$

and we define the angle for which this expression vanished as

$$\cos \theta_{35}^0 = \frac{2}{\beta_3 x_3 x_5} \left[1 - \Delta - x_3 - x_5 + \frac{1}{2} x_3 x_5 \right]. \quad (\text{C.73})$$

Moreover, the integration measure in spherical coordinates becomes

$$d^{d-1}\mathbf{p}_3 = \frac{\hat{s}^{\frac{d-2}{2}} (x_3 \beta_3)^{d-3}}{2^{d-2}} \omega_3 dx_3 d\Omega_{d-2}^{(3)}, \quad (\text{C.74})$$

hence

$$dR_3 = \frac{(\mu^2)^{4-d} \hat{s}^{d-2}}{4(2\pi)^{2d-3} 4^{d-2}} \int dx_3 dx_5 d\Omega_{d-2}^{(3)} d\Omega_{d-2}^{(5)} (\beta_3 x_3 x_5)^{d-3} \frac{2}{s \beta_3 x_3 x_5} \delta(\cos \theta_{35} - \cos \theta_{35}^0). \quad (\text{C.75})$$

The angular elements are:

$$\begin{aligned} d\Omega_{d-2}^{(3)} &= \int \sin^{d-3} \theta_{35} \sin^{d-4} \phi_2 \cdots \sin \phi_{d-3} d\theta_{35} d\phi_2 \cdots d\phi_{d-2} \\ &= \left[\int \sin^{d-4} \phi_2 \cdots \sin \phi_{d-3} d\phi_2 \cdots d\phi_{d-2} \right] (1 - \cos^2 \theta_{35})^{\frac{d-4}{2}} d \cos \theta_{35} \\ &= \Omega_{d-3} (1 - \cos^2 \theta_{35})^{\frac{d-4}{2}} d \cos \theta_{35}, \end{aligned} \quad (\text{C.76})$$

$$d\Omega_{d-2}^{(5)} = \Omega_{d-4} (1 - \cos^2 \theta_{15})^{\frac{d-4}{2}} \sin^{d-4} \varphi_{35} d \cos \theta_{15} d\varphi_{35}.$$

The integral over the solid angle yields:

$$\Omega_n = \frac{2\pi^{\frac{n+1}{2}}}{\Gamma(\frac{n+1}{2})}, \quad (\text{C.77})$$

therefore

$$\begin{aligned} dR_3 &= \frac{(\mu^2)^{4-d} \hat{s}^{d-3}}{(2\pi)^{2d-3} 4^{d-2}} \frac{2\pi^{\frac{d-2}{2}} \pi^{\frac{d-3}{2}}}{\Gamma(\frac{d-2}{2}) \Gamma(\frac{d-3}{2})} \times \\ &\quad \times dx_3 dx_5 d \cos \theta_{15} d\varphi_{35} (1 - \cos^2 \theta_{35}^0)^{\frac{d-4}{2}} (1 - \cos^2 \theta_{15})^{\frac{d-4}{2}} \sin^{d-4} \varphi_{35} (\beta_3 x_3 x_5)^{d-4} \\ &= \frac{\hat{s}}{(4\pi)^4} \frac{4^{2\epsilon} \pi^{\frac{1}{2}}}{\Gamma(1-\epsilon) \Gamma(\frac{1}{2}-\epsilon)} \left(\frac{4\pi\mu^2}{\hat{s}} \right)^{2\epsilon} \times \\ &\quad \times dx_3 dx_5 d \cos \theta_{15} d\varphi_{35} (1 - \cos^2 \theta_{35}^0)^{-\epsilon} (1 - \cos^2 \theta_{15})^{-\epsilon} \sin^{-2\epsilon} \varphi_{35} (\beta_3 x_3 x_5)^{-2\epsilon}. \end{aligned} \quad (\text{C.78})$$

At last, using the following identity:

$$\Gamma\left(\frac{1}{2} - n\right) = 4^n \sqrt{\pi} \frac{\Gamma(1-2n)}{\Gamma(1-n)}, \quad (\text{C.79})$$

the phase-space integral becomes

$$dR_3 = \frac{\hat{s}}{(4\pi)^4} \left(\frac{4\pi\mu^2}{\hat{s}x_3x_5} \right)^{2\epsilon} \left(\beta_3^2 \frac{1 - \cos^2 \theta_{35}^0}{4} \right)^{-\epsilon} \frac{(1 - \cos^2 \theta_{15})^{-\epsilon} \sin^{-2\epsilon} \varphi_{35}}{\Gamma(1 - 2\epsilon)} dx_3 dx_5 d\cos \theta_{15} d\varphi_{35}. \quad (\text{C.80})$$

The dR_3 can be manipulated such that a R_2 factors, and the general integration boundaries of the fractions of the momenta x_3 and x_5 are set from 0 to 1. Notice that

$$\begin{aligned} \frac{1 - \cos \theta_{35}^0}{2} &= \frac{1}{2\beta_3} \left[\beta_3 - 1 + 2 \frac{(1 - x_4) + \Delta}{x_3 x_5} \right], \\ \frac{1 + \cos \theta_{35}^0}{2} &= \frac{1}{2\beta_3} \left[\beta_3 - 1 + 2 \frac{(1 - x_3)(1 - x_5) - \Delta}{x_3 x_5} \right], \\ x_3^2 x_5^2 \beta_3^2 \frac{1 - \cos^2 \theta_{35}^0}{4} &= (1 - x_4)(1 - x_3)(1 - x_5) - \mu_{H_1}^2 x_5^2 + \Delta[2(1 - x_3 - x_5) + x_3 x_5 - \Delta]. \end{aligned} \quad (\text{C.81})$$

Defining the variable z to be the fraction of the invariant Higgs-pair mass Q^2 with respect to $\sqrt{\hat{s}}$

$$z = \frac{Q^2}{\hat{s}} = \frac{(p_3 + p_4)^2}{\hat{s}} = 1 - x_5 \implies x_5 = 1 - z, \quad dx_5 = -dz, \quad (\text{C.82})$$

the Eq. (C.81) simplifies:

$$x_3^2 x_5^2 \beta_3^2 \frac{1 - \cos^2 \theta_{35}^0}{4} = (x_3 - z)(1 - x_3)z - \mu_{H_1}^2 (1 - z)^2 + \Delta[2(z - x_3) + x_3(1 - z) - \Delta]. \quad (\text{C.83})$$

Defining $x_3 = 1 - y$, the expression reads

$$x_3^2 x_5^2 \beta_3^2 \frac{1 - \cos^2 \theta_{35}^0}{4} = (1 - y - z)yz - \mu_{H_1}^2 (1 - z)^2 + \Delta[-2(1 - y - z) + (1 - y)(1 - z) - \Delta]. \quad (\text{C.84})$$

Finally, letting $y = (1 - z)x$, Eq. (C.81) reads

$$\begin{aligned} x_3^2 x_5^2 \beta_3^2 \frac{1 - \cos^2 \theta_{35}^0}{4} &= (1 - z)^2 z(1 - x)x - \mu_{H_1}^2 (1 - z)^2 - (1 - z)\Delta[1 - (1 + z)x] - \Delta^2, \\ &= z(1 - z)^2 \left[(1 - x)x - \frac{\mu_{H_1}^2}{z} - \frac{\Delta[1 - (1 + z)x]}{z(1 - z)} - \frac{\Delta^2}{z(1 - z)^2} \right] \end{aligned} \quad (\text{C.85})$$

This change of variables leads to the following integration measure:

$$\begin{aligned} \int_0^{1 - (\mu_{H_1} + \mu_{H_2})^2} dx_5 \int_{x_3^-}^{x_3^+} dx_3 &= \int_{(\mu_{H_1} + \mu_{H_2})^2}^1 dz \int_{x_-}^{x_+} dx (1 - z), \\ x^\pm &= \frac{1}{2} \left(1 + \frac{\Delta(1 + z)}{z(1 - z)} \pm \beta_z \right), \quad \beta_z = \sqrt{\left[1 - \frac{(\mu_{H_2} + \mu_{H_1})^2}{z} \right] \left[1 - \frac{(\mu_{H_2} - \mu_{H_1})^2}{z} \right]}. \end{aligned} \quad (\text{C.86})$$

Notice that the parameter β_z strongly resembles the β defined in the context of the $2 \rightarrow 2$ scattering: recalling the definition of Σ and Δ , a simple manipulation of its expression yields

$$\beta_z = \sqrt{1 - \frac{2\Sigma}{z} + \frac{\Delta^2}{z^2}}, \quad (\text{C.87})$$

that shows an explicit dependence on the fraction of total energy of the Higgs-pair invariant mass.

Important quantities are related to a combination of the boundaries of x_\pm :

$$x_+ - x_- = \beta_z, \quad x_+ x_- = \frac{\mu_{H_1}^2}{z} + \frac{\Delta}{(1 - z)z} + \frac{\Delta^2}{(1 - z)^2 z}, \quad (\text{C.88})$$

that can be plugged into Eq. (C.85) to obtain a very compact form.

Introducing a variable r such that it runs through the limit of integration of x , the term involving the $\cos^2 \theta_{35}^0$ becomes:

$$\begin{aligned} x &= x_- + (x_+ - x_-)r, \\ x_3^2 x_5^2 \beta_3^2 \frac{1 - \cos^2 \theta_{35}^0}{4} &= -(1-z)^2 z (x - x_-)(x - x_+) \\ &= (1-z)^2 z (x_+ - x_-)^2 r(1-r) \\ &= (1-z)^2 z \beta_z^2 r(1-r). \end{aligned} \quad (\text{C.89})$$

Therefore, the 3-particle phase space element becomes:

$$dR_3 = \frac{\hat{s} \beta_z^{1-2\epsilon}}{(4\pi)^4} \left(\frac{4\pi\mu^2}{\hat{s}} \right)^{2\epsilon} [r^{-\epsilon}(1-r)^{-\epsilon} \sin^{-2\epsilon} \varphi_{35} d\varphi_{35}] \frac{z^{-\epsilon}(1-z)^{1-2\epsilon}(1-\cos^2 \theta_{15})^{-\epsilon}}{\Gamma(1-2\epsilon)} dz d\cos \theta_{15}. \quad (\text{C.90})$$

The term in the parenthesis can be integrated

$$\begin{aligned} \int_0^\pi \sin^{-2\epsilon} \varphi_{35} d\varphi_{35} &= 4^\epsilon \pi \frac{\Gamma(1-2\epsilon)}{\Gamma^2(1-\epsilon)}, \\ \int_0^1 r^{-\epsilon}(1-r)^{-\epsilon} dr &= \frac{\Gamma^2(1-\epsilon)}{\Gamma(2-2\epsilon)}, \end{aligned} \quad (\text{C.91})$$

therefore

$$\begin{aligned} dR_3 &= 4^\epsilon \pi \frac{\hat{s} \beta_z^{1-2\epsilon}}{(4\pi)^4} \left(\frac{4\pi\mu^2}{\hat{s}} \right)^{2\epsilon} \frac{z^{-\epsilon}(1-z)^{1-2\epsilon}(1-\cos^2 \theta_{15})^{-\epsilon}}{\Gamma(2-2\epsilon)} dz d\cos \theta_{15} \\ &= \left[\frac{\beta_z^{1-2\epsilon}}{8\pi} \left(\frac{4\pi\mu^2}{\hat{s}z} \right)^\epsilon \frac{\Gamma(1-\epsilon)}{\Gamma(2-2\epsilon)} \right] \left(\frac{4\pi\mu^2}{\hat{s}z} \right)^\epsilon \frac{\hat{s}z}{32\pi^2} \frac{z^{-1+\epsilon}(1-z)^{1-2\epsilon}}{\Gamma(1-\epsilon)} \left(\frac{1-\cos^2 \theta_{15}}{4} \right)^{-\epsilon} dz d\cos \theta_{15}. \end{aligned} \quad (\text{C.92})$$

The variable z can be expressed again in terms of the invariant Higgs-pair momentum Q^2 as follows

$$\begin{aligned} dR_3 &= \left[\frac{\beta_z^{1-2\epsilon}}{8\pi} \left(\frac{4\pi\mu^2}{Q^2} \right)^\epsilon \frac{\Gamma(1-\epsilon)}{\Gamma(2-2\epsilon)} \right] \frac{Q^2}{32\pi^2} \left(\frac{4\pi\mu^2}{Q^2} \right)^\epsilon \frac{z^{-1+\epsilon}(1-z)^{1-2\epsilon}}{\Gamma(1-\epsilon)} \left(\frac{1-\cos^2 \theta_{15}}{4} \right)^{-\epsilon} dz d\cos \theta_{15} \\ &= R_2 \frac{Q^2}{32\pi^2} \left(\frac{4\pi\mu^2}{Q^2} \right)^\epsilon \frac{z^{-1+\epsilon}(1-z)^{1-2\epsilon}}{\Gamma(1-\epsilon)} \left(\frac{1-\cos^2 \theta_{15}}{4} \right)^{-\epsilon} dz d\cos \theta_{15} \end{aligned} \quad (\text{C.93})$$

We remark that β_z is essentially the same β defined for the 2-particle phase space since it has been factorized from the 3-particle one and it contains information only on the $2 \rightarrow 2$ subprocess. This factorization is crucial for a coherent definition of the infrared subtraction terms expressed in Chapter 3.

C.2.2 Differential cross section: real corrections

As for the virtual corrections, the real contributions have the following differential partonic cross section:

$$\begin{aligned} d\Delta \hat{\sigma}_{ij} &= \frac{dR_3}{2\hat{s}} \overline{|\mathcal{M}_{ij}|^2} \\ &= R_2 \frac{dz d\cos \theta_{15}}{64\pi^2} \left(\frac{4\pi\mu^2}{Q^2} \right)^\epsilon \frac{z^\epsilon(1-z)^{1-2\epsilon}}{\Gamma(1-\epsilon)} \left(\frac{1-\cos^2 \theta_{15}}{4} \right)^{-\epsilon} \overline{|\mathcal{M}_{ij}|^2} \\ &= R_2 \frac{dz d\cos \theta_{15}}{64\pi^2} \left(\frac{4\pi\mu^2}{Q^2} \right)^\epsilon \frac{z^\epsilon(1-z)^{1-2\epsilon}}{\Gamma(1-\epsilon)} \left(\frac{1-\cos^2 \theta_{15}}{4} \right)^{-\epsilon} C_{\text{col}}^{ij} C_{\text{pol}}^{ij} C_{\text{spin}}^{ij} \sum_{\text{ext.}} |\mathcal{M}_{ij}|^2. \end{aligned} \quad (\text{C.94})$$

Each channel contributing to the real corrections has a different color, polarization and spin average. Below, the definitions of the quantities occurring in Eq. (C.94) are presented.

$q\bar{q} \rightarrow \mathbf{H}_1\mathbf{H}_2g$

$$C_{\text{pol}}^{q\bar{q}} = 1, \quad C_{\text{spin}}^{q\bar{q}} = \frac{1}{4}, \quad C_{\text{col}}^{q\bar{q}} = \frac{1}{9},$$

$$\begin{aligned} \sum_{\text{ext.}} |\mathcal{M}_{q\bar{q}}|^2 &= \sum_{\text{spin}} \sum_{\text{pol}} \sum_{\text{col}} T_{ij}^a T_{ji}^a \bar{v}(p_2) \gamma_\mu u(p_1) \bar{u}(p_1) \gamma_\rho v(p_2) \epsilon_\sigma^{*h}(p_5) \epsilon_\nu^h(p_5) \mathcal{M}_{q\bar{q}}^{*\rho\sigma} \mathcal{M}_{q\bar{q}}^{\mu\nu} \\ &= \left(\sum_{\text{spin}} \bar{v}(p_2) \gamma_\mu u(p_1) \bar{u}(p_1) \gamma_\rho v(p_2) \right) \left(\sum_h \epsilon_\sigma^{*h}(p_5) \epsilon_\nu^h(p_5) \right) \left(\sum_{i,j,a} T_{ij}^a T_{ji}^a \right) \mathcal{M}_{q\bar{q}}^{*\rho\sigma} \mathcal{M}_{q\bar{q}}^{\mu\nu} \\ &= \text{Tr} \left[\not{p}_1 \gamma_\rho \not{p}_2 \gamma_\mu \right] (-g_{\sigma\nu}) \text{Tr} \left[\delta_{N_c^2-1} \right] \mathcal{M}_{q\bar{q}}^{*\rho\sigma} \mathcal{M}_{q\bar{q}}^{\mu\nu} \\ &= -32 [p_{1\rho} p_{2\mu} - (p_1 \cdot p_2) g_{\rho\mu} + p_{2\rho} p_{1\mu}] g_{\sigma\nu} \mathcal{M}_{q\bar{q}}^{*\rho\sigma} \mathcal{M}_{q\bar{q}}^{\mu\nu}. \end{aligned} \quad (\text{C.95})$$

$qg \rightarrow \mathbf{H}_1\mathbf{H}_2q$

$$C_{\text{pol}}^{qg} = \frac{1}{(d-2)}, \quad C_{\text{spin}}^{qg} = \frac{1}{2}, \quad C_{\text{col}}^{qg} = \frac{1}{24},$$

$$\begin{aligned} \sum_{\text{ext.}} |\mathcal{M}_{qg}|^2 &= \sum_{\text{spin}} \sum_{\text{pol}} \sum_{\text{col}} T_{ij}^a T_{ji}^a \bar{u}(p_5) \gamma_\mu u(p_1) \bar{u}(p_1) \gamma_\rho u(p_5) \epsilon_\sigma^{*h}(p_2) \epsilon_\nu^h(p_2) \mathcal{M}_{qg}^{*\rho\sigma} \mathcal{M}_{qg}^{\mu\nu} \\ &= \left(\sum_{\text{spin}} \bar{u}(p_5) \gamma_\mu u(p_1) \bar{u}(p_1) \gamma_\rho u(p_5) \right) \left(\sum_h \epsilon_\sigma^{*h}(p_2) \epsilon_\nu^h(p_2) \right) \left(\sum_{i,j,a} T_{ij}^a T_{ji}^a \right) \mathcal{M}_{qg}^{*\rho\sigma} \mathcal{M}_{qg}^{\mu\nu} \\ &= \text{Tr} \left[\not{p}_1 \gamma_\rho \not{p}_5 \gamma_\mu \right] (-g_{\sigma\nu}) \text{Tr} \left[\delta_{N_c^2-1} \right] \mathcal{M}_{qg}^{*\rho\sigma} \mathcal{M}_{qg}^{\mu\nu} \\ &= -32 [p_{1\rho} p_{5\mu} - (p_1 \cdot p_5) g_{\rho\mu} + p_{5\rho} p_{1\mu}] g_{\sigma\nu} \mathcal{M}_{qg}^{*\rho\sigma} \mathcal{M}_{qg}^{\mu\nu}. \end{aligned} \quad (\text{C.96})$$

$gg \rightarrow \mathbf{H}_1\mathbf{H}_2g$

$$C_{\text{pol}}^{gg} = \frac{1}{(d-2)^2}, \quad C_{\text{spin}}^{gg} = 1, \quad C_{\text{col}}^{gg} = \frac{1}{64},$$

$$\begin{aligned} \sum_{\text{ext.}} |\mathcal{M}_{gg}|^2 &= \sum_{\text{pol}} \sum_{\text{col}} f^{abc} f^{abc} \epsilon_\rho^{*h_1}(p_1) \epsilon_\mu^{h_1}(p_1) \epsilon_\sigma^{*h_2}(p_2) \epsilon_\nu^{h_2}(p_2) \epsilon_\beta^{h_5}(p_5) \epsilon_\alpha^{*h_5}(p_5) \mathcal{M}_{gg}^{*\rho\sigma\beta} \mathcal{M}_{gg}^{\mu\nu\alpha} \\ &= \left(\sum_{h_1} \epsilon_\rho^{*h_1}(p_1) \epsilon_\mu^{h_1}(p_1) \right) \left(\sum_{h_2} \epsilon_\sigma^{*h_2}(p_2) \epsilon_\nu^{h_2}(p_2) \right) \left(\sum_{h_5} \epsilon_\beta^{h_5}(p_5) \epsilon_\alpha^{*h_5}(p_5) \right) \left(\sum_{a,b,c} f^{abc} f^{abc} \right) \mathcal{M}_{gg}^{*\rho\sigma\beta} \mathcal{M}_{gg}^{\mu\nu\alpha}, \\ &= -N_c(N_c^2 - 1) [g_{\mu\rho} g_{\nu\sigma} g_{\alpha\beta} + A_{\mu\rho, \nu\sigma, \alpha\beta}] \mathcal{M}_{gg}^{*\rho\sigma\beta} \mathcal{M}_{gg}^{\mu\nu\alpha} \\ &= -24 [g_{\mu\rho} g_{\nu\sigma} g_{\alpha\beta} + A_{\mu\rho, \nu\sigma, \alpha\beta}] \mathcal{M}_{gg}^{*\rho\sigma\beta} \mathcal{M}_{gg}^{\mu\nu\alpha} \\ A_{\mu\rho, \nu\sigma, \alpha\beta} &= \left(-g_{\mu\rho} + \frac{p_{1\{\mu} q_{1\rho\}}}{p_1 \cdot q_1} \right) \left(-g_{\nu\sigma} + \frac{p_{2\{\nu} q_{2\sigma\}}}{p_2 \cdot q_2} \right) \left(-g_{\alpha\beta} + \frac{p_{5\{\alpha} q_{5\beta\}}}{p_5 \cdot q_5} \right) - g_{\mu\rho} g_{\nu\sigma} g_{\alpha\beta}. \end{aligned} \quad (\text{C.97})$$

The amplitudes contributing to the $q\bar{q}$ and qg channels can be built from the LO diagrams by putting an incoming gluon off-shell and attaching a fermion line to it (Appendix H). This fact allows to factor out from the amplitudes the quantities that have to be added. Moreover, the presence of a single on-shell gluon in the final state allows to use the QED-like Ward identities, and the axial term of the polarization can be dropped.

The gg channel is a bit different, since it contains pentagon diagrams. They cannot be constructed from the LO diagrams. These contributions do not even represent a gauge-invariant subset of the amplitude. In addition, if one does not want to consider the ghost contributions, the polarization sums have to be performed over the physical polarization states since in the usual Lorenz gauge no Ward identity ensures the cancellation of the unphysical ones. In Eq. (C.97), the tensor A would vanish in QED ones contracted with the full amplitude because of the on-shell Ward identities; in QCD this argument is not anymore valid, and in general it will give a non-zero contribution.

Appendix D

Passarino-Veltmann reduction

The Feynman integrals contributing at each order of a perturbative QFT expansion do not form an linearly-independent set: it can be shown [149] that every one-loop tensor integral can be expressed as a linear combination of scalar integrals. Such independent integrals are called *master integrals*. The decomposition of a tensor integral in terms of its master integrals is called *reduction*. Several algorithms allow the reduction to master integrals, both at *integral* and *integrand* level. In this Appendix the Passarino-Veltmann reduction algorithm is presented with explicit examples.

Consider the following set of denominators:

$$\begin{aligned} D_0 &= k^2 - m_t^2, & D_1 &= (k - p_1)^2 - m_t^2, & D_2 &= (k + p_2)^2 - m_t^2, \\ p_1^2 &= 0, & p_2^2 &\neq 0, & (p_1 + p_2)^2 &= m_{H_j}^2, \\ D_{H_j} &= (k + p_1 + p_2)^2 - m_t^2, \end{aligned} \quad (\text{D.1})$$

and the general scalar integrals:

$$A_0(m_0^2) = \int_k \frac{1}{[k^2 - m_0^2]}, \quad (\text{D.2})$$

$$B_0(q^2; m_0^2, m_1^2) = \int_k \frac{1}{[k^2 - m_0^2][(k + q)^2 - m_1^2]}, \quad (\text{D.3})$$

$$C_0(q_1^2, q_2^2, (q_2 - q_1)^2; m_0^2, m_1^2, m_2^2) = \int_k \frac{1}{[k^2 - m_0^2][(k + q_1)^2 - m_1^2][(k + q_2)^2 - m_2^2]}. \quad (\text{D.4})$$

When all denominators have the same mass, instead of writing the full list, a redefinition of the argument will be performed such that $\{m_t^2, \dots, m_t^2\} = \bar{m}_t^2$. The integrals built with D_i , $i = \{0, 1, 2\}$ defined before are:

$$\begin{aligned} B_0(p_2^2; \bar{m}_t^2) &= \int_k \frac{1}{D_0 D_2}, & B_0(0; \bar{m}_t^2) &= \int_k \frac{1}{D_0 D_1}, \\ C_0(0, p_2^2, m_{H_j}^2; \bar{m}_t^2) &= \int_k \frac{1}{D_0 D_1 D_2}. \end{aligned} \quad (\text{D.5})$$

and through a shift $k \rightarrow k + p_1$, an additional integral can be defined

$$\int_k \frac{1}{D_1 D_2} = \int_k \frac{1}{D_0 D_{H_j}} = B_0(m_{H_j}^2; \bar{m}_t^2). \quad (\text{D.6})$$

In the following section, the reduction of the 2-point and 3-point integrals is presented.

D.1 Reduction to scalar integrals

D.1.1 2-point tensor integrals

We firstly have to express the scalar products containing at least one loop momenta in terms of denominators, so that

$$k^2 = D_0 + m_t^2, \quad k \cdot p_1 = -\frac{1}{2}(D_1 - D_0), \quad k \cdot p_2 = \frac{1}{2}(D_2 - D_0 - p_2^2). \quad (\text{D.7})$$

The strategy will be the same for each tensor integral:

- defining the tensor structure of the tensor integral;
- contracting both the tensor integral and the tensor structure for its tensor basis;
- inverting the system to find the tensor coefficients.

Coefficient B_i

The simplest example is the rank-1 $B_0(p_2^2, \bar{m}_t^2)$ integral. It can be written in terms of its tensor structure:

$$\int_k \frac{k^\mu}{D_0 D_2} = B_1 p_2^\mu, \quad (\text{D.8})$$

where B_1 is a coefficient depending on the kinematic invariants and masses. Contracting both side of Eq. (D.8) with p_2^μ , the equation reads

$$\begin{aligned} B_1 p_2^2 &= \int_k \frac{k \cdot p_2}{D_0 D_2} \\ &= \frac{1}{2} \left(\int_k \frac{1}{D_0} - \int_k \frac{1}{D_2} - p_2^2 \int_k \frac{1}{D_0 D_2} \right) \\ &= -\frac{1}{2} B_0(p_2^2, \bar{m}_t^2) p_2^2, \end{aligned} \quad (\text{D.9})$$

where we have used the identities of Eq. (D.7) and the identity

$$\int_k \frac{1}{D_0} = \int_k \frac{1}{D_2}, \quad (\text{D.10})$$

follows from the shift $k \rightarrow k - p_2$. Inverting Eq. (D.9), the rank-1 $B_0(p_2^2, \bar{m}_t^2)$ is given by

$$\int_k \frac{k^\mu}{D_0 D_2} = -\frac{1}{2} B_0(p_2^2, \bar{m}_t^2) p_2^\mu. \quad (\text{D.11})$$

Coefficient B_{ij}

Similarly, the rank-2 $B_0(p_2^2, \bar{m}_t^2)$ has the following tensor structure

$$\int_k \frac{k^\mu k^\nu}{D_0 D_2} = B_{00} g^{\mu\nu} + B_{11} p_2^\mu p_2^\nu. \quad (\text{D.12})$$

Contracting both sides with its tensor basis, a system involving the coefficients B_{00} and B_{11} is defined:

$$\begin{pmatrix} 1 & m_t^2 \\ \frac{1}{2} p_2^2 & \frac{1}{4} (p_2^2)^2 \end{pmatrix} \begin{pmatrix} A_0(m_t^2) \\ B_0(p_2^2, \bar{m}_t^2) \end{pmatrix} = \begin{pmatrix} d & p_2^2 \\ p_2^2 & (p_2^2)^2 \end{pmatrix} \begin{pmatrix} B_{00} \\ B_{11} \end{pmatrix}, \quad (\text{D.13})$$

whose solution is

$$\begin{aligned} \begin{pmatrix} B_{00} \\ B_{11} \end{pmatrix} &= \frac{1}{(d-1)(p_2^2)^2} \begin{pmatrix} (p_2^2)^2 & -p_2^2 \\ -p_2^2 & d \end{pmatrix} \begin{pmatrix} 1 & m_t^2 \\ \frac{1}{2} p_2^2 & \frac{1}{4} (p_2^2)^2 \end{pmatrix} \begin{pmatrix} A_0(m_t^2) \\ B_0(p_2^2, \bar{m}_t^2) \end{pmatrix} \\ &= \frac{1}{(d-1)(p_2^2)^2} \frac{1}{4} \begin{pmatrix} 2(p_2^2)^2 A_0(m_t^2) + (p_2^2)^2 (4m_t^2 - p_2^2) B_0(p_2^2, \bar{m}_t^2) \\ 2p_2^2 (d-2) A_0(m_t^2) - p_2^2 (4m_t^2 - dp_2^2) B_0(p_2^2, \bar{m}_t^2) \end{pmatrix}, \end{aligned} \quad (\text{D.14})$$

and

$$\begin{aligned} \int_k \frac{k^\mu k^\nu}{D_0 D_2} &= \left[\frac{2(p_2^2)^2 A_0(m_t^2) + (p_2^2)^2 (4m_t^2 - p_2^2) B_0(p_2^2, \bar{m}_t^2)}{4(d-1)(p_2^2)^2} \right] g^{\mu\nu} \\ &+ \left[\frac{2p_2^2 (d-2) A_0(m_t^2) - p_2^2 (4m_t^2 - dp_2^2) B_0(p_2^2, \bar{m}_t^2)}{4(d-1)(p_2^2)^2} \right] p_2^\mu p_2^\nu. \end{aligned} \quad (\text{D.15})$$

D.2 3-point tensor integrals

Coefficient C_i

The rank-1 C_0 is

$$\int_k \frac{k^\mu}{D_0 D_1 D_2} = C_1 p_1^\mu + C_2 p_2^\mu. \quad (\text{D.16})$$

where the tensor integral has already been set. Contracting both sides of Eq. (D.16) for the tensor basis, the system for evaluating the coefficients C_1 and C_2 can be written as

$$\mathbf{I} = \int_k \frac{1}{D_0 D_1 D_2} \begin{pmatrix} k \cdot p_1 \\ k \cdot p_2 \end{pmatrix} = \begin{pmatrix} 0 & p_1 \cdot p_2 \\ p_1 \cdot p_2 & p_2^2 \end{pmatrix} \begin{pmatrix} C_1 \\ C_2 \end{pmatrix} = \mathbb{G} \mathbf{C}, \quad (\text{D.17})$$

where \mathbb{G} is the Gram matrix. Its determinant is

$$G = -(p_1 \cdot p_2)^2, \quad (\text{D.18})$$

and its inverse is

$$\mathbb{G}^{-1} = \frac{1}{G} \begin{pmatrix} p_2^2 & -p_1 \cdot p_2 \\ -p_1 \cdot p_2 & 0 \end{pmatrix}. \quad (\text{D.19})$$

The left-hand side written in terms of scalar integrals is

$$\mathbf{I} = \frac{1}{2} \begin{pmatrix} B_0(q_2^2; \bar{m}_t^2) - B_0(m_{H_j}^2; \bar{m}_t^2) \\ B_0(0; \bar{m}_t^2) - B_0(m_{H_j}^2; \bar{m}_t^2) - p_2^2 C_0(0, p_2^2, m_{H_j}^2; \bar{m}_t^2) \end{pmatrix}. \quad (\text{D.20})$$

Finally, inverting the Gram matrix, the coefficients of the tensor expansion are given by

$$\begin{aligned} C_1 &= \frac{1}{2G} \left[p_2^2 (p_1 \cdot p_2) C_0(0, p_2^2, m_{H_j}^2; \bar{m}_t^2) + ((p_1 \cdot p_2) - p_2^2) B_0(m_{H_j}^2; \bar{m}_t^2) \right. \\ &\quad \left. + q_2^2 B_0(q_2^2; \bar{m}_t^2) - (p_1 \cdot p_2) B_0(0; \bar{m}_t^2) \right], \\ C_2 &= \frac{(p_1 \cdot p_2)}{2G} \left[B_0(m_{H_j}^2; \bar{m}_t^2) - B_0(q_2^2; \bar{m}_t^2) \right], \end{aligned} \quad (\text{D.21})$$

and the rank-1 integral becomes

$$\begin{aligned} \int_k \frac{k^\mu}{D_0 D_1 D_2} &= \frac{1}{2G} \left[p_2^2 (p_1 \cdot p_2) C_0(0, p_2^2, m_{H_j}^2; \bar{m}_t^2) + ((p_1 \cdot p_2) - p_2^2) B_0(m_{H_j}^2; \bar{m}_t^2) \right. \\ &\quad \left. + q_2^2 B_0(q_2^2; \bar{m}_t^2) - (p_1 \cdot p_2) B_0(0; \bar{m}_t^2) \right] p_1^\mu \\ &\quad + \frac{(p_1 \cdot p_2)}{2G} \left[B_0(m_{H_j}^2; \bar{m}_t^2) - B_0(q_2^2; \bar{m}_t^2) \right] p_2^\mu. \end{aligned} \quad (\text{D.22})$$

Coefficient C_{ij}

Similarly, the rank-2 integral can be decomposed as

$$\int_k \frac{k^\mu k^\nu}{D_0 D_1 D_2} = C_{00} g^{\mu\nu} + \sum_{i=1}^2 C_{ij} p_i^\mu p_j^\nu, \quad (\text{D.23})$$

where we already expressed it as a general tensor depending on p_1 and p_2 .

Contracting the r.h.s. with respectively $g^{\mu\nu}$, $p_1^\mu p_1^\nu$, $p_1^\mu p_2^\nu$, $p_2^\mu p_1^\nu$ and $p_2^\mu p_2^\nu$ we can generate a system:

$$\mathbb{G} \mathbf{C} = \begin{pmatrix} d & 0 & (p_1 \cdot p_2) & (p_1 \cdot p_2) & p_2^2 \\ 0 & 0 & 0 & 0 & (p_1 \cdot p_2)^2 \\ (p_1 \cdot p_2) & 0 & 0 & (p_1 \cdot p_2)^2 & (p_1 \cdot p_2) p_2^2 \\ (p_1 \cdot p_2) & 0 & (p_1 \cdot p_2)^2 & 0 & (p_1 \cdot p_2) p_2^2 \\ p_2^2 & (p_1 \cdot p_2) & (p_1 \cdot p_2) p_2^2 & (p_1 \cdot p_2) p_2^2 & (p_2^2)^2 \end{pmatrix} \begin{pmatrix} C_{00} \\ C_{11} \\ C_{12} \\ C_{21} \\ C_{22} \end{pmatrix}. \quad (\text{D.24})$$

The contraction of the l.h.s. is:

$$\mathbf{I} = \begin{pmatrix} B_0(m_{H_j}^2; \bar{m}_t^2) + m_t^2 C_0(0, p_2^2, m_{H_j}^2; \bar{m}_t^2) \\ \frac{1}{4} B_0(p_2^2; \bar{m}_t^2)(p_1 \cdot p_2) - \frac{1}{4} B_0(m_{H_j}^2; \bar{m}_t^2)(p_1 \cdot p_2) \\ \frac{1}{4} B_0(p_2^2; \bar{m}_t^2) p_2^2 - \frac{1}{4} B_0(m_{H_j}^2; \bar{m}_t^2)(p_2^2 - p_1 \cdot p_2) \\ \frac{1}{4} B_0(p_2^2; \bar{m}_t^2) p_2^2 - \frac{1}{4} B_0(m_{H_j}^2; \bar{m}_t^2)(p_2^2 - p_1 \cdot p_2) \\ \frac{1}{4} B_0(0; \bar{m}_t^2)(p_1 \cdot p_2 - p_2^2) + \frac{1}{4} B_0(m_{H_j}^2; \bar{m}_t^2)(2p_2^2 - p_1 \cdot p_2) + \frac{1}{4} (p_2^2)^2 C_0(0, p_2^2, m_{H_j}^2; \bar{m}_t^2) \end{pmatrix}. \quad (\text{D.25})$$

The determinant of the matrix \mathbb{G} can be written in terms of the Gram determinant:

$$\det \mathbb{G} = (d-2)[(p_1 \cdot p_2)^2]^4 = (d-2)G^4. \quad (\text{D.26})$$

Finally, inverting \mathbb{M} , we can get the expression of the coefficients \mathbf{C} with $\mathbf{C} = \mathbb{G}^{-1}\mathbf{I}$. Due to gauge invariance, we are only interested in A_{00} and A_{21} , whose values are

$$C_{00} = -\frac{(p_1 \cdot p_2)(p_2^2 + 2(p_1 \cdot p_2))B_0(m_{H_j}^2; \bar{m}_t^2) - (p_1 \cdot p_2)p_2^2 B_0(p_2^2; \bar{m}_t^2) + 4m_t^2(p_1 \cdot p_2)^2 C_0(0, p_2^2, m_{H_j}^2; \bar{m}_t^2)}{4(d-2)G},$$

$$C_{21} = -\frac{(p_1 \cdot p_2)((d-4)(p_1 \cdot p_2) - p_2^2)B_0(m_{H_j}^2; \bar{m}_t^2) + (p_1 \cdot p_2)p_2^2 B_0(p_2^2; \bar{m}_t^2) - 4m_t^2(p_1 \cdot p_2)^2 C_0(0, p_2^2, m_{H_j}^2; \bar{m}_t^2)}{4(d-2)G}. \quad (\text{D.27})$$

The procedure explained in this Appendix is the core of the Passarino-Veltmann reduction, which can be extended to boxes D_0 and pentagons E_0 . The complexity of the tensor coefficients rapidly increases with the number of external legs and tensor-rank. The Gram determinants G strongly depend on the kinematics, and they introduce strong numerical instabilities when the phase space integral is performed: high-rank integrals increase its power of G in the denominator, and regions where G becomes small can lead to strong cancellation and loss of numerical precision.

D.3 Recurrence relations

An alternative to the reduction down to scalar integrals is represented by the recurrence relations. Once that the scalar integrals are defined, a rank- r integral can be expressed in terms of a tensor basis, where its coefficients depend on the rank- $(r-1)$ ones. This means that the coefficients of such tensors can be obtained by iteration starting from the scalar integrals. In general, every rank contributes with one power of inverse Gram determinant, which lead to the potential numerical problems expressed in the previous Section.

B_{ij} coefficients

Consider the tensor structure of the rank-2 2-point integrals

$$\int_k \frac{k^\mu k^\nu}{D_0 D_2} = B_{00} g^{\mu\nu} + B_{11} p_2^\mu p_2^\nu. \quad (\text{D.28})$$

In complete analogy of what has been done in the previous section, contracting both sides with the momentum p^μ and the metric tensor $g^{\mu\nu}$, two equations can be obtained

$$g_{\mu\nu} \int_k \frac{k^\mu k^\nu}{D_0 D_2} = B_{00} d + B_{11} p_2^2,$$

$$p_2^\nu \int_k \frac{k^\mu k^\nu}{D_0 D_2} = B_{00} p_2^\mu + B_{11} p_2^2 p_2^\mu. \quad (\text{D.29})$$

Using the relations of Eq. (D.7), and expressing the rank-1 integrals with their tensor structure, the l.h.s. becomes

$$g_{\mu\nu} \int_k \frac{k^\mu k^\nu}{D_0 D_2} = A_0(m_t^2) + m_t^2 B_0(p_2^2; \bar{m}_t^2),$$

$$p_2^\nu \int_k \frac{k^\mu k^\nu}{D_0 D_2} = \frac{p_2^\mu}{2} \int_k \frac{1}{D_0} - \frac{p_2^2}{2} \int_k \frac{k^\mu}{D_0 D_2}$$

$$= \frac{1}{2} A_0(m_t^2) p_2^\mu - \frac{p_2^2}{2} B_1 p_2^\mu. \quad (\text{D.30})$$

Therefore, the system of equations can be solved for the coefficients B_{ij}

$$\begin{pmatrix} B_{00} \\ B_{11} \end{pmatrix} = \frac{1}{2(d-1)p_2^2} \begin{pmatrix} 2p_2^2 & -p_2^2 \\ -2 & d \end{pmatrix} \begin{pmatrix} A_0(m_t^2) + m_t^2 B_0(p_2^2; \bar{m}_t^2) \\ A_0(m_t^2) - p_2^2 B_1 \end{pmatrix}, \quad (\text{D.31})$$

and using the fact that $G = p_2^2$, the coefficients B_{ij} are given by

$$\begin{aligned} B_{00} &= \frac{1}{2(d-1)} [A_0(m_t^2) + 2m_t^2 B_0(p_2^2; \bar{m}_t^2) + p_2^2 B_1(p_2^2; \bar{m}_t^2)], \\ B_{11} &= \frac{1}{2(d-1)G} [(d-2)A_0(m_t^2) - 2m_t^2 B_0(p_2^2; \bar{m}_t^2) - dp_2^2 B_1(p_2^2; \bar{m}_t^2)]. \end{aligned} \quad (\text{D.32})$$

Thus, the coefficients B_{00} and B_{11} of the rank-2 2-points integrals depend explicitly on B_1 , namely the coefficient of the rank-1 2-points tensor integral, which in turn is related to the scalar integral B_0 through the Eq. (D.9).

C_{ij} coefficients

The rank-2 3-points integrals have the following tensor structure:

$$\int_k \frac{k^\mu k^\nu}{D_0 D_1 D_2} = C_{00} g^{\mu\nu} + \sum_{i=1}^2 C_{ij} p_i^\mu p_j^\nu, \quad (\text{D.33})$$

Contracting both sides for the external momenta, a system of four equations can be built:

$$\begin{aligned} p_1^\nu \int_k \frac{k^\mu k^\nu}{D_0 D_1 D_2} &= +\frac{1}{2} [B_1(m_{H_j}^2; \bar{m}_t^2) + B_0(m_{H_j}^2; \bar{m}_t^2)] p_1^\mu \\ &\quad + \frac{1}{2} [B_1(m_{H_j}^2; \bar{m}_t^2) - B_1(p_2; \bar{m}_t^2)] p_2^\mu \\ &= [C_{00} + C_{12}(p_1 \cdot p_2)] p_1^\mu + C_{22} p_2^\mu, \end{aligned} \quad (\text{D.34})$$

$$\begin{aligned} p_2^\nu \int_k \frac{k^\mu k^\nu}{D_0 D_1 D_2} &= \frac{1}{2} [B_1(p_2^2; \bar{m}_t^2) - B_1(m_{H_j}^2; \bar{m}_t^2) - B_0(m_{H_j}^2; \bar{m}_t^2) - p_2^2 C_1] p_1^\mu \\ &\quad + \frac{1}{2} [B_1(m_{H_j}^2; \bar{m}_t^2) + p_2^2 C_2] p_2^\mu \\ &= [C_{11}(p_1 \cdot p_2) + C_{12} p_2^2] p_1^\mu + [C_{00} + C_{21}(p_1 \cdot p_2) + C_{22} p_2^2] p_2^\mu, \end{aligned}$$

which lead to the following system and its solution

$$\begin{aligned} \begin{pmatrix} B_1(m_{H_j}^2; \bar{m}_t^2) + B_0(m_{H_j}^2; \bar{m}_t^2) - 2C_{00} \\ B_1(p_2^2; \bar{m}_t^2) - B_1(m_{H_j}^2; \bar{m}_t^2) - B_0(m_{H_j}^2; \bar{m}_t^2) - p_2^2 C_1 \\ B_1(m_{H_j}^2; \bar{m}_t^2) - B_1(p_2^2; \bar{m}_t^2) \\ B_1(m_{H_j}^2; \bar{m}_t^2) + p_2^2 C_2 - 2C_{00} \end{pmatrix} &= 2 \begin{pmatrix} 0 & (p_1 \cdot p_2) & 0 & 0 \\ (p_1 \cdot p_2) & p_2^2 & 0 & 0 \\ 0 & 0 & 0 & (p_1 \cdot p_2) \\ 0 & 0 & (p_1 \cdot p_2) & p_2^2 \end{pmatrix} \begin{pmatrix} C_{11} \\ C_{21} \\ C_{12} \\ C_{22} \end{pmatrix} \\ &\Downarrow \\ \begin{pmatrix} C_{11} \\ C_{21} \\ C_{12} \\ C_{22} \end{pmatrix} &= \frac{1}{2G} \begin{pmatrix} p_2^2 & -(p_1 \cdot p_2) & 0 & 0 \\ -(p_1 \cdot p_2) & 0 & 0 & 0 \\ 0 & 0 & p_2^2 & -(p_1 \cdot p_2) \\ 0 & 0 & -(p_1 \cdot p_2) & 0 \end{pmatrix} \begin{pmatrix} B_1(m_{H_j}^2; \bar{m}_t^2) + B_0(m_{H_j}^2; \bar{m}_t^2) - 2C_{00} \\ B_1(p_2^2; \bar{m}_t^2) - B_1(m_{H_j}^2; \bar{m}_t^2) - B_0(m_{H_j}^2; \bar{m}_t^2) - p_2^2 C_1 \\ B_1(m_{H_j}^2; \bar{m}_t^2) - B_1(p_2^2; \bar{m}_t^2) \\ B_1(m_{H_j}^2; \bar{m}_t^2) + p_2^2 C_2 - 2C_{00} \end{pmatrix} \\ &\Downarrow \\ C_{11} &= \frac{(p_2^2 + p_1 \cdot p_2) B_1(m_{H_j}^2; \bar{m}_t^2) + (p_2^2 + p_1 \cdot p_2) B_0(m_{H_j}^2; \bar{m}_t^2) - 2p_2^2 C_{00} - (p_1 \cdot p_2) B_1(p_2^2; \bar{m}_t^2) + p_2^2 (p_1 \cdot p_2) C_1}{2G}, \\ C_{12} &= \frac{(p_2^2 - p_1 \cdot p_2) B_1(m_{H_j}^2; \bar{m}_t^2) - p_2^2 B_1(p_2^2; \bar{m}_t^2) - (p_1 \cdot p_2) p_2^2 C_2 + (p_1 \cdot p_2) 2C_{00}}{2G}, \\ C_{21} &= \frac{B_1(p_2^2; \bar{m}_t^2) - B_1(m_{H_j}^2; \bar{m}_t^2) - B_0(m_{H_j}^2; \bar{m}_t^2) - p_2^2 C_1}{2}, \\ C_{22} &= \frac{B_1(m_{H_j}^2; \bar{m}_t^2) + p_2^2 C_2 - 2C_{00}}{2} \end{aligned} \quad (\text{D.35})$$

where we defined the Gram determinant $G = -(p_1 \cdot p_2)^2$. The remaining C_{00} coefficient can be found by contracting the Eq. (D.33) with the metric tensor $g^{\mu\nu}$ and using the results found in Eq. (D.35).

As for the previous example, the C_{ij} tensor coefficients are related to the C_i and B_i ones, which in turn are related to the C_0 and B_0 scalar integrals. The generalization of this procedure for the rank- r n -points tensor integrals is straightforward: 1. find the Lorentz basis on which the rank- r tensor integral can be projected; 2. define the equality between the tensor integral and its decomposition of such tensor basis; 3. contract both sides of the equation found in 2. for every external momentum; 4. express the rank- $(r - 1)$ in terms of its tensor structure; 5. solve the system with respect to the coefficients of the rank- r tensor structure. It can be shown that it is possible to build a master equation which holds for any rank- r n -points tensor integral and relates its tensor coefficients to the rank- $(r - 1)$ n -points (or lower) ones (See e.g. Ref. [170, 171]).

Appendix E

Evaluating the basis of one-loop integrals

One-loop amplitudes can be written as a combination of scalar integrals: the minimal requirement for the evaluation of such amplitudes is to know how to calculate the integral basis. There exist many methods [172–177] for expressing one-loop scalar integrals into series expansions in ϵ . In this Appendix the calculation of the simpler scalar integrals will be presented by using the standard technique involving Feynman parametrization and the tadpole integral.

The tadpole integral is defined by:

$$A_0(m_t^2) = \int_k \frac{1}{k^2 - m_t^2}. \quad (\text{E.1})$$

The integral over the loop momentum is

$$\int_k \frac{(k^2)^\alpha}{[k^2 - q^2 - M^2]^n} = (-1)^{(n-\alpha)} \frac{\Gamma(n - \alpha - \frac{d}{2})\Gamma(\alpha + \frac{d}{2})}{\Gamma(n)\Gamma(\frac{d}{2})} \frac{1}{[q^2 + M^2]^{n-\alpha-\frac{d}{2}}}, \quad (\text{E.2})$$

and it can be applied directly on Eq. (E.1). It reads

$$\begin{aligned} A_0(m_t^2) &= -\frac{\Gamma(1 - \frac{d}{2})}{\Gamma(1)} \frac{1}{(m_t^2)^{1-\frac{d}{2}}} \\ &= -m_t^2 \frac{\Gamma(1 + \epsilon)}{\epsilon(\epsilon - 1)} (m_t^2)^{-\epsilon} \\ &= m_t^2 (m_t^2)^{-\epsilon} \Gamma(1 + \epsilon) \left(\frac{1}{\epsilon} + 1 \right) + O(\epsilon). \end{aligned} \quad (\text{E.3})$$

For more complex integrands, the Feynman parametrization allows the integrand to take the tadpole-like form. However, additional integrations over the Feynman parameters have to be performed, making the calculation of one-loop scalar integrals highly non-trivial. In the following Section, the 2-points and 3-points scalar integrals will be calculated up to the order $O(1)$.

E.1 2-points scalar integrals

$B_0(q^2, \bar{m}_t^2)$

The integral $B_0(q^2, \bar{m}_t^2)$ is

$$B_0(q^2, \bar{m}_t^2) = \int_k \frac{1}{[k^2 - m_t^2][(k+q)^2 - m_t^2]}. \quad (\text{E.4})$$

Writing $B_0(q^2, \bar{m}_t^2)$ in terms of Feynman parameters, it reads:

$$B_0(q^2, \bar{m}_t^2) = \frac{\Gamma(2)}{\Gamma(1)\Gamma(1)} \int_k \int_0^1 dx_1 dx_2 \frac{\delta(1 - x_1 - x_2)}{[(k^2 - m_t^2)x_1 + ((k+q)^2 - m_t^2)x_2]^2}, \quad (\text{E.5})$$

Rearranging the terms in the denominator and integrate over x_1 it becomes

$$\begin{aligned} B_0(q^2, \overline{m}_t^2) &= \int_k \int_0^1 dx_2 \frac{1}{[k^2 + (2k \cdot q + q^2)x_2 - m_t^2]^2} \\ &= \int_k \int_0^1 dx_2 \frac{1}{[k^2 + q^2 x_2(1-x_2) - m_t^2]^2}, \end{aligned} \quad (\text{E.6})$$

where the shift $k \rightarrow k - qx_1$ has been applied. Using Eq. (E.2) the integral becomes

$$B_0(q^2, \overline{m}_t^2) = \frac{\Gamma(2 - \frac{d}{2})}{\Gamma(2)} \int_0^1 \frac{dx_2}{[m_t^2 - q^2 x_2(1-x_2)]^{2-\frac{d}{2}}}, \quad (\text{E.7})$$

and by setting $d = 4 - 2\epsilon$ and renaming $x_2 = x$ it reads

$$\begin{aligned} B_0(q^2, \overline{m}_t^2) &= \Gamma(\epsilon) \int_0^1 \frac{dx}{[m_t^2 - q^2 x_2(1-x)]^\epsilon} \\ &= (m_t^2)^{-\epsilon} \frac{\Gamma(1+\epsilon)}{\epsilon} \int_0^1 \frac{dx}{\left[1 - \frac{q^2}{m_t^2} x(1-x)\right]^\epsilon}. \end{aligned} \quad (\text{E.8})$$

Expanding the last expression up to the finite order and defining $\frac{q^2}{m_t^2} = \rho$, $B_0(q^2, \overline{m}_t^2)$ reads

$$B_0(q^2, \overline{m}_t^2) = \Gamma(1+\epsilon)(m_t^2)^{-\epsilon} \left[\frac{1}{\epsilon} - \int_0^1 dx \log[1 - \rho x(1-x)] \right]. \quad (\text{E.9})$$

The integral in the parenthesis can be evaluated analytically:

$$\begin{aligned} \tau = \frac{4}{\rho}, \quad g(\tau) &= \frac{\sqrt{1-\tau}}{2} \log \left(-\frac{1 + \sqrt{1-\tau}}{1 - \sqrt{1-\tau}} \right), \\ &\quad \downarrow \\ \int_0^1 dx \log[1 - \rho x(1-x)] &= 2[g(\tau) - 1], \end{aligned} \quad (\text{E.10})$$

Therefore, the analytical expansion of the 2-point scalar integral is

$$B_0(q^2, \overline{m}_t^2) = \Gamma(1+\epsilon)(m_t^2)^{-\epsilon} \left[\frac{1}{\epsilon} + 2 - 2g(\tau) \right]. \quad (\text{E.11})$$

An important limit of this integral is obtained for $q^2 \rightarrow 0$:

$$B_0(0, \overline{m}_t^2) = (m_t^2)^{-\epsilon} \frac{\Gamma(1+\epsilon)}{\epsilon}. \quad (\text{E.12})$$

The derivative of $B_0(p^2; \overline{m}_t)$ is given by:

$$\frac{d}{dq^2} B_0(q^2, \overline{m}_t^2) = -\Gamma(1+\epsilon)(m_t^2)^{-\epsilon} 2g'(\tau(q^2)), \quad (\text{E.13})$$

$$g'(\tau(q^2)) = \frac{\tau^2}{8m_t^2} \left(\frac{g(\tau)}{1-\tau} + \frac{1}{\tau} \right), \quad (\text{E.14})$$

and the on-shell limit of the derivative of $B_0(q^2, \overline{m}_t^2)$ is

$$\frac{d}{dq^2} B_0(0, \overline{m}_t^2) \sim \Gamma(1+\epsilon)(m_t^2)^{-\epsilon} \frac{1}{6m_t^2}. \quad (\text{E.15})$$

$B_0(p^2; \bar{0})$

A particular case arises when we set the internal masses to zero, i.e. $m_t^2 \rightarrow 0$.

$$\begin{aligned} B_0(q^2, \bar{0}) &= \frac{\Gamma(2 - \frac{d}{2})}{\Gamma(2)} \int_0^1 dx \frac{1}{[-q^2 x(1-x)]^{2 - \frac{d}{2}}} \\ &= (-q^2)^{\frac{d}{2} - 2} \Gamma\left(2 - \frac{d}{2}\right) \int_0^1 dx x^{\frac{d}{2} - 2} (1-x)^{\frac{d}{2} - 2}, \end{aligned} \quad (\text{E.16})$$

the last term can be written in terms of Gamma functions:

$$\int_0^1 t^{x-1} (1-t)^{y-1} dt = \frac{\Gamma(x)\Gamma(y)}{\Gamma(x+y)}. \quad (\text{E.17})$$

Hence

$$\begin{aligned} B_0(q^2, \bar{m}_t^2) &= (-q^2)^{\frac{d}{2} - 2} \Gamma\left(2 - \frac{d}{2}\right) \frac{\Gamma(\frac{d}{2} - 1)\Gamma(\frac{d}{2} - 1)}{\Gamma(d - 2)} \\ &= (-q^2)^{-\epsilon} \Gamma(\epsilon) \frac{\Gamma(1 - \epsilon)\Gamma(1 - \epsilon)}{\Gamma(2(1 - \epsilon))}. \end{aligned} \quad (\text{E.18})$$

$B_0(p^2; m_t, 0)$

Consider the integral

$$B_0(p^2; m_t^2, 0) = \int_k \frac{1}{[k^2 - m_t^2](k+p)^2}. \quad (\text{E.19})$$

Using the same steps as for the equal mass case, the 2-point integral reads

$$\begin{aligned} B_0(p^2; m_t^2, 0) &= \int_k \int_0^1 \frac{dx}{[k^2 + 2k \cdot px + p^2 x - m_t^2(1-x)]^2} \\ &= \int_k \int_0^1 \frac{dx}{[k^2 + p^2 x(1-x) - m_t^2(1-x)]^2} \\ &= \frac{\Gamma(2 - \frac{d}{2})}{\Gamma(2)} \int_0^1 \frac{dx}{[m_t^2(1-x) - p^2 x(1-x)]^{2 - \frac{d}{2}}} \\ &= (m_t^2)^{\frac{d}{2} - 2} \Gamma\left(2 - \frac{d}{2}\right) \int_0^1 (1-x)^{\frac{d}{2} - 2} \left(1 - \frac{p^2}{m_t^2} x\right)^{\frac{d}{2} - 2} dx \\ &= (m_t^2)^{\frac{d}{2} - 2} \Gamma\left(2 - \frac{d}{2}\right) \int_0^1 (1-x)^{\frac{d}{2} - 2} (1 - \rho x)^{\frac{d}{2} - 2} dx. \end{aligned} \quad (\text{E.20})$$

The hypergeometric function is defined as

$$B(b, c-b)_2F_1(a, b; c; z) = \int_0^1 x^{b-1} (1-x)^{c-b-1} (1-zx)^{-a} dx, \quad (\text{E.21})$$

where

$$B(x, y) = \frac{\Gamma(x+y)}{\Gamma(x)\Gamma(y)}. \quad (\text{E.22})$$

With these definitions, Eq. (E.20) reads

$$\begin{aligned} B_0(p^2; m_t^2, 0) &= (m_t^2)^{\frac{d}{2} - 2} \Gamma\left(2 - \frac{d}{2}\right) \int_0^1 (1-x)^{\frac{d}{2} - 1 - 1} (1 - \rho x)^{-(2 - \frac{d}{2})} dx \\ &= (m_t^2)^{\frac{d}{2} - 2} \Gamma\left(2 - \frac{d}{2}\right) B\left(1, \frac{d}{2} - 1\right) {}_2F_1\left(2 - \frac{d}{2}, 1; \frac{d}{2}; \rho\right) \\ &= (m_t^2)^{\frac{d}{2} - 2} \Gamma\left(2 - \frac{d}{2}\right) \left(\frac{d}{2} - 1\right) {}_2F_1\left(2 - \frac{d}{2}, 1; \frac{d}{2}; \rho\right) \\ &= (m_t^2)^{-\epsilon} \Gamma(\epsilon) (1 - \epsilon) {}_2F_1(\epsilon, 1; 2 - \epsilon; \rho). \end{aligned} \quad (\text{E.23})$$

Hypergeometric functions can be expanded as follows

$$\begin{aligned} {}_2F_1(a, b; c; z) &= \sum_{n=0}^{\infty} \frac{(a)_n (b)_n}{(c)_n} \frac{z^n}{n!} \\ &= {}_2F_1(b, a; c; z), \end{aligned} \quad (\text{E.24})$$

$$(x)_n = \begin{cases} 1 & n = 0 \\ x(x+1) \cdots (x+n-1) & n > 0 \end{cases} = \frac{\Gamma(x+n)}{\Gamma(x)},$$

hence, they can be written as

$$\begin{aligned} {}_2F_1\left(1, \epsilon; 2 - \epsilon; \frac{\rho^2}{m_t^2}\right) &= \sum_{n=0}^{\infty} \frac{(a)_n (b)_n}{(c)_n} \frac{\rho^n}{n!} \\ &= \sum_{n=0}^{\infty} \frac{(1)_n (\epsilon)_n}{(2 - \epsilon)_n} \frac{\rho^n}{n!} \\ &= \frac{\Gamma(2 - \epsilon)}{\Gamma(1)\Gamma(\epsilon)} \sum_{n=0}^{\infty} \frac{\Gamma(1+n)\Gamma(\epsilon+n)}{\Gamma(2 - \epsilon + n)} \frac{\rho^n}{\Gamma(1+n)} \\ &= \frac{\Gamma(2 - \epsilon)}{\Gamma(\epsilon)} \sum_{n=0}^{\infty} \frac{\Gamma(\epsilon+n)}{\Gamma(2 - \epsilon + n)} \rho^n \\ &= \frac{\Gamma(2 - \epsilon)}{\Gamma(\epsilon)} \left[\frac{\Gamma(\epsilon)}{\Gamma(2 - \epsilon)} + \frac{\Gamma(1 + \epsilon)}{\Gamma(3 - \epsilon)} \rho + \frac{\Gamma(2 + \epsilon)}{\Gamma(4 - \epsilon)} \rho^2 + \cdots \right] \\ &= 1 + \frac{\Gamma(2 - \epsilon)}{\Gamma(\epsilon)} \frac{\Gamma(1 + \epsilon)}{\Gamma(3 - \epsilon)} \rho + \frac{\Gamma(2 - \epsilon)}{\Gamma(\epsilon)} \frac{\Gamma(2 + \epsilon)}{\Gamma(4 - \epsilon)} \rho^2 + \cdots \\ &= 1 + \frac{\epsilon}{(2 - \epsilon)} \rho + \frac{\epsilon(1 + \epsilon)}{(2 - \epsilon)(3 - \epsilon)} \rho^2 + \cdots \end{aligned} \quad (\text{E.25})$$

Looking closely at the definition of ${}_2F_1$, the m -th term is

$$\frac{\epsilon(\epsilon+1)(\epsilon+2) \cdots (\epsilon+n-1)}{(2-\epsilon)(3-\epsilon) \cdots (2-\epsilon+n-1)} = \frac{\epsilon((n-1)! + O(\epsilon))}{(n+1)! + O(\epsilon)}. \quad (\text{E.26})$$

Thanks to this expression, and by using the derivative of a rational function, the m -th term becomes

$$\begin{aligned} \frac{d}{d\epsilon} \frac{f(\epsilon)}{g(\epsilon)} &= \frac{f'(\epsilon)g(\epsilon) - f(\epsilon)g'(\epsilon)}{g^2(\epsilon)} \\ \implies \frac{[(n-1)! + O(\epsilon)][(n+1)! + O(\epsilon)] - O(\epsilon)}{[(n+1)! + O(\epsilon)]^2} &= \frac{(n-1)!}{(n+1)!} + O(\epsilon). \end{aligned} \quad (\text{E.27})$$

Thus, the expansion around $\epsilon = 0$ reads

$$\begin{aligned} {}_2F_1\left(1, \epsilon; 2 - \epsilon; \frac{\rho^2}{m_t^2}\right) &= {}_2F_1(1, 0; 2; \rho) + \epsilon \frac{d}{d\epsilon} {}_2F_1(1, \epsilon; 2 - \epsilon; \rho) \Big|_{\epsilon=0} + O(\epsilon^2) \\ &= 1 + \epsilon \left[\frac{\rho}{2} + \frac{\rho^2}{6} + \cdots \right] + O(\epsilon^2) \\ &= 1 + \epsilon \sum_{n=1}^{\infty} \frac{(n-1)!}{(n+1)!} \rho^n + O(\epsilon^2) \\ &= 1 + \epsilon \rho \sum_{n=0}^{\infty} \frac{n!}{(n+2)!} \rho^n + O(\epsilon^2) \\ &= 1 + \epsilon \rho \sum_{n=0}^{\infty} \frac{\Gamma(1+n)\Gamma(1+n)}{\Gamma(3+n)} \frac{\rho^n}{n!} + O(\epsilon^2) \\ &= 1 + \epsilon \rho \frac{\Gamma(1)\Gamma(1)}{\Gamma(3)} {}_2F_1(1, 1; 3; \rho) + O(\epsilon^2) \\ &= 1 + \epsilon \frac{\rho}{2} {}_2F_1(1, 1; 3; \rho) + O(\epsilon^2). \end{aligned} \quad (\text{E.28})$$

The hypergeometric function in the last identity is

$$\begin{aligned}
{}_2F_1(1, 1; 3; \rho) &= 2 \int_0^1 dx \frac{(1-x)}{(1-\rho x)} \\
&= \frac{2}{\rho} \left[\frac{(1-\rho)}{\rho} \int_0^1 \frac{(-\rho) dt}{(1-\rho t)} + 1 \right] \\
&= \frac{2}{\rho} \left[\frac{(1-\rho)}{\rho} \log(1-\rho) + 1 \right].
\end{aligned} \tag{E.29}$$

Hence

$${}_2F_1\left(1, \epsilon; 2 - \epsilon; \frac{p^2}{m_t^2}\right) = 1 + \epsilon \left[\frac{(1-\rho)}{\rho} \log(1-\rho) + 1 \right] + O(\epsilon^2), \tag{E.30}$$

and finally, the $B_0(p^2; m_t^2, 0)$ around $\epsilon = 0$ is

$$\begin{aligned}
B_0(p^2; m_t^2, 0) &= (m_t^2)^{-\epsilon} \Gamma(1+\epsilon) \left(\frac{1}{\epsilon} - 1 \right) {}_2F_1(\epsilon, 1; 2 - \epsilon; \rho) \\
&= (m_t^2)^{-\epsilon} \Gamma(1+\epsilon) \left[\frac{1}{\epsilon} + \frac{(1-\rho)}{\rho} \log(1-\rho) \right] + O(\epsilon).
\end{aligned} \tag{E.31}$$

E.2 3-point scalar integrals

$C_0(0, p_2^2, m_{H_j}^2; \overline{m}_t^2)$

Consider the integral

$$\begin{aligned}
C_0(0, p_2^2, m_{H_j}^2; \overline{m}_t^2) &= \int_k \frac{1}{[k^2 - m_t^2][(k-p_1)^2 - m_t^2][(k+p_2)^2 - m_t^2]}, \\
p_1^2 &= 0, \quad p_2^2 = m_{H_j}^2.
\end{aligned} \tag{E.32}$$

Doing the same steps done for the 2-points integrals, $C_0(0, p_2^2, m_{H_j}^2; \overline{m}_t^2)$ reads

$$\begin{aligned}
C_0(0, p_2^2, m_{H_j}^2; \overline{m}_t^2) &= \frac{\Gamma(3)}{\Gamma(1)\Gamma(1)\Gamma(1)} \int_k \int_0^1 \frac{dx_1 dx_2 dx_3 \delta(1-x_1-x_2-x_3)}{[(k^2 - m_t^2)x_3 + ((k-p_1)^2 - m_t^2)x_1 + ((k+p_2)^2 - m_t^2)x_2]^3} \\
&= 2 \int_0^1 dx_2 \int_0^{1-x_2} dx_1 \int_k \frac{1}{[k^2 - 2k \cdot (p_1 x_1 - p_2 x_2) + p_2^2 x_2 - m_t^2]^3} \\
&= 2 \int_0^1 dx_2 \int_0^{1-x_2} dx_1 \int_k \frac{1}{[k^2 + 2(p_1 \cdot p_2)x_1 x_2 + p_2^2 x_2(1-x_2) - m_t^2]^3}.
\end{aligned} \tag{E.33}$$

Shifting the Feynman parameters as $x_1 \rightarrow x_1(1-x_2)$ and $x_2 \rightarrow x_2$, and rewriting $(p_1 \cdot p_2) = (p_1 + p_2)^2 - p_2^2 = m_{H_j}^2 - p_2^2$, C_0 reads

$$\begin{aligned}
C_0(0, p_2^2, m_{H_j}^2; \overline{m}_t^2) &= 2 \int_0^1 dx_1 dx_2 \int_k \frac{1-x_2}{[k^2 + 2(p_1 \cdot p_2)x_1 x_2(1-x_2) + p_2^2 x_2(1-x_2) - m_t^2]^3} \\
&= 2 \int_0^1 dx_1 dx_2 \int_k \frac{1-x_2}{[k^2 + m_{H_j}^2 x_1 x_2(1-x_2) - p_2^2 x_1 x_2(1-x_2) + p_2^2 x_2(1-x_2) - m_t^2]^3}.
\end{aligned} \tag{E.34}$$

After integrating the expression with respect to the loop momentum, and expressing it in terms of ϵ , C_0 becomes:

$$C_0(0, p_2^2, m_{H_j}^2; \overline{m}_t^2) = -\Gamma(1+\epsilon) \int_0^1 \frac{(1-x_2) dx_1 dx_2}{[m_t^2 - p_2^2 x_2(1-x_2) + (m_{H_j}^2 - p_2^2) x_2(1-x_2) x_1]^{1+\epsilon}}. \tag{E.35}$$

This expression is already finite, so one can immediately set $\epsilon = 0$ at integrand level. Furthermore, defining $\rho_H = m_{H_j}^2/m_t^2$ and $\rho_2 = p_2^2/m_t^2$

$$C_0(0, p_2^2, m_{H_j}^2; \overline{m}_t^2) = -\frac{\Gamma(1+\epsilon)}{m_t^2} (m_t^2)^{-\epsilon} \int_0^1 \frac{(1-x_2) dx_1 dx_2}{[1 - \rho_2 x_2(1-x_2) + (\rho_H - \rho_2) x_2(1-x_2) x_1]}. \tag{E.36}$$

Integration over x_1 yields this expression:

$$\begin{aligned}
& \int_0^1 \frac{(1-x_2)dx_1dx_2}{[1-\rho_2x_2(1-x_2)+(\rho_H-\rho_2)x_2(1-x_2)x_1]} = \\
&= \frac{1}{(\rho_H-\rho_2)} \int_0^1 \frac{dx_2}{x_2} \int_0^1 dx_1 \frac{(\rho_H-\rho_2)x_2(1-x_2)dx_1}{[1-\rho_2x_2(1-x_2)+(\rho_H-\rho_2)x_2(1-x_2)x_1]} = \\
&= \frac{1}{(\rho_H-\rho_2)} \int_0^1 \frac{dx_2}{x_2} \log [1-\rho_2x_2(1-x_2)+(\rho_H-\rho_2)x_2(1-x_2)x_1] \Big|_{x_1=0}^{x_1=1} \\
&= \frac{1}{(\rho_H-\rho_2)} \left[\int_0^1 \frac{dx}{x} \log [1-\rho_Hx(1-x)] - \int_0^1 \frac{dx}{x} \log [1-\rho_2x(1-x)] \right].
\end{aligned} \tag{E.37}$$

Lastly, defining

$$\begin{aligned}
\tau &= \frac{4}{\rho_H}, \quad \lambda = \frac{4}{\rho_2}, \quad f(\tau) = -\frac{1}{4} \log^2 \left[-\frac{1+\sqrt{1-\tau}}{1-\sqrt{1-\tau}} \right], \\
\int_0^1 \frac{dx}{x} \log [1-\rho_2x(1-x)] &= -2f(\lambda), \\
\int_0^1 \frac{dx}{x} \log [1-\rho_Hx(1-x)] &= -2f(\tau),
\end{aligned} \tag{E.38}$$

the integral can be performed analytically

$$\int_0^1 \frac{(1-x_2)dx_1dx_2}{[1-\rho_2x_2(1-x_2)-(\rho_H-\rho_2)x_2(1-x_2)x_1]} = -\frac{2}{(\rho_H-\rho_2)} [f(\tau) - f(\lambda)]. \tag{E.39}$$

and, expressing ρ_2 and ρ_H respectively in terms of λ and τ :

$$\int_0^1 \frac{(1-x_2)dx_1dx_2}{[1-\rho_2x_2(1-x_2)-(\rho_H-\rho_2)x_2(1-x_2)x_1]} = -\frac{1}{2} \frac{\tau\lambda}{\tau-\lambda} [f(\tau) - f(\lambda)]. \tag{E.40}$$

Finally, $C_0(0, p_2^2, m_{H_j}^2; \bar{m}_t^2)$ takes the following analytical expression

$$C_0(0, p_2^2, m_{H_j}^2; \bar{m}_t^2) = \frac{\Gamma(1+\epsilon)}{m_t^2} (m_t^2)^{-\epsilon} \left[\frac{\tau\lambda}{2} \frac{f(\tau) - f(\lambda)}{\tau - \lambda} \right]. \tag{E.41}$$

The one-loop integrals evaluated in this Appendix have direct application both at LO and at NLO, where they are involved in the real corrections and the one-particle-reducible contributions. 4-points and 5-points integrals are much more complex, and when it is needed, a numerical approach would be more convenient.

E.2.1 Scaleless scalar integrals

Within the dimensional regularization, the scaleless Feynman integrals vanish [178]. Consider the integral

$$J_\alpha = \int_k (k^2)^\alpha, \quad [J_\alpha] = [M]^{d+2\alpha}. \tag{E.42}$$

A first naive argument for it to vanish is the dimensionality. The integral J_α does not contain any physical scale apart from the loop momentum k ; the loop momentum is integrated out, so that its dimensionality has to be absorbed by some other dimensionful quantity. Since such scale is absent, it must vanish: $J_\alpha = 0, \forall \alpha$.

Another argument is related with a constructive definition of the Feynman integrals as a function of the dimension $d \in \mathbb{C}$ and its analytical continuation. Consider the integral

$$\int_k \frac{(k^2)^\alpha}{(k^2 - m^2)} + \frac{J_\alpha}{m^2} = \int_k \frac{(k^2)^{\alpha+1}}{(k^2 - m^2)m^2}. \tag{E.43}$$

The left and the right-hand side are exact identities. The analytical evaluation of the integrals appearing in Eq. (E.43) is

$$\begin{aligned} \int_k \frac{(k^2)^\alpha}{(k^2 - m^2)} &= (-1)^{1-\alpha} \frac{\Gamma(\alpha + \frac{d}{2})\Gamma(1 - \alpha - \frac{d}{2})}{\Gamma(1)\Gamma(\frac{d}{2})} (m^2)^{\frac{1}{2}-1-\alpha} \\ \frac{1}{m^2} \int_k \frac{(k^2)^{\alpha+1}}{(k^2 - m^2)} &= (-1)^{-\alpha} \frac{\Gamma(1 + \alpha + \frac{d}{2})\Gamma(-\alpha - \frac{d}{2})}{\Gamma(1)\Gamma(\frac{d}{2})} (m^2)^{\frac{1}{2}-1-\alpha} \\ &= (-1)^{1-\alpha} \frac{\Gamma(\alpha + \frac{d}{2})\Gamma(1 - \alpha - \frac{d}{2})}{\Gamma(1)\Gamma(\frac{d}{2})} (m^2)^{\frac{1}{2}-1-\alpha}. \end{aligned} \quad (\text{E.44})$$

The two integrals have the same analytical expression: this fact brings Eq. (E.43) into the state that

$$\int_k \frac{(k^2)^\alpha}{(k^2 - m^2)} + \frac{J_\alpha}{m^2} = \int_k \frac{(k^2)^\alpha}{(k^2 - m^2)} \implies J_\alpha = 0. \quad (\text{E.45})$$

Rigorously, this result is true for $-2(\alpha+1) < d \leq -2\alpha$. The extension for every $d \in \mathbb{C}$ can be done by means of the analytical continuation. More details on the constructive approach to the d -dimensional integrations can be found in Ref. [178]. A direct consequence of Eq. (E.45) is that the general one-loop massless tadpoles vanish

$$A_0(0) = \int_k \frac{1}{k^2} = J_{-1} = 0. \quad (\text{E.46})$$

In dimensional regularization, the scaleless integrals vanish because of Eq. (E.45) and (E.46). The n -point scaleless one-loop integrals is:

$$\begin{aligned} I_1^n(\bar{0}; \bar{0}) &= \int_k \frac{1}{D_0 \cdots D_n}, \\ D_i &= (k + q_i)^2, \quad q_0 = 0, \quad (q_i \cdot q_j) = 0 \quad \forall i, j \in \{1, \dots, n\}. \end{aligned} \quad (\text{E.47})$$

The Feynman parametrization of $I_1^n(\bar{0}; \bar{0})$ yields

$$\begin{aligned} I_1^n(\bar{0}; \bar{0}) &= \int_k \int_0^1 \frac{\delta(1 - x_0 - \cdots - x_n)}{(x_0 D_0 + \cdots + D_n x_n)^{n+1}} dx_0 \cdots dx_n \\ &= \int_k \int_0^1 dx_1 \int_0^{1-x_1} dx_2 \cdots \int_0^{1-x_1-\cdots-x_n} dx_n \frac{dx_1 \cdots dx_n}{[k^2 + 2k \cdot Q]^{n+1}} \\ &= \int_k \int_0^1 dx_1 \cdots dx_n \frac{(1-x_1)^{n-1} (1-x_2)^{n-2} \cdots (1-x_{n-1})}{[k^2 + 2k \cdot Q]^{n+1}}, \end{aligned} \quad (\text{E.48})$$

such that $Q = \sum_{i=1}^n p_i x_i$ and $Q^2 = 0$. Completing the square in the denominator and shifting $k \rightarrow k - Q$, the integration over the Feynman parameters yields:

$$\begin{aligned} I_1^n(\bar{0}; \bar{0}) &= \int_k \int_0^1 dx_1 \cdots dx_n \frac{(1-x_1)^{n-1} (1-x_2)^{n-2} \cdots (1-x_{n-1})}{[(k+Q)^2]^{n+1}} \\ &= \int_k \int_0^1 dx_1 \cdots dx_n \frac{x_1^{n-1} x_2^{n-2} \cdots x_{n-1}}{(k^2)^{n+1}} \\ &= \frac{1}{n!} \int_k \frac{1}{(k^2)^{n+1}} = \frac{J_{-n-1}}{n!}. \end{aligned} \quad (\text{E.49})$$

This fact shows that each scaleless n -point one-loop scalar integral can be related to a massless tadpole integral with the power of the denominator equal to the number of external legs. Eq. (E.49) can be generalized by taking into account denominators with positive indices¹. This generalization involves the only replacement $n \rightarrow \sum_{i=1}^n a_i$, where a_i is the (positive) power of the denominator D_i .

¹For negative indices one can use either integral or integrand reduction methods in order to obtain a combination of scalar integrals with positive powers of the denominators.

The vanishing of the scaleless one-loop integrals can be shown at multi-loop level as well:

$$I_l^n(\bar{0}; \bar{0}) = \int_{k_1 \dots k_l} \frac{1}{\prod_{i=1}^l \prod_{j=1}^{n_i} D_{ij}}, \quad (E.50)$$

$$D_{ij} = (k_i + q_{ij})^2, \quad q_{i0} = 0, \quad (q_{ij} \cdot q_{rs}) = 0,$$

$$\forall i, r \in \{1, \dots, l\}, j \in \{1, \dots, n_i\}, s \in \{1, \dots, n_r\}.$$

The Feynman parametrization yields

$$I_l^n(\bar{0}; \bar{0}) = \int_{k_1 \dots k_l} \int_0^1 \frac{\delta(1 - x_1 - \dots - x_n)}{(x_1 D_{11} + \dots + D_{ln_l} x_n)^n} dx_1 \dots dx_n$$

$$= \int_{k_1 \dots k_l} \int_0^1 \frac{\delta(1 - x_1 - \dots - x_n)}{(\mathbf{k}^T \cdot A \mathbf{k} + 2\mathbf{q}^T \cdot \mathbf{k})^n} dx_1 \dots dx_n, \quad (E.51)$$

where $n = \sum_{i,j} n_{ij}$, $\mathbf{k}^T = (k_1, \dots, k_l)$ is the vector containing all the loop momenta k_i and \mathbf{q} contains a combination of the internal momenta q with coefficients depending on the parameters x_i . The matrix A (symmetric) admits a decomposition $A = S^T S$ such that $S^T = S$. Hence,

$$I_l^n(\bar{0}; \bar{0}) = \int_{k_1 \dots k_l} \int_0^1 \frac{\delta(1 - x_1 - \dots - x_n)}{[(S\mathbf{k})^T \cdot S\mathbf{k} + 2\mathbf{q}^T \cdot \mathbf{k}]^n} dx_1 \dots dx_n. \quad (E.52)$$

Applying the rotation $k \rightarrow S^{-1}k$, the Jacobian is $d^d k_1 \dots d^d k_l \rightarrow \det(S^{-1}) d^d k_1 \dots d^d k_l$,

$$I_l^n(\bar{0}; \bar{0}) = \int_{k_1 \dots k_l} \int_0^1 \frac{1}{\det^l(S)} \frac{\delta(1 - x_1 - \dots - x_n)}{[\mathbf{k}^2 + 2\mathbf{q}^T \cdot (S^{-1}\mathbf{k})]^n} dx_1 \dots dx_n$$

$$= \int_{k_1 \dots k_l} \int_0^1 \frac{1}{\det(S)} \frac{\delta(1 - x_1 - \dots - x_n)}{[\mathbf{k}^2 + 2(S^{-1}\mathbf{q})^T \cdot \mathbf{k}]^n} dx_1 \dots dx_n, \quad (E.53)$$

and the shift $k \rightarrow k - S^{-1}\mathbf{q}$

$$I_l^n(\bar{0}; \bar{0}) = \int_0^1 \frac{\delta(1 - x_1 - \dots - x_n)}{\det^l(S)} dx_1 \dots dx_n \int_{k_1 \dots k_l} \frac{1}{[\mathbf{k}^2]^n}$$

$$= C \int_{k_1 \dots k_l} \frac{1}{[k_1^2 + \dots + k_l^2]^n}, \quad (E.54)$$

where C is the factor containing the integral over the Feynman parameters. Notice that the loop integral has the following structure

$$I_l^n(\bar{0}; \bar{0}) = \frac{C}{(i\pi^{\frac{d}{2}})^l} \int \frac{dk_{0,1} \dots dk_{0,l} d^{d-1}\bar{k}_1 \dots d^{d-1}\bar{k}_l}{[(k_{0,1})^2 + \dots + (k_{0,l})^2 - |\bar{k}_1|^2 - \dots - |\bar{k}_l|^2]^n}. \quad (E.55)$$

The time and space components can be grouped as follows:

$$dk_{0,1} \dots dk_{0,l} = d\Omega_{l-1} |K_0|^{l-1} d|K_0| = d^l K_0$$

$$d^{d-1}\bar{k}_1 \dots d^{d-1}\bar{k}_l = d\bar{k}_{11} \dots d\bar{k}_{1d-1} d\bar{k}_{21} \dots d\bar{k}_{ld-1} = d\Omega_{l(d-1)-1} |\mathbf{K}|^{l(d-1)-1} d|\mathbf{K}| = d^{l(d-1)} \mathbf{K}, \quad (E.56)$$

therefore

$$I_l^n(\bar{0}; \bar{0}) = \frac{C}{(i\pi^{\frac{d}{2}})^l} \int \frac{d^l K_0 d^{l(d-1)} \mathbf{K}}{(K_0^2 - |\mathbf{K}|^2)^n} = C \int_K \frac{d^d K}{[K^2]^n} = C J_{-n}. \quad (E.57)$$

The Eq. (E.57) hides a subtlety: its metric tensor is not anymore the standard Minkowski metric with signature $(1, d-1)$, but $(l, d-l)$. However, this very same calculation could have done in the Euclidean space by means of the Wick rotation, leading to a non-ambiguous definition of the scalar products. Moreover, it can be shown [178] that for dimensionally regularized integrals the following relation holds:

$$\int d^{d_1} k_1 \int d^{d_2} k_2 f(k_1^2 + k_2^2) = \int d^{d_1+d_2} K f(K^2), \quad K = (k_1, k_2), \quad (E.58)$$

from which Eq. (E.57) follows, after inverting the Wick rotation.

It is important to notice that there are scaleless integrals for which their vanishing value comes from a non-trivial interplay between UV and IR divergences. This fact can be shown explicitly from the massless bubble:

$$B_0(0; 0, 0) = \int_k \frac{1}{k^2(k+p)^2}, \quad p^2 = 0. \quad (\text{E.59})$$

The Feynman parametrization yields

$$B_0(0; 0, 0) = \int_0^1 \int_k \frac{dx}{[k^2 + 2x(k \cdot p)]^2} = \int_0^1 \int_k \frac{dx}{[k^2]^2} = \int_k \frac{1}{[k^2]^2} = J_{-2}. \quad (\text{E.60})$$

Instead of directly setting it to zero, the reason why it vanishes can be shown by analytically integrating the loop momentum:

$$\begin{aligned} B_0(0; 0, 0) &= \frac{1}{i\pi^{\frac{d}{2}}} \int \frac{dk^0 d^{(d-1)}\bar{k}}{[(k^0)^2 - |\bar{k}|^2]^2} \\ &= -\frac{\pi^{1-\frac{d}{2}}}{2} \int \frac{d^{(d-1)}\bar{k}}{[|\bar{k}|^2]^{\frac{3}{2}}} \\ &= -\frac{\pi^{1-\frac{d}{2}}}{4} \int d\Omega_{d-2} \int_0^\infty \frac{d\bar{k}^2}{[\bar{k}^2]^{3-\frac{d}{2}}}. \end{aligned} \quad (\text{E.61})$$

Renaming $\bar{k}^2 = y$, setting $d = 4 - 2\epsilon$ and integrating over the solid angle $d\Omega_{d-2}$:

$$B_0(0; 0, 0) = -4^{-\epsilon} \frac{\Gamma(1-\epsilon)}{\Gamma(2-2\epsilon)} \int_0^\infty \frac{dy}{y^{1+\epsilon}}. \quad (\text{E.62})$$

There is no way to make the integral of Eq. (E.62) converge by acting on the ϵ parameter. However, an appropriate analytical continuation with respect to ϵ ensures its vanishing behaviour. It is possible to recover this behaviour by splitting the integration regions at a scale Λ and imposing two different conditions on ϵ :

$$\int_0^\infty \frac{dy}{y^{1+\epsilon}} = \int_0^\Lambda \frac{dy}{y^{1+\epsilon}} + \int_\Lambda^\infty \frac{dy}{y^{1+\epsilon}}. \quad (\text{E.63})$$

The first term diverges if $\epsilon > 0$; the second one if $\epsilon < 0$. Imposing $\epsilon_{\text{IR}} = \epsilon < 0$ for the first term and $\epsilon_{\text{UV}} = \epsilon > 0$ for the second, the integral in the l.h.s. is not divergent anymore:

$$\begin{aligned} \int_0^\infty \frac{dy}{y^{1+\epsilon}} &= -\frac{1}{\epsilon_{\text{IR}}} \frac{1}{y^{\epsilon_{\text{IR}}}} \Big|_\Lambda^0 - \frac{1}{\epsilon_{\text{UV}}} \frac{1}{y^{\epsilon_{\text{UV}}}} \Big|_\Lambda^\infty \\ &= -\frac{\Lambda^{-\epsilon_{\text{IR}}}}{\epsilon_{\text{IR}}} + \frac{\Lambda^{-\epsilon_{\text{UV}}}}{\epsilon_{\text{UV}}} \\ &= \left(-\frac{1}{\epsilon_{\text{IR}}} + \log(\Lambda) \right) + \left(\frac{1}{\epsilon_{\text{UV}}} - \log(\Lambda) \right) + O(\epsilon_{\text{UV}}, \epsilon_{\text{IR}}) \\ &= \left(\frac{1}{\epsilon_{\text{UV}}} - \frac{1}{\epsilon_{\text{IR}}} \right) + O(\epsilon_{\text{UV}}, \epsilon_{\text{IR}}), \end{aligned} \quad (\text{E.64})$$

which turns to be independent on the choice of the scale Λ . Thus, the massless bubble becomes

$$B_0(0; 0, 0) = 4^{-\epsilon} \frac{\Gamma(1-\epsilon)}{\Gamma(2-2\epsilon)} \left(\frac{1}{\epsilon_{\text{IR}}} - \frac{1}{\epsilon_{\text{UV}}} \right). \quad (\text{E.65})$$

The vanishing behaviour of $B_0(0; 0, 0)$ is related to an exact cancellation between the UV and IR poles. The UV pole extracted in this way is the one that is canceled by $\overline{\text{MS}}$ counterterms for massless quark self-energies.

Appendix F

Utilities

In this Appendix, some useful identities used to make the expressions compact are presented. In the first Section, identities involving the kinematical variables and the transverse momentum are presented. In the last Section, the transformations regarding the Feynman parameters are shown for the one-loop case.

F.1 Useful kinematical identities

In the context of this thesis, the transverse momentum p_T^2 has been defined as follows:

$$p_T^2 = \frac{(\hat{t} - m_{H_1}^2)(\hat{u} - m_{H_1}^2) - \hat{s}m_{H_1}^2}{\hat{s}}. \quad (\text{F.1})$$

Momentum conservation relates the \hat{s} , \hat{t} and \hat{u} , and p_T^2 can take different expressions, for examples:

$$\begin{aligned} \hat{s}p_T^2 &= (\hat{t} - m_{H_1}^2)(\hat{u} - m_{H_1}^2) - \hat{s}m_{H_1}^2 \\ &= -(\hat{t} - m_{H_1}^2)(\hat{t} - m_{H_2}^2) - \hat{s}\hat{t} \\ &= \hat{t}\hat{u} - m_{H_1}^2 m_{H_2}^2. \end{aligned} \quad (\text{F.2})$$

Moreover, looking back to Appendix C, the \hat{t} variable runs from t_- to t_+ , defined as

$$\hat{t}_\pm = -\frac{\hat{s}}{2}(1 - \Sigma \mp \beta). \quad (\text{F.3})$$

Combinations of \hat{t} and \hat{t}_\pm can be defined:

$$\begin{aligned} \hat{t}_+ \hat{t}_- &= m_{H_1}^2 m_{H_2}^2, \\ \hat{t}_+ - \hat{t}_- &= \hat{s}\beta, \\ \hat{t}_+ + \hat{t}_- &= -\hat{s}(1 - \Sigma), \\ \hat{t} - \hat{t}_+ &= -\frac{\hat{s}\beta}{2}(1 + \cos\theta) = -\frac{(\hat{t}_+ - \hat{t}_-)}{2}(1 + \cos\theta), \\ \hat{t} - \hat{t}_- &= \frac{\hat{s}\beta}{2}(1 - \cos\theta) = \frac{(\hat{t}_+ - \hat{t}_-)}{2}(1 - \cos\theta), \end{aligned} \quad (\text{F.4})$$

so that

$$\begin{aligned} \hat{s}p_T^2 &= \hat{t}\hat{u} - m_{H_1}^2 m_{H_2}^2 \\ &= \frac{\hat{s}^2}{4}(1 - \Sigma - \beta \cos\theta)(1 - \Sigma + \beta \cos\theta) - \hat{t}_+ \hat{t}_- \\ &= \frac{\hat{s}^2}{4}[(1 - \Sigma)^2 - \beta^2 \cos^2\theta] - \hat{t}_+ \hat{t}_- \\ &= \frac{1}{4}[(\hat{t}_+ + \hat{t}_-)^2 - (\hat{t}_+ - \hat{t}_-)^2 \cos^2\theta] - \hat{t}_+ \hat{t}_- \\ &= \frac{1}{4}(\hat{t}_+ - \hat{t}_-)^2(1 - \cos^2\theta) \\ &= -(\hat{t} - \hat{t}_+)(\hat{t} - \hat{t}_-). \end{aligned} \quad (\text{F.5})$$

It is possible to define the $d\hat{t}$ element as follows

$$\frac{d\hat{t}}{\hat{s}p_T^2} = -\frac{d\hat{t}}{(\hat{t}-\hat{t}_-)(\hat{t}-\hat{t}_+)}. \quad (\text{F.6})$$

The partial fractioning on the denominator yields

$$\frac{d\hat{t}}{\hat{s}p_T^2} = -\frac{d\hat{t}}{(\hat{t}_+ - \hat{t}_-)} \left[\frac{1}{(\hat{t} - \hat{t}_+)} - \frac{1}{(\hat{t} - \hat{t}_-)} \right]. \quad (\text{F.7})$$

It is easy to show that the identity

$$(\hat{t} - \hat{t}_+) = -(\hat{u} - \hat{t}_-), \quad (\text{F.8})$$

is valid and, therefore

$$\frac{d\hat{t}}{\hat{s}p_T^2} = \frac{d\hat{t}}{(\hat{t}_+ - \hat{t}_-)} \left[\frac{1}{(\hat{t} - \hat{t}_-)} + \frac{1}{(\hat{u} - \hat{t}_-)} \right]. \quad (\text{F.9})$$

The partonic cross section can be written as the integral of a function depending on the kinematic variables with respect to \hat{t}

$$\int_{\hat{t}_-}^{\hat{t}_+} \frac{d\hat{t}}{\hat{s}p_T^2} f(\hat{t}, \hat{u}) = \int_{\hat{t}_-}^{\hat{t}_+} \frac{d\hat{t}}{(\hat{t}_+ - \hat{t}_-)} \left[\frac{f(\hat{t}, \hat{u})}{(\hat{t} - \hat{t}_-)} + \frac{f(\hat{t}, \hat{u})}{(\hat{u} - \hat{t}_-)} \right]. \quad (\text{F.10})$$

The second term can be written with the same denominator of the first one by noting that

$$\int_{\hat{t}_-}^{\hat{t}_+} d\hat{t} \frac{f(\hat{t}, \hat{u})}{(\hat{u} - \hat{t}_-)} = \int_{\hat{t}_-}^{\hat{t}_+} d\hat{t} \frac{f(\hat{u}, \hat{t})}{(\hat{t} - \hat{t}_-)}, \quad (\text{F.11})$$

and so

$$\int_{\hat{t}_-}^{\hat{t}_+} \frac{d\hat{t}}{\hat{s}p_T^2} f(\hat{t}, \hat{u}) = \int_{\hat{t}_-}^{\hat{t}_+} \frac{d\hat{t}}{(\hat{t}_+ - \hat{t}_-)} \frac{f(\hat{t}, \hat{u}) + f(\hat{u}, \hat{t})}{(\hat{t} - \hat{t}_-)}. \quad (\text{F.12})$$

The integral of Eq. (F.12) shows manifestly the logarithmic instabilities that lie in the boundary of the integration region. In Chapter 4 these instabilities have been tamed with a dedicated change of variables.

F.2 Feynman Parameter Tricks

The numerical integration of the Feynman integrals requires fixed boundaries, which for the Feynman parameters is a hypercube. In this Section the manipulations of the Feynman parameters which have been performed to obtain the convenient integration volume will be presented. The strategies presented in this Section have been employed for setting the integrands

F.2.1 Boundaries

Consider the integral measure occurring in a Feynman integral after its parameterization (for a 4-point integral):

$$\int_0^1 d\hat{x}_1 d\hat{x}_2 d\hat{x}_3 d\hat{x}_4 \delta \left(1 - \sum_{i=1}^4 \hat{x}_i \right), \quad (\text{F.13})$$

Extending a parameter domain to the real axis:

$$\int_{-\infty}^{\infty} d\hat{x}_1 d\hat{x}_2 d\hat{x}_3 d\hat{x}_4 \delta \left(1 - \sum_{i=1}^4 \hat{x}_i \right) \prod_{i=1}^4 \theta(x_i) \theta(1 - x_i). \quad (\text{F.14})$$

Now the delta function can be legitimately integrated with respect to x_4

$$\int_{-\infty}^{\infty} d\hat{x}_1 d\hat{x}_2 d\hat{x}_3 \theta \left(\sum_{i=1}^3 \hat{x}_i \right) \theta \left(1 - \sum_{i=1}^3 \hat{x}_i \right) \prod_{i=1}^3 \theta(\hat{x}_i) \theta(1 - \hat{x}_i). \quad (\text{F.15})$$

The first two Heaviside distributions yield the conditions

$$\theta(\hat{x}_1 + \hat{x}_2 + \hat{x}_3)\theta(1 - \hat{x}_1 - \hat{x}_2 - \hat{x}_3) \geq 0 \iff -\hat{x}_1 - \hat{x}_2 \leq \hat{x}_3 \leq 1 - \hat{x}_1 - \hat{x}_2. \quad (\text{F.16})$$

Because of the $\theta(\hat{x}_3)\theta(1 - \hat{x}_3)$ function, the lower limit for \hat{x}_3 has to be in between 0 and 1:

$$0 \leq -\hat{x}_1 - \hat{x}_2 \leq 1 \iff \hat{x}_1 = 0 \wedge \hat{x}_2 = 0. \quad (\text{F.17})$$

Hence the lower limit for x_3 has to be 0.

Same argument holds for the upper limit for \hat{x}_3 , except that now it does not get a single value, but a condition over \hat{x}_2 :

$$0 \leq 1 - \hat{x}_1 - \hat{x}_2 \leq 1 \implies \hat{x}_2 \geq -\hat{x}_1 \wedge \hat{x}_2 \leq 1 - \hat{x}_1. \quad (\text{F.18})$$

As for the first condition, for $\hat{x}_1 > 0$, the lower limit on \hat{x}_2 is zero.

Putting all the conditions together, the integration region is

$$\begin{aligned} & \theta\left(\sum_{i=1}^3 \hat{x}_i\right) \theta\left(1 - \sum_{i=1}^3 \hat{x}_i\right) \prod_{i=1}^3 \theta(\hat{x}_i)\theta(1 - \hat{x}_i) \geq 0 \\ \implies & 0 \leq \hat{x}_1 \leq 1 \wedge 0 \leq \hat{x}_2 \leq 1 - \hat{x}_1 \wedge 0 \leq \hat{x}_3 \leq 1 - \hat{x}_1 - \hat{x}_2, \end{aligned} \quad (\text{F.19})$$

therefore,

$$\int_0^1 d\hat{x}_1 d\hat{x}_2 d\hat{x}_3 d\hat{x}_4 \delta\left(1 - \sum_{i=1}^4 \hat{x}_i\right) = \int_0^1 d\hat{x}_1 \int_0^{1-\hat{x}_1} d\hat{x}_2 \int_0^{1-\hat{x}_1-\hat{x}_2} d\hat{x}_3. \quad (\text{F.20})$$

This argument can be extended for any number of Feynman parameters

$$\int_0^1 d^{n+1}\hat{x} \delta\left(1 - \sum_{i=1}^{n+1} \hat{x}_i\right) = \int_0^1 \cdots \int_0^{1-\hat{x}_1-\cdots-\hat{x}_n} d^n \hat{x}, \quad d^n \hat{x} = \prod_{j=1}^n d\hat{x}_j. \quad (\text{F.21})$$

Note that the order of the integrations is totally arbitrary:

$$\int_0^1 d\hat{x}_1 d\hat{x}_2 d\hat{x}_3 \delta\left(1 - \sum_{i=1}^3 \hat{x}_i\right) = \int_0^1 d\hat{x}_1 \int_0^{1-\hat{x}_1} d\hat{x}_2 = \int_0^1 d\hat{x}_2 \int_0^{1-\hat{x}_2} d\hat{x}_1. \quad (\text{F.22})$$

This fact leads to the first trick: whenever a pattern that resembles the r.h.s. of Eq. (F.21) shows up, the integration order can be permuted to the most convenient one.

F.2.2 Transformations

To achieve the numerical integration, the variables have to be transformed such that the new integration volume is the n -dimensional unit cube $\mathcal{C} = [0, 1]^n$. The easiest way is to use the following transformation

$$\begin{cases} \hat{x}_i = \left[\prod_{j=1}^{i-1} (1 - x_j)\right] x_i, & i > 1 \\ \hat{x}_i = x_i, & i = 1 \end{cases} \quad (\text{F.23})$$

$$d^n \hat{x} = \left(\prod_{i=1}^{n-1} (1 - x_i)^{n-i}\right) d^n x,$$

hence

$$\int_0^1 d^{n+1}\hat{x} \delta\left(1 - \sum_{i=1}^{n+1} \hat{x}_i\right) = \int_0^1 d^n x \left(\prod_{i=1}^{n-1} (1 - x_i)^{n-i}\right). \quad (\text{F.24})$$

Focusing on the previous example, we can write:

$$\int_0^1 d\hat{x}_1 d\hat{x}_2 d\hat{x}_3 d\hat{x}_4 \delta\left(1 - \sum_{i=1}^4 \hat{x}_i\right) = \int_0^1 dx_1 dx_2 dx_3 (1 - x_1)^2 (1 - x_2). \quad (\text{F.25})$$

Note that the integration boundaries are invariant on the shift $x_i \rightarrow 1 - x_i$:

$$\int_0^1 dx f(x) = \int_0^1 dx f(1-x). \quad (\text{F.26})$$

Therefore, this shift can occasionally be convenient:

$$\begin{aligned} \int_0^1 d\hat{x}_1 d\hat{x}_2 d\hat{x}_3 d\hat{x}_4 \delta\left(1 - \sum_{i=1}^4 \hat{x}_i\right) &= \int_0^1 dx_1 dx_2 dx_3 (1-x_1)^2 (1-x_2) \\ &= \int_0^1 dx_1 dx_2 dx_3 (x_1^2 x_2) \end{aligned} \quad (\text{F.27})$$

The Eq. (F.23) offers a general change of variable for mapping the domain of the Feynman parameters in $[0, 1]^n$. However, the complexity of the mapping increases with the number of Feynman parameters, and issues related with the end-point subtractions can arise. At NLO, a dedicated change of variables have been chosen for treating the two-loop integrals for the virtual contributions, which has been presented in Chapter 3. Here below a sketch of the strategy employed in the construction of the change of variables at NLO is presented with LO examples.

Example 1

Let I be a one-loop 4-point integral. Using Feynman parametrization it reads

$$I = \int_0^1 d\hat{x}_2 \int_0^{1-\hat{x}_2} d\hat{x}_1 \int_0^{1-\hat{x}_1-\hat{x}_2} d\hat{x}_3 \frac{f(\hat{x}_1, \hat{x}_2, \hat{x}_3)}{[\hat{N}_1^2(\hat{x}_1, \hat{x}_2, \hat{x}_3)]^p},$$

$$\hat{N}_1^2(\hat{x}_1, \hat{x}_2, \hat{x}_3) = 1 - \hat{x}_2(1 - \hat{x}_1 - \hat{x}_2)\rho_s - \hat{x}_3(\hat{x}_1 + \hat{x}_2)(\rho_t - \rho_{H_1}) - \hat{x}_2\hat{x}_3(\rho_u - \rho_{H_1}) - \hat{x}_3(1 - \hat{x}_3)\rho_{H_1}. \quad (\text{F.28})$$

Applying the first transformation $x_1 = 1 - \hat{x}_1 - \hat{x}_2$, the expression reads

$$I = \int_0^1 d\hat{x}_2 \int_0^{1-\hat{x}_2} dx_1 \int_0^{x_1} d\hat{x}_3 \frac{f(x_1, \hat{x}_2, \hat{x}_3)}{[\hat{N}_1^2(x_1, \hat{x}_2, \hat{x}_3)]^p} \quad (\text{F.29})$$

$$\hat{N}_1^2(\hat{x}_1, \hat{x}_2, \hat{x}_3) = 1 - \hat{x}_2 x_1 \rho_s - \hat{x}_3(1 - x_1)(\rho_t - \rho_{H_1}) - \hat{x}_2 \hat{x}_3(\rho_u - \rho_{H_1}) - \hat{x}_3(1 - \hat{x}_3)\rho_{H_1}$$

Switching the boundaries for \hat{x}_2 and x_1 , I becomes

$$\int_0^1 d\hat{x}_2 \int_0^{1-\hat{x}_2} dx_1 \int_0^{x_1} d\hat{x}_3 \frac{f(x_1, \hat{x}_2, \hat{x}_3)}{[\hat{N}_1^2(x_1, \hat{x}_2, \hat{x}_3)]^p} = \int_0^1 dx_1 \int_0^{1-x_1} d\hat{x}_2 \int_0^{x_1} d\hat{x}_3 \frac{f(x_1, \hat{x}_2, \hat{x}_3)}{[\hat{N}_1^2(x_1, \hat{x}_2, \hat{x}_3)]^p}. \quad (\text{F.30})$$

Finally, setting the boundaries from 0 to 1 through the transformation $\hat{x}_2 = (1 - x_1)x_2$ and $\hat{x}_3 = x_1 x_3$, the total transformation is

$$\begin{cases} \hat{x}_1 = (1 - x_1)(1 - x_2) \\ \hat{x}_2 = x_2(1 - x_1) \\ \hat{x}_3 = x_1 x_3 \end{cases}. \quad (\text{F.31})$$

Hence, the full integral reads

$$I = \int_0^1 dx_1 dx_2 dx_3 \frac{f(x_1, \hat{x}_2, \hat{x}_3)}{[\hat{N}_1^2(x_1, \hat{x}_2, \hat{x}_3)]^p} x_1(1 - x_1). \quad (\text{F.32})$$

Notice that the Jacobian depends on a single variable.

Example 2

The Feynman parametrization brings the integral for \mathcal{M}_2 in the following form:

$$I = \int_0^1 d\hat{x}_3 \int_0^{1-\hat{x}_3} d\hat{x}_2 \int_0^{1-\hat{x}_3-\hat{x}_2} d\hat{x}_1 \frac{f(\hat{x}_1, \hat{x}_2, \hat{x}_3)}{[\hat{N}_2^2(\hat{x}_1, \hat{x}_2, \hat{x}_3)]^p}, \quad (\text{F.33})$$

$$\begin{aligned} \hat{N}_1^2(\hat{x}_1, \hat{x}_2, \hat{x}_3) &= 1 - \hat{x}_3(1 - \hat{x}_2 - \hat{x}_3)\rho_{\hat{u}} - \hat{x}_3(1 - \hat{x}_1 - \hat{x}_2 - \hat{x}_3)\rho_s + \\ &\quad - (\hat{x}_2 + \hat{x}_3)(1 - \hat{x}_1 - \hat{x}_2 - \hat{x}_3)\rho_{\hat{t}} - (\hat{x}_2 + \hat{x}_3)(1 - \hat{x}_1 - \hat{x}_2 - \hat{x}_3)\rho_{H_1}. \end{aligned}$$

The first replacement will be $\alpha = 1 - \hat{x}_1 - \hat{x}_2 - \hat{x}_3 \implies \hat{x}_1 = 1 - \alpha - \hat{x}_2 - \hat{x}_3$. Therefore

$$I = \int_0^1 d\hat{x}_3 \int_0^{1-\hat{x}_3} d\hat{x}_2 \int_0^{1-\hat{x}_3-\hat{x}_2} d\alpha. \quad (\text{F.34})$$

Exchanging the integration order and performing the change of variables $\beta = 1 - \hat{x}_2 - \hat{x}_3$, I becomes

$$\begin{aligned} \int_0^1 d\hat{x}_3 \int_0^{1-\hat{x}_3} d\hat{x}_2 \int_0^{1-\hat{x}_3-\hat{x}_2} d\alpha &= \int_0^1 d\alpha \int_0^{1-\alpha} d\hat{x}_3 \int_0^{1-\alpha-\hat{x}_3} d\hat{x}_2 \\ &= \int_0^1 d\alpha \int_0^{1-\alpha} d\hat{x}_3 \int_\alpha^{1-\hat{x}_3} d\beta. \end{aligned} \quad (\text{F.35})$$

The domain for (α, β) is the upper triangle inscribed into the square $[0, 1]^2$. Exchanging the integration variables, the boundaries can be mapped into the unit cube by means of the following identities

$$\begin{aligned} \int_0^1 d\alpha \int_0^{1-\alpha} d\hat{x}_3 \int_\alpha^{1-\hat{x}_3} d\beta &= \int_0^1 d\hat{x}_3 \int_0^{1-\hat{x}_3} d\alpha \int_\alpha^{1-\hat{x}_3} d\beta \\ &= \int_0^1 d\hat{x}_3 \int_0^{1-\hat{x}_3} d\beta \int_0^\beta d\alpha \\ &= \int_0^1 d\beta \int_0^{1-\beta} d\hat{x}_3 \int_0^\beta d\alpha \\ &= \int_{\mathcal{C}} d\bar{x} x_1 (1 - x_1). \end{aligned} \quad (\text{F.36})$$

Collecting all the change of variables, the mapping reads

$$\begin{aligned} \hat{x}_1 &= 1 - \alpha - \hat{x}_2 - \hat{x}_3 \implies \hat{x}_1 = \beta - \alpha = x_1(1 - x_2) \\ \hat{x}_2 &= 1 - \beta - \hat{x}_3 \implies \hat{x}_2 = 1 - \beta - (1 - \beta)x_3 = (1 - x_1)(1 - x_3) \\ \hat{x}_3 &= (1 - \beta)x_3 \implies \hat{x}_3 = (1 - x_1)x_3. \end{aligned} \quad (\text{F.37})$$

Appendix G

Running of α_s in QCD

In this Appendix, the evaluation of the counterterms for α_s in the $\overline{\text{MS}}$ scheme for the $N_f = 5$ active massless flavours with the top-quark mass decoupled from the running will be presented.

G.1 Gluon propagator

Figure G.1: Diagrams contributing to the gluon propagator.

The gluon propagator expressed in its form factor reads

$$i\delta^{ab}(p^2 g^{\mu\nu} - p^\mu p^\nu)\Pi_0(p^2) = \mathcal{M}_{\text{VP}}^{\mu\nu,ab} + \mathcal{M}_{\text{PI}}^{\mu\nu,ab} + \mathcal{M}_{\text{G}}^{\mu\nu,ab} \quad (\text{G.1})$$

and the counterterm behaves such that

$$\Pi_0(p^2) - \delta_3 = \text{finite}. \quad (\text{G.2})$$

G.1.1 Massless flavours

$$\begin{aligned} \mathcal{M}_{\text{VP}}^{\mu\nu,ab} &= -\frac{i}{(4\pi)^2} (4\pi\mu^2)^{2-\frac{d}{2}} \int_k (-ig_s \gamma^\mu T^a) \frac{i\cancel{k}}{k^2} (-ig_s \gamma^\nu T^b) \frac{i(\cancel{k} + \cancel{p})}{(k+p)^2} \\ &= -\frac{1}{2} \frac{ig_s^2}{(4\pi)^2} \delta^{ab} (4\pi\mu^2)^{2-\frac{d}{2}} \int_k \frac{\text{Tr}[\gamma^\mu \cancel{k} \gamma^\nu (\cancel{k} + \cancel{p})]}{k^2 (k+p)^2} \\ &= -\frac{ig_s^2}{2(4\pi)^2} \delta^{ab} (4\pi\mu^2)^{2-\frac{d}{2}} 4 \left[2 \int_k \frac{k^\mu k^\nu}{k^2 (k+p)^2} + \int_k \frac{k^\mu p^\nu + p^\mu k^\nu}{k^2 (k+p)^2} - g^{\mu\nu} \int_k \frac{(k^2 + k \cdot p)}{k^2 (k+p)^2} \right] \\ &= -\frac{ig_s^2}{(4\pi)^2} \delta^{ab} [p^2 g^{\mu\nu} - p^\mu p^\nu] \left(\frac{4\pi\mu^2}{-p^2} \right)^\epsilon \Gamma(1+\epsilon) \frac{2}{3} \frac{1}{\epsilon} \end{aligned} \quad (\text{G.3})$$

Summing over the massless flavours, we obtain

$$\mathcal{M}_{\text{VP}}^{\mu\nu,ab} = -\frac{ig_s^2}{(4\pi)^2} \delta^{ab} [p^2 g^{\mu\nu} - p^\mu p^\nu] \left(\frac{4\pi\mu^2}{-p^2} \right)^\epsilon \Gamma(1+\epsilon) \frac{2N_f}{3} \frac{1}{\epsilon} + \text{finite}. \quad (\text{G.4})$$

The triple gauge boson interaction diagram is given by

$$\begin{aligned}\mathcal{M}_{\text{TI}}^{\mu\nu,ab} &= \frac{1}{2} \frac{i}{(4\pi)^2} (4\pi\mu^2)^{2-\frac{d}{2}} \int_k (-g_s f^{acd} [g^{\mu\alpha}(k+2p)^\beta + g^{\alpha\beta}(-2k-p)^\mu + g^{\beta\mu}(k-p)^\alpha]) \times \\ &\times \left(\frac{-ig_{\alpha\rho}\delta^{ce}}{k^2} \right) (-g_s f^{ebf} [g^{\rho\nu}(k+2p)^\sigma + g^{\nu\sigma}(k-p)^\rho + g^{\sigma\rho}(-2k-p)^\nu]) \left(\frac{-ig_{\sigma\beta}\delta^{df}}{(k+p)^2} \right) \\ &= \frac{1}{2} \frac{ig_s^2}{(4\pi)^2} f^{acd} f^{bcd} (4\pi\mu^2)^{2-\frac{d}{2}} \int_k \frac{\mathcal{N}^{\mu\nu}}{D_0 D_1},\end{aligned}\quad (\text{G.5})$$

where

$$\begin{aligned}\mathcal{N}^{\mu\nu} &= [g^{\mu\rho}(k+2p)^\sigma + g^{\rho\sigma}(-2k-p)^\mu + g^{\sigma\mu}(k-p)^\rho] [g^{\rho\nu}(k+2p)^\sigma + g^{\nu\sigma}(k-p)^\rho + g^{\sigma\rho}(-2k-p)^\nu] \\ &= 2(2d-3)k^\mu k^\nu + (2d-3)(k^\mu p^\nu + p^\mu k^\nu) + (d-6)p^\mu p^\nu + g^{\mu\nu}[2(k\cdot p) + 2k^2 + 5p^2]\end{aligned}\quad (\text{G.6})$$

The PV reduction applied to the integral yields

$$\int_k \frac{\mathcal{N}^{\mu\nu}}{D_0 D_1} = \frac{[(6d-5)p^2 g^{\mu\nu} - (7d-6)p^\mu p^\nu]}{2(d-1)} B_0(p^2; \bar{0}), \quad (\text{G.7})$$

so that

$$\mathcal{M}_{\text{TI}}^{\mu\nu,ab} = \frac{C_A}{2} \frac{ig_s^2}{(4\pi)^2} \delta^{ab} (4\pi\mu^2)^{2-\frac{d}{2}} \frac{[(6d-5)p^2 g^{\mu\nu} - (7d-6)p^\mu p^\nu]}{2(d-1)} B_0(p^2; \bar{0}), \quad (\text{G.8})$$

which is not transverse.

The ghost contribution is needed to remove the contribution of the unphysical degrees of freedom:

$$\begin{aligned}\mathcal{M}_G^{\mu\nu,ab} &= -\frac{i}{(4\pi)^2} (4\pi\mu^2)^{2-\frac{d}{2}} \int_k (-g_s f^{cae}(k+p)^\mu) \left(\frac{i\delta^{cd}}{(k+p)^2} \right) (-g_s f^{fbd} k^\nu) \left(\frac{i\delta^{ef}}{k^2} \right) \\ &= -\frac{ig_s^2}{(4\pi)^2} f^{ace} f^{bce} (4\pi\mu^2)^{2-\frac{d}{2}} \left[\int_k \frac{k^\mu k^\nu}{k^2(k+p)^2} + p^\mu \int_k \frac{k^\nu}{k^2(k+p)^2} \right] \\ &= \frac{C_A}{2} \frac{ig_s^2}{(4\pi)^2} \delta^{ab} (4\pi\mu^2)^{2-\frac{d}{2}} \left[\frac{p^2 g^{\mu\nu} + (d-2)p^\mu p^\nu}{2(d-1)} \right] B_0(p^2; \bar{0})\end{aligned}\quad (\text{G.9})$$

The sum of the ghost contribution and the non-abelian bubble contribution recovers the transversality of the propagator tensor:

$$\mathcal{M}_{\text{TI}}^{\mu\nu,ab} + \mathcal{M}_G^{\mu\nu,ab} = \frac{ig_s^2}{(4\pi)^2} \delta^{ab} (p^2 g^{\mu\nu} - p^\mu p^\nu) \left(\frac{4\pi\mu^2}{-p^2} \right)^\epsilon \Gamma(1+\epsilon) \frac{5C_A}{3} \frac{1}{\epsilon} + \text{finite}. \quad (\text{G.10})$$

In massless QCD with N_f active flavours, the divergent part is

$$\Pi_0^{\mu\nu} = \frac{g_s^2}{(4\pi)^2} \left(\frac{4\pi\mu^2}{-p^2} \right)^\epsilon \Gamma(1+\epsilon) \left(\frac{5C_A}{3} - \frac{2N_f}{3} \right) \frac{1}{\epsilon} + \text{finite}, \quad (\text{G.11})$$

which is canceled by the following $\overline{\text{MS}}$ counterterm

$$\delta'_3 = \frac{g_s^2}{(4\pi)^2} \left(\frac{4\pi\mu^2}{\mu_R^2} \right)^\epsilon \Gamma(1+\epsilon) \left(\frac{5C_A}{3} - \frac{2N_f}{3} \right) \frac{1}{\epsilon}. \quad (\text{G.12})$$

G.1.2 Top-mass contribution

$$\begin{aligned}\mathcal{M}_{\text{VP}}^{\mu\nu,ab} &= -\frac{i}{(4\pi)^2} (4\pi\mu^2)^{2-\frac{d}{2}} \int_k (-ig_s \gamma^\mu T^a) \frac{i(\not{k} + m_t)}{[k^2 - m_t^2]} \left(-ig_s \gamma^\nu T^b \right) \frac{i(\not{k} + \not{p} + m_t)}{[(k+p)^2 - m_t^2]} \\ &= -\frac{ig_s^2}{(4\pi)^2} \text{Tr}[T^a T^b] (4\pi\mu^2)^{2-\frac{d}{2}} \int_k \frac{\text{Tr}[\gamma^\mu (\not{k} + m_t) \gamma^\nu (\not{k} + \not{p} + m_t)]}{[k^2 - m_t^2][(k+p)^2 - m_t^2]} \\ &= -\frac{ig_s^2}{2(4\pi)^2} \delta^{ab} (4\pi\mu^2)^{2-\frac{d}{2}} \int_k \frac{\mathcal{N}^{\mu\nu}}{D_0 D_1}.\end{aligned}\quad (\text{G.13})$$

Expanding the trace, we obtain

$$\begin{aligned}\mathcal{N}^{\mu\nu} &= \text{Tr}[\gamma^\mu \not{k} \gamma^\nu (\not{k} + \not{p})] + m_t^2 \text{Tr}[\gamma^\mu \gamma^\nu] \\ &= 4[2k^\mu k^\nu + k^\mu p^\nu + p^\mu k^\nu - g^{\mu\nu} k \cdot (k + p) + m_t^2 g^{\mu\nu}],\end{aligned}\quad (\text{G.14})$$

and the PV reduction of this amplitude (see Appendix D) yields

$$\begin{aligned}\mathcal{M}_{\text{VP}}^{\mu\nu,ab} &= -\frac{2ig_s^2}{(4\pi)^2} \delta^{ab} (4\pi\mu^2)^{2-\frac{d}{2}} \left[2 \int_k \frac{k^\mu k^\nu}{D_0 D_1} + \int_k \frac{k^\mu p^\nu + p^\mu k^\nu}{D_0 D_1} + g^{\mu\nu} \int_k \frac{m_t^2 - k \cdot (k + p)}{D_0 D_1} \right] \\ &= -\frac{ig_s^2}{(4\pi)^2} \delta^{ab} (4\pi\mu^2)^{2-\frac{d}{2}} \frac{[(d-2)p^2 + 4m_t^2] B_0(p^2; \bar{m}_t^2) - 2(d-2) A_0(m_t^2)}{(d-1)} \left(g^{\mu\nu} - \frac{p^\mu p^\nu}{p^2} \right) \\ &= -\frac{ig_s^2}{(4\pi)^2} \delta^{ab} (4\pi\mu^2)^\epsilon \left\{ \frac{[2(1-\epsilon)p^2 + 4m_t^2]}{(3-2\epsilon)} B_0(p^2; \bar{m}_t^2) - \frac{4(1-\epsilon)}{(3-2\epsilon)} A_0(m_t^2) \right\} \left(g^{\mu\nu} - \frac{p^\mu p^\nu}{p^2} \right) \\ &= -\frac{ig_s^2}{(4\pi)^2} \delta^{ab} [p^2 g^{\mu\nu} - p^\mu p^\nu] (4\pi\mu^2)^\epsilon \left(\frac{1}{3-2\epsilon} \right) \left\{ \left[2(1-\epsilon) + \frac{4m_t^2}{p^2} \right] B_0(p^2; \bar{m}_t^2) - \frac{4(1-\epsilon)}{p^2} A_0(m_t^2) \right\}\end{aligned}\quad (\text{G.15})$$

Therefore, the form factor $\Pi_t(p^2)$ of $\mathcal{M}_{\text{VP}}^{\mu\nu,ab}$ with the top quark in the loop reads

$$\Pi_t(p^2) = -\frac{g_s^2}{(4\pi)^2} (4\pi\mu^2)^\epsilon \left(\frac{1}{3-2\epsilon} \right) \left\{ \left[2(1-\epsilon) + \frac{4m_t^2}{p^2} \right] B_0(p^2; \bar{m}_t^2) - \frac{4(1-\epsilon)}{p^2} A_0(m_t^2) \right\}. \quad (\text{G.16})$$

The on-shell limit of this form factor is useful to check the proper cancellation of the wave function corrections due to the top-quark contributions. Expanding Eq. (G.16) around $p^2 = 0$:

$$\begin{aligned}\Pi_t(p^2) &= -\frac{g_s^2}{(4\pi)^2} (4\pi\mu^2)^\epsilon \left(\frac{1}{3-2\epsilon} \right) \left\{ \frac{1}{p^2} [4m_t^2 B_0(0; \bar{m}_t^2) - 4(1-\epsilon) A_0(m_t^2)] \right. \\ &\quad \left. + \left[2(1-\epsilon) B_0(0; \bar{m}_t^2) + 4m_t^2 \frac{d}{dp^2} B_0(0; \bar{m}_t^2) \right] + O(p^2) \right\} \\ &= -\frac{g_s^2}{(4\pi)^2} \left(\frac{4\pi\mu^2}{m_t^2} \right)^\epsilon \frac{\Gamma(1+\epsilon)}{3-2\epsilon} \left\{ \left[\frac{2}{\epsilon} - \frac{4}{3} \right] + O(p^2) \right\},\end{aligned}\quad (\text{G.17})$$

and around $\epsilon = 0$:

$$\Pi_t(p^2) = -\frac{g_s^2}{(4\pi)^2} \left(\frac{4\pi\mu^2}{m_t^2} \right)^\epsilon \Gamma(1+\epsilon) \frac{2}{3} \frac{1}{\epsilon} + O(p^2, \epsilon) \quad (\text{G.18})$$

Here, the derivative of the bubble integral presented in Appendix E has been used. Therefore, the form factor for an on-shell gluon is

$$\Pi_t(0) = -\frac{g_s^2}{(4\pi)^2} \left(\frac{4\pi\mu^2}{m_t^2} \right)^\epsilon \Gamma(1+\epsilon) \frac{2}{3} \frac{1}{\epsilon}. \quad (\text{G.19})$$

The on-shell limit presented in Eq. (G.19) takes part in the wave function correction of the NLO: their contribution, shown in Figure G.2, is the product of two form factors:

$$\Pi_t(0) F_j^{(0)} = -\frac{g_s^2}{(4\pi)^2} \left(\frac{4\pi\mu^2}{m_t^2} \right)^\epsilon \Gamma(1+\epsilon) \frac{2}{3} \frac{1}{\epsilon} F_j^{(0)}. \quad (\text{G.20})$$

The vacuum polarization diagrams are the only ones that receive contributions that depend on the top mass: this fact can be exploited to build a counterterm that makes the top quark decouple from the running of α_s . The decoupling can be enforced by the condition

$$\delta_3 - \delta'_3 - \Pi_t(0) = \text{finite} \quad (\text{G.21})$$

where δ_3 is the total vacuum polarization counterterm and δ'_3 is the massless vacuum polarization counterterm. The explicit expression of δ_3 in the $\overline{\text{MS}}$ scheme is

$$\delta_3 = \frac{g_s^2}{(4\pi)^2} \left(\frac{4\pi\mu^2}{\mu_R^2} \right)^\epsilon \Gamma(1+\epsilon) \left[\left(\frac{5C_A - 2(N_f + 1)}{3} \right) \frac{1}{\epsilon} - \frac{2}{3} \log \left(\frac{\mu_R^2}{m_t^2} \right) \right]. \quad (\text{G.22})$$

Later on, the decoupling of the top mass from the running of α_s will be shown explicitly.

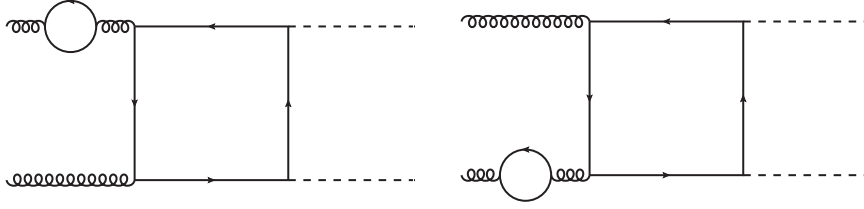


Figure G.2: Wave-function corrections due to top-quark loops.

G.2 Quark Self-energy

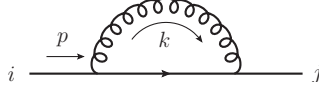


Figure G.3: Diagram contributing to the massless quark self-energy.

The self-energy diagram and its counterterm can be expressed as

$$\begin{aligned} -i\not{p}\delta^{ij}\Sigma(p^2) &= \mathcal{M}_0^{(f)}, \\ \Sigma(p^2) - \delta_2 &= \text{finite}. \end{aligned} \quad (\text{G.23})$$

and the amplitude can be written as:

$$\begin{aligned} \mathcal{M}_0^{(f)} &= \frac{i}{(4\pi)^2} (4\pi\mu^2)^{2-\frac{d}{2}} \int_k (-ig_s\gamma^\mu T^a) \frac{i\not{k}}{k^2} (-ig_s\gamma^\nu T^b) \frac{-ig^{\mu\nu}\delta^{ab}}{(k-p)^2} \\ &= -\frac{ig_s^2}{(4\pi)^2} T^a T^a (4\pi\mu^2)^{2-\frac{d}{2}} \int_k \frac{\gamma^\mu \not{k} \gamma_\mu}{k^2 (k-p)^2} \\ &= \frac{ig_s^2}{(4\pi)^2} C_F \delta^{ij} (4\pi\mu^2)^{2-\frac{d}{2}} \int_k \frac{(d-2)\not{k}}{k^2 (k-p)^2} \\ &= \frac{ig_s^2}{(4\pi)^2} C_F \delta^{ij} (4\pi\mu^2)^{2-\frac{d}{2}} \frac{(d-2)}{2} \not{p} B_0(p^2, \bar{0}), \end{aligned} \quad (\text{G.24})$$

where p^2 is the off-shellness of the quark propagator. The pole structure is:

$$\begin{aligned} \mathcal{M}_0^{(f)} &= \frac{ig_s^2}{(4\pi)^2} C_F \delta^{ij} \left(\frac{4\pi\mu^2}{-p^2} \right)^\epsilon \Gamma(1+\epsilon) \not{p} \frac{1}{\epsilon} + \text{finite} \\ \Sigma_0(p^2) &= -\frac{g_s^2}{(4\pi)^2} C_F \left(\frac{4\pi\mu^2}{-p^2} \right)^\epsilon \Gamma(1+\epsilon) \frac{1}{\epsilon} + \text{finite} \end{aligned} \quad (\text{G.25})$$

and its $\overline{\text{MS}}$ counterterm is

$$\delta_2 = -\frac{g_s^2}{(4\pi)^2} C_F \left(\frac{4\pi\mu^2}{\mu_R^2} \right)^\epsilon \Gamma(1+\epsilon) \frac{1}{\epsilon} \quad (\text{G.26})$$

G.3 Vertices

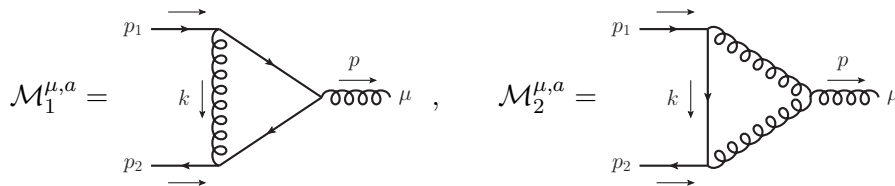


Figure G.4: Diagrams contributing to the vertex corrections

Lastly, we need the vertex diagrams. This contribution has the following structure:

$$\begin{aligned} -ig_s T^a \gamma^\mu \Gamma_{\text{vert}}(p_1, p_2) &= \mathcal{M}_1^{\mu,a} + \mathcal{M}_2^{\mu,a} \\ \Gamma_{\text{vert}}(p_1, p_2) + \delta_1 &= \text{finite} \end{aligned} \quad (\text{G.27})$$

The amplitude for $\mathcal{M}_1^{\mu,a}$ is

$$\begin{aligned} \mathcal{M}_1^{\mu,a} &= \frac{i}{(4\pi)^2} (4\pi\mu^2)^{2-\frac{d}{2}} \int_k (-ig_s \gamma^\sigma T^c) \frac{i(-\not{k} - \not{p}_2)}{(k+p_2)^2} (-ig_s \gamma^\mu T^a) \frac{i(-\not{k} + \not{p}_1)}{(k-p_1)^2} (-ig_s \gamma^\rho T^b) \frac{-ig^{\sigma\rho} \delta^{bc}}{k^2} \\ &= -\frac{ig_s^3}{(4\pi)^2} T^b T^a T^b (4\pi\mu^2)^{2-\frac{d}{2}} \int_k \frac{\gamma^\sigma (\not{k} + \not{p}_2) \gamma^\mu (\not{k} - \not{p}_1) \gamma_\sigma}{k^2 (k-p_1)^2 (k+p_2)^2} \end{aligned} \quad (\text{G.28})$$

Since the scalar triangle C_0 is finite, we can already drop the terms that generates such integrals.

$$\mathcal{M}_1^{\mu,a} = -\frac{ig_s^3}{(4\pi)^2} T^b T^a T^b (4\pi\mu^2)^{2-\frac{d}{2}} \int_k \frac{\gamma^\sigma \not{k} \gamma^\mu \not{k} \gamma_\sigma - \gamma^\sigma \not{k} \gamma^\mu \not{p}_1 \gamma_\sigma + \gamma^\sigma \not{p}_2 \gamma^\mu \not{k} \gamma_\sigma}{k^2 (k-p_1)^2 (k+p_2)^2} + \text{finite} \quad (\text{G.29})$$

Using the PV reduction, it is possible to show that the terms proportional to \not{k} do not develop any pole. It relies on the pole structure of B_0 , which is independent on the kinematics. Therefore, the rank-1 tensor integrals produce finite terms.

Neglecting rank-1 terms, the amplitude reads:

$$\begin{aligned} \mathcal{M}_1^{\mu,a} &= -\frac{ig_s^3}{(4\pi)^2} T^b T^a T^b (4\pi\mu^2)^{2-\frac{d}{2}} \int_k \frac{\gamma^\sigma \not{k} \gamma^\mu \not{k} \gamma_\sigma}{k^2 (k-p_1)^2 (k+p_2)^2} + \text{finite} \\ &= \frac{ig_s^3}{(4\pi)^2} T^b T^a T^b (4\pi\mu^2)^{2-\frac{d}{2}} \int_k \frac{(d-2)(2k^\mu \not{k} - k^2 \gamma^\mu)}{k^2 (k-p_1)^2 (k+p_2)^2} + \text{finite} \end{aligned} \quad (\text{G.30})$$

Applying the PV reduction on this last term, we obtain the following pole term:

$$\begin{aligned} \mathcal{M}_1^{\mu,a} &= -\frac{ig_s^3}{(4\pi)^2} T^b T^a T^b \left(\frac{4\pi\mu^2}{-p^2} \right)^\epsilon \Gamma(1+\epsilon) \frac{\gamma^\mu}{\epsilon} + \text{finite} \\ &= -\frac{ig_s^3}{(4\pi)^2} (C_F - \frac{1}{2} C_A) T^a \left(\frac{4\pi\mu^2}{-p^2} \right)^\epsilon \Gamma(1+\epsilon) \frac{\gamma^\mu}{\epsilon} + \text{finite} \end{aligned} \quad (\text{G.31})$$

The second diagram can be written as

$$\begin{aligned} \mathcal{M}_2^{\mu,a} &= \frac{i}{(4\pi)^2} (4\pi\mu^2)^{2-\frac{d}{2}} \int_k (-ig_s \gamma^\beta T^c) \frac{i\not{k}}{k^2} (-ig_s \gamma^\alpha T^b) \frac{-ig^{\alpha\sigma}}{(k-p_1)^2} \frac{-ig^{\beta\rho}}{(k+p_2)^2} \times \\ &\quad (-g_s f^{bac}) [g^{\sigma\mu} (-k+2p_1+p_2)^\rho + g^{\mu\rho} (-k-p_1-2p_2)^\sigma + g^{\rho\sigma} (2k-p_1+p_2)^\mu] \\ &= \frac{g_s^3}{(4\pi)^2} f^{bac} T^c T^b (4\pi\mu^2)^\epsilon \int_k \frac{\gamma^\rho \not{k} \gamma^\sigma}{k^2 (k-p_1)^2 (k+p_2)^2} \times \\ &\quad [g^{\sigma\mu} (-k+2p_1+p_2)^\rho + g^{\mu\rho} (-k-p_1-2p_2)^\sigma + g^{\rho\sigma} (2k-p_1+p_2)^\mu]. \end{aligned} \quad (\text{G.32})$$

For reasons which are completely analogous to the previous diagram, terms which are proportional to rank-0 and rank-1 integrals will generate finite terms. Therefore:

$$\begin{aligned} \mathcal{M}_2^{\mu,a} &= \frac{g_s^3}{(4\pi)^2} f^{bac} T^c T^b (4\pi\mu^2)^\epsilon \int_k \frac{\gamma^\rho \not{k} \gamma^\sigma [2g^{\rho\sigma} k^\mu - g^{\sigma\mu} k^\rho - g^{\mu\rho} k^\sigma]}{k^2 (k-p_1)^2 (k+p_2)^2} + \text{finite} \\ &= \frac{g_s^3}{(4\pi)^2} f^{bac} T^c T^b (4\pi\mu^2)^\epsilon \int_k \frac{[2\gamma^\sigma \not{k} \gamma_\sigma k^\mu - \gamma^\mu \not{k} \not{k} - \not{k} \not{k} \gamma^\mu]}{k^2 (k-p_1)^2 (k+p_2)^2} + \text{finite} \\ &= \frac{g_s^3}{(4\pi)^2} f^{abc} T^c T^b (4\pi\mu^2)^\epsilon \int_k \frac{[(d-2)\not{k} k^\mu + k^2 \gamma^\mu]}{k^2 (k-p_1)^2 (k+p_2)^2} + \text{finite}, \end{aligned} \quad (\text{G.33})$$

and lastly, the PV reduction yields:

$$\mathcal{M}_2^{\mu,a} = -\frac{ig_s^3}{(4\pi)^2} \frac{3}{2} C_A T^a \left(\frac{4\pi\mu^2}{-p^2} \right)^\epsilon \Gamma(1+\epsilon) \frac{\gamma^\mu}{\epsilon} + \text{finite}, \quad (\text{G.34})$$

which leads to the following total contribution:

$$\Gamma_{\text{vert}}(p_1, p_2) = \frac{g_s^2}{(4\pi)^2} (C_F + C_A) \left(\frac{4\pi\mu^2}{-p^2} \right)^\epsilon \Gamma(1+\epsilon) \frac{1}{\epsilon} + \text{finite}, \quad (\text{G.35})$$

and to the following $\overline{\text{MS}}$ counterterm

$$\delta_1 = -\frac{g_s^2}{(4\pi)^2} (C_F + C_A) \left(\frac{4\pi\mu^2}{\mu_R^2} \right)^\epsilon \Gamma(1 + \epsilon) \frac{1}{\epsilon}. \quad (\text{G.36})$$

G.4 $\overline{\text{MS}}$ scheme for α_s with $N_f = 5$ massless flavours with the top quark decoupled

From the fermion field and mass renormalization of the QCD Lagrangian it is possible to access the renormalization of the strong coupling constant:

$$\alpha_{s,0} = \frac{Z_1^2}{Z_2^2 Z_3} \alpha_s. \quad (\text{G.37})$$

Expanding the latter with respect to the number of loops, the bare coupling in terms of the renormalized one reads

$$\begin{aligned} \alpha_{s,0} &= \alpha_s (1 + 2\delta_1 - 2\delta_2 - \delta_3) + O(\delta_i^2) \\ &= \alpha_s + \delta\alpha_s + O(\alpha_s^2). \end{aligned} \quad (\text{G.38})$$

Therefore, the one-loop counterterm for the strong coupling reads:

$$\frac{\delta\alpha_s}{\alpha_s} = 2\delta_1 - 2\delta_2 - \delta_3 \quad (\text{G.39})$$

which gives the following explicit form:

$$\frac{\delta\alpha_s}{\alpha_s} = \frac{\alpha_s}{(4\pi)} \left(\frac{4\pi\mu^2}{\mu_R^2} \right)^\epsilon \Gamma(1 + \epsilon) \left[-\frac{33 - 2(N_f + 1)}{3\epsilon} + \frac{2}{3} \log \left(\frac{\mu_R^2}{m_t^2} \right) \right]. \quad (\text{G.40})$$

It is possible to see explicitly the decoupling of the top mass from the running of α_s from the definition of the β -function [179–182]. Differentiating the Eq. (G.38) with respect to the renormalization scale μ_R^2 :

$$\mu_R^2 \frac{d\alpha_{s,0}}{d\mu_R^2} = 0 = \mu_R^2 \frac{d\alpha_s}{d\mu_R^2} + \mu_R^2 \frac{d\delta\alpha_s}{d\mu_R^2} + O(\alpha_s^2) \quad (\text{G.41})$$

since the bare coupling is independent on the renormalization scale. The first term of the r.h.s. of Eq. (G.41) is the definition of the one-loop beta function; the second term is its analytical expression, which gives:

$$\beta = \mu_R^2 \frac{d\alpha_s}{d\mu_R^2}, \quad \beta = \frac{\alpha_s}{(4\pi)} \left(\frac{4\pi\mu^2}{\mu_R^2} \right)^\epsilon \Gamma(1 + \epsilon) \left(11 - \frac{2}{3}N_f \right). \quad (\text{G.42})$$

This beta function is manifestly independent of the top quark contribution, and it gets contributions only from the massless flavours.

Appendix H

Feynman Diagrams for $gg \rightarrow H_1 H_2$

In this Appendix, the complete set of Feynman diagrams involved in the $gg \rightarrow H_1 H_2$ NLO cross section is presented.

H.1 Real corrections

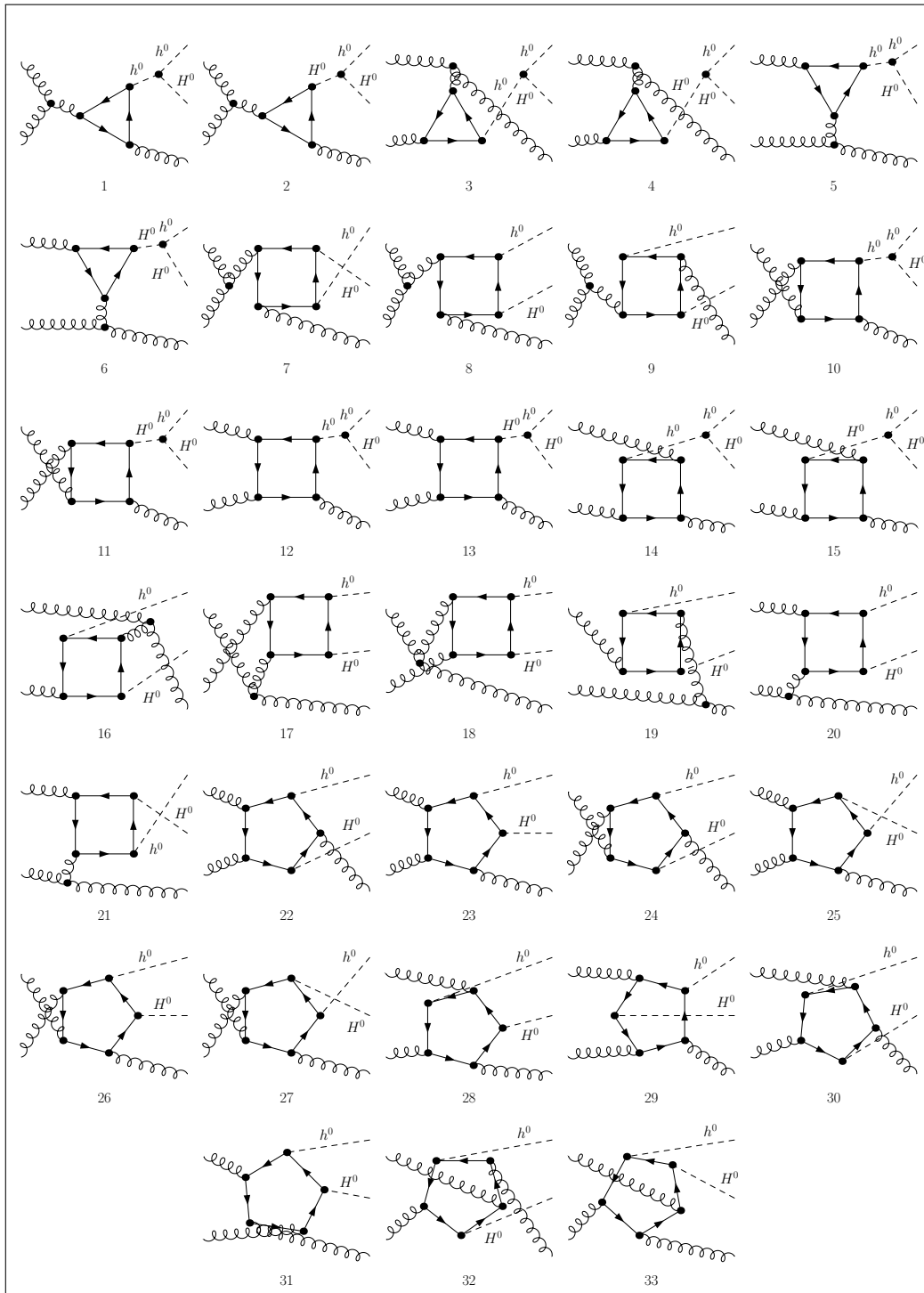


Figure H.1: Diagrams contributing to $\hat{\sigma}_{gg}$.

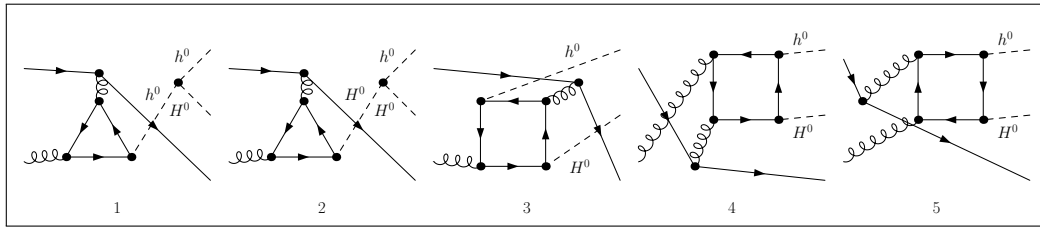


Figure H.2: Diagrams contributing to $\hat{\sigma}_{qq}$.

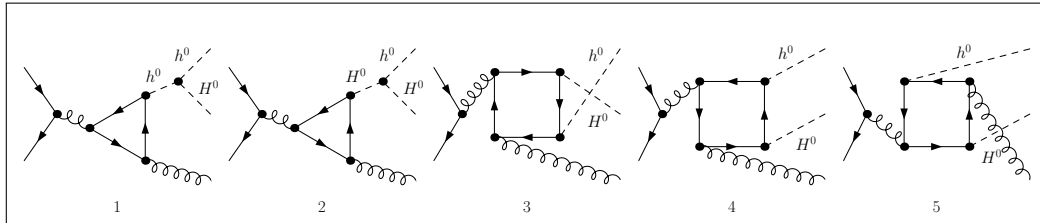


Figure H.3: Diagrams contributing to $\hat{\sigma}_{q\bar{q}}$.

H.2 Virtual contributions

H.2.1 Vertex contributions

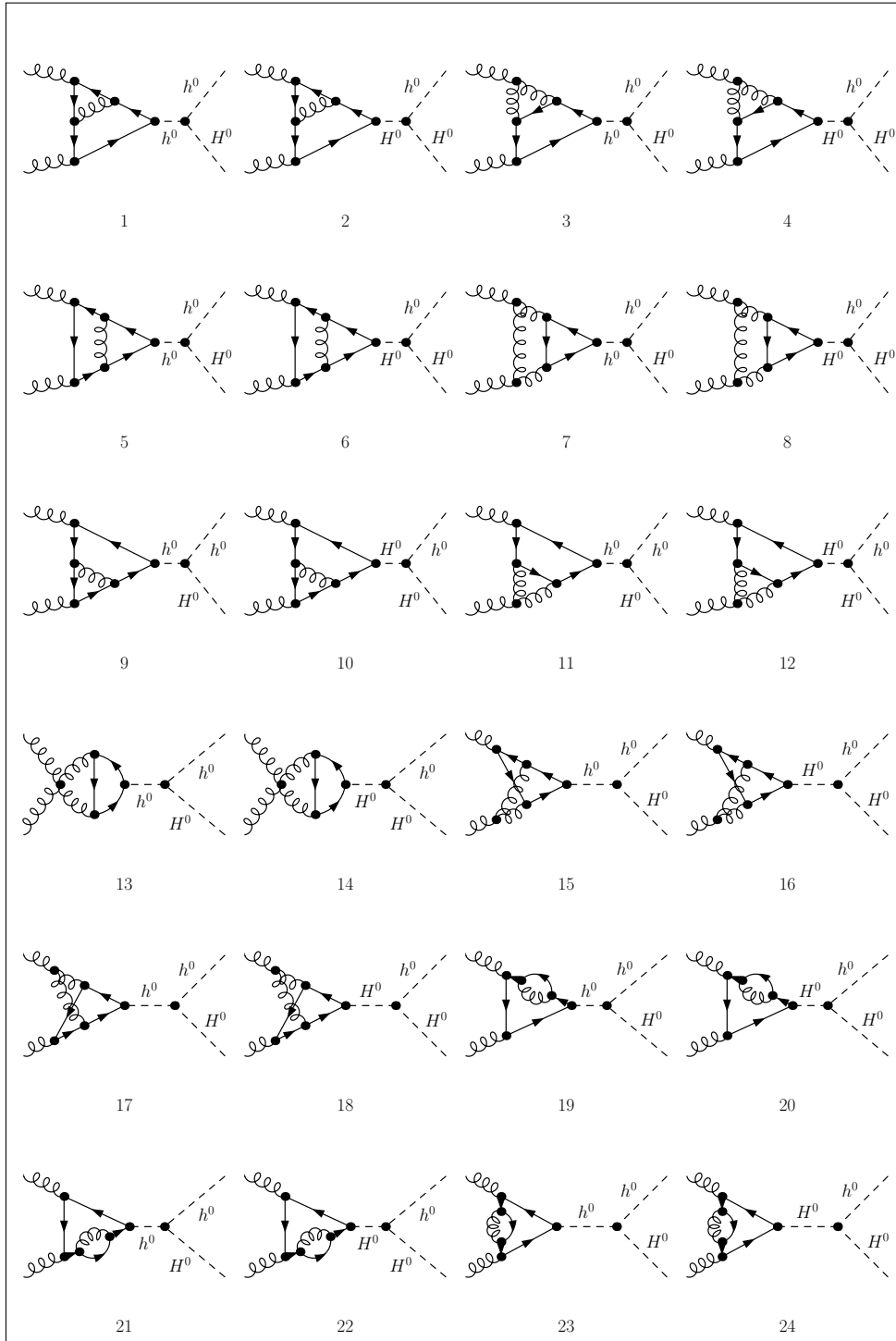


Figure H.4: Triangle contributions.

H.2.2 Box contributions

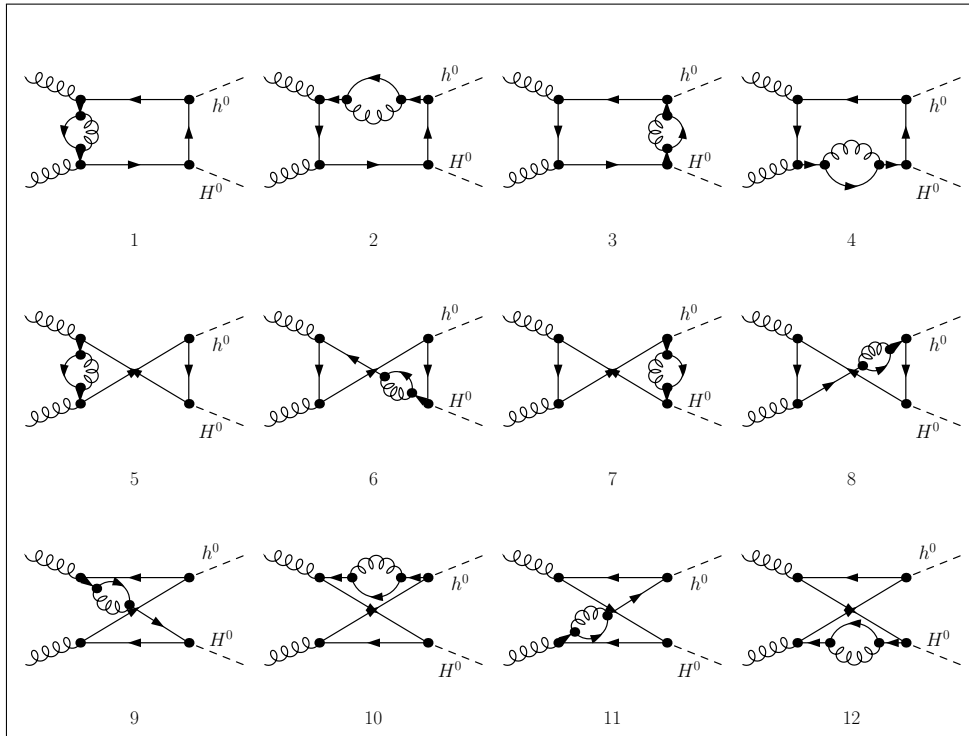


Figure H.5: Topology 1.

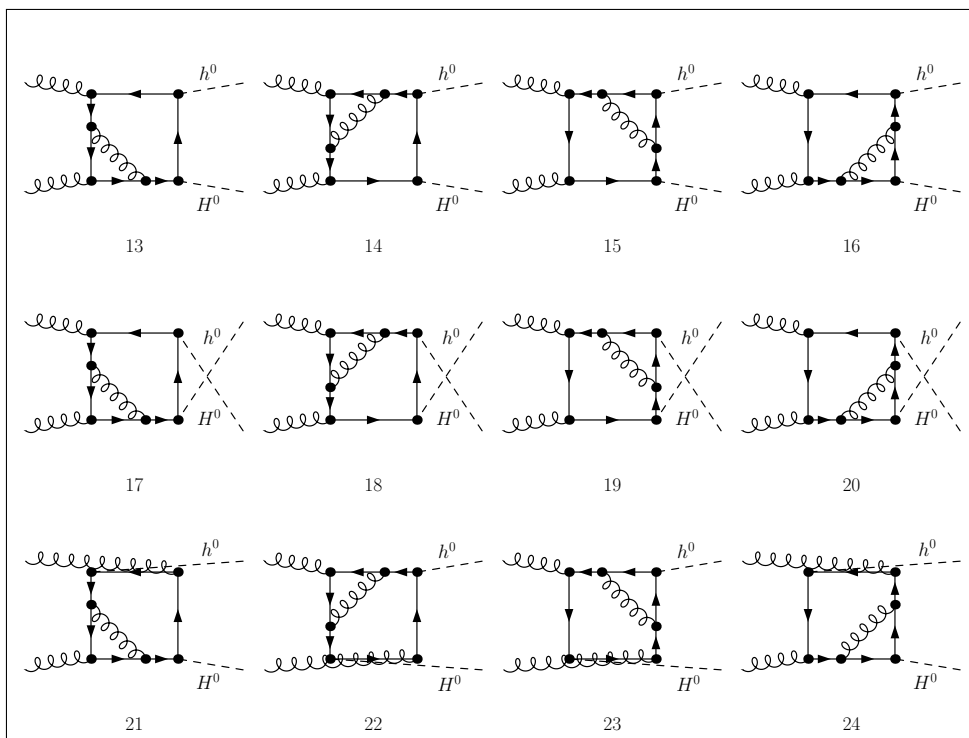


Figure H.6: Topology 2.

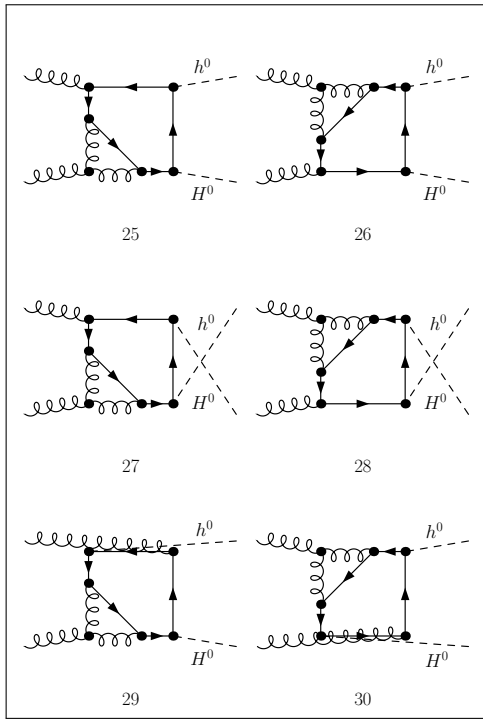


Figure H.7: Topology 3.

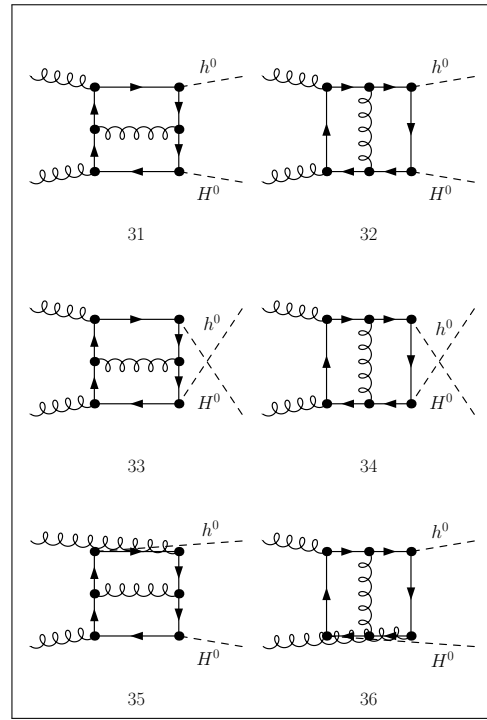


Figure H.8: Topology 4.

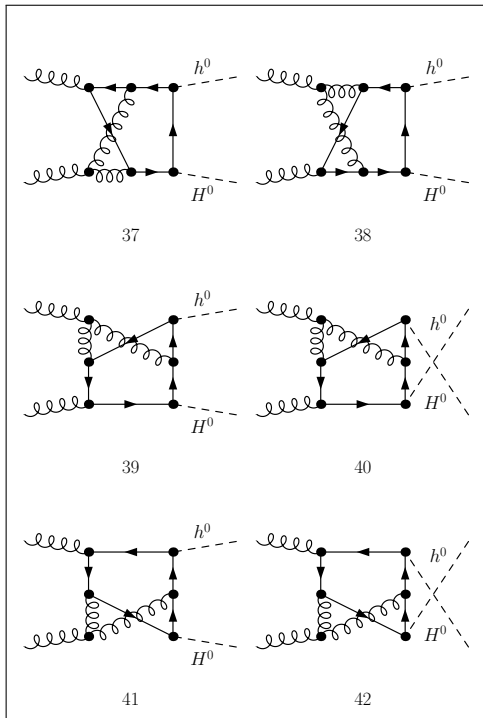


Figure H.9: Topology 5.

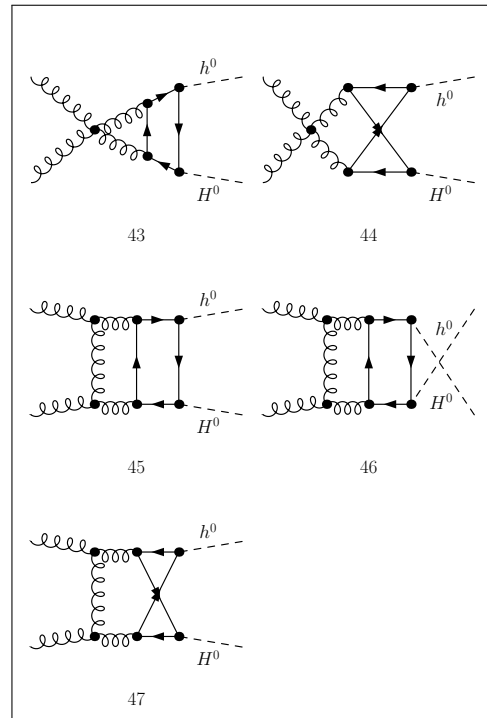


Figure H.10: Topology 6.

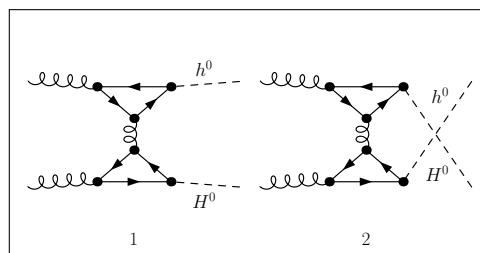


Figure H.11: One-particle reducible diagrams.

Appendix I

Feynman Rules

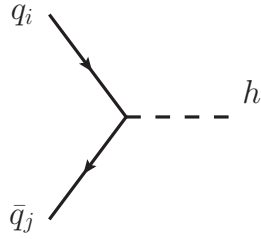
In this Appendix, the Feynman rules coming from the 2HDM and the QCD, relevant for this thesis, are depicted.

I.1 2HDM scalar propagators and Yukawa couplings

Scalar propagators

$$-\text{---}^h\text{---} = \frac{i}{q^2 - m_h^2}, \quad h \in \{H_1, H_2, A, H^+, H^-\},$$

Yukawa couplings



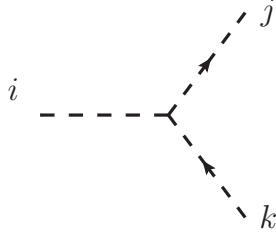
$$h \in \{H_1, H_2, A, H^+, H^-\}$$

$$\begin{aligned} \bar{q}_i q_j H_1 &= -i \frac{m_q}{v} \delta_{ij} Y_1, \\ \bar{q}_i q_j H_2 &= -i \frac{m_q}{v} \delta_{ij} Y_2, \\ \bar{q}_i q_j A &= -\frac{m_q}{v} \gamma^5 \delta_{ij} Y_A, \\ \bar{u}_i d_j H^+ &= -\frac{i}{v} V_{ij} Y_+^{ij}, \\ \bar{d}_i u_j H^- &= -\frac{i}{v} V_{ij}^* Y_-^{ij} \end{aligned}$$

		type I	type II	type X	type Y
Y_1	up quarks	$\frac{\cos \alpha}{\sin \beta}$	$\frac{\cos \alpha}{\sin \beta}$	$\frac{\cos \alpha}{\sin \beta}$	$\frac{\cos \alpha}{\sin \beta}$
	down quarks	$\frac{\cos \alpha}{\sin \beta}$	$-\frac{\sin \alpha}{\cos \beta}$	$\frac{\cos \alpha}{\sin \beta}$	$-\frac{\sin \alpha}{\cos \beta}$
Y_2	up quarks	$\frac{\sin \alpha}{\sin \beta}$	$\frac{\sin \alpha}{\sin \beta}$	$\frac{\sin \alpha}{\sin \beta}$	$\frac{\sin \alpha}{\sin \beta}$
	down quarks	$\frac{\sin \alpha}{\sin \beta}$	$\frac{\cos \alpha}{\cos \beta}$	$\frac{\sin \alpha}{\sin \beta}$	$\frac{\cos \alpha}{\cos \beta}$
Y_A	up quarks	$\cot \beta$	$\cot \beta$	$\cot \beta$	$\cot \beta$
	down quarks	$-\cot \beta$	$\tan \beta$	$-\cot \beta$	$\tan \beta$

type I, type X		type II, type Y	
Y_+^{ij}	$\sqrt{2} [m_{d_j} \cot \beta P_R - m_{u_i} \cot \beta P_L]$	$-\sqrt{2} [m_{d_j} \tan \beta P_R + m_{u_i} P_L \cot \beta]$	
Y_-^{ij}	$\sqrt{2} [m_{d_i} \cot \beta P_L - m_{u_j} \cot \beta P_R]$	$-\sqrt{2} [m_{d_i} \tan \beta P_L + m_{u_j} \cot \beta P_R]$	

I.2 2HDM trilinear Higgs couplings



$$\lambda_{ijk} = -i3 \frac{c_{ijk}}{v}$$

$$i, j, k \in \{H_1, H_2, A, H^+, H^-\}$$

$$c_{111} = \frac{m_{H_1}^2 [2 \cos(\alpha + \beta) + \sin 2\alpha \sin(\beta - \alpha)] - \lambda_5 v^2 \cos(\alpha + \beta) \cos^2(\beta - \alpha)}{\sin 2\beta},$$

$$c_{112} = \frac{\cos(\beta - \alpha) [2 \sin 2\alpha (2m_{H_1}^2 + m_{H_2}^2) - \lambda_5 v^2 (3 \sin 2\alpha - \sin 2\beta)]}{6 \sin 2\beta},$$

$$c_{122} = -\frac{\sin(\beta - \alpha) [2 \sin 2\alpha (m_{H_1}^2 + 2m_{H_2}^2) - \lambda_5 v^2 (3 \sin 2\alpha + \sin 2\beta)]}{6 \sin 2\beta},$$

$$c_{222} = -\frac{m_{H_2}^2 [\cos(\beta - \alpha) \sin(2\alpha) - 2 \sin(\alpha + \beta)] + \lambda_5 v^2 \sin(\alpha + \beta) \sin^2(\beta - \alpha)}{\sin 2\beta},$$

$$c_{1AA} = \sin(\beta - \alpha) (2m_A^2 - m_{H_1}^2) + \frac{\cos(\alpha + \beta) (2m_{H_1}^2 - \lambda_5 v^2)}{3 \sin 2\beta},$$

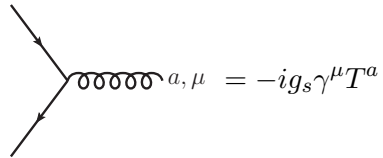
$$c_{2AA} = \cos(\beta - \alpha) (2m_A^2 - m_{H_2}^2) + \frac{\sin(\alpha + \beta) (2m_{H_2}^2 - \lambda_5 v^2)}{3 \sin 2\beta},$$

$$c_{1+-} = \sin(\beta - \alpha) (2m_+^2 - m_{H_1}^2) + \frac{\cos(\alpha + \beta) (2m_{H_1}^2 - \lambda_5 v^2)}{3 \sin 2\beta},$$

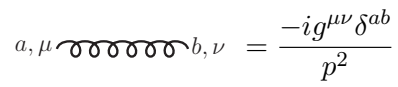
$$c_{2+-} = \cos(\beta - \alpha) (2m_+^2 - m_{H_2}^2) + \frac{\sin(\alpha + \beta) (2m_{H_2}^2 - \lambda_5 v^2)}{3 \sin 2\beta}.$$

I.3 SM QCD Feynman rules

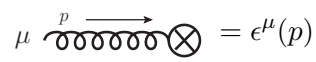
$$\frac{p \longrightarrow}{q} = \frac{i(\not{p} + m_q)}{p^2 - m_q^2}$$



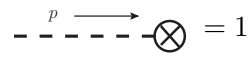
$$a, \mu = -ig_s \gamma^\mu T^a$$



$$a, \mu \quad b, \nu = \frac{-ig^{\mu\nu} \delta^{ab}}{p^2}$$



$$\mu \quad p = \epsilon^\mu(p)$$



$$p = 1$$

Bibliography

- [1] Peter W. Higgs. Broken Symmetries and the Masses of Gauge Bosons. *Phys. Rev. Lett.*, 13:508–509, 1964.
- [2] F. Englert and R. Brout. Broken Symmetry and the Mass of Gauge Vector Mesons. *Phys. Rev. Lett.*, 13:321–323, 1964.
- [3] Peter W. Higgs. Spontaneous Symmetry Breakdown without Massless Bosons. *Phys. Rev.*, 145:1156–1163, 1966.
- [4] G.S. Guralnik, C.R. Hagen, and T.W.B. Kibble. Global Conservation Laws and Massless Particles. *Phys. Rev. Lett.*, 13:585–587, 1964.
- [5] G. Aad, T. Abajyan, B. Abbott, J. Abdallah, S. Abdel Khalek, A.A. Abdelalim, O. Abdinov, R. Aben, B. Abi, M. Abolins, and et al. Observation of a new particle in the search for the standard model higgs boson with the atlas detector at the lhc. *Physics Letters B*, 716(1):129, Sep 2012.
- [6] S. Chatrchyan, V. Khachatryan, A.M. Sirunyan, A. Tumasyan, W. Adam, E. Aguilo, T. Bergauer, M. Dragicevic, J. Er, C. Fabjan, and et al. Observation of a new boson at a mass of 125 gev with the cms experiment at the lhc. *Physics Letters B*, 716(1):3061, Sep 2012.
- [7] S. Chatrchyan, V. Khachatryan, A. M. Sirunyan, A. Tumasyan, W. Adam, E. Aguilo, T. Bergauer, M. Dragicevic, J. Er, C. Fabjan, and et al. Study of the mass and spin-parity of the higgs boson candidate via its decays to z boson pairs. *Physical Review Letters*, 110(8), Feb 2013.
- [8] G. Aad, T. Abajyan, B. Abbott, J. Abdallah, S. Abdel Khalek, O. Abdinov, R. Aben, B. Abi, M. Abolins, O.S. AbouZeid, and et al. Evidence for the spin-0 nature of the higgs boson using atlas data. *Physics Letters B*, 726(1-3):120144, Oct 2013.
- [9] John F. Gunion, Howard E. Haber, Gordon L. Kane, and Sally Dawson. *The Higgs Hunter’s Guide*, volume 80. 2000.
- [10] G.C. Branco, P.M. Ferreira, L. Lavoura, M.N. Rebelo, Marc Sher, and Joao P. Silva. Theory and phenomenology of two-Higgs-doublet models. *Phys. Rept.*, 516:1–102, 2012.
- [11] Sally Dawson, Christoph Englert, and Tilman Plehn. Higgs Physics: It ain’t over till it’s over. *Phys. Rept.*, 816:1–85, 2019.
- [12] A. Djouadi, W. Kilian, M. Mühlleitner, and P.M. Zerwas. Testing higgs self-couplings at e^+e^- linear colliders. *The European Physical Journal C*, 10(1):2743, Aug 1999.
- [13] G. Cynolter, E. Lendvai, and G. Pocsik. Resonance production of three neutral supersymmetric Higgs bosons at LHC. *Acta Phys. Polon. B*, 31:1749–1757, 2000.
- [14] Milada Margarete Mühlleitner. *Higgs particles in the standard model and supersymmetric theories*. PhD thesis, Hamburg U., 2000.

- [15] E. Accomando et al. Physics at the CLIC multi-TeV linear collider. In *11th International Conference on Hadron Spectroscopy*, CERN Yellow Reports: Monographs, 6 2004.
- [16] Tilman Plehn and Michael Rauch. Quartic higgs coupling at hadron colliders. *Physical Review D*, 72(5), Sep 2005.
- [17] U. Baur, T. Plehn, and David L. Rainwater. Determining the Higgs Boson Selfcoupling at Hadron Colliders. *Phys. Rev. D*, 67:033003, 2003.
- [18] Ulrich Baur, Tilman Plehn, and David L. Rainwater. Measuring the Higgs Boson Self Coupling at the LHC and Finite Top Mass Matrix Elements. *Phys. Rev. Lett.*, 89:151801, 2002.
- [19] U. Baur, T. Plehn, and D. Rainwater. Examining the higgs boson potential at lepton and hadron colliders: A comparative analysis. *Physical Review D*, 68(3), Aug 2003.
- [20] U. Baur, T. Plehn, and David L. Rainwater. Probing the Higgs selfcoupling at hadron colliders using rare decays. *Phys. Rev. D*, 69:053004, 2004.
- [21] Matthew J. Dolan, Christoph Englert, and Michael Spannowsky. Higgs self-coupling measurements at the LHC. *JHEP*, 10:112, 2012.
- [22] Vernon Barger, Lisa L. Everett, C.B. Jackson, and Gabe Shaughnessy. Higgs-Pair Production and Measurement of the Triscalar Coupling at LHC(8,14). *Phys. Lett. B*, 728:433–436, 2014.
- [23] J. Baglio, A. Djouadi, R. Grber, M.M. Mühlleitner, J. Quevillon, and M. Spira. The measurement of the higgs self-coupling at the lhc: theoretical status. *Journal of High Energy Physics*, 2013(4), Apr 2013.
- [24] F. Maltoni, E. Vryonidou, and M. Zaro. Top-quark mass effects in double and triple Higgs production in gluon-gluon fusion at NLO. *JHEP*, 11:079, 2014.
- [25] Chih-Ting Lu, Jung Chang, Kingman Cheung, and Jae Sik Lee. An exploratory study of Higgs-boson pair production. *JHEP*, 08:133, 2015.
- [26] Prospects for HH measurements at the HL-LHC. 12 2018.
- [27] Philipp Roloff, Ulrike Schnoor, Rosa Simoniello, and Boruo Xu. Double Higgs boson production and Higgs self-coupling extraction at CLIC. 1 2019.
- [28] Eleonora Rossi. Measurement of Higgs-boson self-coupling with single-Higgs and double-Higgs production channels. 10 2020.
- [29] Biagio Di Micco, Maxime Gouzevitch, Javier Mazzitelli, and Caterina Vernieri. Higgs boson potential at colliders: status and perspectives. *Reviews in Physics*, page 100045, Aug 2020.
- [30] D. de Florian et al. Handbook of LHC Higgs Cross Sections: 4. Deciphering the Nature of the Higgs Sector. 2/2017, 10 2016.
- [31] Vernon Barger, Lisa L. Everett, C.B. Jackson, and Gabe Shaughnessy. Higgs-pair production and measurement of the triscalar coupling at lhc(8,14). *Physics Letters B*, 728:433436, Jan 2014.
- [32] S. Dawson, S. Dittmaier, and M. Spira. Neutral higgs-boson pair production at hadron colliders: Qcd corrections. *Physical Review D*, 58(11), Nov 1998.
- [33] R. Frederix, S. Frixione, V. Hirschi, F. Maltoni, O. Mattelaer, P. Torrielli, E. Vryonidou, and M. Zaro. Higgs pair production at the LHC with NLO and parton-shower effects. *Phys. Lett. B*, 732:142–149, 2014.
- [34] Daniel de Florian and Javier Mazzitelli. Higgs Boson Pair Production at Next-to-Next-to-Leading Order in QCD. *Phys. Rev. Lett.*, 111:201801, 2013.

- [35] Jonathan Grigo, Kirill Melnikov, and Matthias Steinhauser. Virtual corrections to higgs boson pair production in the large top quark mass limit. *Nuclear Physics B*, 888:1729, Nov 2014.
- [36] Ding Yu Shao, Chong Sheng Li, Hai Tao Li, and Jian Wang. Threshold resummation effects in Higgs boson pair production at the LHC. *JHEP*, 07:169, 2013.
- [37] Daniel de Florian and Javier Mazzitelli. Higgs pair production at next-to-next-to-leading logarithmic accuracy at the LHC. *JHEP*, 09:053, 2015.
- [38] Long-Bin Chen, Hai Tao Li, Hua-Sheng Shao, and Jian Wang. Higgs boson pair production via gluon fusion at N³LO in QCD. *Phys. Lett. B*, 803:135292, 2020.
- [39] Jonathan Grigo, Jens Hoff, and Matthias Steinhauser. Higgs boson pair production: top quark mass effects at NLO and NNLO. *Nucl. Phys. B*, 900:412–430, 2015.
- [40] Jonathan Grigo, Jens Hoff, Kirill Melnikov, and Matthias Steinhauser. On the Higgs boson pair production at the LHC. *Nucl. Phys. B*, 875:1–17, 2013.
- [41] Jonathan Grigo, Jens Hoff, Kirill Melnikov, and Matthias Steinhauser. Higgs boson pair production at the LHC: top-quark mass effects at next-to-leading order. *PoS*, RADCOR2013:006, 2013.
- [42] Ramona Grber, Andreas Maier, and Thomas Rauh. Reconstruction of top-quark mass effects in higgs pair production and other gluon-fusion processes. *Journal of High Energy Physics*, 2018(3), Mar 2018.
- [43] Joshua Davies, Ramona Gröber, Andreas Maier, Thomas Rauh, and Matthias Steinhauser. Padé approach to top-quark mass effects in gluon fusion amplitudes. *PoS*, RADCOR2019:079, 2019.
- [44] Joshua Davies, Go Mishima, Matthias Steinhauser, and David Wellmann. Double-higgs boson production in the high-energy limit: planar master integrals. *Journal of High Energy Physics*, 2018(3), Mar 2018.
- [45] Joshua Davies, Go Mishima, Matthias Steinhauser, and David Wellmann. Double higgs boson production at nlo in the high-energy limit: complete analytic results. *Journal of High Energy Physics*, 2019(1), Jan 2019.
- [46] Joshua Davies, Gudrun Heinrich, Stephen P. Jones, Matthias Kerner, Go Mishima, Matthias Steinhauser, and David Wellmann. Double Higgs boson production at NLO: combining the exact numerical result and high-energy expansion. *JHEP*, 11:024, 2019.
- [47] S. Borowka, N. Greiner, G. Heinrich, S.P. Jones, M. Kerner, J. Schlenk, and T. Zirke. Full top quark mass dependence in Higgs boson pair production at NLO. *JHEP*, 10:107, 2016.
- [48] K.G. Chetyrkin and F.V. Tkachov. Integration by parts: The algorithm to calculate ϵ -functions in 4 loops. *Nuclear Physics B*, 192(1):159 – 204, 1981.
- [49] S. Laporta. High precision calculation of multiloop Feynman integrals by difference equations. *Int. J. Mod. Phys. A*, 15:5087–5159, 2000.
- [50] Gudrun Heinrich. Sector Decomposition. *Int. J. Mod. Phys. A*, 23:1457–1486, 2008.
- [51] John C. Collins, Davison E. Soper, and George F. Sterman. Factorization of Hard Processes in QCD. *Adv. Ser. Direct. High Energy Phys.*, 5:1–91, 1989.
- [52] Davison E. Soper. Parton distribution functions. *Nuclear Physics B - Proceedings Supplements*, 53(1-3):6980, Feb 1997.

- [53] R. P. Feynman. Space-time approach to quantum electrodynamics. *Phys. Rev.*, 76:769–789, Sep 1949.
- [54] E.W.Nigel Glover and J.J. van der Bij. HIGGS BOSON PAIR PRODUCTION VIA GLUON FUSION. *Nucl. Phys. B*, 309:282–294, 1988.
- [55] Gerard 't Hooft and M.J.G. Veltman. Regularization and Renormalization of Gauge Fields. *Nucl. Phys. B*, 44:189–213, 1972.
- [56] C. G. Bollini and J. J. Giambiagi. Dimensional Renormalization: The Number of Dimensions as a Regularizing Parameter. *Nuovo Cim. B*, 12:20–26, 1972.
- [57] G. 't Hooft. Dimensional regularization and the renormalization group. *Nuclear Physics B*, 61:455–468, 1973.
- [58] T. Kinoshita. Mass singularities of Feynman amplitudes. *J. Math. Phys.*, 3:650–677, 1962.
- [59] T. D. Lee and M. Nauenberg. Degenerate systems and mass singularities. *Phys. Rev.*, 133:B1549–B1562, Mar 1964.
- [60] S. Catani and M.H. Seymour. A general algorithm for calculating jet cross sections in nlo qcd. *Nuclear Physics B*, 485(1-2):291419, Feb 1997.
- [61] S. Catani and M.H. Seymour. The dipole formalism for the calculation of qcd jet cross sections at next-to-leading order. *Physics Letters B*, 378(1):287 – 301, 1996.
- [62] Stefano Catani, Stefan Dittmaier, Michael H. Seymour, and Zoltan Trecsnyi. The dipole formalism for next-to-leading order qcd calculations with massive partons. *Nuclear Physics B*, 627(1-2):189265, Apr 2002.
- [63] S. Frixione, Z. Kunszt, and A. Signer. Three-jet cross sections to next-to-leading order. *Nuclear Physics B*, 467(3):399442, May 1996.
- [64] David A. Kosower. Antenna factorization of gauge-theory amplitudes. *Physical Review D*, 57(9):54105416, May 1998.
- [65] A. Gehrmann-De Ridder and M Ritzmann. Nlo antenna subtraction with massive fermions. *Journal of High Energy Physics*, 2009(07):041041, Jul 2009.
- [66] G Peter Lepage. A new algorithm for adaptive multidimensional integration. *Journal of Computational Physics*, 27(2):192 – 203, 1978.
- [67] Julien Baglio, Francisco Campanario, Seraina Glaus, Margarete Mühlleitner, Michael Spira, and Juraj Streicher. Gluon fusion into Higgs pairs at NLO QCD and the top mass scheme. *Eur. Phys. J. C*, 79(6):459, 2019.
- [68] J. Baglio, F. Campanario, S. Glaus, M. Mühlleitner, J. Ronca, M. Spira, and J. Streicher. Higgs-Pair Production via Gluon Fusion at Hadron Colliders: NLO QCD Corrections. *JHEP*, 04:181, 2020.
- [69] J. Baglio, F. Campanario, S. Glaus, M. Mühlleitner, J. Ronca, and M. Spira. $gg \rightarrow HH$: Combined Uncertainties. 8 2020.
- [70] Murray Gell-Mann. A Schematic Model of Baryons and Mesons. *Phys. Lett.*, 8:214–215, 1964.
- [71] G. Zweig. *An $SU(3)$ model for strong interaction symmetry and its breaking. Version 2*, pages 22–101. 2 1964.
- [72] David J. Gross and Frank Wilczek. Ultraviolet behavior of non-abelian gauge theories. *Phys. Rev. Lett.*, 30:1343–1346, Jun 1973.

- [73] H. David Politzer. Reliable perturbative results for strong interactions? *Phys. Rev. Lett.*, 30:1346–1349, Jun 1973.
- [74] M.Y. Han and Yoichiro Nambu. Three Triplet Model with Double SU(3) Symmetry. *Phys. Rev.*, 139:B1006–B1010, 1965.
- [75] H. Fritzsch, Murray Gell-Mann, and H. Leutwyler. Advantages of the Color Octet Gluon Picture. *Phys. Lett. B*, 47:365–368, 1973.
- [76] D.J. Gross and Frank Wilczek. Asymptotically Free Gauge Theories - I. *Phys. Rev. D*, 8:3633–3652, 1973.
- [77] H.David Politzer. Asymptotic Freedom: An Approach to Strong Interactions. *Phys. Rept.*, 14:129–180, 1974.
- [78] S.L. Glashow. Partial Symmetries of Weak Interactions. *Nucl. Phys.*, 22:579–588, 1961.
- [79] Abdus Salam and John Clive Ward. Electromagnetic and weak interactions. *Phys. Lett.*, 13:168–171, 1964.
- [80] Steven Weinberg. A model of leptons. *Phys. Rev. Lett.*, 19:1264–1266, Nov 1967.
- [81] Kazuhiko Nishijima. Charge Independence Theory of V Particles. *Prog. Theor. Phys.*, 13(3):285–304, 1955.
- [82] M. Gell-Mann. The interpretation of the new particles as displaced charge multiplets. *Nuovo Cim.*, 4(S2):848–866, 1956.
- [83] Gerard 't Hooft. Renormalizable Lagrangians for Massive Yang-Mills Fields. *Nucl. Phys. B*, 35:167–188, 1971.
- [84] Nicola Cabibbo. Unitary symmetry and leptonic decays. *Phys. Rev. Lett.*, 10:531–533, Jun 1963.
- [85] Makoto Kobayashi and Toshihide Maskawa. CP Violation in the Renormalizable Theory of Weak Interaction. *Prog. Theor. Phys.*, 49:652–657, 1973.
- [86] B. Pontecorvo. Inverse beta processes and nonconservation of lepton charge. *Sov. Phys. JETP*, 7:172–173, 1958.
- [87] Ziro Maki, Masami Nakagawa, and Shoichi Sakata. Remarks on the Unified Model of Elementary Particles. *Progress of Theoretical Physics*, 28(5):870–880, 11 1962.
- [88] P.A. Zyla et al. Review of Particle Physics. *PTEP*, 2020(8):083C01, 2020.
- [89] Howard E. Haber and Gordon L. Kane. The Search for Supersymmetry: Probing Physics Beyond the Standard Model. *Phys. Rept.*, 117:75–263, 1985.
- [90] Jihn E. Kim. Light Pseudoscalars, Particle Physics and Cosmology. *Phys. Rept.*, 150:1–177, 1987.
- [91] R.D. Peccei and Helen R. Quinn. CP Conservation in the Presence of Instantons. *Phys. Rev. Lett.*, 38:1440–1443, 1977.
- [92] Neil Turok and John Zadrozny. Electroweak baryogenesis in the two doublet model. *Nucl. Phys. B*, 358:471–493, 1991.
- [93] James M. Cline, Kimmo Kainulainen, and Axel P. Vischer. Dynamics of two Higgs doublet CP violation and baryogenesis at the electroweak phase transition. *Phys. Rev. D*, 54:2451–2472, 1996.

- [94] Lars Fromme, Stephan J Huber, and Michael Seniuch. Baryogenesis in the two-higgs doublet model. *Journal of High Energy Physics*, 2006(11):038038, Nov 2006.
- [95] T.D. Lee. A Theory of Spontaneous T Violation. *Phys. Rev. D*, 8:1226–1239, 1973.
- [96] Nilendra G. Deshpande and Ernest Ma. Pattern of Symmetry Breaking with Two Higgs Doublets. *Phys. Rev. D*, 18:2574, 1978.
- [97] K.G. Klimenko. On Necessary and Sufficient Conditions for Some Higgs Potentials to Be Bounded From Below. *Theor. Math. Phys.*, 62:58–65, 1985.
- [98] John F. Gunion and Howard E. Haber. The CP conserving two Higgs doublet model: The Approach to the decoupling limit. *Phys. Rev. D*, 67:075019, 2003.
- [99] Felix Kling, Shufang Su, and Wei Su. 2hdm neutral scalars under the lhc. *Journal of High Energy Physics*, 2020(6), Jun 2020.
- [100] Shinya Kanemura and Kei Yagyu. Unitarity bound in the most general two Higgs doublet model. *Phys. Lett. B*, 751:289–296, 2015.
- [101] I.F. Ginzburg and I.P. Ivanov. Tree-level unitarity constraints in the most general 2HDM. *Phys. Rev. D*, 72:115010, 2005.
- [102] Johan Bijnens, Jie Lu, and Johan Rathsman. Constraining General Two Higgs Doublet Models by the Evolution of Yukawa Couplings. *JHEP*, 05:118, 2012.
- [103] Vernon D. Barger, J.L. Hewett, and R.J.N. Phillips. New Constraints on the Charged Higgs Sector in Two Higgs Doublet Models. *Phys. Rev. D*, 41:3421–3441, 1990.
- [104] Benjamin W. Lee, C. Quigg, and H.B. Thacker. Weak Interactions at Very High-Energies: The Role of the Higgs Boson Mass. *Phys. Rev. D*, 16:1519, 1977.
- [105] M. Carena and H.E. Haber. Higgs boson theory and phenomenology. *Progress in Particle and Nuclear Physics*, 50(1):63152, Jan 2003.
- [106] Emmanuel A. Paschos. Diagonal neutral currents. *Phys. Rev. D*, 15:1966–1972, Apr 1977.
- [107] Sheldon L. Glashow and Steven Weinberg. Natural Conservation Laws for Neutral Currents. *Phys. Rev. D*, 15:1958, 1977.
- [108] Antonio Pich and Paula Tuzn. Yukawa alignment in the two-higgs-doublet model. *Physical Review D*, 80(9), Nov 2009.
- [109] Antonio Pich and Paula Tuzon. The aligned two-higgs doublet model, 2010.
- [110] H. Serdio. Yukawa alignment in a multi higgs doublet model: An effective approach. *Physics Letters B*, 700(2):133138, Jun 2011.
- [111] Laura Lopez Honorez, Emmanuel Nezri, Josep F. Oliver, and Michel H.G. Tytgat. The Inert Doublet Model: An Archetype for Dark Matter. *JCAP*, 02:028, 2007.
- [112] Ernest Ma. Verifiable radiative seesaw mechanism of neutrino mass and dark matter. *Physical Review D*, 73(7), Apr 2006.
- [113] ERNEST MA. Common origin of neutrino mass, dark matter, and baryogenesis. *Modern Physics Letters A*, 21(23):17771781, Jul 2006.
- [114] DEBASISH MAJUMDAR and AMBAR GHOSAL. Dark matter candidate in a heavy higgs model: Direct detection rates. *Modern Physics Letters A*, 23(24):20112022, Aug 2008.

- [115] Alejandra Melfo, Miha Nemevek, Fabrizio Nesti, Goran Senjanovi, and Yue Zhang. Inert doublet dark matter and mirror/extra families after xenon100. *Physical Review D*, 84(3), Aug 2011.
- [116] I. F. Ginzburg, K. A. Kanishev, M. Krawczyk, and D. Sokoowska. Evolution of the universe to the present inert phase. *Physical Review D*, 82(12), Dec 2010.
- [117] Tommi Alanne, Kimmo Kainulainen, Kimmo Tuominen, and Ville Vaskonen. Baryogenesis in the two doublet and inert singlet extension of the Standard Model. *JCAP*, 08:057, 2016.
- [118] Marcela Carena, David Garcia, Ulrich Nierste, and Carlos E.M. Wagner. Effective lagrangian for the interaction in the mssm and charged higgs phenomenology. *Nuclear Physics B*, 577(1-2):88120, Jun 2000.
- [119] Jaume Guasch, Petra Haffiger, and Michael Spira. MSSM Higgs decays to bottom quark pairs revisited. *Phys. Rev. D*, 68:115001, 2003.
- [120] Sacha Davidson and Howard E. Haber. Basis-independent methods for the two-Higgs-doublet model. *Phys. Rev. D*, 72:035004, 2005. [Erratum: Phys.Rev.D 72, 099902 (2005)].
- [121] Emanuele Bagnaschi, Felix Brümmer, Wilfried Buchmüller, Alexander Voigt, and Georg Weiglein. Vacuum stability and supersymmetry at high scales with two Higgs doublets. *JHEP*, 03:158, 2016.
- [122] Kaustubh Agashe, Roberto Contino, and Alex Pomarol. The Minimal composite Higgs model. *Nucl. Phys. B*, 719:165–187, 2005.
- [123] Martin Schmaltz and David Tucker-Smith. Little higgs theories. *Annual Review of Nuclear and Particle Science*, 55(1):229270, Dec 2005.
- [124] Csaba Csaki, Christophe Grojean, and John Terning. Alternatives to an Elementary Higgs. *Rev. Mod. Phys.*, 88(4):045001, 2016.
- [125] Indrani Chakraborty and Anirban Kundu. Two-higgs doublet models confront the naturalness problem. *Physical Review D*, 90(11), Dec 2014.
- [126] Gustavo Burdman, Carlos E.F. Haluch, and Ricardo D. Matheus. Is the LHC Observing the Pseudo-scalar State of a Two-Higgs Doublet Model ? *Phys. Rev. D*, 85:095016, 2012.
- [127] P. M. Ferreira, Rui Santos, Marc Sher, and Joo P. Silva. Could the lhc two-photon signal correspond to the heavier scalar in two-higgs-doublet models? *Physical Review D*, 85(3), Feb 2012.
- [128] Georges Aad et al. Measurements of the Higgs boson production and decay rates and constraints on its couplings from a combined ATLAS and CMS analysis of the LHC pp collision data at $\sqrt{s} = 7$ and 8 TeV. *JHEP*, 08:045, 2016.
- [129] Study of the double Higgs production channel $H(\rightarrow b\bar{b})H(\rightarrow \gamma\gamma)$ with the ATLAS experiment at the HL-LHC. 1 2017.
- [130] T. Plehn, M. Spira, and P.M. Zerwas. Pair production of neutral higgs particles in gluon-gluon collisions. *Nuclear Physics B*, 479(1-2):4664, Nov 1996.
- [131] O.J.P. boli, G.C. Marques, S.F. Novaes, and A.A. Natale. Twin higgs-boson production. *Physics Letters B*, 197(1):269 – 272, 1987.
- [132] Duane A. Dicus, Chung Kao, and Scott S.D. Willenbrock. Higgs boson pair production from gluon fusion. *Physics Letters B*, 203(4):457 – 461, 1988.
- [133] Wai-Yee Keung. Double Higgs From $W - W$ Fusion. *Mod. Phys. Lett. A*, 2:765, 1987.

- [134] Kalpana J. Kallianpur. Pair-production of higgs bosons via heavy quark annihilation. *Physics Letters B*, 215(2):392 – 396, 1988.
- [135] A. Dobrovolskaya and V. Novikov. On heavy Higgs boson production. *Z. Phys. C*, 52:427–436, 1991.
- [136] Vernon D. Barger, Tao Han, and R.J.N. Phillips. Double Higgs Boson Bremsstrahlung From W and Z Bosons at Supercolliders. *Phys. Rev. D*, 38:2766, 1988.
- [137] M. Moretti, S. Moretti, F. Piccinini, R. Pittau, and A.D. Polosa. Higgs boson self-couplings at the LHC as a probe of extended Higgs sectors. *JHEP*, 02:024, 2005.
- [138] A. Djouadi, M. Spira, and P.M. Zerwas. Production of Higgs bosons in proton colliders: QCD corrections. *Phys. Lett. B*, 264:440–446, 1991.
- [139] S. Dawson. Radiative corrections to Higgs boson production. *Nucl. Phys. B*, 359:283–300, 1991.
- [140] D. Graudenz, M. Spira, and P. M. Zerwas. Qcd corrections to higgs-boson production at proton-proton colliders. *Phys. Rev. Lett.*, 70:1372–1375, Mar 1993.
- [141] M. Spira, A. Djouadi, D. Graudenz, and R.M. Zerwas. Higgs boson production at the lhc. *Nuclear Physics B*, 453(1-2):1782, Oct 1995.
- [142] Charalampos Anastasiou, Stefan Bucherer, and Zoltan Kunszt. Hpro: A nlo monte-carlo for higgs production via gluon fusion with finite heavy quark masses. *Journal of High Energy Physics*, 2009(10):068068, Oct 2009.
- [143] Roberto Bonciani, Giuseppe Degrossi, Pier Paolo Giardino, and Ramona Gröber. Analytical Method for Next-to-Leading-Order QCD Corrections to Double-Higgs Production. *Phys. Rev. Lett.*, 121(16):162003, 2018.
- [144] S. Borowka, N. Greiner, G. Heinrich, S.P. Jones, M. Kerner, J. Schlenk, U. Schubert, and T. Zirke. Higgs Boson Pair Production in Gluon Fusion at Next-to-Leading Order with Full Top-Quark Mass Dependence. *Phys. Rev. Lett.*, 117(1):012001, 2016. [Erratum: Phys.Rev.Lett. 117, 079901 (2016)].
- [145] Christian Schubert. On the gamma(5) problem of dimensional renormalization. 12 1993.
- [146] Stephen L. Adler. Axial vector vertex in spinor electrodynamics. *Phys. Rev.*, 177:2426–2438, 1969.
- [147] J.S. Bell and R. Jackiw. A PCAC puzzle: $\pi^0 \rightarrow \gamma\gamma$ in the σ model. *Nuovo Cim. A*, 60:47–61, 1969.
- [148] P. Breitenlohner and D. Maison. Dimensionally Renormalized Green’s Functions for Theories with Massless Particles. 2. *Commun. Math. Phys.*, 52:55, 1977.
- [149] G. Passarino and M. Veltman. One-loop corrections for e+e annihilation into $\mu^+\mu^-$ in the weinberg model. *Nuclear Physics B*, 160(1):151 – 207, 1979.
- [150] Michael Spira. HIGLU: A program for the calculation of the total Higgs production cross-section at hadron colliders via gluon fusion including QCD corrections. 10 1995.
- [151] T. Hahn. Generating and calculating one loop Feynman diagrams with FeynArts, FormCalc, and LoopTools. In *6th International Workshop on New Computing Techniques in Physics Research: Software Engineering, Artificial Intelligence Neural Nets, Genetic Algorithms, Symbolic Algebra, Automatic Calculation*, 4 1999.
- [152] Vladyslav Shtabovenko, Rolf Mertig, and Frederik Orellana. FeynCalc 9.3: New features and improvements. *Comput. Phys. Commun.*, 256:107478, 2020.

- [153] L. F. Richardson. The approximate arithmetical solution by finite differences of physical problems involving differential equations, with an application to the stresses in a masonry dam. *Philosophical Transactions of the Royal Society of London. Series A, Containing Papers of a Mathematical or Physical Character*, 210:307–357, 1911.
- [154] Jon Butterworth, Stefano Carrazza, Amanda Cooper-Sarkar, Albert De Roeck, Jol Feltesse, Stefano Forte, Jun Gao, Sasha Glazov, Joey Huston, Zahari Kassabov, and et al. Pdf4lhc recommendations for lhc run ii. *Journal of Physics G: Nuclear and Particle Physics*, 43(2):023001, Jan 2016.
- [155] L. A. Harland-Lang, A. D. Martin, P. Motylinski, and R. S. Thorne. Parton distributions in the lhc era: Mmht 2014 pdfs. *The European Physical Journal C*, 75(5), May 2015.
- [156] Massimiliano Grazzini, Gudrun Heinrich, Stephen Jones, Stefan Kallweit, Matthias Kerner, Jonas M. Lindert, and Javier Mazzitelli. Higgs boson pair production at NNLO with top quark mass effects. *JHEP*, 05:059, 2018.
- [157] G. Degrossi, M. Fedele, and P.P. Giardino. Constraints on the trilinear higgs self coupling from precision observables. *Journal of High Energy Physics*, 2017(4), Apr 2017.
- [158] R. Grber, M. Mühlleitner, M. Spira, and J. Streicher. Nlo qcd corrections to higgs pair production including dimension-6 operators. *Journal of High Energy Physics*, 2015(9), Sep 2015.
- [159] Daniel de Florian, Ignacio Fabre, and Javier Mazzitelli. Higgs boson pair production at nnlo in qcd including dimension 6 operators. *Journal of High Energy Physics*, 2017(10), Oct 2017.
- [160] G. Buchalla, M. Capozzi, A. Celis, G. Heinrich, and L. Scyboz. Higgs boson pair production in non-linear effective field theory with full mt-dependence at nlo qcd. *Journal of High Energy Physics*, 2018(9), Sep 2018.
- [161] A. Djouadi, W. Kilian, M. Mühlleitner, and P.M. Zerwas. Production of neutral higgs-boson pairs at lhc. *The European Physical Journal C*, 10(1):4549, Aug 1999.
- [162] Xin Li and M.B. Voloshin. Remarks on double higgs boson production by gluon fusion at threshold. *Physical Review D*, 89(1), Jan 2014.
- [163] N. Gray, David J. Broadhurst, W. Grafe, and K. Schilcher. Three Loop Relation of Quark (Modified) Ms and Pole Masses. *Z. Phys. C*, 48:673–680, 1990.
- [164] K.G. Chetyrkin. Quark mass anomalous dimension to o (s4). *Physics Letters B*, 404(1-2):161165, Jul 1997.
- [165] K. G. Chetyrkin and M. Steinhauser. Short-distance mass of a heavy quark at order α_s^3 . *Physical Review Letters*, 83(20):40014004, Nov 1999.
- [166] K.G. Chetyrkin and M. Steinhauser. The relation between the and the on-shell quark mass at order s3. *Nuclear Physics B*, 573(3):617651, May 2000.
- [167] Kirill Melnikov and Timo van Ritbergen. The three-loop relation between the and the pole quark masses. *Physics Letters B*, 482(1-3):99108, Jun 2000.
- [168] Michael Spira. Effective multi-higgs couplings to gluons. *Journal of High Energy Physics*, 2016(10), Oct 2016.
- [169] Marvin Gerlach, Florian Herren, and Matthias Steinhauser. Wilson coefficients for higgs boson production and decoupling relations to os4O (α_s^4). *Journal of High Energy Physics*, 2018(11), Nov 2018.
- [170] Ansgar Denner and S. Dittmaier. Reduction schemes for one-loop tensor integrals. *Nucl. Phys. B*, 734:62–115, 2006.

- [171] Francisco Campanario. Towards $pp \rightarrow VVjj$ at NLO QCD: Bosonic contributions to triple vector boson production plus jet. *JHEP*, 10:070, 2011.
- [172] G. Barucchi and G. Ponzano. Differential equations for oneloop generalized feynman integrals. *Journal of Mathematical Physics*, 14:396–401, 03 1973.
- [173] A. V. Kotikov. Differential equations method: New technique for massive Feynman diagrams calculation. *Phys. Lett.*, B254:158–164, 1991.
- [174] T. Gehrmann and E. Remiddi. Differential equations for two-loop four-point functions. *Nuclear Physics B*, 580(1-2):485518, Jul 2000.
- [175] Ettore Remiddi. Differential equations for Feynman graph amplitudes. *Nuovo Cim.*, A110:1435–1452, 1997.
- [176] Mario Argeri and Pierpaolo Mastrolia. Feynman diagrams and differential equations. *International Journal of Modern Physics A*, 22(24):43754436, Sep 2007.
- [177] Mario Argeri, Stefano Di Vita, Pierpaolo Mastrolia, Edoardo Mirabella, Johannes Schlenk, Ulrich Schubert, and Lorenzo Tancredi. Magnus and Dyson Series for Master Integrals. *JHEP*, 03:082, 2014.
- [178] John C. Collins. *Renormalization: An Introduction to Renormalization, The Renormalization Group, and the Operator Product Expansion*, volume 26 of *Cambridge Monographs on Mathematical Physics*. Cambridge University Press, Cambridge, 1986.
- [179] J. Collins, F. Wilczek, and A. Zee. Low-energy manifestations of heavy particles: Application to the neutral current. *Phys. Rev. D*, 18:242–247, Jul 1978.
- [180] William J. Marciano. Flavor thresholds and Λ in the modified minimal-subtraction scheme. *Phys. Rev. D*, 29:580–582, Feb 1984.
- [181] P. Nason, S. Dawson, and R.K. Ellis. The total cross section for the production of heavy quarks in hadronic collisions. *Nuclear Physics B*, 303(4):607 – 633, 1988.
- [182] K.G. Chetyrkin, Bernd A. Kniehl, and M. Steinhauser. Decoupling relations to $O(\alpha_s^3)$ and their connection to low-energy theorems. *Nucl. Phys. B*, 510:61–87, 1998.

Acknowledgements

It has been a long journey up here, a journey that I could never have ended without the precious help and support from many colleagues and friends.

First of all, I would like to thank my thesis director, Dr. Francisco Campanario for the immense patience, the fruitful discussions, for sharing his countless codes and knowledge with me, for all the hours spent into the debugging, but especially for giving me the possibility of joining this project and of collaborating with many amazing physicists, allowing me to do this first priceless experience as a researcher. I also would like to thank all my collaborators Dr. Julien Baglio, Dr. Seraina Glaus, Prof. Dr. Margarete Müllheitner and Dr. Michael Spira: Dr. Julien Baglio for sharing with me the struggle of the cross-check of the real corrections (which is still currently incomplete), for the hospitality at the CERN and for all the discussions; Dr. Seraina Glaus and Prof. Dr. Margarete Müllheitner for hosting me for the one-month stay at the KIT; Dr. Michael Spira for the explanations regarding all the theoretical background of this project in their tiniest details.

I thank also the colleagues of the MUONE collaboration for permitting me to contribute to this immense project that, for reasons of time, I did not included in this thesis. In particular I would like to thank Prof. Pierpaolo Mastrolia for being a guide and to push forward the calculation of the virtual corrections of the μe -scattering despite of all the issues. I would also thank Amedeo Primo and Ulrich Schubert for the help in the composition of all the parts of the calculation.

I would like to thank my colleague and friend William Torres for the irreplaceable support, discussions, trouble-shooting, for correcting my silly mistakes, for his help and discussions over AIDA, and for a lot of other things that I am definitely forgetting. But you know me Will. I would also thank Ivan Rosario, my office mate and colleague for his help, kindness, for the extremely interesting and not only physics-related discussions, and for the help with the abstract. I also thank Andres, Jesus and Selomit for the trying to teach me the castellano, without any actual success: I am not that good student after all. I also thank all my past office mates, colleagues and companions that accompanied me through this experience.

Last but not least, ringrazio i miei genitori Bruno e Lina per avermi supportato, spronato e creduto in me in ogni momento, senza se e senza ma. Senza di voi, oltre a non arrivare fino a qui, chissà se mai avrei avuto la forza di fare questa esperienza lontano da casa. Questo è un cammino che mi porterà spesso lontano da voi, ma per sempre considererò voi la mia "casa". Spero un giorno di rendervi davvero orgogliosi.

– Jonathan